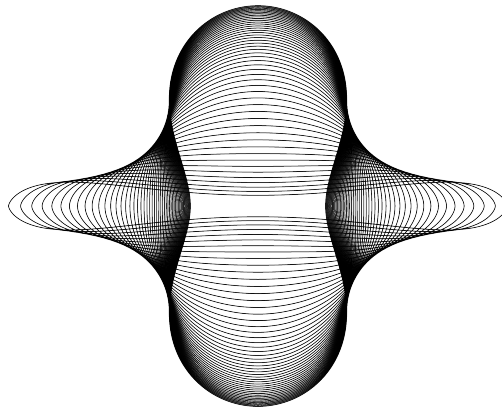# Deformation behavior of elastic shells and biological cells

Jonas Hegemann

A thesis presented for the degree of

Doctor rerum naturalium

Chair of Theoretical Physics Ib
Physics Department
TU Dortmund University
Germany
Dortmund, February 2018

Abstract

An elastic shell on the micro-scale filled with a suitable *passive* or *active* phase is what we refer to as a *microcapsule*. This work covers several classes of microcapsules spanning from *static* elastic shells under hydrostatic loads to animal cells made from a *dynamic* cytoskeleton interacting with a surrounding elastic shell. Both are microcapsules, the former enclosing a passive phase and the latter enclosing an active phase. Whereas passive microcapsules are important from a technical point of view, active microcapsules are predominantly relevant in biology. Both branches merge in the experimental realization of biological systems for which specially designed elastic containers are required. Deformations of microcapsules induced by constant axisymmetric loads are well described by classical continuum theories. These allow for reverse-engineering techniques, i.e., inferring information on the elastic material properties from shape profiles. Due to chemical activity, animal cells are, however, far from equilibrium and symmetry. Thus, they require refined models that account for the *physical* dynamics of the cytoskeleton, whose activity originates in *chemical* reactions. Enduring energy consumption results in a perpetually changing filament structure, where filaments grow stochastically and exert polymerization forces onto the shell. In turn, the shell exerts elastic forces onto filaments slowing down filament growth. This complex interplay between filament dynamics and shape changes of the elastic shell exhibits *collective phenomena*.

In the first part of this work, we employ elastic shell theory to investigate elastic shells filled with a fluid phase. We focus on rotationally symmetric shapes in three dimensions and calculate these from elastic shape equations in static force equilibrium. To determine the shell's elastic moduli from pendant capsule images we introduce an efficient open source software and demonstrate its applicability by numerous examples. As an extension, we introduce a novel shape analysis concerning elastic capsules adsorbed to planar liquid-liquid interfaces. Together, these two methods form a comprehensive framework to quantify the elastic properties of materials from experimental setups by non-contact techniques.

In the second part of this work, we employ a discrete elastic shell model without symmetry requirements in two dimensions. Dynamic microtubules placed inside the shell stochastically apply deformations to the shell. Investigating this non-equilibrium model with regard to its dynamic properties, we find that microtubules synchronize when interacting via an elastic shell, as found in an animal cell. Implementing regulatory mechanisms, we rationalize experimental observations concerning cell polarization, i.e., we find persistently polarized shapes by employing mutual exclusive feedback mechanisms with membrane associated proteins, which allow for breaking the spherical symmetry as it is necessary for cells that migrate or swim.

Zusammenfassung

Eine elastische Schale auf der Mikroskala, die mit einer geeigneten *passiven* oder *aktiven* Phase gefüllt ist, bezeichnen wir als *Mikrokapsel.* Diese Arbeit behandelt mehrere Klassen von Mikrokapseln, die von *statischen* elastischen Schalen unter hydrostatischer Belastung bis zu tierischen Zellen, in welchen ein *dynamisches* Zytoskelett mit einer umgebenden elastischen Schale interagiert, reichen. Während passive Mikrokapseln (erstere) wichtig im Hinblick auf technische Anwendungen sind, haben aktive Mikrokapseln (letztere) hauptsächlich biologische Relevanz. Beide Zweige verschmelzen in der experimentellen Realisierung biologischer Systeme, für die spezielle elastische Kontainer erforderlich sind. Verformungen von Mikrokapseln, die durch konstante achsensymmetrische Belastungen induziert werden, sind durch klassische Kontinuums-Theorien gut beschrieben. Diese ermöglichen Reverse-Engineering-Techniken, das heißt Rückschlüsse auf die elastischen Materialeigenschaften aus Formprofilen zu ziehen. Aufgrund der chemischen Aktivität sind tierische Zellen jedoch weit entfernt von Gleichgewicht und Symmetrie. So erfordern sie verfeinerte Modelle, in denen die *physikalische* Dynamik des Zytoskeletts, dessen Aktivität in *chemischen* Reaktionen entsteht, berücksichtigt wird. Der permanente Energieverbrauch führt zu einer sich ständig verändernden Filamentstruktur, bei der die Filamente stochastisch wachsen und Polymerisationskräfte auf die Schale ausüben. Die Schale wiederum übt elastische Kräfte auf die Filamente aus und verlangsamt so das Filamentwachstum. Dieses komplexe Zusammenspiel von Filamentdynamik und Formänderungen der elastischen Schale bringt *kollektive Phänomene* hervor.

Im ersten Teil dieser Arbeit untersuchen wir theoretisch elastische Schalen, die mit einer flüssigen Phase gefüllt sind. Wir konzentrieren uns auf rotationssymmetrische Formen in drei Dimensionen und berechnen diese aus elastischen Formgleichungen im statischen Kraftgleichgewicht. Um die Elastizitätsmoduln der Schale anhand von Bildern hängender Kapseln zu bestimmen, stellen wir eine leistungsfähige Open-Source-Software vor und zeigen anhand zahlreicher Beispiele ihre Anwendbarkeit. Als Erweiterung stellen wir eine neuartige Formanalyse für elastische Kapseln vor, die an planaren Flüssig-Flüssig-Grenzflächen adsorbiert sind. Zusammen bilden diese beiden Methoden einen umfassenden Rahmen zur Quantifizierung der elastischen Eigenschaften von Werkstoffen aus Versuchsaufbauten durch berührungslose Verfahren.

Im zweiten Teil dieser Arbeit verwenden wir ein diskretes elastisches Schalenmodell ohne Symmetrieanforderungen in zwei Dimensionen. Dynamische Mikrotubuli im Inneren der Schale verformen diese stochastisch. Die Untersuchung dieses Nichtgleichgewichtsmodells hinsichtlich seiner dynamischen Eigenschaften zeigt, dass sich Mikrotubuli bei der Interaktion über eine elastische Hülle synchronisieren. Indem wir regulatorische Mechanismen implementieren, machen wir experimentelle Beobachtungen zur Zellpolarisation plausibel, d. h. wir finden persistent polarisierte Formen durch den Einsatz von sich gegenseitig ausschließenden Rückkopplungsmechanismen mit Membran-assoziierten Proteinen, die es erlauben die sphärische Symmetrie zu brechen, wie es für migrierende oder schwimmende Zellen notwendig ist.

Contents

1 Outline of the thesis

This thesis has been supervised by Prof. Jan Kierfeld at TU Dortmund University. A brief outline of the content and important results is given below.

An elastic shell on the micro-scale filled with a suitable passive or active phase is what we refer to as a *microcapsule*. In this thesis, we cover two classes of microcapsules, namely elastic shells subjected to hydrostatic loads (surface tension and pressure) and elastic shells subjected to dynamic forces exerted by active filament structures. The former is relevant in several technical and clinical applications as will be pointed out in chapter 2, whereas the latter serves as a model for animal cells, which are essential biological building blocks, as will be pointed out in chapter 3.

Both classes of microcapsules have crucial properties in common. They provide isolated or regulated compartments serving as cargo containers in case of simple shells and, additionally, as chemical reactors in case of animal cells. The term 'compartment' is generally defined as a closed spatial barrier of arbitrary shape. Compartments are necessary for the protection of the cargo or providing the required chemical conditions for filament assembly. Shells or membranes (thin shells) are flexible compartments and exhibit elastic properties, such that they dynamically change their shape when they are subjected to forces as, for example, shells in a cell colony. In addition to external forces exerted by neighboring cells or the extracellular matrix, internal polymerization forces exerted by filament growth likewise induce shape changes and give rise to feedback mechanisms. Due to the diversity of shape change phenomena it is important to gain a deeper understanding of these flexible compartments.

As a part of this, we introduce the framework of classical elastic shell theory in chapter 2 and review elastic shape equations. These have been used successfully within reverse-engineering techniques in the past [1]. In this thesis, we consider two different hydrostatic setups, which are (i) a capsule adsorbed to a liquid-liquid interface (sec. 2.1) and (ii) a capsule hanging from a capillary like in a pendant drop tensiometer (sec. 2.2). First, we present a shape analysis for (i) employing the full set of elastic constants while including the bending rigidity (sec. 2.1). We derive analytic expressions that allow us to determine the surface Young modulus and the bending modulus of the shell material from experimentally accessible quantities. We show that the surface Young modulus can be obtained by measuring the height of the capsule or, alternatively, the contact angle at the three phase contact line. The bending modulus can be obtained from the surface tension in the interface plane, the thickness of the capsule layer, and the surface curvature in meridional direction at the three phase contact line. The results concerning elastic capsules at liquid-liquid interfaces originate from a collaboration with Dr. Horst-Holger Boltz and have, to the date of handing in this thesis, been submitted as a regular article to the Soft Matter Journal [2]. The shape analysis of adsorbed capsules is a novel approach that suffers so far from lacking experimental data. However, soft elastic microcapsules are promising candidates for emulsification purposes, because their adsorption energy is significantly increased compared to filled soft particles. We apply the shape analysis to (ii) using a reduced set of elastic constants while neglecting the bending rigidity (sec. 2.2). The bending rigidity is determined afterwards in a separate wrinkle analysis. The shape analysis for capsules in pendant drop tensiometers (sec. 2.2) is relevant in research and industry, which is why we give a detailed description of the corresponding numerical analysis in sec. 2.3 and provide the source code [3] under a GPL

license [4]. The results concerning pendant elastic capsules originate from a collaboration with the chair of physical chemistry of Prof. Heinz Rehage at TU Dortmund University and have been published in the Journal of Colloid and Interface Science [5].

Apart from technical applications, we note that animal cells are the most complex microcapsules found on earth. Their activity expresses in a huge number of proteins that collaborate and, thus, form a collective. The result is a mechanical machine with abilities to sense its environment and to perform different actions. Theoretical physics can only approach this complexity by massive coarse-graining, i.e., focusing on the macroscopic properties. In this thesis, we incrementally develop such an approach. We start by presenting cell mechanics with an extensive introduction in chapter 3. Thereafter we cover the stochastic (and force-dependent) dynamics of single microtubules in section 3.1. Employing this framework we pursue mean-field approaches for a single microtubule interacting with an elastic barrier in section 3.2 and multiple microtubules interacting collectively with a shared elastic barrier in section 3.3. The latter has been investigated in [6] but we provide an improved version of this theory. In section 3.4 we develop a two-dimensional stochastic simulation model and identify the key features found in both theories from sections 3.2 and 3.3. Finally, in section 3.5, we include the Rac-Rho feedback mechanism into the two-dimensional simulation model and study polymerization phenomena. We find persistent cellular polarization employing two coupled feedback mechanisms involving microtubule dynamics and the Rho GTPases Rac and Rho. The results concerning cell mechanics have, to the date of handing in this thesis, not been published.

In chapter 4 we summarize our results and give a perspective for possible future work.

2 Deformation behavior of static elastic shells under hydrostatic loads

> "The willow which bends to the tempest, often escapes better than the oak which resists it; and so in great calamities, it sometimes happens that light and frivolous spirits recover their elasticity and presence of mind sooner than those of a loftier character."

Albert Schweizer

Microcapsules, "hollow microparticles composed of a solid shell surrounding a core-forming space available to permanently or temporarily entrapped substances" [7] (Fig. 2.1), are both an **important artificial construct used in many applications** as well as an essential model for biologically relevant elastic containers, such as cells, vesicles, virus capsules and red blood cells [8–20]. The solid shell can be comprised of, amongst others, colloidosomes [21, 22], copolymer vesicles [23], polymer multilayers [12], or bacteria [24], and gives rise to elastic properties allowing for tunable deformability and mechanical adaptation. The core-forming space can be made from liquids, polymer matrices (gel-like), or solid cores [19], with the typical situation being a capsule enclosing a liquid phase. For all applications, a characterization of the mechanical properties of the capsule shell, i.e., its elastic moduli, is necessary [25, 26].

The exact composition of the solid shell and the core-forming space depends on the specific application, where **requirements might be of chemical, biological or mechanical nature**. Drugs are the main application of microcapsules nowadays [16]. In medicine, microcapsules enable targeted release of incorporated drugs or cells under certain conditions [12, 13]. Moreover, microcapsules are used for food [14], textiles [15], cosmetics [16], self-healing materials [17, 18, 27] and powders [19].

Elasticity protects microcapsules from breakage or rupture by converting externally applied forces into deformation energy. This enables microcapsules to resist high external loads, pass through thin capillaries, and take diverse shapes. In order to ensure their function, microcapsules need to be probed and manipulated. In vivo, red blood cells change their shape to enter or pass thin blood vessels. This is a crucial ability and therefore continuously tested by the human spleen [28], which picks out cells having lost their elasticity due to aging. Microcapsules can also be stress-tested in vitro by exposing them to hypertonic solutions [29] or shear stress [30], and have been successfully functionalized with magnetic/gold particles allowing for positioning via applied magnetic fields, but also for opening via laser irradiation [31].

Talking about elasticity, we need to differentiate between **bending and stretching elasticity**. Depending on the material structure one of them may dominate or both contribute equally. Vesicles exhibit a vast shape diversity that is purely determined by bending energy and inextensibility [36]. A good example where both bending and stretching contribute are red blood cells, which likewise exhibit a vast shape diversity [37]. Many artificial microcapsules are made from polymeric materials that predominantly exhibit stretching elasticity [5]. In general, assuming an isotropic and homogeneous material, the
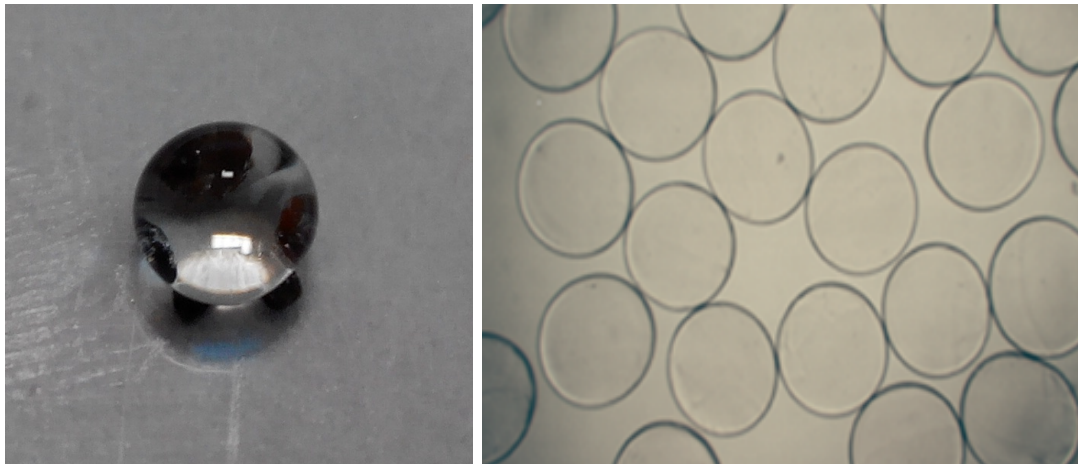
Figure 2.1: Left: Droplet holding a spherical shape on 5 grains of hydrophobic sand, licensed under CC BY-SA 4.0 [32] and provided via Creative Commons [33]. The surface tension prevents wetting of the surface and maintains the cluster of water molecules. **Right:** Alginate-chitosan microcapsules observed through a microscope, licensed under CC BY 3.0 [34] and provided via Creative Commons [35].

dominating contribution can be identified from the ratio of stretching and bending energy which is $\sim (R_0/H)^2$ [38] for a spherical shell of size R_0 and thickness H. Bending becomes important if R_0 and H are of the same order, i.e., $R_0 \sim H$. In the stretching dominated regime we have, however, $R_0 \gg H$, corresponding to a thin shell. In addition to bending and stretching, shells that have been assembled at a liquid interface are also subject to surface tension, which can be easily included in the elastic description [1]. The impact of surface tension on the elastic properties is usually small for mm sized capsules, but becomes increasingly important for smaller capsules of size $\sim 100\,\mathrm{nm}$ [39].

Many aspects of elastic shells have been discussed in literature, predominantly **buckling and wrinkling** [40–47], where the elasticity regimes just discussed play an important role. Apart from purely elastic features of the membrane, different constraints can be included in the theoretical description, such as **volume and area constraints**. For red blood cells or vesicles both constraints apply [37, 48]. In general, volume constraints apply for shells with an impermeable membrane being filled with an incompressible liquid, whereas area constraints apply for inextensible shells.

Elastic shell theory is not only applicable to microcapsules, it also applies on larger scales, e.g., for domes or gas containers [49]. The microcapsules we are interested in can be referred to the **micro-scale** ranging in size from μm to mm and are primarily relevant in biology as well as in technical applications. In contrast to the larger macroscopic scales, where objects compete with wind blasts or gas pressure, microcapsules on the micro-scale have to deal with hydrostatic forces, thermal fluctuations, or force exertion by filaments. Probing capsules on the micro-scale is thus more challenging from a technical point of view. The **visual microcapsule analysis techniques** provided in this work give rise to numerous possible applications in research departments and, being highly performant, these techniques are also suitable for industrial usage.

In the following two sections, we study **deformations of microcapsules in two different hydrostatic setups**. At first, we study **elastic microcapsules adsorbed to liquid-liquid interfaces** and introduce the elastic shape equations in their most general form for shells of finite thickness. We explore the full range of capsule shapes and discuss the limit of membranes, i.e., infinitesimal thin shells. In this limit, we also study **pendant**

elastic capsules, which can be prepared in pendant drop tensiometers. We provide a software, which determines the elastic constants from pendant capsule images by full shape analyses and we show that this method is widely applicable to different materials. In future work, the software for pendant capsules could be extended to capsules at liquid-liquid interfaces. The required theoretical groundwork will be established in the following section.

2.1 Elastic shells adsorbed to planar liquid-liquid interfaces

We investigate the deformation of elastic microcapsules adsorbed at liquid-liquid interfaces [2]. An initially spherical elastic capsule at a liquid-liquid interface undergoes equatorial stretching due to the liquid-liquid surface tension and becomes lens- or discus-shaped, depending on its bending rigidity. The resulting elastic capsule deformation is qualitatively similar, but distinct from the deformation of a liquid droplet into a liquid lens at a liquid-liquid interface. During capsule deformation at the liquid-liquid interface into a lens-like shape the adsorption energy, which is proportional to the occupied interface area, increases significantly leading to mechanical stabilization of the interface. This effect is useful in applications regarding foams and emulsion stabilization and is stronger for hollow soft elastic capsules as compared to filled soft particles. We discuss the deformed shapes of droplets or capsules adsorbed at liquid-liquid interfaces for a whole range of different surface elasticities: from droplets (only surface tension) leading to liquid lenses, to membrane covered droplets (finite stretching modulus, zero bending modulus) leading to the elastic lenses, to microcapsules (finite stretching and bending modulus) leading to rounded elastic lenses. We calculate capsule shapes at liquid-liquid interfaces numerically using shape equations from non-linear elastic shell theory. We also present theoretical results for the contact angle (or, alternatively, the capsule height) and the meridional capsule curvature at the three phase contact line, which provide methods to estimate elastic moduli from experimental shapes.

There have been various studies concerning hard particles at liquid-liquid interfaces [50, 51] that might be extended to deformable particles in the future resulting in an additional degree of tunability. Recently, the spreading of filled soft particles made from crosslinked gels (microgel particles) at liquid-liquid interfaces has been investigated experimentally [52], by molecular dynamics simulations [53, 54], and analytically [55]. When it comes to collective phenomena, experiments with microgel particles with solid silica cores have revealed complex packing phenomena at the interface [56]. Interfaces with soft shell hard particles also exhibit special elasticity with constitutive relations that change upon hard core contact [57]. Soft particles at liquid-liquid interfaces are efficient emulsifiers because they stretch during adsorption [55]. During deformation at the liquid-liquid interface a soft particle assumes a lens-like shape [53, 54], which increases the occupied interface area and, thus, the adsorption energy. Increased adsorption energies lead to a significantly more stable interface. In Ref. [58] the adsorption stability of nanoparticles at liquid-liquid interfaces has been investigated as a function of the particle shape, where it turns out that oblate shapes are most stable due to the high area occupation within the interface. This effect is more pronounced the softer the particle is. Therefore, hollow elastic capsules with a thin elastic shell, which are much softer than filled particles, are very attractive candidates to improve emulsification further. We will characterize their deformation behavior in detail in this section and show that elastic capsules or droplets at a liquid-liquid interface take discus-like shapes due to surface tension in the interface plane, which leads to an expansion of the capsule equator.

Whereas a liquid-liquid surface tension always exerts *tensile* equatorial tensions, there are also realizations of *contractile* equatorial tensions, which are impossible at a liquid-liquid interface. Positive (contractile) line tension leads to dumbbell shapes (equatorially

constricted spheres), e.g., for two component vesicles with phase separation [59], or during mitosis [60], where the tension is exerted by the contractile actin ring. The qualitative difference between these two cases is sketched in Fig. 2.2D.

Our perspective on capsule deformation by (interfacial) equatorial tension is that this constitutes an independent hydrostatic method of probing the deformation behavior and, thus, the elastic properties of microcapsules. Understanding the deformation under known external loads allows for elastometry, i.e, the determination of the elastic properties of the capsule's shell, which in turn can be used to infer information about the physics and chemistry of the shell as, for example, its state of crosslinking. We will show that the overall shape of the deformed capsule, i.e., the height or contact angle of the lens-like shape allows us to infer information about the Young's modulus of the capsule shell, whereas the meridional curvature at the 'tips' of the lens, i.e., across the equator where the tensile tension acts allows us to infer information about the bending modulus of the shell. Other elastometry methods following the same philosophy are the study of deformations of pendant capsules under volume changes to obtain elastic moduli as investigated in Refs. [1, 5, 61], the study of the edge curvature of a buckled shapes to obtain the bending modulus [44], or the study of shapes of osmotically buckled capsules to infer the osmotic pressure [62].

We study a model microcapsule under the influence of planar localized tensions, either extensile or contractile. The resulting shapes are given by the interplay of external loads and internal elasticity while accounting for possible additional constraints, such as volume (incompressibility) and area (local or global inextensibility) constraints. We focus on the volume constraint assuming incompressible liquids and impermeable shells as this is most relevant for applications. If the shell material has been assembled at a liquid-liquid interface, e.g., oil droplets in water, the interfacial surface tension gives an additional contribution to the elastic properties. One has to distinguish between the simpler *symmetric* case, where these interfacial surface tensions are equal in both liquid phases, which also leads to symmetric shapes, and the more general *asymmetric* case.

The section is structured as follows: at first, we introduce our model of a microcapsule, its solution using shape equations and the way how external loads and constraints are incorporated. Then, we discuss the resulting shapes in three elasticity regimes: the droplet regime, in which we only consider the effects of surface tension and incompressibility, the membrane regime corresponding to a shell of vanishing thickness but with finite Young's modulus, and the shell regime, where we also account for bending moments and transverse shear stress due to the shell's finite thickness. We will provide complete numerical solutions on the more general asymmetric case but, regarding analytic solutions, we focus on the symmetric case. We then show how the maximal capsule curvature at the liquid-liquid interface depends on the bending rigidity of the capsule shell and how this relation can be employed to measure the capsule's bending rigidity. Finally, we discuss the enhancement of the adsorption energy for hollow capsules.

2.1.1 Model

In this section, we introduce an elastic description (Hookean shell) suitable for shells of finite thickness as this is the most general case. Later on, we will simplify this description to discuss the cases of vanishing thickness (Hookean membrane without bending rigidity) and, ultimately, vanishing Young's modulus (liquid droplet).

We consider an elastic shell of thickness H whose resting shape is a sphere with radius R_0. In the limit of a thin shell, $H \ll R_0$, made from an isotropic and homogeneous elastic material we can map the three-dimensional elasticity onto an effective two-dimensional description with a two-dimensional Young's modulus $Y_{2D} = Y_{3D}H$ and a bending modulus
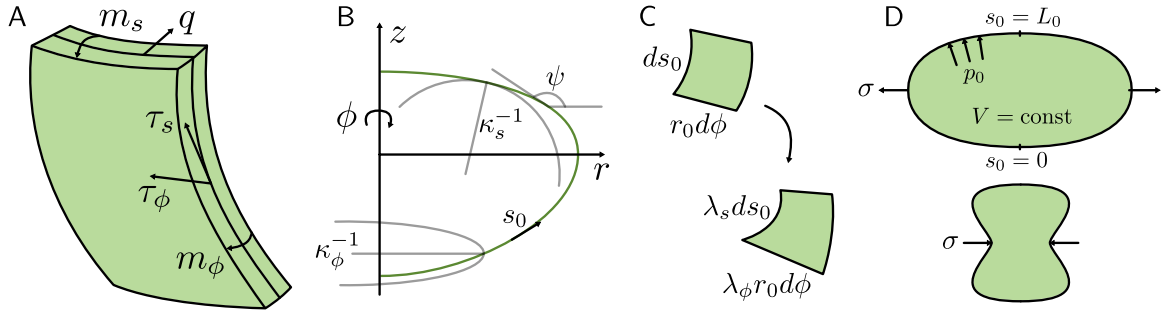
Figure 2.2: A) Forces and torques acting on an infinitesimal membrane patch. Both forces and torques are integrated over the thickness H of the material, which is assumed to be constant. **B)** Shape profile given by the shape equations. The shape profile generates a surface of revolution describing a three-dimensional axisymmetric object. The curvatures κ_ϕ and κ_s determine the local bending energy. **C)** Stretching of an infinitesimal membrane patch. The strains λ_ϕ and λ_s determine the local stretching energy. **D)** Two classes of deformations. Positive interface loads $\sigma > 0$ induce equatorial expansion, whereas negative interface loads $\sigma < 0$ induce equatorial compression and, thus, indentation. Assuming an incompressible liquid inside the capsule leads to volume conservation, which is controlled by a hydrostatic pressure difference $p_0 = p_{\text{in}} - p_{\text{out}}$.

given by [63]

$$E_{\mathrm{B}} = \frac{Y_{2\mathrm{D}}H^2}{12(1 - \nu_{2\mathrm{D}}^2)}, \tag{2.1}$$

where $\nu_{2\mathrm{D}}$ is the two-dimensional Poisson ratio taking values $-1 \leq \nu_{2\mathrm{D}} \leq 1$. Choosing R_0 as unit of length and $Y_{2\mathrm{D}}$ as unit of tension, the dimensionless bending modulus is given by

$$\tilde{E}_{\mathrm{B}} = \frac{E_B}{Y_{2\mathrm{D}}R_0^2} = \frac{1}{\gamma_{\mathrm{FvK}}} = \frac{H^2}{R_0^2}, \tag{2.2}$$

where γ_{FvK} is the Föppl-von-Kármán number. Note that we use the same units throughout the paper, i.e., we measure tensions in units of $Y_{2\mathrm{D}}$ and lengths in units of R_0. Using these natural units we transform quantities x to their dimensionless counterparts $\tilde{x}$. The last equality in (2.2) holds for a thin shell made from an isotropic and homogeneous elastic material according to eq. (2.1). By fixing Poisson's ratio $\nu_{2\mathrm{D}} = 1/2$ (corresponding to a linearly incompressible bulk material) the capsule's elastic response to external forces is solely determined by the dimensionless bending modulus $\tilde{E}_{\mathrm{B}}$. Typical values for microcapsules range within $\tilde{E}_{\mathrm{B}} = 10^{-10} \ldots 10^{-1}$ assuming $E_{\mathrm{B}} = 10^{-16} \ldots 10^{-14}\,\mathrm{Nm}$, $Y_{2\mathrm{D}} = 10^{-2} \ldots 10^{0}\,\mathrm{N/m}$ and $R_0 = 10^{-6} \ldots 10^{-3}\,\mathrm{m}$ [5]. Finally, we note that there are applications in which the relation (2.1) and its underlying assumption of a three-dimensional homogeneous elastic material are not applicable; this only invalidates (2.1) but the Hookean elasticity and constitutive relations can still be formulated by a two-dimensional Young's modulus and a dimensionless bending modulus.

We consider the elastic shell as a surface of revolution around the z-axis. The shell contour is given in cylindrical coordinates $(r(s_0), z(s_0))$, where s_0 is the arc length of the undeformed shape and r is the distance from the z-axis (Fig. 2.2B,D). The total arc length of the contour is L_0, i.e., $0 \leq s \leq L_0$. The arc length element of the deformed shape derives as $\mathrm{d}s = \sqrt{r'(s_0)^2 + z'(s_0)^2}\,\mathrm{d}s_0$, and the unit tangent vector $\boldsymbol{e}_s = (\cos\psi, \sin\psi)$, where ψ is the arc between $\boldsymbol{e}_s$ and the r-axis, gives the orientation of a capsule patch relative to the axis of symmetry. From $\boldsymbol{e}_s$ we construct the surface normal vector $\boldsymbol{n} = (\sin\psi, -\cos\psi)$. The undeformed reference shape shall be given by a circle with rest radius

R_0, i.e., $(R_0 \sin(\pi s_0/L_0), z_0 + R_0(1 - \cos(\pi s_0/L_0)))$, which generates (by revolution around the z-axis) a sphere with radius R_0 whose lower apex is located at z_0. With *apex* we refer to the intersection point of capsule and axis of symmetry. Changing only z_0 corresponds to a translation of the center of mass, which is initially located at the height of the interface $(z_0 = -R_0)$.

The effect of external loads will be a deformation, which we quantify in terms of strains that we can use together with an energy functional to compute the capsule's elastic response, i.e., the restoring stresses. Stretching deformations with respect to the undeformed spherical shape can be expressed in terms of the stretches (Fig. 2.2C) $\lambda_s = \mathrm{d}s/\mathrm{d}s_0$ and $\lambda_\phi = r/r_0$, and bending deformations in terms of the principal curvatures (Fig. 2.2B) $\kappa_s = \mathrm{d}\psi/\mathrm{d}s$ and $\kappa_\phi = \sin\psi/r$, which derive from the second fundamental form of a surface of revolution [64]. We consider stretches and curvatures relative to the undeformed shape, i.e., use the strains $e_{s,\phi} = \lambda_{s,\phi} - 1$ and bending strains $K_{s,\phi} = \lambda_{s,\phi}\kappa_{s,\phi} - \kappa_{s_0,\phi_0}$. We consider hyperelastic materials, whose elastic energy can be expressed in terms of a local energy density, and use a Hookean surface energy density [63]

$$
\begin{aligned}
w(s_0)\mathrm{d}A_0 = \Big(& \frac{Y_{2\mathrm{D}}}{2(1 - \nu_{2\mathrm{D}}^2)}(e_s^2 + 2\nu_{2\mathrm{D}}e_s e_\phi + e_\phi^2) \\
& + \frac{E_\mathrm{B}}{2}(K_s^2 + 2\nu_{2\mathrm{D}}K_s K_\phi + K_\phi^2) + \lambda_s \lambda_\phi \gamma \Big)\mathrm{d}A_0.
\end{aligned}
\tag{2.3}
$$

The three terms in the energy density correspond to the three contributions from stretching, from bending, and from the fluid interface. We explicitly state the undeformed surface element $\mathrm{d}A_0$ to highlight the fact that this energy functional operates on the undeformed surface which is important for computing stresses from it. We note that, apart from being arguably the most simple though non-trivial choice, this energy functional (with $\nu_{2\mathrm{D}} = 1/2$) also correctly describes the low-strain behavior of more sophisticated energy functionals, e.g., of the Mooney-Rivlin type [63]. For the reference shape, we use $w = \gamma$ corresponding to the situation that the two-dimensional capsule shell is initially formed at a liquid interface with surface tension γ (and, therefore, with a rest shape that is given by the Laplace-Young equation).

Taking derivatives of w with respect to the strains $e_{s,\phi}$ gives the tensions $\tau_{s,\phi}$; taking derivatives with respect to the curvatures $K_{s,\phi}$ gives the bending moments $m_{s,\phi}$ (see Fig. 2.2A). This gives the corresponding constitutive relations of the capsule material,

$$
\begin{aligned}
\tau_{s,\phi} &= \frac{1}{\lambda_{\phi,s}}\frac{\partial w}{\partial e_{s,\phi}} = \frac{Y_{2\mathrm{D}}}{1 - \nu_{2\mathrm{D}}^2}\frac{1}{\lambda_{\phi,s}}(e_{s,\phi} + \nu_{2\mathrm{D}}e_{\phi,s}) + \gamma, \\
m_{s,\phi} &= \frac{1}{\lambda_{\phi,s}}\frac{\partial w}{\partial K_{s,\phi}} = \frac{E_\mathrm{B}}{\lambda_{\phi,s}}(K_{s,\phi} + \nu_{2\mathrm{D}}K_{\phi,s}),
\end{aligned}
\tag{2.4}
$$

which are nonlinear since the Cauchy stresses are defined with respect to the deformed arc length, but the surface energy density measures lengths in terms of the undeformed arc length. Note that the surface tension γ gives a constant and isotropic contribution to the tensions τ_s and τ_ϕ because the shell has been formed at a liquid interface with surface tension γ.

One important class of systems where the Hookean elasticity eq. (2.3) is not applicable are capsules made of a membrane that is (virtually) inextensible, e.g., vesicles and (to a lesser extent) red blood cells. There are strategies [65] for implementing this local inextensibility constraint (by demanding $\lambda_\phi \lambda_s \equiv 1$) in a similar shape equation based setup as we will present in the next section but we refrain from covering these materials here and focus on
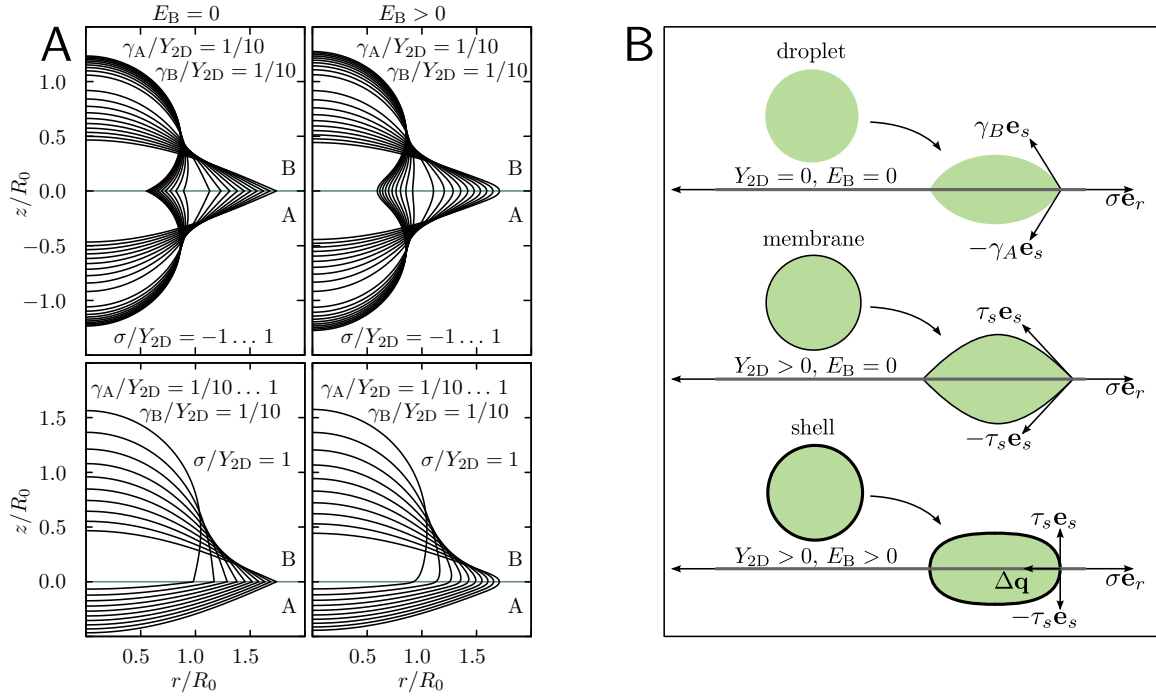
Figure 2.3: A) Shape evolutions for the elastic lens (left) and the elastic shell (right). *The upper two shape evolutions* show the symmetric case, where $\gamma_A = \gamma_B$. Here, in addition to discus shapes occurring at liquid-liquid interfaces, dumbbell shapes resulting from a contractile equatorial tension are shown, but these are unstable in the asymmetric case. *In the lower two shape evolutions* the surface tension γ_A in the lower half space is increased step-wise, which would ultimately lead to desorption into phase B. **B)** Sketch of the deformation following adsorption to an interface (here between liquid phases A and B) for a liquid droplet (upper row), membrane coated droplet (mid row), and a shell coated droplet or microcapsule (lower row). A liquid droplet deforms into a lenticular shape. Such a liquid lens consists of two spherical caps with a kink at the interface, where surface tensions are balanced. Adsorption of a thin spherical elastic capsule to a planar liquid-liquid interface yields an elastic lens, where the kink at the interface is still preserved but shapes are less spherical. Finally, adsorption of an elastic shell leads to rounded edges due to a finite thickness of the material. Tangential stresses τ_s, the liquid surface tensions σ acting along the liquid interface and, for shells, the discontinuity Δq in the normal transverse shear force density q have to balance each other at the contact line.

microcapsules, whose membrane is a thin shell of a homogeneous isotropic three-dimensional bulk material. From a technical perspective, the treatment of capsules with conserved area is also more demanding as the undeformed shape cannot be a sphere, because the combined volume and area constraints only allow for non-spherical rest shapes in general.

2.1.2 Shape equations

The equilibrium shape of an infinitesimal thin shell is described by local stress equilibrium in (i) tangential and (ii) normal direction. Elastic shells of finite thickness additionally require

(iii) torque (bending moment) balance. This yields a set of three balance conditions [44, 63]

$$
\begin{array}{ll}
\text{(i)} & 0 = -\dfrac{\cos\psi}{r}\tau_\phi + \dfrac{1}{r}\dfrac{\mathrm{d}(r\tau_s)}{\mathrm{d}s} - \kappa_s q - p_s, \\[2ex]
\text{(ii)} & 0 = -p + \kappa_\phi\tau_\phi + \kappa_s\tau_s + \dfrac{1}{r}\dfrac{\mathrm{d}(rq)}{\mathrm{d}s}, \\[2ex]
\text{(iii)} & 0 = \dfrac{\cos\psi}{r}m_\phi - \dfrac{1}{r}\dfrac{\mathrm{d}(rm_s)}{\mathrm{d}s} - q,
\end{array}
\tag{2.5}
$$

which have to be satisfied locally for each $s_0 \in [0, L_0]$ along the shape profile. Here, q is the *transverse shear stress*; it describes a normal force density that arises from shearing a membrane patch as shown in Fig. 2.2A. It is important to note that q is of order $\mathcal{O}(H)$ since it acts on the cross-section of the shell, and is, thus, only needed for shells of finite thickness or, in other word, for shells with bending rigidity. For Hookean membranes without bending rigidity, we have $q = 0$ and $m_s = m_\phi = 0$, i.e., all terms in the moment equilibrium (iii) vanish and only the two stress equilibria are needed. For a liquid droplet the tensions have no elastic contribution and $\tau_s = \tau_\phi = \gamma = \text{const}$, such that the stress equilibria further simplify.

In combination with the constitutive laws (2.4) and three differential equations following from our cylindrical parametrization the stress and moment equilibrium (2.5) lead to the full system of shape equations for a Hookean shell (see Fig. 2.2A-C)

$$
\begin{array}{l}
r'(s_0)=\lambda_s\cos\psi, \quad z'(s_0)=\lambda_s\sin\psi, \quad \psi'(s_0)=\lambda_s\kappa_s, \\[2ex]
\tau_s'(s_0) = \lambda_s\left(\dfrac{\tau_\phi - \tau_s}{r}\cos\psi + \kappa_s q + p_s\right), \\[2ex]
m_s'(s_0) = \lambda_s\left(\dfrac{m_\phi - m_s}{r}\cos\psi - q\right), \\[2ex]
q'(s_0) = \lambda_s\left(-\kappa_s\tau_s - \kappa_\phi\tau_\phi - \dfrac{q}{r}\cos\psi + p\right),
\end{array}
\tag{2.6}
$$

where $p = p_0 + p_n$ is the total normal pressure and p_s is the shear-pressure. Since we consider a closed microcapsule encapsulating an incompressible liquid phase, p will have a hydrostatic contribution, p_0, that has to be fixed by a volume constraint, see below. External forces enter via the normal and shear-pressure as also described below. The first three equations are geometric relations. The fourth and sixth equations in (2.6) describe the tangential and normal force equilibrium, respectively. The fifth equation is the equilibrium of bending moments. The shape equations (2.6) are closed by eliminating λ_s and τ_ϕ by using the two constitutive relations for stresses and strains from eq. (2.4), using the geometric relation $\kappa_\phi = \sin\psi/r$, and eliminating and κ_s and m_ϕ by using the two constitutive relations for bending moments and bending strains from eq. (2.4). This procedure is explained in detail in Ref. [44].

The shape equations (2.6) introduced above describe a Hookean shell. The Hookean membrane, but also the liquid droplet, derive from (2.6) as limit cases. The shell becomes a membrane in the limit $H \approx 0$, i.e., $E_{\mathrm{B}} \approx 0$, which also implies $m_s = 0$ and $q = 0$. The additional limit $Y_{2\mathrm{D}} \approx 0$ gives a liquid droplet, where the tangential stresses $\tau_s = \tau_\phi = \gamma$ can be eliminated from (2.6), yielding the Laplace-Young equation.

The system (2.6) is completed by specifying boundary conditions at the apices. As the capsule is closed and kinks are absent, we have $r(0) = r(L_0) = 0$ and $\psi(0) = \pi - \psi(L_0) = 0$. Absence of point loads at the apices requires $q(0) = q(L_0) = 0$ (as will be shown below, see eq. (2.1.4)). The boundary conditions to the remaining quantities are a priori unknown and fixed by a shooting method, during which we shoot from both apices (this is necessary as

the system becomes singular for $r \approx 0$) towards the liquid-liquid interface. For the Hookean shell we need to fix the values of three remaining shooting parameters z, τ_s, m_s at each apex and, thus, require six additional matching conditions at the interface. For the Hookean membrane we have $m_s = 0$ and only need to fix two shooting parameters z, τ_s, at each apex and, thus, need four additional matching conditions at the interface.

We translate the z-coordinate such that the liquid-liquid interface is located at $z = 0$. The capsule then consists of two solution branches $z > 0$ and $z < 0$, for which we will use superscripts $+$ and $-$, respectively. We also introduce $s_0 = \ell$ as the arc length at which the liquid-liquid interface is located. The first obvious matching conditions are $z^+(\ell) = z^-(\ell) = 0$ (which fix the shooting parameters $z(0)$ and $z(L_0)$) and $r^+(\ell) = r^-(\ell) \equiv r(\ell)$ from requiring a closed capsule. For a shell with bending rigidity we also have the requirement $\psi^+(\ell) = \psi^-(\ell)$ because a kink in the capsule shell costs an infinite bending energy. Membranes and droplets, however, will exhibit such kinks and $\psi^+(\ell)$ and $\psi^-(\ell)$ can freely adjust.

For a shell, these are four matching conditions such that two matching conditions are missing. This will be a Young-Dupré equation for the force equilibrium at the contact line between capsule and liquid interface and a corresponding moment equilibrium. For a membrane, these are three matching conditions, and one matching condition is missing, which will be a Young-Dupré equation. Moreover, we will need a condition to determine the arc length value $s_0 = \ell$, where the interface is located. In the symmetric case of identical liquids outside the capsule, we simply have $\ell = L_0/2$ by symmetry, whereas ℓ has to be determined separately by energy minimization in the general asymmetric case. The missing conditions also depend on the external load by the surface tension of the liquid-liquid interface and will be discussed below in Sec. 2.1.4 in detail.

2.1.3 External loads

Pressure

Assuming an incompressible liquid within the capsule and an impermeable membrane leads to conservation of the capsule volume

$$V = \int \pi r^2 \mathrm{d}z = \int_0^{L_0} \pi r^2 \lambda_s \sin \psi \mathrm{d}s_0 = V_0 \equiv \frac{4\pi}{3} R_0^3.$$

The volume constraint $V = V_0 = $ const has to be satisfied by adjusting the hydrostatic pressure p_0, which serves as a Lagrange parameter. In practice, the volume constraint is realized by including it in the shooting method, i.e., by using p_0 as shooting parameter to obtain a given volume V_0 at the end of the integration along the contour. It is important to note that we will always assume that both liquid phases outside the capsule have the *same* pressure and, thus, have a *planar* interface.

If p_0 is not interpreted as Lagrange parameter we have actual pressure control. Then the pressure p_0 is prescribed and determines the capsule volume $V = V(p_0)$. Solutions for pressurized capsules are numerically simpler to obtain and possibly exhibit more diverse shapes due to the lacking volume constraint.

Another possibility, which is intermediate between pure pressure and pure volume control, is osmotic pressure control [62]. Then the osmotic pressure inside the capsule becomes a function of the capsule volume $p_0 = p_0(V)$, the shape of which depends on the osmolyte concentration. For high osmolyte concentrations inside the capsule tends to assume an osmotically preferred volume and the situation resembles volume control. At low osmolyte concentrations the pressure is almost fixed over a wide range of volumes. We restrict

ourselves here to capsules with a constant volume in which the hydrostatic pressure adapts accordingly.

Surface tensions

The most important effect here is capsule or droplet deformation by the surface tension between the two liquid interfaces. The frame of reference is chosen such that the planar interface of the two immiscible liquid phases, A and B (Fig. 2.3), is located at $z = 0$. As there is also a surface tension contribution to the elastic energy of the capsule shell, see eq. (2.3), and this contribution will depend in general on whether the capsule is in contact with liquid phase A or B, we have to consider three surface tensions γ_A (A-capsule), γ_B (B-capsule), and σ (A-B). We will refer to the latter one as the *interface load* as the surface tension σ is responsible for stretching the capsule. In this setup (Fig. 2.3), $\gamma \equiv \gamma(s_0)$ (see eq. (2.3)) is a function of the arc length s_0, i.e.,

$$\gamma(s_0) = \begin{cases} \gamma_A & z(s_0) < 0 \\ \gamma_B & z(s_0) > 0. \end{cases}$$

As $z(s_0)$ will be a monotonous function in the regime we are interested in we can simplify this to

$$\gamma(s_0) = \begin{cases} \gamma_A & s_0 < \ell \\ \gamma_B & s_0 > \ell. \end{cases}$$

with $z(\ell) = 0$. Since these surface tensions arise from capsule-liquid interfaces (A-C and B-C), they can be directly included in the elastic energy functional (2.3) and also transfer to the constituting laws (2.4). The symmetric case corresponds to $\gamma_A = \gamma_B$.

In contrast, external forces arise from the liquid-liquid interface (A-B) and, thus, are handled as point loads acting on the contour, though actually acting on a great circle when rotating the shape profile. In practice, this means that we employ adequate boundary conditions or matching conditions for the forces τ_s and q to include these point loads. Therefore, we decompose the external forces in normal and tangential contributions, which are localized to a specific arc length ℓ by employing a delta distribution. The liquid-liquid AB-interface induces a point force density (see Fig. 2.3B)

$$\boldsymbol{f}_\sigma(s_0) = \sigma\delta(z)\boldsymbol{e}_r = \sigma\delta(s_0 - \ell)\boldsymbol{e}_r$$

leading to normal and tangential pressure contributions

$$p_n = \boldsymbol{f}_\sigma \cdot \boldsymbol{n} = \sigma\delta(s_0 - \ell)\sin\psi,$$
$$p_s = -\boldsymbol{f}_\sigma \cdot \boldsymbol{e}_s = -\sigma\delta(s_0 - \ell)\cos\psi.$$

The total normal pressure is then given by $p = p_0 + p_n$, where p_0 gives a constant contribution acting as a Lagrange parameter on the capsule volume as described above. Note that for elastic shells in the symmetric case, $\gamma_A = \gamma_B$, we have $p_s = 0$ due to $\psi(\ell) = \pi/2$ which is required by reflection symmetry with respect to the liquid-liquid interface at $z = 0$.

Gravity

If the capsule desorbs from the interface, external forces vanish and the capsule will take a spherical shape as this is the stress-free ground state. Re-adsorption to the interface will

only take place randomly if the capsule can make contact with the interface again, e.g., due to Brownian motion or by gravitational forces, which arise in the presence of density differences.

Interfacial adsorption of a droplet or capsule requires three immiscible phases of similar densities ρ_A, ρ_B, and ρ_C. In this section we only discuss the artificial and thereby most simple case $\rho_A = \rho_B = \rho_C$, but different densities between exterior and interior liquid can be easily included in the theoretical description by including them into the hydrostatic pressure, $p_0 \to p_0 - \Delta\rho g(z - z_0)$, where p_0 is the pressure at the lower apex, g is the gravitational acceleration, and $\Delta\rho$ is the density difference inner and outer phase. Note that the latter has to be defined piecewise with respect to the two different outer phases.

2.1.4 Matching conditions at the interface

At the liquid-liquid interface at $z = 0$ and $s_0 = \ell$ the shape equations (2.6) have to be complemented by matching conditions. We argued above that six matching conditions are needed for a Hookean shell, whose shape is obtained by the full set (2.6) of six shape equations, whereas only four matching conditions are needed for a Hookean membrane, which is described by four shape equations ($m_s = 0$ and $q = 0$ in eqs. (2.6)). Moreover, we need to determine the parameter ℓ itself by energy minimization in the general asymmetric case. For the symmetric case $\gamma_A = \gamma_B$ we have $\ell = L_0/2$ by symmetry.

We already mentioned the obvious matching conditions

$$z^+(\ell) = z^-(\ell) = 0 \ \text{ and } \ r^+(\ell) = r^-(\ell) \equiv r(\ell)$$

from requiring a closed capsule. The two matching conditions for z fix the shooting parameters $z(0)$ and $z(L_0)$. From continuity of r also continuity of $\lambda_\phi = r/r_0$ immediately follows. For a shell with bending rigidity we also have the requirement

$$\psi^+(\ell) = \psi^-(\ell) \tag{2.7}$$

because a kink in the capsule shell costs an infinite bending energy. Membranes and droplets, however, will exhibit such kinks and $\psi^+(\ell)$ and $\psi^-(\ell)$ can freely adjust. From continuity of r and ψ, also the continuity of the curvature $\kappa_\phi = \sin\psi/r$ follows.

All remaining matching conditions can be derived based on the variational calculus introduced in Ref. [44] by minimizing the total free energy $G = \int w(s_0)\mathrm{d}A_0 - p_0 V - \sigma\pi r^2(\ell)$ or (using eq. (2.1.3))

$$G = \int_0^\ell \mathrm{d}s_0 \left(2\pi r_0 w^- - p_0\pi(r^-)^2\lambda_s^- \sin\psi^-\right)$$
$$+ \int_\ell^{L_0} \mathrm{d}s_0 \left(2\pi r_0 w^+ - p_0\pi(r^+)^2\lambda_s^+ \sin\psi^+\right) - \sigma\pi r(\ell)^2, \tag{2.8}$$

where the energy $-\sigma\pi r^2(\ell)$ is the potential for the point force $\boldsymbol{f}_\sigma$ from eq. (2.1.3). The free energy G has to be extremized with respect to the function $r^\pm(s_0)$ and $\psi^\pm(s_0)$ as well as with respect to the location ℓ of the liquid-liquid interface. The total variations $\delta r \equiv (r + \delta r)(\ell + \delta\ell) - r(\ell) = \delta r(\ell) + r'(\ell)\delta\ell$ at the variable interface position ℓ have to fulfill the continuity conditions $\delta r^- = \delta r^+$ and, for a shell, $\delta\psi^- = \delta\psi^+$. Each continuity condition entails a corresponding Weierstrass-Erdmann condition, and because of the variable interface position we obtain an additional transversality condition.

The variation of G gives the additional algebraic relation [44]

$$q \cos \psi + \tau_s \sin \psi = \frac{1}{2} p_0 r,$$

for $s_0 \neq \ell$, which corresponds to a first integral of the shape equations and can replace the shape equation for q in (2.6). Equation (2.1.4) also implies that $q = 0$ at the apices where $r = 0$ and $\psi = 0$ or π, which justifies the boundary conditions $q(0) = q(L_0) = 0$. At the interface at $s_0 = \ell$ the right hand side of eq. (2.1.4) is continuous such that we also obtain a continuity condition

$$\left(q^+ \cos \psi^+ + \tau_s^+ \sin \psi^+ \right) \big|_\ell$$
$$= \left(q^- \cos \psi^- + \tau_s^- \sin \psi^- \right) \big|_\ell = \frac{1}{2} p_0 r(\ell) \tag{2.9}$$

The same condition can be derived from the following conserved quantity $U(s) = \text{const}$, which has been found in Ref. [66, 67],

$$U = 2\pi r (q \cos \psi + \tau_s \sin \psi)$$
$$- 2\pi \int_0^s \mathrm{d}\tilde{s} ((p_0 + p_n) \cos \psi + p_s \sin \psi)$$
$$= 2\pi r (q \cos \psi + \tau_s \sin \psi) - \pi p_0 r^2,$$

where we used eq. (2.1.3) for p_n and p_s to obtain the last equality. Because of $U(0) = 0$ at the apex, we have $U(s) = \text{const} = 0$ resulting again in the continuity condition (2.9). From the force contributions in eq. (2.1.4) it is also apparent that the continuity condition (2.9) describes a force equilibrium in the z-direction at the contact line between capsule and liquid interface and is, thus, a Young-Dupré equation (see also Fig. 2.3B). The liquid interface is not exerting forces in the z-direction and, thus, σ does not enter eq. (2.9); discontinuities in the normal shear force density q and in the tangential force density τ_s have to cancel in z-direction.

Equating all boundary terms $\propto \delta r^+ = \delta r^-$ in the variation δG to zero we obtain the Weierstrass-Erdmann condition

$$\left(q^+ \sin \psi^+ - \tau_s^+ \cos \psi^+ \right) \big|_\ell$$
$$= \left(q^- \sin \psi^- - \tau_s^- \cos \psi^- \right) \big|_\ell + \sigma, \tag{2.10}$$

which describes the force equilibrium in the radial direction at the contact line between capsule and liquid interface and is, thus, a second Young-Dupré equation (see Fig. 2.3B). Discontinuities in the normal shear force density q and in the tangential force density τ_s in r-direction have to cancel with the tension σ, which also acts in r-direction.

Likewise, equating boundary terms $\propto \delta \psi^+ = \delta \psi^-$ in δG to zero, we obtain another Weierstrass-Erdmann condition

$$m_s^+(\ell) = m_s^-(\ell), \tag{2.11}$$

which holds for shells and describes the moment equilibrium at the contact line. Continuity of m_s and κ_ϕ (see above) also entails continuity of κ_s and m_ϕ and, thus, of the entire bending energy density.
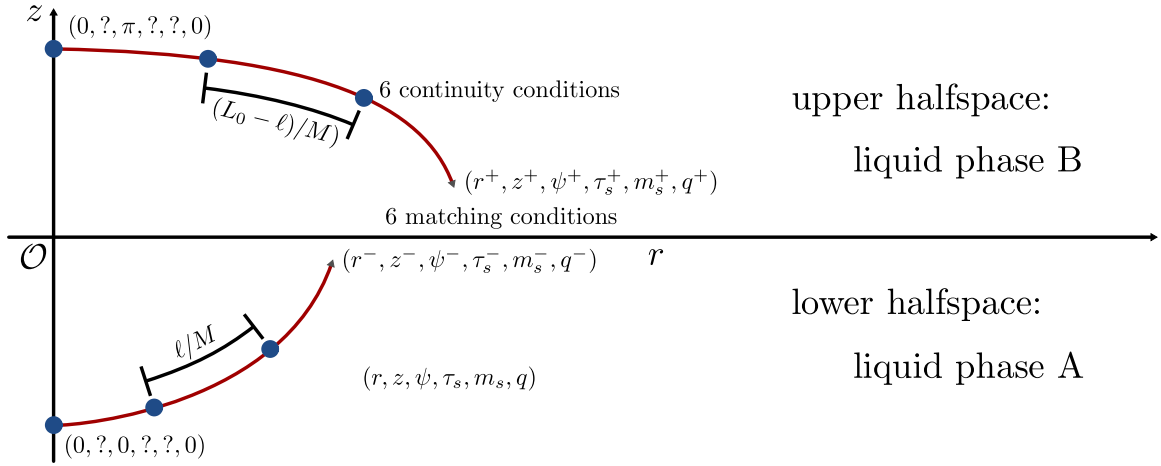
Figure 2.4: Illustration of the multiple shooting method applied to numerically solve the shape equations. The r-z-plane is separated by a liquid-liquid interface at $z = 0$ arising from two different liquid phases A and B residing in the lower and upper half space, respectively. The lower and upper branches are integrated from the apices on the z-axis to the interface on the r-axis, where we employ matching conditions corresponding to the different limit cases (Hookean membrane and Hookean shell) as discussed in this section.

Equating all boundary terms $\propto \delta\ell$ in the variation δG to zero, we obtain a transversality condition

$$\left(w^+ - \lambda_s^+ \lambda_\phi^+ \tau_s^+\right)\Big|_\ell = \left(w^- - \lambda_s^- \lambda_\phi^- \tau_s^-\right)\Big|_\ell.$$

Because the bending energy part of w is continuous, it follows that the discontinuity in w across the interface is exactly due to the discontinuity in γ, which jumps from γ_A for $z < 0$ to γ_B for $z > 0$. This means, in turn, that the stretching elasticity part of w is also continuous. Because λ_ϕ is continuous (see above), also λ_s and, thus, the elastic parts of the tensions $\tau_s - \gamma$ and $\tau_\phi - \gamma$ have to be continuous across the interface then.

2.1.5 Shooting method

In our numerical treatment, we will not employ the transversality condition in the form (2.1.4) but prefer to numerically minimize the total energy with respect to ℓ. Changing the interface arc length ℓ for this minimization requires a re-meshing in the shooting method (Fig. 2.4), which we will discuss here briefly. To achieve numerical stability we subdivide each solution branch in M segments. At each intermediate point we gain six shooting parameters and six continuity conditions (for the general shell case). The $(-)$-branch is integrated counter-clockwise over the interval $[0, \ell]$ starting at $s_0 = 0$ and ending at $s_0 = \ell$, the $(+)$-branch is integrated clockwise over $[\ell, L_0]$ starting at $s_0 = L_0$ and ending at $s_0 = \ell$. Both branches thus start at the axis of rotation and match at the interface. When the interface arc length ℓ is changed, the segmentation of the shape has to be adapted, such that the $(-)$-branch is integrated over the intervals $[k\ell/M, (k+1)\ell/M]$ where $k = 0, \ldots, M-1$, and the $(+)$-branch is integrated over the intervals $[L_0 - (k+1)(L_0-\ell)/M, L_0 - k(L_0-\ell)/M]$. During the minimization (2.8) we iteratively change the segmentation of the shape, i.e., change ℓ until the total free energy G reaches its minimum.

2.1.6 Shell, membrane and droplet regime

In the following, we discuss numerical solutions of the shape equations for the general asymmetric case for three different types of interface elasticity: liquid lenses, lens-shaped capsules with a Hookean membrane (elastic lenses), and capsules with Hookean shell elasticity as shown in Fig. 2.3A. We specify shape equations and the matching conditions for the three different regimes.

Liquid lens

The liquid lens is the simplest case discussed in this section, as it is obtained in the absence of any elastic tension, $Y_{2D} \approx 0$ ($\tau_s = \tau_\phi = \gamma$) and $E_B \approx 0$ ($q = 0$ and $m_s = m_\phi = 0$). For this liquid surface there is no reference shape and surface tension and incompressibility determine the droplet shape. From the local force balance condition $p_0 dV = \sigma dA$, we obtain the Laplace-Young equation,

$$p_0 = \gamma(\kappa_s + \kappa_\phi), \tag{2.12}$$

which can be recast as a set of three shape equations

$$r'(s_0) = \cos\psi, \quad z'(s_0) = \sin\psi,$$
$$\psi'(s_0) = p_0/\gamma - \sin\psi/r, \tag{2.13}$$

using cylindrical parametrization. This set of equations also directly derives from (2.6) by employing the limits given above. The resulting shapes have *constant* mean curvature according to the Laplace equation (2.12) (or according to $\kappa_s + \kappa_\phi = \psi' + \sin\psi/r = \text{const}$ in (2.13)), which only allows lens shapes that are composed of two spherical caps with the same radius R.

For the numerical determination of the shape of the liquid lens we shoot from both apices with boundary conditions $r(0) = r(L_0) = 0$ and $\psi(0) = \pi - \psi(L_0) = 0$. We will determine two shooting parameters $z(0)$ and $z(L_0)$ such that $z^+(\ell) = z^-(\ell) = 0$. Because we have three shape equations (2.12), there are no free shooting parameters left. There are, however, three matching conditions at the AB-interface at $s_0 = \ell$: the Young-Dupré equations (2.9) and (2.10) for force equilibrium in z- and r-direction, respectively, which become ($q = 0$, $\tau_s^- = \tau_\phi^- = \gamma_A$, $\tau_s^+ = \tau_\phi^+ = \gamma_B$)

$$f_1 = \gamma_A \cos\psi^-(\ell) - \gamma_B \cos\psi^+(\ell) - \sigma = 0$$
$$f_2 = \gamma_A \sin\psi^-(\ell) - \gamma_B \sin\psi^+(\ell) = 0 \tag{2.14}$$

and the continuity condition $r^-(\ell) = r^+(\ell)$. For the liquid lens, there is no reference shape, and these matching conditions have to be used to determine the arc lengths $L_0 - \ell$ and ℓ of the upper and lower part. We thus have three matching conditions for two unknown parameters ℓ and L_0 (the reason is the existence of the first integral U [44, 67]). Numerically, we find that working with such an over-determined system of matching conditions leads to faster convergence of the shooting method. We note that liquid lenses exhibit a kink at the interface, i.e., there is no continuity of ψ at the AB-interface. We also note that, because there is no elastic energy or reference shape, L_0 is not fixed beforehand by the reference shape and ℓ does not have to be determined from energy minimization as will be the case for Hookean membranes and shells.

Elastic lens

In case of finite stretching resistance Y_{2D}, but vanishing bending rigidity $E_B \approx 0$, i.e., vanishing shell thickness $H \approx 0$, we have an elastic lens with Hookean membrane elasticity with vanishing bending moments $m_s = m_\phi = 0$ and vanishing transverse shear stress $q = 0$. The system (2.6) reduces to four coupled nonlinear differential equations

$$
\begin{aligned}
& r^{'}(s_0) = \lambda_s \cos \psi, \quad z^{'}(s_0) = \lambda_s \sin \psi, \\
& \psi^{'}(s_0) = \lambda_s (p - \kappa_\phi \tau_\phi)/\tau_s, \\
& \tau_s^{'}(s_0) = \lambda_s \left(\frac{\tau_\phi - \tau_s}{r} \cos \psi + p_s \right).
\end{aligned}
\tag{2.15}
$$

Shapes are still similar to liquid lenses, and there is a kink at the AB-interface because there is no continuity of ψ.

For the numerical determination of the elastic lens shape we shoot from both apices with boundary conditions $r(0) = r(L_0) = 0$ and $\psi(0) = \pi - \psi(L_0) = 0$. The two shooting parameters $z(0)$ and $z(L_0)$ are determined from $z^+(\ell) = z^-(\ell) = 0$. Because we have four shape equations (2.15), there are two free shooting parameters $\tau_s(0)$ and $\tau_s(L_0)$ left, which have to be determined from matching conditions at the AB-interface at $s_0 = \ell$.

As for a liquid lens, there are three matching conditions: the Young-Dupré equations (2.9) and (2.10) for force equilibrium in z- and r-direction, respectively, which become ($q = 0$)

$$
\begin{aligned}
f_1 &= \tau_s^-(\ell) \cos \psi^-(\ell) - \tau_s^+(\ell) \cos \psi^+(\ell) - \sigma = 0 \\
f_2 &= \tau_s^-(\ell) \sin \psi^-(\ell) - \tau_s^+(\ell) \sin \psi^+(\ell) = 0,
\end{aligned}
\tag{2.16}
$$

and the continuity condition $r^-(\ell) = r^+(\ell)$. These three matching conditions are used to determine the two shooting parameters $\tau_s(0)$ and $\tau_s(L_0)$. Again, we have an over-determined system of matching conditions (due to the first integral U) but using all three conditions leads to faster convergence of the shooting method. Finally, the arc length position ℓ of the AB-interface is determined by total energy minimization.

In the symmetric case, where $\gamma_A = \gamma_B$ and $\psi^-(\ell) = \pi - \psi^+(\ell)$, we find $\tau_s^-(\ell) = \tau_s^+(\ell)$. Note that the tensions τ_s^- and τ_s^+ include the liquid interface tensions γ_A and γ_B in addition to elastic contributions. In the symmetric case the shooting parameters τ_s at the upper and lower apices are identical and thereby only one parameter is left. Symmetry with respect to the liquid-liquid interface also inherently satisfies the conditions $r^+(\ell) - r^-(\ell) = 0$ and $f_2 = 0$ such that we are left with exactly one matching conditions $f_1 = 0$ from the Young-Dupré equation (2.10) for force equilibrium in r-direction.

Numerically calculated shapes of elastic lenses are shown in Fig. 2.3A both for tensile ($\sigma > 0$) and contractile ($\sigma < 0$) equatorial tensions. The resulting lens shapes also appear to be similar to liquid lens shapes composed of two spherical caps. We will exploit this similarity for an analytical approximation in the next section, which also shows that this approximation is not exact, i.e., elastic lens shapes are similar, but distinct from liquid lens shapes.

Elastic shells

Finally, we incorporate the effect of a finite bending rigidity. Then we have the full set (2.6) of six shape equations. We shoot from both apices with boundary conditions $r(0) = r(L_0) = 0$, $\psi(0) = \pi - \psi(L_0) = 0$ and $q(0) = q(L_0) = 0$. The two shooting parameters $z(0)$ and $z(L_0)$ are determined from $z^+(\ell) = z^-(\ell) = 0$. Now we have four free shooting parameters $\tau_s(0)$,

$\tau_s(L_0)$, $m_s(0)$, and $m_s(L_0)$ left, which have to be determined from matching conditions at the AB-interface at $s_0 = \ell$.

There are five matching conditions at the AB-interface: the continuity conditions $r^-(\ell) = r^+(\ell)$ and also $\psi^+(\ell) = \psi^-(\ell)$ (see eq. (2.7)) because kinks in the capsule shell are now suppressed by bending energy. Moreover, we also have the continuity condition $m_s^+(\ell) = m_s^-(\ell)$ (see eq. (2.11)) from the moment equilibrium at the AB-interface and two Young-Dupré equations (2.9) and (2.10) for force equilibrium in z- and r-direction. The two Young-Dupré equations can be rearranged into direct jump conditions for τ_s and q at the AB-interface,

$$q^+(\ell) - q^-(\ell) = \sigma \sin \psi^-(\ell)$$
$$\tau_s^+(\ell) - \tau_s^-(\ell) = -\sigma \cos \psi^-(\ell).$$

Again, we have an over-determined system of five matching conditions for four shooting parameters (due to the first integral U) and also here we achieve faster convergence employing all five matching conditions. The arc length position ℓ of the AB-interface is determined by total energy minimization.

Fig. 2.5 (right) shows numerically calculated capsule shapes for the symmetric case for varying bending modulus, Fig. 2.3A shows shapes for varying liquid-liquid surface tension σ, both for tensile ($\sigma > 0$) and contractile ($\sigma < 0$) equatorial tensions. For decreasing bending moduli the rounded kink at the AB-interface becomes increasingly sharp and approaches the elastic lens shape. We will quantify this relation in the following section in order to establish the kink curvature as experimentally accessible observable, which allows us to infer the bending modulus of the capsule material.

2.1.7 Lens height and contact angle

As it is evident from eq. (2.13) liquid lens shapes exhibit constant curvature and, thus, can be constructed from spherical caps. In this section, we use this fact to obtain an exact analytical result for the contact angle and the height of liquid lenses. We generalize this approach to elastic lenses by taking also elastic stresses into account and obtain an approximative theory, which gives the contact angle and the height of an elastic lens by solving numerically a single algebraic equation. Finally, these theoretical results enable a determination of Young's modulus of an elastic lens by a *single* measurement of the height *or* the contact angle.

Exact solution for liquid lenses

Lenticular liquid shapes, e.g., on solid substrates have been discussed in literature [68] and analytical solutions for liquid lenses at liquid-liquid interfaces can be obtained analogously. We restrict ourselves here to the symmetric case $\gamma \equiv \gamma_A = \gamma_B$. The total energy of the system is given by

$$E = \gamma A - \sigma A_B, \tag{2.17}$$

where A is the total area of the liquid lens and A_B the occupied cross-section area within the liquid-liquid interface plane. We use the fact that the liquid lens is composed of two spherical caps of equal radius $R = 2\gamma/p_0$ (for the symmetric case) according to the Laplace equation (2.12), and of equal base radius R_B. Then $A = 2\pi(R^2 + h^2)$ is the surface of the lens (two spherical caps) and $A_B = \pi R_B^2$ the occupied cross-section area within the liquid-liquid interface plane. Here, h denotes the height of the spherical caps, which is

related to R_B and R via $R_B^2 = 2Rh - h^2$, see also Fig. 2.6 for the involved quantities. In the following, we measure lengths in units of the radius R_0 of a spherical droplet of the same volume $V \equiv 4\pi R_0^3 / 3$ and thereby introduce reduced quantities $\tilde{h} = h/R_0$ and $\tilde{R} = R/R_0$. For a fixed volume,

$$\tilde{V} = \frac{\pi \tilde{h}}{3} \left(3\tilde{R} - \tilde{h}\right) = \frac{4\pi}{3} = \tilde{V}_0,$$

the radius R and the height h are related by

$$\tilde{R}(\tilde{h}) = \frac{1}{3} \left(\frac{2}{\tilde{h}^2} + \tilde{h}\right). \tag{2.18}$$

We can now write the free energy (2.17) as a function of the reduced height $\tilde{h}$, minimize with respect to the reduced height $\tilde{h}$, and find

$$\tilde{h} = \frac{2^{1/3}(2 - \sigma/\gamma)^{1/3}}{(4 + \sigma/\gamma)^{1/3}}, \tag{2.19}$$

from which we also obtain the opening angle

$$\theta(\tilde{h}) \equiv \arccos(1 - \tilde{h}/\tilde{R}(\tilde{h})) \tag{2.20}$$

and, finally, the pressure

$$p_0(\tilde{h}) = \frac{2\gamma}{\tilde{R}(\tilde{h})} = \frac{6\tilde{h}^2 \gamma}{2 + \tilde{h}^3}$$

from the Laplace-Young equation. Relations (2.19) and (2.20) for liquid lenses are in good agreement with solutions for elastic membrane lenses (see Fig. 2.5 (left)) in the corresponding limit $\gamma \gg Y_{2D}$. Relation (2.19) can likewise be obtained by solving $f_1 = 0$ in (2.14) employing the volume constraint (2.18) in combination with the relations $\theta = \psi^-(\ell) = \pi - \psi^+(\ell)$ and $\gamma_A = \gamma_B$.

Approximative solution for elastic lenses

For the symmetric case, we can derive an approximative analytical solution for the elastic membrane shape based on a spherical cap approximation. We investigate partially spherical solutions, because, intuitively, the difference between a liquid droplet and a liquid droplet coated with an elastic 'skin' should be negligible for small interface loads as also suggested by the numerically calculated shapes of elastic lenses in Fig. 2.3A. Force balance for an unloaded spherical cap implies a constant tension $\tau_s = \text{const}$ [69] such that, additionally, $\tau_s = \tau_\phi$ must hold to fulfill the force balance conditions (2.5) (i).

Deforming a hemisphere into a spherical cap by uniform strains leads, however, to anisotropic tensions $\tau_s \neq \tau_\phi$. The spherical cap has only one free parameter, which is its reduced height $\tilde{h}$, as it already has been introduced above in the context of liquid lenses. From geometrical arguments (see Fig. 2.6) we can calculate the uniform stretches λ_s and λ_ϕ for the deformation into a spherical cap,

$$\lambda_s = \frac{2\theta(\tilde{h})}{\pi} \tilde{R}(\tilde{h}) \quad \text{and} \quad \lambda_\phi = \tilde{R}_B = \tilde{R}(\tilde{h}) \sin(\theta(\tilde{h})), \tag{2.21}$$
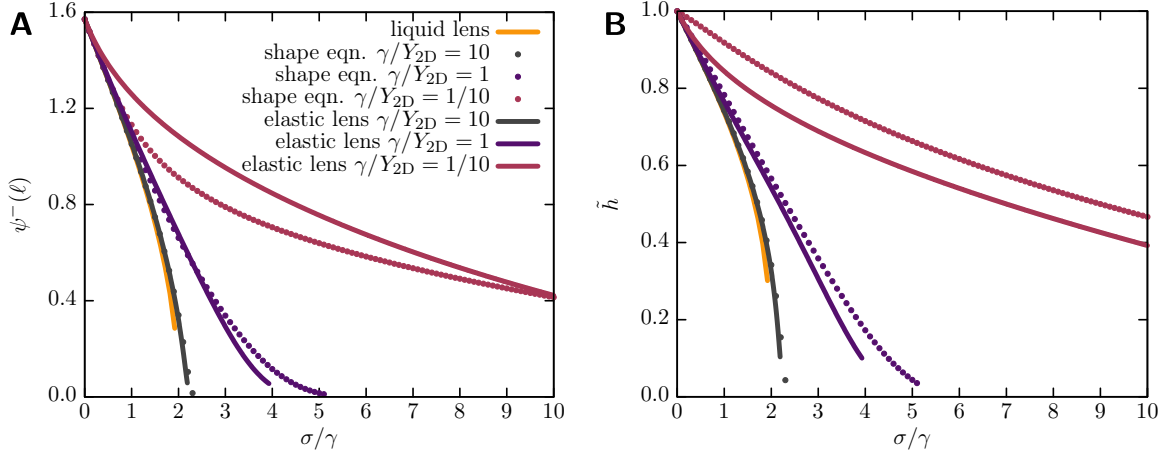
Figure 2.5: A) Opening angle θ as a function of tension σ/γ for the symmetric case: comparison of liquid lens result (2.19) and spherical cap approximation (2.22) for the elastic lens with numerical results from solving the shape equations (2.15). Dots are numerical results for the elastic lens in three different regimes, which are (i) fluid regime $\gamma/Y_{2D} \gg 1$, (ii) crossover regime $\gamma/Y_{2D} \sim 1$, and (iii) elastic regime $\gamma/Y_{2D} \ll 1$. **B)** Analogous comparison for the reduced height $\tilde{h} = h/R_0$ as a function of the tension σ/γ for the symmetric case.

where $\tilde{R}(\tilde{h})$ is the reduced radius as given by the function (2.18) and $\theta(\tilde{h})$ is the opening angle of the spherical caps according to (2.20), which is related to the slope angle ψ via $\theta = \psi^-(\ell) = \pi - \psi^+(\ell)$. Obviously $\lambda_s < \lambda_\phi$ because $\theta < \pi/2$ and $R > R\sin\theta$, i.e., the stretches (2.21) are anisotropic. Inserting these stretches into the constitutive relations (2.4) we also obtain anisotropic stresses, $\tau_s < \tau_\phi$. Therefore, assuming constant tensions in a spherical cap formed from a hemispherical rest shape violates the force balance conditions (2.5). For $\gamma \geq Y_{2D}$, i.e., small deviations from the fluid-like behavior deviations from force balance are also small, and we can use spherical caps as an approximation.

Inserting the uniform strains (2.21) into the constitutive relations (2.4) gives the stresses $\tau_s(\tilde{h})$ and $\tau_\phi(\tilde{h})$ as a function of the reduced spherical cap height $\tilde{h}$. To satisfy the Young-Dupré equation we employ $f_1 = 0$ from eq. (2.16) in the symmetric case, i.e., $\theta = \psi^-(\ell) = \pi - \psi^+(\ell)$ and $\gamma_A = \gamma_B$, to obtain

$$\sigma = 2\tau_s(\tilde{h})\cos\theta(\tilde{h}) \tag{2.22}$$

for the height h of the spherical cap. The pressure p_0 is then also a function of h,

$$p_0(\tilde{h}) = \frac{3\tilde{h}^2(\tau_s(\tilde{h}) + \tau_\phi(\tilde{h}))}{2 + \tilde{h}^3}.$$

Solutions of (2.22) are in good agreement with numerical simulations, see Fig. 2.5 (left) within the range of the fluid and the crossover regime, i.e., for $\gamma \geq Y_{2D}$. Even for $\gamma \leq Y_{2D}$ we find acceptable agreement. The solutions we obtain from (2.22) violate, however, the force balance condition (2.5) (i), which explicitly demonstrates that already a simple Hookean stretching energy leads to non-trivial shapes. Note that we, instead of solving (2.22), we could likewise minimize the free energy for the elastic lens, which is obtained analogously to (2.17), but with an additional elastic energy term as in (2.3).

Equation (2.22) can also be used to determine Young's modulus Y_{2D} and the pressure p_0 from a single measurement of the cap height h or the contact angle θ, if the surface tensions σ and γ are known. Two height measurements of the same capsule at different
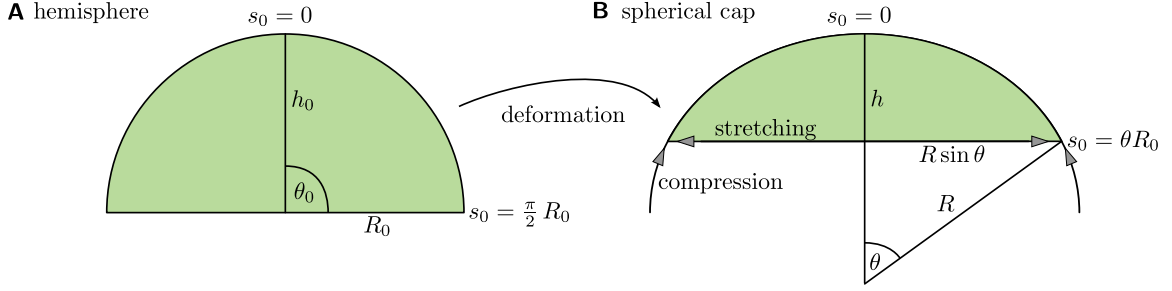
Figure 2.6: Deforming a hemispherical rest shape **A** into a spherical cap **B**. The resulting spherical cap has constant tension $\tau_s = \text{const}$ in meridional direction, constant tension $\tau_\phi = \text{const}$ in circumferential direction, but tensions are anisotropic, i.e., $\tau_s \neq \tau_\phi$ violating the force balance conditions (2.5) (i). We conclude that spherical caps with hemispherical rest shape exhibit inhomogeneous stresses in order to fulfill (2.5) (i).

surface tensions σ or at different capsule volumes V_0 could be used to determine Young's modulus Y_{2D} and Poisson's ration ν_{2D}.

2.1.8 Curvature at the interface

From Fig. 2.5 (right) it is clear that the bending modulus of the shell's material controls the curvature of the capsule at the liquid-liquid interface, i.e., smaller bending resistance leads to sharper bends with smaller radius of curvature at the liquid-liquid interface. Therefore, measurements of the curvature at the interface can provide information on the bending modulus E_B, provided that we can quantify the scaling law relating between both quantities. We will show analytically in the following paragraph that curvature at the interface and bending modulus are, indeed related by a simple scaling relation, which is also verified numerically in Fig. 2.8.

Pogorelov approximation

In Fig. 2.8 we find a scaling $\kappa_s \sim E_{\mathrm{B}}^{-1/2}$ for the curvature κ_s at the interface from numerical simulations. We can derive this scaling from an adaption of Pogorelov's theory [70] as it has been used in Ref. [45, 71]. We start from an elastic lens shape for vanishing bending rigidity $E_B \approx 0$, which is described by the contour $(r(s_0), z(s_0))$ and has a sharp edge at the AB-interface. If the bending rigidity is introduced, the shape becomes rounded at the edge, which is described by an additional displacement field $(v(s_0), u(s_0))$ such that

$$(r(s_0), z(s_0)) \rightarrow (r(s_0) + v(s_0), z(s_0) + u(s_0)).$$

during rounding. Rounding involves two additional energies contributing to the shape: the additional bending energy U_B associated with the bending rigidity and an additional mechanical work U_σ performed against that the surface tension σ because rounding displaces the three phase contact line against the surface tension σ as can be clearly seen in Fig. 2.5 (right).

Since the interface load acts in radial direction, it is reasonable to assume that $u(s_0) = 0$, i.e., only radial shape perturbations occur. This allows us to write the total energy change, induced by bending and pulling against σ while starting at the elastic lens, as

$$U = U_B + U_\sigma = 2 \int_\ell^{\ell+\epsilon} ds_0 \left[\pi R_D E_{\mathrm{B}} v''(s_0)^2 - \pi R_D \sigma v(s_0) \delta(s_0 - \ell) \right] \qquad (2.23)$$
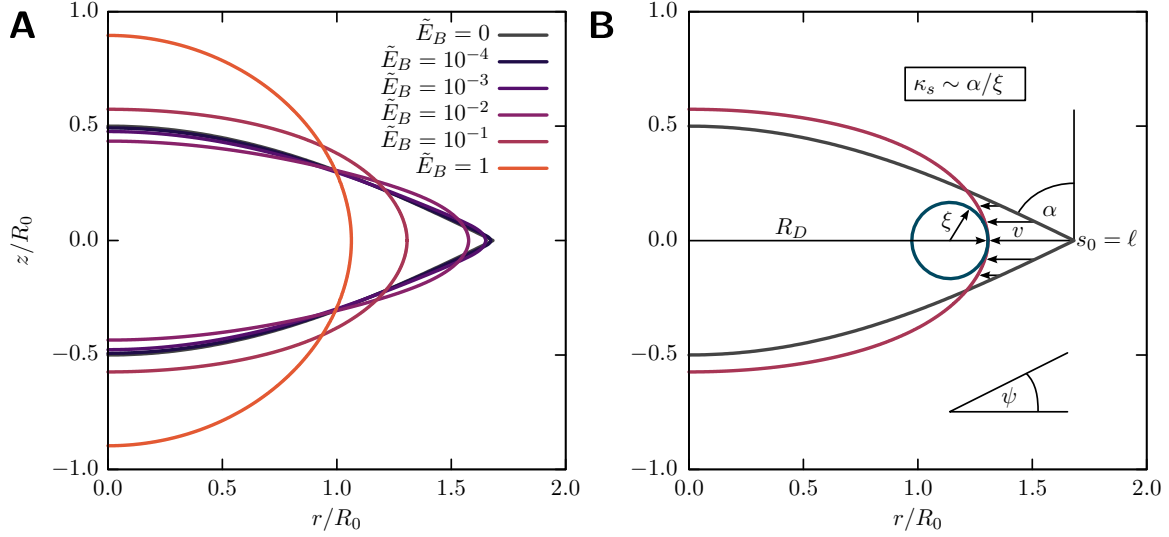
Figure 2.7: A) Shapes with increasing bending modulus. The bending modulus of the shell's material obviously determines the curvature at the liquid-liquid interface at $z = 0$ where the interface load σ pulls the equator outwards. Increasing the bending modulus increases the radius of curvature at the interface. Shapes were calculated in the elastic regime with $\gamma/Y_{2D} = 1/10$. **B)** Illustration of the geometrical quantities employed within the Pogorelov approximation. We assume that the major contribution to the bending energy is located within a small region of size ξ at $s_0 = \ell$, i.e., the liquid-liquid interface. When the bending energy is switched on, the kink of the elastic lens vanishes and the contact angle α decreases from a finite value to zero. This deformation is quantified by the radial displacement field $v(s_0)$. The curvature at the interface is accessible via $\kappa_s \sim \alpha/\xi$ employing the length scale ξ and the contact angle α.

where ϵ describes a small arc length region over which the kink of the shape is rounded and R_D is the radius of the circle in the interface plane, i.e., the radius of the interface cross-section. In eq. (2.23) we neglect the apparent hoop stretching as well as higher order and constant terms of the bending energy (for a detailed analysis, see Ref. [70]). Throughout the following calculations we use approximations for small α, which is the turning angle of the shape at the interface and related to the opening angle of the elastic lens via $\alpha = \pi/2 - \theta$. To find the corresponding characteristic arc length scale $\xi \sim \alpha\kappa_s^{-1}$ on which the shape gets bent at the interface, we non-dimensionalize eq. (2.23) according to

$$s_0 = \xi\bar{s}_0,$$

$$-v(s_0) = \xi\alpha\bar{v}(\bar{s}_0),$$

$$-v''(s_0) = \frac{d^2v(s_0)}{ds_0^2} = \alpha\frac{\xi d^2\bar{v}(\bar{s}_0)}{\xi^2 d\bar{s}_0^2} = \frac{\alpha}{\xi}\bar{v}(\bar{s}_0)'',$$

and recast the energies in (2.23) as

$$U_B = E_B R_D\frac{\alpha^2}{\xi}\int_{\bar{\ell}}^{\bar{\ell}+\bar{\epsilon}} d\bar{s}_0\bar{v}(\bar{s}_0)''^2,$$

$$U_\sigma = \pi R_D\sigma\xi\alpha\int_{\bar{\ell}}^{\bar{\ell}+\bar{\epsilon}} d\bar{s}_0\bar{v}(\bar{s}_0)\delta(\bar{s}_0 - \bar{\ell}). \tag{2.24}$$
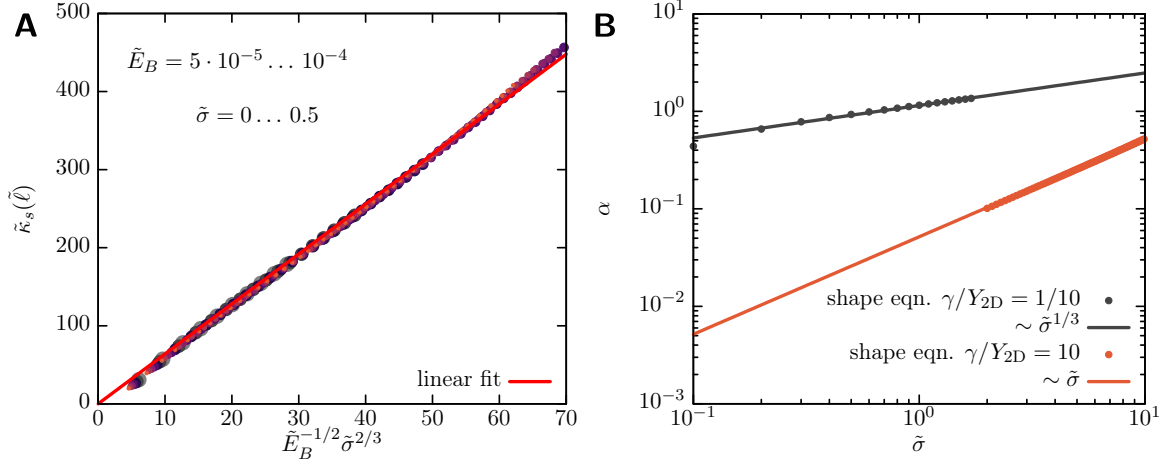
Figure 2.8: A) Numerical verification of the scaling law $\kappa_s \sim E_B^{-1/2}\sigma^{2/3}$ for elastic shells in the purely elastic regime $\gamma = 0$. **B)** Numerical verification of the scaling laws $\alpha \sim \sigma^{1/3}$ in the elastic regime $\gamma \ll Y_{2D}$ and $\alpha \sim \sigma$ in the fluid regime $\gamma \gg Y_{2D}$ both for elastic lenses. (All quantities in dimensionless form, see eq. (2.2).)

Minimizing the total energy $U = U_B + U_\sigma$ with respect to ξ we find the scaling relations

$$\xi \sim \alpha^{1/2}\sqrt{\frac{E_B}{\sigma}},$$
$$U = U_0 \sim R_D \alpha^{3/2}\sqrt{E_B\sigma}. \tag{2.25}$$

The dimensionless integrals in eq. (2.24) only contribute numerical prefactors, the essential result is the scaling behavior of U_0 and ξ. Note that the above scaling relations still depend on α. This dependence can be eliminated by employing the symmetric force balance condition (2.22). Expansion in α gives

$$\alpha \sim \begin{cases} \sigma^{1/3} Y_{2D}^{-1/3}, & \gamma \ll Y_{2D} \quad \text{(elastic)} \\ \sigma\,\gamma^{-1}, & \gamma \gg Y_{2D} \quad \text{(fluid)}, \end{cases}$$

where we differentiate between an elastic and a fluid regime. Both scaling relations are verified numerically in Fig. 2.8 (right), where we obtain $\alpha \sim \sigma^{1/3}$ for the elastic and $\alpha \sim \sigma$ for the fluid regime. Inserting these scaling relations into eq. (2.25) gives

$$\xi \sim \begin{cases} E_B^{1/2}\sigma^{-1/3} Y_{2D}^{-1/6}, & \gamma \ll Y_{2D} \quad \text{(elastic)} \\ E_B^{1/2}\gamma^{-1/2}. & \gamma \gg Y_{2D} \quad \text{(fluid)}. \end{cases}$$

From $\kappa_s \sim \alpha/\xi$ we finally obtain the scaling laws for the shell's curvature at the AB-interface

$$\kappa_s \sim \begin{cases} E_B^{-1/2}\sigma^{2/3} Y_{2D}^{-1/6}, & \gamma \ll Y_{2D} \quad \text{(elastic)} \\ E_B^{-1/2}\sigma\gamma^{-1/2}, & \gamma \gg Y_{2D} \quad \text{(fluid)}, \end{cases} \tag{2.26}$$

which are verified numerically in Fig. 2.8 (left). Note that the exponent of the bending modulus in $\kappa_s \sim E_B^{-1/2}$ is universal, i.e., independent of whether we are in the fluid or elastic regime. For comparison, spherical shells which buckle upon deflation have $\kappa_s \sim E_B^{-1/4}$ at the spherical rim of the indentation [45, 71].
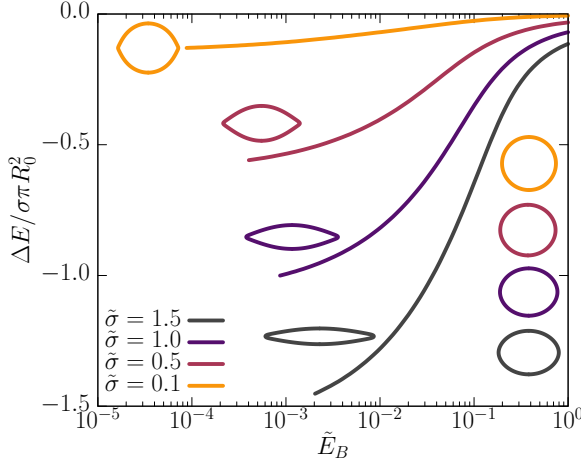
Figure 2.9: Adsorption energy difference $\Delta E / \sigma \pi R_0^2$ between soft and hard particles as a function of the dimensionless bending rigidity $\tilde{E}_B = H^2 / R_0^2$ for different values of the dimensionless liquid tension $\tilde{\sigma} = \sigma / Y_{2D}$. The adsorption energy is strongly enhanced for hollow capsules with small thickness to radius ratios H/R_0 and for large liquid tensions. For the above measurement we used $\gamma/Y_{2D} = 1/10$. The insets show the corresponding capsule shapes.

Experimental perspective

The scaling results presented above are well suited to be used experimentally in order to determine the bending modulus of elastic shells adsorbed to a planar liquid-liquid interface. Provided that the thickness of the layer, the interface load and the shell's curvature at the interface are known or can be measured, the bending modulus is given by

$$E_B = 9.3436 \, H^{1/2} \sigma \kappa_s^{-3/2}, \tag{2.27}$$

where the numerical prefactor in relation (2.26) was determined by a linear fit to the numerical results and Y_{2D} was obtained from the layer's thickness by employing relation (2.1). Note that $\sigma \kappa_s^{-3/2} = \text{const}$, which is why it makes sense to vary the interface load σ in order to improve the statistical significance of such a measurement. This could be achieved by, e.g., adding surfactants to one of the liquid phases A or B that decrease σ with increasing surfactant concentration. The dependence of σ and the surfactant concentration can be determined, e.g., in a pendant drop tensiometer. The curvature κ_s can be obtained from analyzing capsule images and fitting a circle to the capsule edge at the liquid-liquid interface.

2.1.9 Adsorption energy

During deformation at the liquid-liquid interface capsules deform into a lens-like shape, which increases the occupied interface area and, thus, the adsorption energy. This can significantly enhance their efficiency as emulsifiers.

Using our numerical results we can quantify the increase in adsorption energy as a function of the softness of the capsule. The adsorption energy of the soft capsule is given by the total energy gain

$$E_{\text{soft}} = -\sigma \pi r^2(\ell) + \int w(s_0) \mathrm{d}A_0$$

where $\pi r^2(\ell)$ is the occupied circular cross-section area within the liquid-liquid interface plane and the last term the total elastic energy including stretching energy, bending energy, and the surface energy γA. Each capsule at the liquid-liquid interface lowers the interfacial energy by E_{soft} and, thus, decreases the effective surface tension of the liquid-liquid interface.

This effect is stronger for hollow soft elastic capsules as compared to hard particles and becomes more pronounced with decreasing thickness of the capsule. For hard spherical particles of equal size we have an adsorption energy $E_{\text{hard}} = \gamma 4\pi R_0^2 - \sigma \pi R_0^2$. In Fig. 2.9

we numerically quantify the adsorption energy difference between soft and hard particles $\Delta E \equiv E_{\text{soft}} - E_{\text{hard}}$ as a function of the dimensionless bending modulus $\tilde{E}_{\text{B}} = H^2/R_0^2$, which characterizes the thickness of the capsule, see eq. (2.2). This allows us to quantify the enhancement of the adsorption energy due to capsule softness by decreasing $\tilde{E}_{\text{B}}$ or the capsule thickness. For $\tilde{E}_{\text{B}} \sim 1$ the results should become similar to the energy gain for soft filled particles as they have been considered in Refs. [53–55]. Fig. 2.9 then clearly shows that hollow capsules are much more efficient as emulsifiers than filled soft particles (or even a filled hard particle) of equal size.

2.1.10 Conclusion

We investigated shapes of deformed microcapsules adsorbed at liquid-liquid interfaces both by calculating shapes numerically and by analytical approximation methods. We derived shape equations and matching conditions at the liquid-liquid interface for the numerical calculation of shapes and discussed the generic case, i.e., extensible shells of finite thickness and constant volume, as well as two important limiting cases, namely liquid lenses and elastic lenses. The shape equations together with the appropriate matching conditions at the liquid-liquid interface enable us to calculate numerical solutions for each of these cases, see Figs. 2.5 and 2.3.

Liquid lenses shapes are composed of two spherical caps and can be exactly calculated analytically. Elastic lenses exhibit similar shapes, which motivated an approximative theory using spherical caps and leading to a much simpler description by a single algebraic equation (2.22) for the elastic lens shape. The spherical cap approximation becomes exact in the limit of thin $H \ll R$, and soft $\gamma \gg Y_{\text{2D}}$ or weakly stretched capsules with $\sigma \ll \gamma$.

These results can, in principle, be used for elastometry, i.e., to determine the elastic moduli from an experimentally acquired image by fitting numerical solutions of the shape equations to a set of contour points extracted from the image. Other elastometry methods following the same philosophy are the study of deformations of pendant capsules under volume changes to obtain elastic moduli as investigated in Refs. [1, 5, 61], the study of the edge curvature of a buckled shapes to obtain the bending modulus [44], or the study of shapes of osmotically buckled capsules to infer the osmotic pressure [62].

The approximative theory using spherical caps shows that the height or contact angle of the lens-like shape is a simple experimental readout that can be used to determine the Young modulus of the capsule shell if the surface tension σ is known, either by using the approximation by the algebraic equation (2.22) for the elastic lens shape or by using numerical results for the relation between height and Young modulus.

For shells of finite thickness we also found the relation between the curvature at the interface, the bending modulus, Young's modulus and the interface load, see eq. (2.27), which can be used to determine the bending modulus from a curvature measurement at the interface, provided Young's modulus has been determined before, e.g., by elastometry methods as just described for elastic lenses, or the method described in Ref. [5] by preparing a pendant capsule.

In principle, the results presented in this paper allow us to determine the full set of elastic constants from shape profiles of elastic capsules adsorbed to liquid-liquid interfaces. Similar methods exist for the pendant capsule method, which has been shown to be widely applicable to experimental data [5]. We extend this method to capsules at liquid-liquid interfaces. Unfortunately, there is no experimental data available yet.

Finally, we could show that hollow elastic microcapsules can be much more effective in reducing the interfacial energy than filled soft particles or even hard particles of the same size, see Fig. 2.9. During capsule deformation at the liquid-liquid interface into a lens-like

shape the adsorption energy, which is proportional to the occupied interface area, increases significantly. This shows that hollow microcapsules could be much more efficient in foam and emulsion stabilization than filled particles of comparable size.

In the following section, we stick to the Hookean membrane approximation and provide a performance optimized version of the algorithm first developed in [1].

2.2 Elastic capsules prepared in a pendant drop tensiometer

Classical elastic shell theory enables reverse-engineering techniques that allow for inferring information on the material properties from shape profiles. Thereby, the elastic parameters are varied in the theoretical description until the experimental shape profile is matched. In this section, we rigorously apply this method to pendant elastic capsules using the Hookean membrane approximation. We like to stress either, that both the elastic laws and the hydrostatic setup are replaceable, i.e., the method is universally applicable.

We provide a C/C++ software for the shape analysis of deflated elastic capsules in a pendant capsule geometry, which is based on an elastic description of the capsule material as a quasi two-dimensional elastic membrane using shell theory. Pendant capsule elastometry provides a new in-situ and non-contact method for interfacial rheology of elastic capsules that goes beyond determination of the Gibbs- or dilational modulus from area-dependent measurements of the surface tension using pendant drop tensiometry, which can only give a rough estimate of the elastic capsule properties as they are based on a purely liquid interface model. Given an elastic model of the capsule membrane, pendant capsule elastometry determines optimal elastic moduli by fitting numerically generated axisymmetric shapes optimally to an experimental image. For each digitized image of a deflated capsule elastic moduli can be determined, if another image of its undeformed reference shape is provided. Within this paper, we focus on nonlinear Hookean elasticity because of its low computational cost and its wide applicability, but also discuss and implement alternative constitutive laws. For Hookean elasticity, Young's surface modulus (or, alternatively, area compression modulus) and Poisson's ratio are determined; for Mooney-Rivlin elasticity, the Rivlin modulus and a dimensionless shape parameter are determined; for neo-Hookean elasticity, only the Rivlin modulus is determined, using a fixed dimensionless shape parameter. Comparing results for different models we find that nonlinear Hookean elasticity is adequate for most capsules. If series of images are available, these moduli can be evaluated as a function of the capsule volume to analyze hysteresis or aging effects depending on the deformation history or to detect viscoelastic effects for different volume change rates. An additional wrinkling wavelength measurement allows the user to determine the bending modulus, from which the layer thickness can be derived. We verify the method by analyzing several materials, compare the results to available rheological measurements, and review several applications. We make the software available under the GPL license at `github.com/jhegemann/opencapsule`.

Encapsulation applications employ closed microcapsules, but often capsules can likewise be produced in a pendant or hanging capsule geometry, where the capsule is not closed and the capsule edge is attached to a capillary [10, 72–79]. Such capsules can be produced by self-assembly onto a droplet hanging from a capillary or onto an air bubble rising from a capillary, or by interfacial crosslinking at the interface of a pendant droplet [1]. An advantage of this pendant capsule geometry is that volume reduction or pressure application can easily be realized by fluid suction through the capillary and it, thus, offers a simple way of micromanipulation for mechanical characterization.

The related pendant droplet tensiometry is a standard tool to determine the surface tension of a liquid interface using the Laplace-Young equation to model the droplet shape

[80–83], which is commercially available. The same Laplace-Young analysis has frequently been applied to pendant elastic capsules with different shell materials or droplets coated with solid-like layers of adsorbed particles [72, 75–77, 84–89] resulting in the determination of an 'effective surface tension' γ describing the solid shell interface of surface area A. Changing the surface area A in deflation experiments, the so-called Gibbs- or dilational modulus $E_{\text{Gibbs}} = \mathrm{d}\gamma/\mathrm{d}\ln A$ can be calculated. Pendant drop tensiometry can also be applied to droplets or capsules with a viscoelastic interface by employing oscillating droplets [72, 85, 87–89]; then a complex dilational modulus can be obtained, which includes a real elastic and an imaginary loss part. The elastic dilational modulus is equal to the area compression modulus K_{2D} for a fluid interface or for a two-dimensional solid interface in a planar Langmuir-Blodgett trough geometry. Application of the same concept to pendant elastic capsules gives misleading results because of inhomogeneous and anisotropic elastic stresses in the capsule geometry and the existence of a curved undeformed reference shape of the capsule [1, 72–74, 79]. In Ref. [1], an elastic model based on shell theory has been developed which is capable of describing capsule shapes in a deflation experiment more realistically. Similar elastic models have been formulated in Refs. [72–74, 79]. In Ref. [1] this approach has been extended to the pendant capsule elastometry method, where the elastic model is used to determine two elastic constants, the surface Young modulus Y_{2D} and Poisson's ratio ν_{2D}, by optimally fitting calculated shapes to experimental images. Pendant capsule elastometry has already been applied to OTS-capsules and hydrophobin-coated bubbles [1] but also to bacterial films at interfaces [24].

Here, we want to present and make publicly available a much more efficient implementation of the pendant capsule elastometry method as a C/C++ software with a high degree of numerical efficiency and automation. In contrast to Ref. [1], where elastic constants were optimized on a grid in parameter space to optimally match the experimental shape profile, we optimize elastic constants in continuous parameter space, which improves both performance and accuracy. Moreover, we go beyond Ref. [1] and generalize the shape analysis method to other constitutive laws. In particular we investigate the behavior of the shape analysis method in combination with Mooney-Rivlin or neo-Hookean elasticity models, which are commonly used for inextensible polymeric materials.

These significant improvements turn the analysis into a strong tool to investigate different materials in a short time and on a large scale. We demonstrate these capabilities by analyzing a variety of deformation experiments for different materials. In pendant capsule elastometry Young's modulus and Poisson's ratio (or the Rivlin modulus and the dimensionless shape parameter) of the two-dimensional capsule shell material are obtained from an analysis of a digitized image of the deflated capsule shape and a second image of its undeformed reference shape. If the capsule wrinkles upon deflation, an additional wrinkling wavelength measurement allows us to determine the bending modulus, from which the layer thickness can be derived if the shell material is a thin layer of a three-dimensional isotropic elastic material.

2.2.1 Experimental methods

Several interfacial rheology methods exist, which allow the determination of the elastic properties of the capsule shell material. We review four different rheological methods, which we will use as references for the pendant capsule method described in this paper. Typical experimental methods are (i) surface shear-rheometry [90], (ii) Langmuir-Blodgett trough, (iii) shear flow rheoscope (flow cell) [91], and (iv) spinning drop apparatus [92]. Methods (i) and (ii) work with *planar* membranes of the shell material, whereas methods (iii) and (iv) directly work in the curved capsule geometry, like pendant capsule elastometry does.

Apart from these four methods there are other contact techniques such as probing capsules with AFM tips, micromanipulators, or optical tweezers (see Ref. [26] for a review). Pendant capsule elastometry is a non-contact technique and, in comparison with methods (iii) and (iv), it does not require fluid motion in the surrounding fluid. We focus here on elastic capsule shell materials. For viscoelastic materials there are other interfacial rheology methods available [87], such as double wall ring rheometry [93] or magnetic rod rheometry [94].

In shear-rheometry, a transducer (thin disk or ring) is placed in a circular vessel at a planar liquid-liquid or air-liquid interface; between transducer and container wall a membrane with the shell material is prepared, such that membrane deformations can be applied in circumferential direction. While oscillating at a certain frequency, the mechanical response is measured, which gives the interfacial storage modulus μ' and the loss modulus μ''. From μ' one determines the surface Young modulus $Y_{2D} = 2(1 + \nu_{2D})\mu'$ provided that the Poisson ratio ν_{2D} is known.

In a Langmuir-Blodgett trough, a membrane made from the shell material is prepared in a rectangular vessel at a liquid-liquid or air-liquid interface. During compression of the membrane, the surface tension γ and area A are measured, from which the Gibbs modulus $E_{Gibbs} = d\gamma/d \ln A$ is determined. The Gibbs modulus E_{Gibbs} corresponds to the area compression modulus K_{2D} in the planar trough geometry; we will show that these two parameters differ substantially in the curved capsule geometry.

In a shear flow rheoscope, a closed capsule is placed in a liquid phase between two concentric hollow cylinders. By rotating the cylinders in opposite directions a shear flow is induced, which deforms the capsule. Comparing the shape profile with ellipses gives the compression of the surface and, thus, the surface Young modulus [95].

In a spinning drop apparatus a closed capsule is placed in a cylindrical vessel filled with a fluid. When the vessel is rotated at high frequencies the capsule is exposed to centrifugal forces, which induce a deformation. Similar to the shear flow rheoscope the surface Young modulus is obtained from a shape analysis [92].

2.2.2 Pendant capsule elastometry

The pendant drop apparatus is widely spread in industrial environments and research departments. Typically it is shipped with a software performing a Laplace-Young analysis on captured images in order to determine the surface tension of fluid interfaces. In this paper, we provide a generalized algorithm as a C/C++ software, which is able to perform an analogous shape analysis for elastic membranes in order to determine the surface Young modulus Y_{2D} and the Poisson ratio ν_{2D} (or the Rivlin modulus Y_M and the dimensionless shape parameter Ψ) of the material. In section 2.2.8, we will present examples with several different capsule shell materials, which demonstrate that our software is widely applicable and that pendant capsule elastometry results are in good agreement with other rheological measurements. As compared to pendant drop tensiometry, the shape analysis of pendant elastic capsules comes at the cost of an additional amount of runtime (one or few minutes per image), but enables the proper characterization of the elastic material properties.

In the following, we will focus on pendant elastic capsules produced by interfacial crosslinking, gelation or polymerization, see Fig. 2.10. Consider a droplet of size ~ 1mm hanging from a capillary. The inner (liquid) and outer phase (liquid/air) are separated by a liquid interface with a surface tension compensating the pressure difference. Surfactants, and potentially crosslinkers, are dissolved in the droplet or the surrounding fluid. When forming the droplet, surfactants immediately start to adsorb to the interface and spread over it. During equilibration of bulk and interface surfactant concentrations, the surface tension decreases. Though the interface is now partially occupied by surfactants, it is still a liquid interface
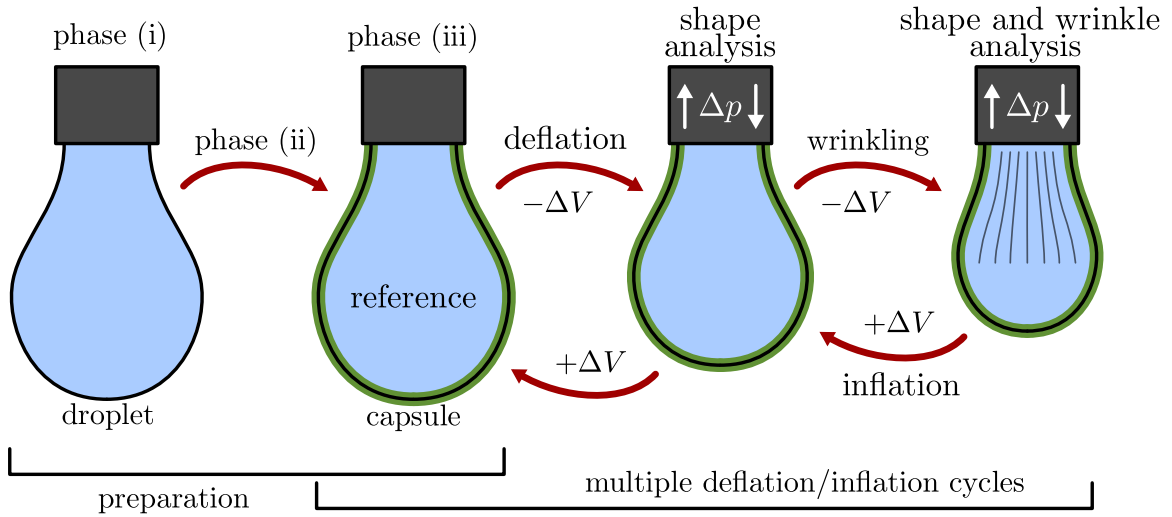
Figure 2.10: Typical experimental procedure in pendant drop elastometry. In a first step, a pendant capsule is prepared by coating a pendant droplet with an elastic shell, for example, by interfacial crosslinking. When the coating process is completed, cyclic pressure/volume changes are applied to the capsule and images are taken continuously during this procedure. Fitting theoretical shapes from the elastic model to the shape profile extracted from the image gives the elastic moduli of the shell membrane. For sufficiently solid and thin materials wrinkles occur upon deflation, which can be analyzed to give the bending modulus of the shell membrane. The procedure allows for multiple inflation-deflation-cycles, which can reveal aging effects or hysteresis. Application of different volume change rates can reveal viscoelastic effects.

obeying the Laplace-Young law. This changes when crosslinkers start to connect previously freely diffusing surfactants and turn the interface into an elastic solid by forming elastic bonds above a threshold concentration for gelation. After completion of this crosslinking process, an elastic capsule in its reference, i.e., undeformed or stress-free shape has been formed.

By slowly reducing the volume of the capsule one observes elastic deformations, which are specific to the microscopic structure of the membrane. We neglect such microscopic details by assuming a homogeneous isotropic material and focus on the set of elastic constants, which describe the macroscopic properties of the membrane. Nonetheless, microscopic effects can be observed in the elastic constants, if these are measured during the course of deflation. Phase transitions that occur as a function of the accessible surface area induce a rapid change in the elastic moduli and are, therefore, detected. Viscoelastic or creep behavior are detected, if elastic moduli change with the rate of volume reduction. Aging effects are detected, if elastic moduli change during the course of multiple cycles of de- and inflation that are applied to the capsule.

The general aim of pendant capsule elastometry is the same as in pendant drop tensiometry, namely to adjust material parameters (elastic constants or surface tension and, eventually, pressure) such that theoretically generated axisymmetric capsule/droplet shapes optimally fit a given experimental shape. The shape of an elastic capsule can be described by classical elastic shell theory (if bending moments are included) or elastic membrane theory (if bending moments are neglected) [96], which requires an elastic material model specified by its constitutive stress-strain relation or a corresponding elastic energy. We neglect bending moments and mainly focus on Hookean membrane elasticity throughout this paper but also discuss Mooney-Rivlin or neo-Hookean elastic membranes, which are also implemented in the software. Each elastic material model is characterized by a set of elastic material
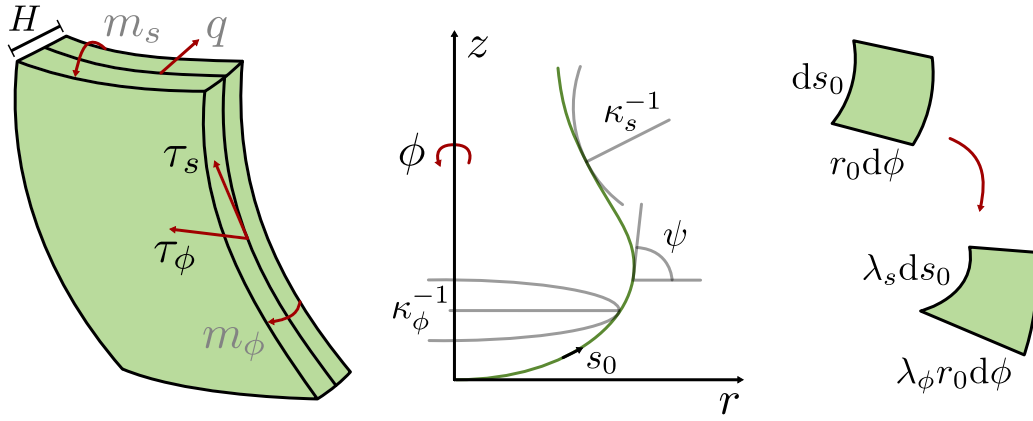
Figure 2.11: Parametrization of the shape equations. Axisymmetric shapes are described by a shape profile in the r-z-plane, which generates a surface of revolution by rotation with respect to the z-axis. The shape equations are integrated over the thickness H of an infinitesimal membrane patch, which is an approximation for thin shells. Forces and torques resulting from curvature are neglected and, thus, depicted in gray.

parameters, such as the surface Young modulus Y_{2D} and the Poisson ratio ν_{2D} in Hookean membrane elasticity (or the Rivlin modulus Y_M and the dimensionless shape parameter Ψ in Mooney-Rivlin membrane elasticity), which we aim to determine by optimally fitting theoretical to experimental shapes. For an elastic material we also need an elastically relaxed reference shape, with respect to which local stretch factors or strains in the material are defined, in order to calculate deformed shapes. This problem will be discussed in Sec. 2.2.3 in detail.

In a pendant capsule geometry (see Fig. 2.10) the capsule is formed hanging from an axisymmetric capillary. Therefore, we assume axisymmetric shapes which can be uniquely described by their shape profile, i.e., the intersection of the capsule surface with a plane. We use cylindrical coordinates to describe axisymmetric shapes (with the z-axis as symmetry axis) and describe the profile as a contour in the r-z-plane, see Fig. 2.11. The shape profile can be trivially acquired experimentally by taking a two-dimensional image from the side.

For a given elastic model, tangential and normal force equilibrium of stresses and external forces at every point on the surface determine the equilibrium shape. The equations of force equilibrium, geometric relations, and constitutive relations can be used to derive a closed system of first order differential equations for r, z, a slope angle ψ (see Fig. 2.11) and the meridional elastic stress τ_s with the arc length s_0 of the undeformed spherical profile as independent variable, which are called shape equations and discussed below in Sec. 2.2.3 in detail. The shape equations use the constitutive relations and are, therefore, specific for the elastic model that is used to describe the capsule material. We discuss shape equations for Hookean elasticity, Mooney-Rivlin, and neo-Hookean materials in detail in Sec. 2.2.3. The solution of the shape equations determines the theoretical shape profile of an axisymmetric shape for a given set of material parameters, a given pressure inside the capsule, and a given elastically relaxed reference shape. We solve the shape equations numerically by a shooting method (see 2.3.3) because boundary conditions have to be applied at both ends of the shape profile, i.e., at the attachment point to the capillary and at the lower apex of the capsule.

Comparison between experiment and theory is achieved by overlaying the theoretical shape and the image, regardless of the employed elastic model. In pendant capsule elastometry elastic material parameters of individual capsules are then determined by fitting the parameters (i.e., elastic moduli) of the model until the theoretical shape (for each parameter

set obtained by solution of the shape equations) optimally matches the contour given in the image. We determine the optimal fit by minimizing the mean-square deviations between image contour points and theoretical contour (see 2.3.4).

This approach works with different constitutive relations with different numbers of elastic moduli, as long as the shape is sensitive to each of the employed material parameters. One prominent example for a parameter, where the shape is rather insensitive to, is the bending modulus E_B for a thin capsule membrane. Therefore, the bending modulus of a thin capsule membrane cannot be determined reliably by fitting to the shape profiles but has to be determined via a different approach, namely the analysis of wrinkle wavelengths. In case of a wrinkling instability, we have to use an effective constitutive relation in the wrinkled part of the shape profile and corresponding effective shape equations, which are also discussed in the next Sec. 2.2.3.

Thus, for the complete pendant elastometry shape analysis we have to handle three major tasks, (i) solving the shape equations for the given elastic model to determine the theoretical deformed shape from the elastically relaxed reference shape, (ii) decoding the contour from the image and (iii) adapting the model parameters (elastic moduli) to fit the contour. Details of the algorithm are described in the Appendix: (i) solving the shape equations by a multiple shooting method in 2.3.3 and determining the reference shape in 2.3.2, (ii) the image processing in 2.3.6, and (iii) parameter determination by shape regression in 2.3.4. In contrast to previous implementations [1], we strongly focus on numerical performance and robustness as well as a high degree of automation and make the resulting C/C++ code publicly available under a GPL License [4]. We also implement shape equations for different constitutive relations for elastic membranes: nonlinear Hookean as in Ref. [1], strictly linear Hookean as in Ref. [72, 74, 79], Mooney-Rivlin, and neo-Hookean membranes as in Ref. [73]. We verify our method by analyzing several materials and comparing the results to rheological measurements.

2.2.3 Shape equations

Liquid reference shape

The shape of a liquid droplet hanging from a capillary can be described by a system of nonlinear differential shape equations with the arc length s_0 of the contour as independent variable,

$$
\begin{aligned}
&r_0^{'}(s_0) = \cos \psi_0, \quad z_0^{'}(s_0) = \sin \psi_0, \\
&\psi_0^{'}(s_0) = (p_0 - \Delta\rho g z_0)/\gamma - \sin \psi_0/r_0
\end{aligned}
\tag{2.28}
$$

(primes denote derivatives $\mathrm{d}/\mathrm{d}s_0$). The z_0-axis is the axis of symmetry, r_0 the radius and ψ_0 the slope angle of the contour. We use quantities with a subscript '0' because we will employ a Laplace-Young fit for the elastically relaxed reference state of our elastic capsule before deformation by volume reduction, see Sec. 2.2.3 below. The first two equations are geometric relations involving the slope angle ψ_0; the third equation is the Laplace-Young force balance equation in cylindrical parametrization, where we use $\kappa_{s_0} = \mathrm{d}\psi_0/\mathrm{d}s_0$ and $\kappa_{\phi_0} = \sin \psi_0/r_0$ for the curvature of the droplet meridional and circumferential direction. Note that the Laplace-Young shape equations (2.28) are already closed, i.e., the right hand side is completely written in terms of the three functions $r_0(s_0)$, $z_0(s_0)$, $\psi_0(s_0)$ on the left hand side. The arc length s_0 varies in the range $[0, L_0]$ and the lower apex is located at $s_0 = 0$ the drop is attached to the capillary at $s_0 = L_0$. The Laplace-Young shape equations are solved with initial conditions $r_0(0) = 0$, $\psi_0(0) = 0$, and $z_0(0) = \zeta$ arbitrary;

the contour length L_0 is determined by the boundary condition $r_0(L_0) = a/2$, where a is the inner capillary diameter. The right hand side of $\psi_0'(0)$ at $s_0 = 0$ is ambiguous using the initial values; L'Hôpital's rule leads to $\psi_0'(0) = (p_0 - \Delta\rho g\zeta)/2\gamma$ at $s_0 = 0$ which is also needed to start the integration of the shape equations. The solution gives the droplet shape $(r_0(s_0), z_0(s_0))$ as a function of the parameters p_0, $\Delta\rho$ and γ. The pressure p_0 is the hydrostatic pressure at the apex (if $\zeta = 0$), $\Delta\rho$ the density difference between the inner and outer phase, and γ the surface tension. The pressure difference $\Delta\rho g z_0$ is induced by gravity.

Elastic membrane materials

The Laplace-Young shape equations (2.28) are well suited for fluid interfaces, but interfacial crosslinking or gelation actually turns the interface into a two-dimensional elastic solid. From classical shell theory and neglecting bending moments one derives the elastic shape equations with the arc length s_0 of the *undeformed* spherical contour as independent variable, [1]

$$r'(s_0) = \lambda_s \cos\psi, \quad z'(s_0) = \lambda_s \sin\psi,$$
$$\psi'(s_0) = \frac{\lambda_s}{\tau_s}\left(p - \Delta\rho g z - \frac{\sin\psi}{r}\tau_\phi\right), \quad (2.29)$$
$$\tau_s'(s_0) = -\lambda_s \frac{\cos\psi}{r}(\tau_s - \tau_\phi)$$

(primes denote derivatives $\mathrm{d}/\mathrm{d}s_0$). The meridional and hoop stretches $\lambda_s = \mathrm{d}s/\mathrm{d}s_0$ and $\lambda_\phi = r/r_0$ capture the elastic deformation state and are, thus, only defined with respect to the undeformed reference shape $r_0(s_0)$ (with subscript '0'); the corresponding strains are $(\lambda_s^2 - 1)/2 \approx \lambda_s - 1$ and $(\lambda_\phi^2 - 1)/2 \approx \lambda_\phi - 1$. Note that s denotes the arc length of the deformed configuration, whereas s_0 denotes the arc length of the undeformed configuration. Fig. 2.11 illustrates the involved quantities. The first to equations are geometric relations involving the slope angle ψ. The third and fourth equations describe normal and tangential force balance, respectively. In the normal force balance, the principal curvatures $\kappa_s = \mathrm{d}\psi/\mathrm{d}s$ and $\kappa_\phi = \sin\psi/r$ have been used.

It is important to note that eqs. (2.29) are still valid regardless of the constitutive relation. This is also the reason why eqs. (2.29) are not yet closed: we have to rearrange the constitutive relations $\tau_s = \tau_s(\lambda_s, \lambda_\phi)$ and $\tau_\phi = \tau_\phi(\lambda_s, \lambda_\phi)$ in order to express τ_ϕ and λ_s on the right hand side of eqs. (2.29) in terms of τ_s and $\lambda_\phi = r/r_0$, i.e., in terms of the functions $\tau_s(s_0)$ and $r(s_0)$ from the left hand side (and the known reference shape $r_0(s_0)$). We will discuss closure of the shape equations for different constitutive relations and also in the presence of wrinkles in the following sections. Once the shape equations (2.29) are closed, they are solved with the boundary conditions $r(0) = 0$, $\psi(0) = 0$, and $z(0) = \zeta$ arbitrary at the capsule apex. A fourth boundary condition $\tau_s(0) = \mu$ at the capsule apex serves as shooting parameter to satisfy the boundary condition $r(L_0) = a/2$ at the capillary (see 2.3.3 for the numerical realization of the shooting method). The right hand sides of $\psi'(0)$ and $\tau_s'(0)$ at $s_0 = 0$ are ambiguous using the initial values; L'Hôpital's rule leads to $\lambda_s(0) = \lambda_\phi(0)$ and isotropic tensions $\tau_s(0) = \tau_\phi(0)$ at the apex. This results in $\tau_s'(0) = 0$ and $\psi_0'(0) = \lambda_s(0)(p - \Delta\rho g\zeta)/2\mu$ at $s_0 = 0$ which are also needed to start the integration.

The pressure p is the hydrostatic pressure at the apex of the deflated shape (if $\zeta = 0$), which is below the pressure p_0 of the reference shape, i.e., $p < p_0$. In principle, information on the pressure p could be experimentally available if pressure measurements are possible. In the current implementation of the method and all applications below, the pressure p serves as Lagrange multiplier that is changed to control the capsule volume and determined from shape fitting along with the elastic moduli.

Nonlinear Hookean elastic membrane

For a Hookean stretching elasticity the meridional and circumferential tensions τ_s and τ_ϕ are related to the stretches λ_s and λ_ϕ by the constitutive relations

$$
\begin{aligned}
\tau_s &= \frac{1}{\lambda_\phi} \frac{Y_{2D}}{1 - \nu_{2D}^2} ((\lambda_s - 1) + \nu_{2D}(\lambda_\phi - 1)) + \gamma, \\
\tau_\phi &= \frac{1}{\lambda_s} \frac{Y_{2D}}{1 - \nu_{2D}^2} ((\lambda_\phi - 1) + \nu_{2D}(\lambda_s - 1)) + \gamma,
\end{aligned}
\tag{2.30}
$$

where Y_{2D} is the surface Young modulus and ν_{2D} Poisson's ratio. Instead of the surface Young modulus Y_{2D} we could also use the surface shear modulus μ' (sometimes called storage modulus G') or the area compression modulus K_{2D} as alternative elastic constants of the membrane material, which are related by

$$
\mu' = \frac{Y_{2D}}{2(1 + \nu_{2D})} = K_{2D} \frac{1 - \nu_{2D}}{1 + \nu_{2D}} \quad \text{and} \quad K_{2D} = \frac{Y_{2D}}{2(1 - \nu_{2D})}.
$$

Although we use a simple Hookean elastic energy, the relations (2.30) are *nonlinear* because of the additional $1/\lambda$-factors, which arise for purely geometrical reasons: the Hookean elastic energy density is defined per undeformed unit area, whereas the Cauchy stresses τ_s and τ_ϕ are defined per deformed unit length. The relations (2.30) still contain an interfacial tension γ because the elastic capsule is formed in the initial shape of a fluid interface. We assume that γ is the tension of the fluid interface in presence of a saturated interfacial surfactant concentration before crosslinking the surfactants to an elastic shell. This assumption is addressed in detail in Sec. 2.2.3.

The system of shape equations (2.29) can now be closed by using on the right hand side the constitutive relation for τ_ϕ from eqs. (2.30), and the relation

$$
\lambda_s = (1 - \nu_{2D}^2)\lambda_\phi \frac{\tau_s - \gamma}{Y_{2D}} - \nu_{2D}(\lambda_\phi - 1) + 1 \quad \text{with} \quad \lambda_\phi = \frac{r}{r_0},
$$

which derives from the constitutive relation for τ_s from eqs. (2.30). The resulting shape equations have also been used in Ref. [1].

Alternative elastic laws

At this point we want to compare to similar approaches to pendant capsule shapes by shape equations in the literature. Shape equations very similar to eqs. (2.29) have been obtained in Refs. [72–74, 79], where the same normal and tangential force balance and geometry relations have been employed, however, in combination with different constitutive relations. In Ref. [73], an incompressible neo-Hookean constitutive relation has been used for the shell material, which is a special case of an incompressible Mooney-Rivlin material. In Refs. [72, 74, 79], a strictly linear Hookean constitutive law has been used, where the $1/\lambda$-factors are missing as compared to the relations (2.30), (note that constitutive linear Hookean laws in Refs. [74, 79] contain some misprints). In Refs. [73, 74], exemplary theoretical shapes have been discussed but no elastic parameters have been determined from systematically fitting theoretical shapes to experimental images, i.e., using a least square minimization algorithm to optimally match the experimental shape with a theoretically generated contour. Therefore, we want to discuss how the shape equations (2.29) can be closed not only for a *nonlinear Hookean membrane* as in (2.2.3) but also for other constitutive relations.

The simplest example is a *strictly linear Hookean membrane*, where the closure is simply lacking one factor λ_ϕ as compared to eq. (2.2.3) [97],

$$\lambda_s = (1 - \nu_{2\mathrm{D}}^2)\frac{\tau_s - \gamma}{Y_{2\mathrm{D}}} - \nu_{2\mathrm{D}}(\lambda_\phi - 1) + 1 \;\; \text{with} \;\; \lambda_\phi = \frac{r}{r_0}.$$

Thus, the closure relations are, as for the nonlinear Hookean membrane, analytically accessible.

The *Mooney-Rivlin membrane model* is frequently used for polymer materials as it describes membranes made from incompressible materials. It describes these materials also deep into the nonlinear regime as it captures effects from strain-stiffening. It has the constitutive relation [97]

$$
\begin{aligned}
\tau_s &= \frac{Y_M}{3\lambda_\phi\lambda_s}\left(\lambda_s^2 - \frac{1}{(\lambda_s\lambda_\phi)^2}\right)\left[\Psi + (1-\Psi)\lambda_\phi^2\right] + \gamma, \\
\tau_\phi &= \frac{Y_M}{3\lambda_\phi\lambda_s}\left(\lambda_\phi^2 - \frac{1}{(\lambda_s\lambda_\phi)^2}\right)\left[\Psi + (1-\Psi)\lambda_s^2\right] + \gamma,
\end{aligned}
\tag{2.31}
$$

where Y_M is the surface Rivlin modulus and Ψ a dimensionless shape parameter. A *neo-Hookean membrane* has $\Psi = 1$. In the limit of small strains a neo-Hookean membrane reduces to a Hookean membrane with $Y_{2\mathrm{D}} = Y_M$ and $\nu_{2\mathrm{D}} = \nu_{3\mathrm{D}} = 1/2$ (for incompressibility). In order to close the shape equations we have to use the constitutive relations (2.31) to find λ_s and τ_ϕ as a function of τ_s and $\lambda_\phi = r/r_0$ in order to replace λ_s and τ_ϕ on the right hand side in the shape equations (2.29), as for the Hookean case. Unfortunately, this involves roots of fourth order polynomials. Therefore, we perform this task numerically in our software. Note that this numerical solution has to be obtained in each step of numerical integration of the shape equations, i.e., during each evaluation of the shape equations, which increases the computational runtime significantly (roughly by a factor of 10) as compared to fits with the nonlinear Hookean relation.

Wrinkling

The above shape equations (2.29) only hold for thin materials $H \ll R$, since we neglected bending elastic energy terms resulting from curvature, which can, in principle, be included into shape equations (see Ref. [44]). This is justified as the bending modulus is expected to scale $E_B \propto H^3$, whereas Young's modulus scales as $Y_{2\mathrm{D}} \propto H$. Consequently, for thin capsule shells, the shape profiles are insensitive to changes in the bending modulus, which makes it practically impossible to infer E_B from fitting theoretical shape contours to experimental images.

Nevertheless, we can determine the bending modulus in a separate analysis of the wrinkle wavelength [1]. Wrinkles in meridional direction are present if $\tau_\phi < 0$, i.e., if compressive stresses occur in circumferential direction (neglecting a small critical Euler stress necessary to trigger wrinkling). This condition determines the extent of the wrinkled region in meridional direction. In order to describe wrinkled shapes violating axisymmetry we use a pseudo-surface $(\bar{r}(s_0), z(s_0))$ (all modified quantities related to the pseudo-surface are denoted with bars) representing the average amplitude of the wrinkling modulation. If $\tau_\phi < 0$, the algorithm switches to a different set of shape equations for the pseudo-surface which is obtained by explicitly setting $\tau_\phi = 0$ [1]. The modified set of shape equations is also obtained from force-balance for the pseudo-surface. The meridional stresses for the pseudo-surface are related to the original stresses by $\bar{\tau}_s = \tau_s\lambda_\phi/\bar{\lambda}_\phi$, where $\bar{\lambda}_\phi = \bar{r}/r_0$ is

the apparent stretch of the pseudo-surface. Together with $\bar{\tau}_\phi = \tau_\phi = 0$ we obtain shape equations for the pseudo-surface,

$$\bar{r}'(s_0) = \lambda_s \cos \bar{\psi}, \quad z'(s_0) = \lambda_s \sin \bar{\psi},$$

$$\bar{\psi}'(s_0) = \frac{\lambda_s}{\bar{\tau}_s}(p - \Delta\rho g z),$$

$$\bar{\tau}_s'(s_0) = -\lambda_s \frac{\cos \bar{\psi}}{\bar{r}}\bar{\tau}_s.$$

(2.32)

Note that these shape equations hold independently of the constitutive relation of the material. Therefore, they are not yet closed. To close these shape equations we need to rearrange the constitutive relations $\bar{\tau}_s = \tau_s(\lambda_s, \lambda_\phi)\lambda_\phi/\bar{\lambda}_\phi$ of the considered model and the wrinkling condition $0 = \tau_\phi(\lambda_s, \lambda_\phi)$ in order to express λ_s in terms of $\bar{\tau}_s$ and $\bar{\lambda}_\phi = \bar{r}/r_0$. We switch to this new set of shape equations (2.32) as soon as $\tau_\phi < 0$ is reached at $s_0 = s_1$ along the contour; this gives a switching condition that also depends on the constitutive relation of the material. We switch back to the shape equations (2.29) without wrinkles as soon as this condition is violated again at $s_0 = s_2 > s_1$. The extent of the wrinkled region is $L_w = s_2 - s_1$.

For a nonlinear Hookean membrane the constitutive relations (2.30) lead to a wrinkling condition

$$\lambda_\phi = 1 - \gamma \frac{1 - \nu_{2D}^2}{Y_{2D}}\lambda_s - \nu_{2D}(\lambda_s - 1)$$

(2.33)

which is also used to identify the wrinkled region $\tau_\phi < 0$ along the contour. The constitutive relations (2.30) also lead to the following expression for λ_s in terms of $\bar{\tau}_s$ and $\bar{\lambda}_\phi = \bar{r}/r_0$,

$$\lambda_s = \frac{\bar{\lambda}_\phi \bar{\tau}_s + Y_{2D} - \gamma(1 + \nu_{2D})}{Y_{2D}(1 - 2\nu_{2D}) - (1 - \nu_{2D}^2)\gamma^2/Y_{2D}},$$

which closes the modified shape equations (2.32) in the wrinkled region.

Similarly we proceed for the constitutive relations of a strictly linear Hookean, and eqs. (2.31) of a Mooney-Rivlin or neo-Hookean membrane in the wrinkled region. For the strictly linear Hookean membrane the wrinkling condition $\tau_\phi = 0$ is given by

$$\lambda_\phi = 1 - \gamma \frac{1 - \nu_{2D}^2}{Y_{2D}} - \nu_{2D}(\lambda_s - 1),$$

where a factor λ_s is missing compared to (2.33). Again, we find a relation for the meridional stretching factor in terms of $\bar{\tau}_s$ and $\bar{\lambda}_\phi = \bar{r}/r_0$,

$$\lambda_s = \frac{Y_{2D}(Y_{2D} + \gamma(\nu - 1))(1 + 2\nu)}{2Y_{2D}^2\nu}$$

$$\pm \frac{\sqrt{Y_{2D}^2(Y_{2D}^2 + \gamma^2(\nu - 1)^2 + 2Y_{2D}(\gamma(\nu - 1) - 2\bar{\lambda}_\phi\bar{\tau}_s\nu))}}{2Y_{2D}^2\nu},$$

where the solution with the negative root has to be chosen.

Unfortunately, for the Mooney-Rivlin membrane analytic expressions are impracticable since they contain roots of fourth order polynomials. However, λ_s and λ_ϕ can be reliably
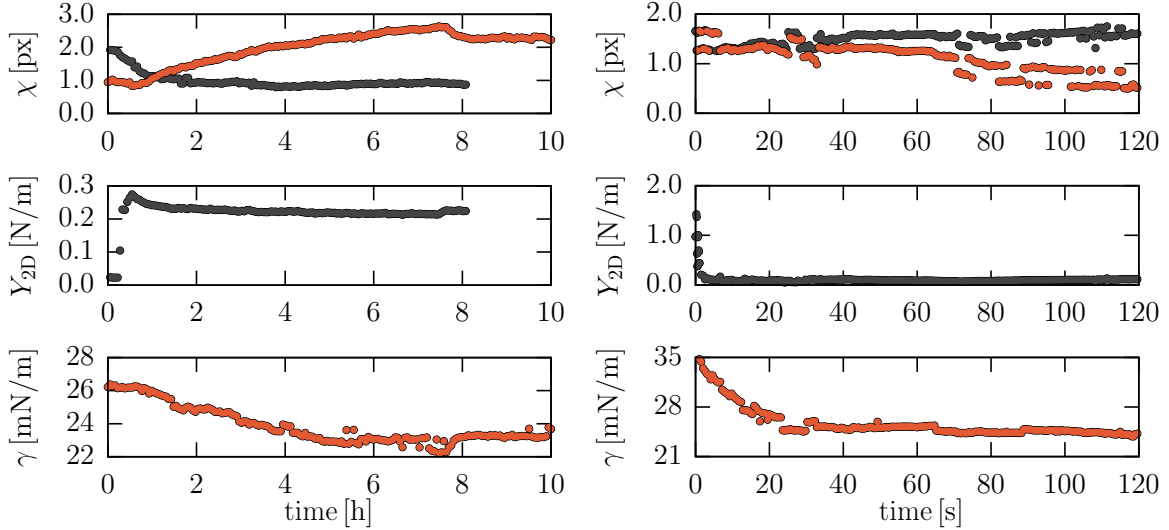
Figure 2.12: The interfacial gelation phase (ii) fitted with a model for liquid interfaces (Laplace-Young, orange) and a model for elastic interfaces (Hooke membrane, gray), where we use the reference shape from the very beginning of phase (ii), i.e., phase (i). No active pressure or volume change have been applied. **Left:** H_2O-droplet coated with $Ce(SO_4)_2$ and CTAB-surfactants in a dodecane phase. **Right:** OTS-capsule, i.e., a *p*-xylol droplet in solution with 1,2,4-trichlorobenzene and coated with OTS in a glycerol-water mixture.

determined by numerically solving

$$\tau_\phi(\lambda_s, \lambda_\phi) = 0 \quad \text{and} \quad \bar{\tau}_s - \tau_s(\lambda_s, \lambda_\phi)\lambda_\phi/\bar{\lambda}_\phi = 0.$$

Note that, in the wrinkled region, λ_s and λ_ϕ have to be determined, whereas in the non-wrinkled region λ_s and τ_ϕ have to be determined. The solution $(\lambda_s, \lambda_\phi)$ of the above set of equations closes the shape equations (2.32) and can, in principle, be obtained in the same way for any constitutive law.

The extent of the wrinkled region where $\tau_\phi < 0$ of course depends on the value of the interfacial tension γ in all constitutive relations (2.30) or (2.31). The fact that we generally obtain good agreement with experiments regarding the extent of the wrinkled region also supports the inclusion of the interfacial tension into the constitutive relations.

2.2.4 Equilibrium shapes

Solutions of the elastic shape equations (2.29) presume an elastically relaxed reference shape, with respect to which elastic strains are defined. The choice of the reference shape is subject to certain assumptions which will be discussed in this section.

Capsule formation by crosslinking or polymerization proceeds via three phases (see Fig. 2.10). In phase (i) we have a liquid drop without any surfactants and a stationary shape (which is a teardrop shape due to gravity). Phase (ii) starts when surfactants and/or crosslinkers are added to one of the bulk phases such that adsorption of surfactants and subsequent crosslinking into a two-dimensional network can occur. If surfactants and/or crosslinkers are dissolved in the droplet or the surrounding fluid, then phase (ii) starts immediately when forming the droplet. In phase (ii) the shape changes and the capsule finally reaches a new equilibrium shape. In phase (iii) the capsule is in its new stationary shape after successful crosslinking; this is the state where the deflation experiment is started.

For the regression of deflated capsule shapes we usually assume that the equilibrium state reached in phase (iii) is identical to the elastically relaxed state and, thus, free of elastic tensions. As discussed above, we also assume in the constitutive relations (2.30) that the surface tension γ gives a constant contribution to the tensions τ_s and τ_ϕ. Then the surface stress in the elastically relaxed state of the membrane is solely determined by the isotropic surface tension γ. We thus assume in (2.30) that the elastically relaxed state can be described as a liquid drop shape using the Laplace-Young equation. Based on these two assumptions we use a Laplace-Young fit for the equilibrium shape in phase (iii).

These two assumptions are based on the following picture for the crosslinking process in phase (ii): When adding surfactants to one of the bulk phases at the beginning of phase (ii), the surface tension typically decreases linearly or exponentially in time until it reaches a plateau at the equilibrium surface tension γ_A. The actual crosslinking of the membrane only happens *after* the plateau at the surface tension γ_A has been reached. During crosslinking the interfacial tension γ_A of the fluid interface remains unchanged. If this picture is valid, we should observe a sagging of the capsule under the action of gravity while a decreasing surface tension gives shapes that can be successfully fitted using the Laplace-Young shape equations (2.28). The sagging should stop when the surface tension reaches the plateau. During this plateau phase the crosslinking is established, while the capsule shape is unchanged. Fig. 2.12 (right) shows an example of an OTS-capsule where all these features can indeed be observed. Fitting the shape using the Laplace-Young shape equations gives only small errors and the interfacial tension γ follows the expected temporal evolution.

There are, however, capsule formation processes which deviate from this picture. Another possible scenario is that the formation of a solid shell by crosslinking happens earlier in phase (ii) but further polymerization during phase (ii) generates elastic strains and stresses. All further shape changes during phase (ii) have to be interpreted as a result of strain and stress generation during the polymerization process, and the capsule shell is pre-stressed in the equilibrium state in phase (iii). Then the elastic reference shape is not exactly known and, in principle, can be any of the shapes encountered in phase (ii). One extreme assumption is that crosslinking is fast and a solid membrane is established right at the beginning of phase (ii). Then the shape in the beginning of phase (ii) directly after addition of surfactants and crosslinkers can be viewed as the elastic reference shape and all subsequent shapes should be fitted with an elastic model using this reference shape. Fits with the elastic model should reveal how strains, stress, and elastic moduli evolve during phase (ii).

In order to decide which choice of reference shape is most appropriate, one can try different fits using different shapes from phase (ii) as elastically relaxed reference shapes (for example, from the end or the beginning of phase (ii)). All shapes before the reference shape are fitted using the Laplace-Young shape equations and described by an interfacial tension γ that decreases in time. All shapes following the reference shape are fitted using the elastic shape equations and described by a surface Young modulus Y_{2D} and a Poisson ratio ν_{2D}, which evolve in time. The reference shape giving the best fits (with smallest errors) should be chosen. Moreover, choices of reference states producing unphysical results, such as a surface Young modulus Y_{2D} which is decreasing in time during the crosslinking process in phase (ii) (more crosslinks or junction points should always increase Y_{2D}), should be discarded.

Two examples are shown in Fig. 2.12. OTS-capsules show the typical sagging in phase (ii) and can be fitted quite well with the Laplace-Young shape equations giving a surface tension γ, which at first decreases linearly or exponentially and then reaches a plateau, consistent with the standard scenario that the shell is crosslinked at the end of phase (ii). But the shapes can also be fitted quite well assuming that crosslinking is established at the beginning of phase (ii); then the observed sagging leads to fits with a decreasing Young modulus Y_{2D} and should, therefore, be discarded as unphysical.

The second, untypical example are H_2O-droplets coated with coagulated films of $Ce(SO_4)_2$ and CTAB-surfactants, which only show little sagging during crosslinking and even develop wrinkles already during phase (ii), which is a strong hint that a solid membrane had been established early in phase (ii). The crosslinking process is much slower for these capsules. Here, fits with the Laplace-Young shape equations give a decreasing γ that reaches a plateau; the resulting fit errors are, however, quite large and growing in time. The assumption that the shape in the beginning of phase (ii) is already crosslinked and can be regarded as the elastically relaxed reference shape gives a Young modulus Y_{2D}, which increases sharply in the beginning of phase (ii) and then reaches a plateau; there is no pronounced decrease in Y_{2D}. Fit errors for this scenario are decreasing in time. The fit errors for the two fitting approaches actually show an intersection point early in phase (ii). Between the beginning of phase (ii) and the intersection point, the capsule shape is adequately described by the liquid model. Beyond the intersection point the elastic model provides a more accurate description than the liquid model. One might conclude that the formation of the network at the interface is completed, when the system passes the intersection point. The surface Young modulus does not change significantly after passing the intersection point, which confirms our conclusion. Comparing fit errors could serve as a simple method to estimate the time needed to built a crosslinked solid shell for different materials or chemical processes.

2.2.5 Software overview

The software and source code [3] provided with this paper are freely available at `github.com/jhegemann/opencapsule` under a GPL license [4]. It is a command line program developed in C/C++ and most compatible with Linux/Unix. Usage is fairly simple and a guideline (README.md) is provided as part of the github repository. We give a brief description of how the program works and how the typical workflow looks like.

Presuming that at least one image of the reference capsule and at least one image of a deformed capsule is given, a first call `OpenCapsule` will establish the workspace, i.e., create folders for the input/output files as well as a standard configuration file. The essential information in the configuration file should be updated according to the needs. In particular, the density difference $\Delta\rho$ between the inner and the outer phase is needed, as well as the outer capillary diameter b. Both can be manipulated via the corresponding environment variables `EXPERIMENT_DENSITY` and `EXPERIMENT_CAPDIAMETER`. In addition, the names and paths of the image files need to be specified. Files have to be listed (separated by colons) next to the environment variables `REFERENCE_SHAPE` and `ELASTIC_SHAPE`. Note that the software searches for images by default in the `./input/`-folder. If images are placed somewhere else, the path should be specified via the variable `INPUT_FOLDER`. Requirements for capsule images are detailed in the appendix.

This suffices to run the first analysis. To check if everything works correctly the command `OpenCapsule -r` should be called, which will analyze the reference shapes and determine the surface tension as an average over all given images and, of course, for each individual image. This analysis can also be used to fit the deformed shapes with the Laplace-Young equation, e.g. to determine the Gibbs-modulus. If the results are satisfactory, the command `OpenCapsule -s` will run the elastic analysis. Both types of analyses are completely automatized. The essential numerical results are placed in the `./global_out/`-folder. The results for the reference shapes are listed in `reference.dat`; the results for the deformed shapes in `sequence.dat`. Though no graphical user interface is provided, the results will be printed in a comprehensive html-report, which can be opened in a web browser. This report contains the original capsule images with an overlay of the theoretical shape and a scale bar (see Fig. 2.13), from which one can instantly judge if the fitting procedure was successful. In case
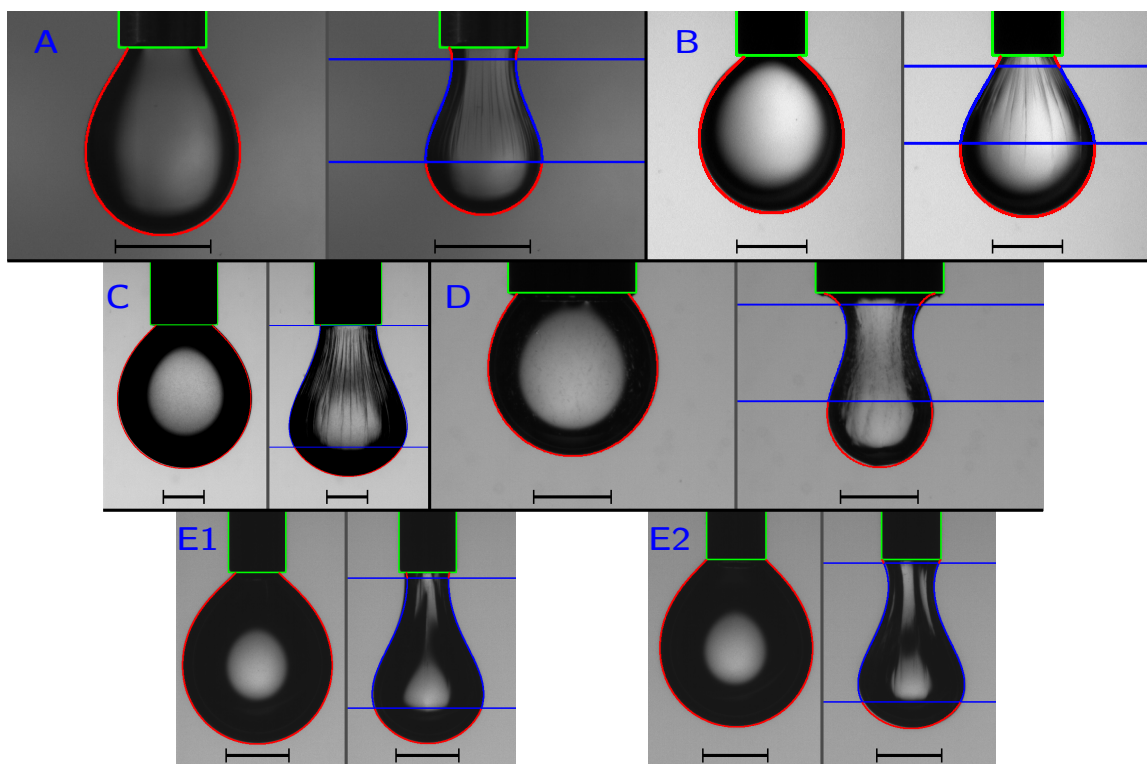
Figure 2.13: Pendant capsule elastometry results for five different types of capsules. The above images are the original input files overlayed with the best fit theoretical contour, the scale-bar is of length 1 mm. These images are automatically generated by our Software. **A)** Reference and deflated shape of a FC-40 droplet coated with supramolecular polymers and crosslinked with cucurbit[8]uril in H_2O [78]. Both the capsule contour and the wrinkling region are perfectly described by the elastic model. The Laplace-Young analysis yields a surface tension $\gamma = 20.0 \, \text{mN/m}$. The elastic analysis yields an area compression modulus $K_{2D} = 44 \, \text{mN/m}$, a Poisson ratio $\nu_{2D} = 0.29$, a bending modulus $E_B = 5 \cdot 10^{-16} \, \text{Nm}$ and a layer thickness $H = 256 \, \text{nm}$. **B)** Reference and deflated shape of a dodecane droplet coated with three layers of PMAA/PVP in H_2O [98]. The Laplace-Young analysis yields a surface tension $\gamma = 13.2 \, \text{mN/m}$. The elastic analysis yields an area compression modulus $K_{2D} = 141 \, \text{mN/m}$, a Poisson ratio $\nu_{2D} = 0.75$, a bending modulus $E_B = 2.20 \cdot 10^{-14} \, \text{Nm}$ and a layer thickness $H = 1.28 \, \mu\text{m}$. **C)** Reference and deflated shape of an OTS-capsule, i.e., *p*-xylol droplet in solution with 1,2,4-trichlorobenzene and coated with OTS in a glycerol-water mixture, see also Fig. 2.16, **D)** Reference and deflated shape of a Span 65 capsule, i.e., H_2O-droplet coated with Span 65 (sorbitan tristearate) in dodecane, see also Fig. 2.15 (left). **E)** Reference and deflated shape of an amino-functionalized polyacrylamide capsule, i.e., H_2O-droplet with Na_2CO_3, N-(3-Aminopropyl)-methacrylamide, and DTAB **E1)** or CTAB **E2)** surfactants, surrounded by an outer phase with *p*-xylol and sebacoyl dichloride, see also Fig. 2.15 (right). For all five capsule types predicted wrinkle regions (blue lines) fit the actual wrinkled area quite well. The wrinkles of the Span 65 capsule are hardly visible by eye, probably because of a very thin shell and, thus, a small wrinkle wavelength. Span 65 is expected to form molecular monolayers, which is consistent with this interpretation.

of failure, one should adapt the configuration file according to the guideline. Setting up a proper configuration file once for a specific capsule type is typically sufficient. Afterwards it can be used without changes for the same type of capsules.

2.2.6 Reference analysis

The shape analysis is split into two batched parts, which are (i) reference shape analysis and (ii) deformed shape analysis. For the former one it is advantageous to analyze as many images as possible showing the same, undeformed state of the capsule. This is particularly necessary if images are slightly blurred from camera shake or capsule motion. Averaging over all images improves accuracy, which is important here, since we use the reference shape and parameters during the complete analysis of the deformed shapes. The reference analysis gives the surface tension γ and the shape profile that is necessary to define the strains in the elastic analysis.

From the experiment we know the outer capillary diameter b and the density difference $\Delta\rho$ both in SI units. Solutions of the shape equations have to match the inner capillary of width a, which is the relevant length scale. This quantity is typically specified by the needle manufacturer, but due to material sediments, which potentially change the effective inner capillary diameter, we prefer to measure it directly from the image. Actually, we determine α in units of the image (pixels) by choosing it as an independent fit parameter that rescales all lengths occuring in the Laplace-Young shape equations. From image processing we also know the outer capillary diameter β in units of the image (pixels). Thus, we find $a = \langle\alpha/\beta\rangle b$, which is the effective inner capillary diameter in SI units. Scaling dimensionless lengths with a transforms them to SI units. We introduce dimensionless quantities $\tilde{p}_0 = ap_0/\gamma$ and $\Delta\tilde{\rho} = a^2\Delta\rho g/\gamma$ and minimize the mean square deviation between shape and contour with respect to the parameter set $\boldsymbol{x}_0 = (\tilde{p}_0, \Delta\tilde{\rho}, \alpha)$. After successful minimization, we obtain the surface tension via $\gamma = a\Delta\rho g/\Delta\tilde{\rho}$. To prepare all contours for the elastic analysis we scale them with $1/\alpha$ and thereby transfer them to dimensionless units.

2.2.7 Elastic analysis

In the elastic regression we determine the area compression modulus K_{2D} and the Poisson ratio ν_{2D} by minimizing the mean-square deviations between image contour points and theoretical contour, i.e., with respect to the parameter set $\boldsymbol{x} = (\tilde{p}, \nu_{2D}, \tilde{K}_{2D})$, where $\tilde{p} = ap/\gamma$ and $\tilde{K}_{2D} = K_{2D}/\gamma$. From these quantities we also obtain the surface Young modulus $Y_{2D} = 2K_{2D}(1 - \nu_{2D})$, see eq. (2.2.3). For the Mooney-Rivlin elasticity model we determine analogously the parameter set $\boldsymbol{x} = (\tilde{p}, \Psi, \tilde{Y}_M)$ within the shape regression. For the neo-Hookean elasticity model we keep $\Psi = 1$ fixed during the shape regression.

It is not required that elastic shapes are ordered chronologically, but it decreases the runtime significantly, since the final parameters of a deformed shape can be used as an initial guess for the following shape, which is probably deformed by a similar extent.

In the current implementation, the pressure p is an additional fit parameter and will also be determined from fitting calculated shapes to an image. In this implementation the elastometry method also serves as pressure measurement and no additional pressure measurement is necessary. If such information is experimentally available from additional measurements, it could be used to improve the results for the elastic moduli, by fixing the pressure to the experimentally obtained value.

After a successful regression we can estimate the bending modulus [1]

$$E_B = \Lambda^4\bar{\tau}_s/16\pi^2 L_w^2$$

by an image analysis of the wrinkles. We determine the length L_w of the wrinkles in meridional direction directly from the shape by finding the zero crossings s_1 and s_2 of $\tau_\phi(s_0)$. The interval $[s_1, s_2]$ in which wrinkles occur sets the meridional extent of the wrinkled region, in which we determine the average meridional tension $\bar{\tau}_s$. It is important to note

that the extent of the wrinkled region is not a fit parameter but is predicted by the shape equations and the wrinkling criterion $\tau_\phi < 0$, according to Sec. 2.2.3. In order to estimate the wrinkling wavelength Λ, we select the wrinkling region from the image and perform an edge detection with high sensitivity and only in horizontal direction to estimate the average distance between the wrinkles, which should correspond to one wavelength Λ. We then count the detected edge pixels N_E and the total number N of pixels in the selected region. The ratio N/N_E now approximately gives the number of wrinkles apparent in the image, if we consider the region as rectangular with equidistant vertical wrinkles. Finally, we use the estimate $\Lambda \approx \pi \bar{r} N_E / N$, where $\bar{r}$ is the capsule radius $r(s_0)$ averaged over the interval $[s_1, s_2]$.

Knowing Y_{2D}, ν_{2D} and E_B, we can directly determine the Föppl von Kármán number $\gamma_{\mathrm{FvK}} = Y_{2D} R_0^2 / E_B$ of the capsule, where R_0 is the maximum capsule radius. If we assume that the shell material is a thin layer of a three-dimensional isotropic elastic material, we additionally find the thickness $H = [12 E_B (1 - \nu_{2D}^2)/Y_{2D})]^{1/2}$ of the layer, where we use $Y_{2D} = Y_{3D} H$, $E_B = Y_{3D} H^3 / 12(1 - \nu_{3D}^2)$ and $\nu_{3D} = \nu_{2D}$.

2.2.8 Applications

In this section we demonstrate the wide applicability of our pendant capsule elastometry software to different capsule materials, see Fig. 2.13. We apply our software to crosslinked polymeric capsule shell materials like OTS (octadecyltrichorosilane) (Fig. 2.13 C) and amino functionalized polyacrylamide (Fig. 2.13 E), as well as more exotic capsule materials like Span 65 [99–101], which is a food emulsifier (Fig. 2.13 D). Moreover, Fig. 2.13 shows analyses of two sorts of capsules from literature, cucurbit[8]uril-capsules that have been introduced and discussed in Ref. [78] (Fig. 2.13 A) and PMAA/PVP-capsules from Ref. [98] (Fig. 2.13 B). In addition, the method has been used previously (in a less advanced implementation) on hydrophobin-coated air bubbles [1].

As can be seen in Fig. 2.13, nonlinear Hookean fits for all capsule materials work well and correctly predict the extents of the wrinkled regions (blue lines). The different capsule materials that could be analyzed have quite diverse area compression moduli ranging from $K_{2D} \sim 50\,\mathrm{mN/m}$ (polyacrylamide capsules and cucurbit[8]uril-crosslinked capsules) to $K_{2D} \sim 4\,\mathrm{N/m}$ (OTS-capsules), which corresponds to two orders of magnitude. The bending moduli from the wrinkle analysis range from $E_B = 5 \cdot 10^{-16}\,\mathrm{Nm}$ (cucurbit[8]uril-crosslinked capsules) to $E_B = 10^{-13}\,\mathrm{Nm}$ (OTS-capsules from Fig. 2.17). For the Span 65 capsules we find even lower bending moduli of order $E_B = 10^{-20}\,\mathrm{Nm}$ assuming a quite short wrinkle wavelengths just below the image resolution. However, the existence of these wrinkles could not be verified experimentally, yet.

Capsules in Fig. 2.13 develop a 'neck' upon deflation. We note that this neck is not associated with any mechanical instability (e.g., a buckling-type instability [44, 71]), i.e., there is no bifurcation between different types of shapes upon deflation but all shapes continuously evolve into the necked shapes. The deflated shapes exhibit high compressive stretches in particular in the wrinkled region as Fig. 2.14 shows, where the resulting stretches λ_s and λ_ϕ are plotted along the deflated contours for all capsules shown in Fig. 2.13 and, indeed, values significantly smaller than 1 occur for λ_ϕ. This raises the question whether nonlinear effects are adequately treated by the nonlinear Hookean material model. This model contains nonlinearities only via the $1/\lambda$-factors in the constitutive relations (2.30), which arise because we use Cauchy stresses defined per deformed unit length in the force-equilibria.

Our model explicitly includes, however, wrinkle formation, which is a nonlinear phenomenon. We actually use a different constitutive relation $\tau_\phi = 0$ (see eqs. (2.32) above) in the wrinkled region, such that a further decrease in the apparent stretch $\bar{\lambda}_\phi = \bar{r}/r_0$ in the
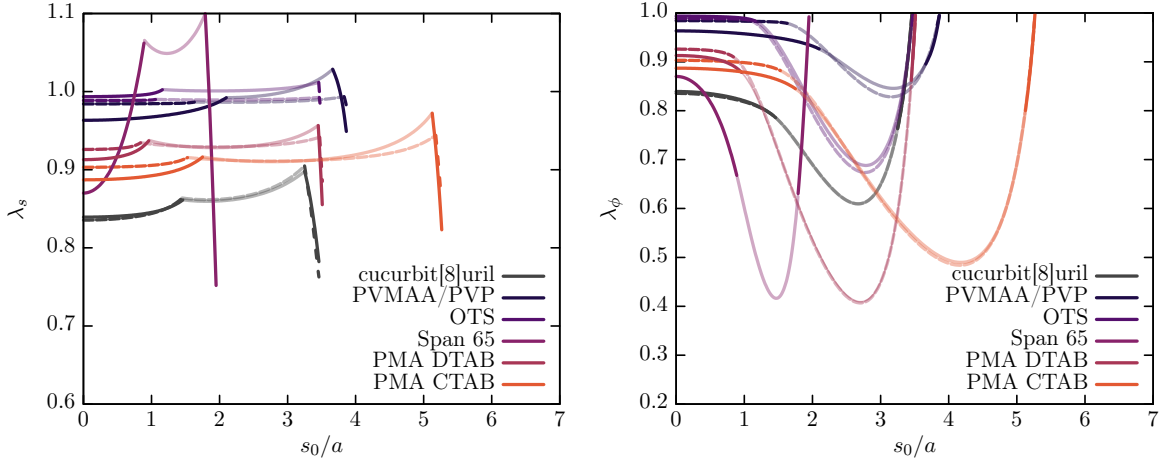
Figure 2.14: Stretching factors $\lambda_{s,\phi}$ along the deflated capsule contours from Fig. 2.13 obtained from shape regressions with the nonlinear Hookean elasticity (solid lines), and the Mooney-Rivlin or neo-Hookean elasticity model (dashed lines). The wrinkled region is indicated by transparent lines (either solid or dashed) for both elasticity models. **Left:** Meridional stretching factor λ_s as a function of the arc length s_0. Except of the cucurbit[8]uril and the Span 65 capsules, all capsules have small strains $|\lambda_s - 1| < 0.1$ and, thus, can be successfully treated with small strain approximations, i.e., the nonlinear Hookean elasticity model. **Right:** Circumferential stretching factor λ_ϕ (apparent stretch $\bar{\lambda}_\phi$ in the wrinkled region) as a function of s_0. Particularly in the wrinkled region, we see significant deviations from the small strain limit $|\lambda_\phi - 1| < 0.1$. In the wrinkled region we use, however, a different constitutive law ($\tau_\phi = 0$) independent of $\bar{\lambda}_\phi$. In the non-wrinkled region, we find again small strains $|\lambda_\phi - 1| < 0.1$ for PVMAA/PVP, OTS, and polyacrylamide capsules.

wrinkled region does no longer lead to increased compressive stresses τ_ϕ but only modifies the effective constitutive law (2.2.3) for the meridional stresses $\bar{\tau}_s$ of the pseudo-surface. Therefore, small values of $\bar{\lambda}_\phi$ in the wrinkled region do *not* imply that a different, more appropriate nonlinear constitutive relation should be used. The results in Fig. 2.14 show that strains $|\lambda_\phi - 1|$ become large only in this wrinkled region. This suggests that usage of the nonlinear Hookean elasticity is justified.

In order to investigate nonlinear effects further, we also performed fits of all capsules from Fig. 2.13 with a nonlinear Mooney-Rivlin or neo-Hookean elasticity model. The resulting best fits for the theoretical contour are not distinguishable from the nonlinear Hookean contours shown in Fig. 2.13, which already suggests that nonlinearities are already adequately treated by the nonlinear Hooke law. In Fig. 2.14 we also compare the stretches resulting from shape regressions with the nonlinear Hookean and the Mooney-Rivlin or neo-Hookean elasticity model for all deflated capsule shapes from Fig. 2.13. We see that strains are similar for both models for any of the capsule materials, except of the Span 65 capsules, where we were not able to obtain a reliable fit result using the Mooney-Rivlin elasticity model. For Span 65 the meridional stretching factor varies strongly with the arc length indicating strongly inhomogeneous stresses, which might be the reason for these problems. Treating the dimensionless shape parameter Ψ within Mooney-Rivlin elasticity as an independent fit variable results in $\Psi \to 1$ for PVMAA/PVP, OTS, polyacrylamide CTAB, and polyacrylamide DTAB capsules. It is noticeable that all these materials give a Poisson ratio $\nu_{2D} > 0.5$ employing the nonlinear Hookean fit. Only for the cucurbit[8]uril capsules, which have a Poisson ratio $\nu_{2D} < 0.5$ we find $\Psi < 1$ and, thus, deviations from the neo-Hookean behavior. This indicates that most of the capsule materials discussed in this paper behave like a neo-Hookean material and, thus, also similar to a nonlinear Hookean
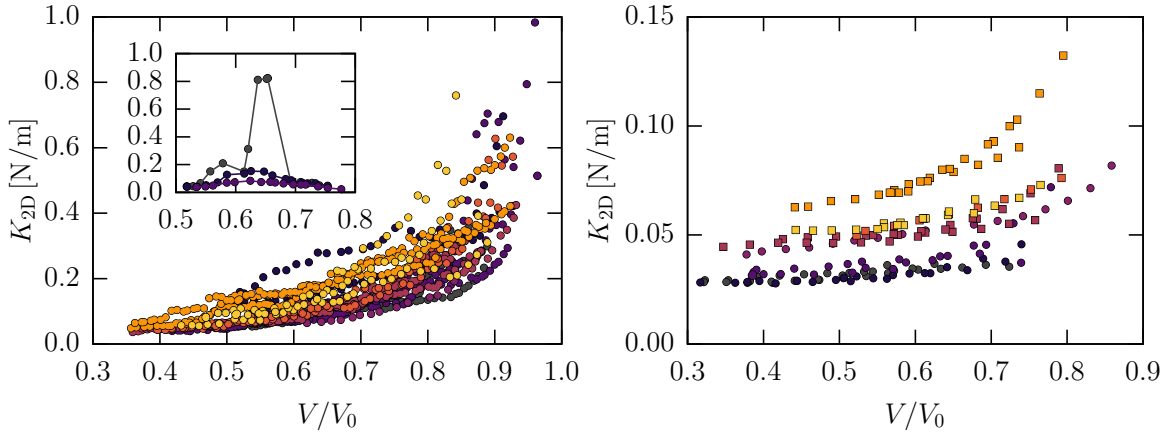
Figure 2.15: Left: Pendant capsule elastometry results for Span 65 capsules, i.e., H_2O-droplets coated with Span 65 (sorbitan tristearate) in dodecane. We analyzed eight individual capsules (color code), most of them fitted over three phases of deflation. The inset also shows the three inflation phases for one of these capsules. The inflation phases differ significantly among the capsules, and there is no generic behavior as for the deflation phases. Among the individual capsules, volume change rates vary between 0.5 and $1.0\mu l/s$. Surface shear-rheometry measurements give $K_{2D} = 0.9N/m$, Langmuir-Blodgett trough $K_{2D} = 0.33N/m$, spinning-drop $K_{2D} = 0.36N/m$, and rheoscope $K_{2D} = 0.54N/m$. Rheological measurements are thus consistent with our method, which also reveals a strong variation of K_{2D} with the volume. The Poisson ratio is roughly given by $\nu_{2D} = 0.8$. **Right:** Pendant capsule elastometry results for polyacrylamide capsules, i.e., H_2O-droplet with Na_2CO_3, N-(3-Aminopropyl)-methacrylamide and DTAB (circles) or CTAB (quads) surfactants. The outer phase consists of *p*-xylol and sebacoyl dichloride. We analyzed four individual CTAB and four individual DTAB capsules, most of them fitted over three phases of deflation. Deformations were applied after 60 minutes equilibration time with the crosslinker. The Poisson ratio is $\nu_{2D} = 0.6$ with DTAB surfactants and $\nu_{2D} = 0.5$ with CTAB surfactants. The values of the area compression modulus are consistent with shear-rheometer measurements, which give $K_{2D} = 30\ldots100mN/m$.

material in the small strain limit. This limit is obviously applicable to PVMAA/PVP, OTS and polyacrylamide capsules, since they all satisfy $|\lambda_s - 1| < 0.1$ over the whole contour, and also $|\lambda_\phi - 1| < 0.1$ in the non-wrinkled region. Because of these results and the fact that Mooney-Rivlin fits require a much higher computational cost, we focus on nonlinear Hookean elasticity in the following, which gives good results for all capsule types.

Where comparison to other rheological measurements is possible, results from pendant droplet elastometry are in good agreement. For PMAA/PVP-capsules, the surface Young modulus of $Y_{2D} = 211mN/m$ agrees with the findings in Ref. [98]. In the following we will discuss results on the OTS-, amino-functionalized polyacrylamide, and Span 65 capsules, which have not been previously discussed in the literature, in more detail. Pendant capsule elastometry allows us to obtain elastic moduli of the two-dimensional capsule shell material for each digitized image of the deflated capsule shape (if at least *one* image of its undeformed reference shape is provided). Therefore elastic moduli can be determined as a function of the deflation volume. If the volume change rate can be controlled, elastic moduli can be determined as a function of the volume change rate to investigate viscoelastic effects. If series of images over one or several deflation cycles are available, we can investigate aging effects, for example, by plastic deformation over many deflation cycles. We will explore these possibilities for OTS-, polyacrylamide, and Span 65 capsules, starting with the latter.

Span 65 capsules

Span 65 has a polar head group connected to three carbon chains leading to intermolecular interactions when adsorbed to a liquid interface. Though not explicitly crosslinked, the material shows elastic properties due to the formation of temporary networks. For Span 65, our method agrees with four different rheological measurements (surface shear-rheometry, Langmuir-Blodgett, spinning-drop method, and shear flow rheoscope), which all give area compression moduli K_{2D} between 0.3 and 0.9 N/m. These fit well to the values $K_{2D} = 0.2\ldots1.0$ N/m obtained by our method for small deformations at $V/V_0 > 0.8$, see Fig. 2.15 (left). The pendant capsule elastometry results in Fig. 2.15 (left) also reveal that the area compression modulus strongly varies with the volume: deflated capsules with $V/V_0 < 0.5$ become very soft with $K_{2D} < 0.1$N/m. This pronounced compression softening can eventually explain the deviations among previous rheological measurements. Upon re-inflating the capsule, the compression modulus exhibits a non-monotonous behavior (see Fig. 2.15 inset) but we do not find a generic pathway among the eight individual capsules that we analyzed. We can, however, speculate based on visual impressions from the images that the capsule material develops overlaps or similar microscopic folds that vanish after complete re-inflation. As a consequence, we see hysteresis but no aging effects as the compression modulus returns to its original value after completing a deformation cycle, see Fig. 2.15 (left). We also do not see a pronounced change of this behavior if the volume change rate is changed. All these results suggest that the compression softening could be a result of reversible rearrangements of the temporary network of the capsule material on time scales, which are short compared to the time scale of volume changes. These reversible rearrangements lead to an apparent decrease of elastic moduli with decreasing volume. In Fig. 2.14 we showed that Span 65 capsules exhibit strongly inhomogeneous strains, which likewise indicates a quite complex elastic behavior. Eventually, one might conclude that Span 65 is not well described by classical elastic models. Specific models that account for the microscopic details of the material have to be developed to analyze the elastic properties of Span 65 in more detail. In contrast to permanently crosslinked polymer membranes Span 65 forms temporarily crosslinked network structures [102]. Within these structures, the applied stresses can relax with time constants of the order of several minutes, which leads to time-dependent transitions from solid into liquid like membranes. This more complicated rheological behavior, can only be described by time-dependent nonlinear constitutive laws. Bending moduli can not be determined directly from the images since the wrinkles are not visible by eye although the shape analysis suggests the existence of wrinkles over an extended region, see Fig. 2.13 D. One could assume a wrinkle wavelength just below the image resolution, which gives $\Lambda \leq 8\,\mu$m, $E_B \leq 2 \cdot 10^{-20}$ Nm, and $H \leq 1.67$ nm. Eventually wrinkles could also be absent in this system because compressive hoop stresses can be relaxed by the rearrangements in the temporary network.

Polyacrylamide capsules

We tested our software also on amino functionalized polyacrylamide capsules formed with two different surfactants CTAB and DTAB, see Fig. 2.15 (right). For the CTAB polyacrylamide capsules we find area compression moduli in the range $K_{2D} = 50\ldots100$ mN/m and a Poisson ratio $\nu_{2D} = 0.5$, for the DTAB polyacrylamide capsules we find $K_{2D} = 30\ldots60$ mN/m and $\nu_{2D} = 0.6$. These values are consistent with surface shear-rheometry measurements giving $K_{2D} = 30\ldots100$ mN/m. Our pendant capsule elastometry results show that the elastic properties of this type of capsule can be tuned by changing only the surfactants (CTAB vs. DTAB) and not the crosslinker. Fig. 2.15 (right) clearly shows that CTAB gives consistently
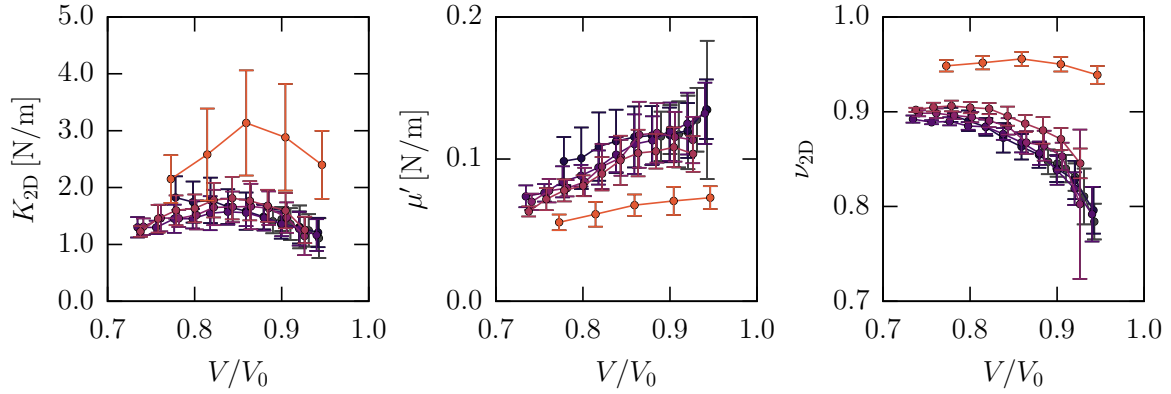
Figure 2.16: Pendant capsule elastometry results for OTS-capsules, i.e., a *p*-xylol droplet in solution with 1,2,4-trichlorobenzene and coated with OTS in a glycerol-water mixture. We analyzed a single individual capsule with a volume change rate of $0.5\,\mu\text{l/s}$ (points) and total volume reductions of $2.5\,\mu\text{l}$ (gray), $5.0\mu\text{l}$ (blue), $7.5\,\mu\text{l}$ (dark violet), $10.0\,\mu\text{l}$ (light violet), $12.5\,\mu\text{l}$ (red). The same capsule was analyzed with step-wise increased volume change rates (1.0, 2.5, 5.0, $7.5\,\mu\text{l/s}$) up to $10\,\mu\text{l/s}$ (orange) and the same total volume reductions. The capsule was subject to 30 cycles of de- and inflation, and we analyzed 1674 images for the first and last five cycles, which allows us to calculate error bars by averaging over small volume ranges. Spinning drop measurements give $K_{2\text{D}} = 3.0\ldots7.5\,\text{N/m}$ and rheoscope measurements $K_{2\text{D}} = 4.0\ldots10\,\text{N/m}$, depending on which Poisson ratio $\nu_{2\text{D}}$ is assumed to obtain $K_{2\text{D}}$ from the actually measured $Y_{2\text{D}}$. These values are slightly higher than our pendant elastometry measurements. For the Poisson ratio we get roughly $\nu_{2\text{D}} = 0.85$, which is slightly above previous measurements predicting $\nu_{2\text{D}} = 0.5\ldots0.8$ [91]. We see that, for the last 5 cycles with a volume change rate of $10.0\,\mu\text{l/s}$ (orange), the material has softened significantly, regarding $Y_{2\text{D}}$ and μ'. The area compression modulus $K_{2\text{D}}$ increased, however, due to an increased Poisson ratio. In principle, these effects could either be induced by aging or by viscoelastic effects. For viscoelastic materials we typically expect a stiffening when volume change rates are increased. Therefore, we suggest that this softening is induced by aging at the intermediate rates 1.0, 2.5, 5.0 and $7.5\,\mu\text{l/s}$ that have been applied before the final $10.0\,\mu\text{l/s}$ rate.

stiffer capsules than DTAB. Bending moduli for the DTAB polyacrylamide capsules are slightly smaller than for the CTAB polyacrylamide capsules. We find $E_B = 10^{-14}\,\text{Nm}$ for CTAB and $E_B = 8 \cdot 10^{-15}\,\text{Nm}$ for DTAB (using images from Fig. 2.13).

OTS capsules

For the OTS-capsules from Fig. 2.16 we find values $K_{2\text{D}} = 1.0\ldots4.0\,\text{N/m}$, which is just slightly below the rheological data from other methods giving $K_{2\text{D}} = 3.0\ldots10.0\,\text{N/m}$ (spinning drop measurements give $K_{2\text{D}} = 3.0\ldots7.5\,\text{N/m}$ and rheoscope measurements $K_{2\text{D}} = 4.0\ldots10\,\text{N/m}$), see Fig. 2.16. In Fig. 2.16, we analyzed a single OTS-capsule for different volume change rates ranging from 0.5 (slow) to $10.0\,\mu\text{l/s}$ (fast). In principle, this enables us to see viscoelastic effects. We expect a viscoelastic material to exhibit a smaller shear modulus μ' for slow deformation such that creep or viscoelastic relaxation is possible. Fig. 2.16 shows that the surface Young modulus and the shear modulus $\mu' = K_{2\text{D}}(1 - \nu_{2\text{D}})/(1 + \nu_{2\text{D}})$ are both significantly decreased for *higher* volume change rates. Therefore, this is probably an effect of aging rather than viscoelastic behavior. It is thereby difficult to explain the increased area compression modulus and Poisson's ratio, which indicates that the capsule material tends to become incompressible due to microscopic effects, that cannot be observed in detail experimentally. However, by exploring volume cycles for a wide range of volume change rates, it should, in principle, be possible to determine the
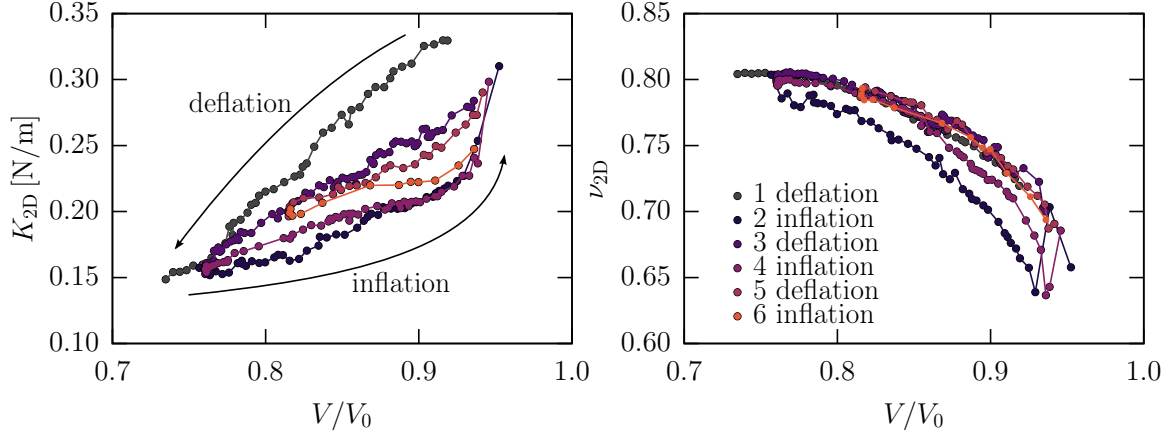
Figure 2.17: We analyze a single OTS-capsule [1], i.e., a H_2O-droplet coated with OTS in *p*-xylol, for three consecutive deflation and inflation cycles. This reveals aging effects: deformations become nearly reversible after two complete deformation cycles. For the first two cycles we clearly see hysteresis. Note that these OTS-capsules exhibit much smaller values of the area compression modulus K_{2D} compared to those in Fig. 2.16. Since both capsule membranes are made from OTS, and both should have a similar thickness ranging from 100 to 1000 nm, we conclude that this has to originate in the different liquid phases that have been used. Here, a water droplet was used in a *p*-xylol phase, whereas for the capsules in Fig. 2.16 a *p*-xylol droplet was used in a glycerin-water mixture. This possibly influences the network forming process, such that capsules from Fig. 2.16 appear more like an incompressible material.

frequency dependence of the surface shear (storage) modulus μ' from these measurements. Therefore, individual capsules should be prepared for each volume change rate to eliminate the influence of aging.

For OTS-capsules (with different liquid phases compared to those in Fig. 2.16) we analyzed aging effects in more detail in Fig. 2.17 by monitoring the change of elastic constants over three consecutive deformation cycles of the same capsule. For this capsule, the deformation behavior becomes approximately reversible only after completing two deflation-inflation cycles. The first two cycles exhibit hysteresis hinting to plastic deformation in the capsule. Similar effects can be seen in Fig. 2.16, where the OTS-capsule was subject to 30 de- and inflation cycles in total. The orange circles show the last five cycles where we observe a softening regarding the shear modulus, a stiffening regarding the area compression modulus, as well as an increased Poisson ratio. For all quantities the volume dependence is weakened. Capsules from Fig. 2.16 obviously exhibit a more complex aging behavior, which can only be caused by the different liquid phases (essentially oil and water phase swapped), because the OTS shell material is the same. However, these results suggests that by iteratively applying small volume change rates and small total volume reductions, capsule deformations can reach a reversible regime, where subsequent deformation cycles yield the same elastic constants and aging is effectively absent. If, however, the volume change rates or total volume reductions are successively increased, aging proceeds and the capsule material becomes even softer.

By applying the wrinkling analysis to the capsules from Fig. 2.16 we measure wrinkling wavelengths $\Lambda = 0.2$ mm leading to a bending modulus of $E_B = 10^{-15} \ldots 10^{-14}$ Nm and a thickness $H = 90 \ldots 290$ nm. Electron microscopy measurements give $H = 100 \ldots 1000$ nm, which roughly agrees. The quality of these estimates depends crucially on the measurement of the wrinkling wavelength since we have $E_B \propto \Lambda^4$. We prefer to measure Λ at the bottom of the wrinkles, because length measurements in the center of the capsule can be better translated to the length scale prescribed by the outer capillary diameter.

2.2.9 Gibbs modulus

Finally, we like to discuss why the Gibbs modulus is not suitable to analyze solid-like elastic shell materials. As mentioned above, the Gibbs modulus $E_{\text{Gibbs}} = \mathrm{d}\gamma/\mathrm{d}\ln A$ is frequently determined from measurements of an 'effective surface tension' γ describing the solid shell interface as a function of the surface area A. We use the term 'effective' here, because, in principle, one cannot determine a surface tension from deformations of a solid shell interface. The Gibbs modulus E_{Gibbs} is equal to the area compression modulus K_{2D} for a fluid interface or for a two-dimensional solid interface in a planar Langmuir-Blodgett trough geometry.

It is possible to determine the Gibbs modulus by using a standard pendant drop tensiometer measuring only the surface tension and the surface area. Commercial pendant drop tensiometers apply sine-like volume changes and determine the complex Gibbs modulus with an elastic and a viscoelastic contribution. This type of analysis is sometimes referred to as the 'oscillating drop' method.

To be consistent with our purely elastic model, we apply a linear fit in the $(\ln A, \gamma)$-plane. For the OTS-capsules we find $E_{\text{Gibbs}} = 40\,\text{mN/m}$, which is two orders of magnitude below the actually measured area compression moduli. Similar results were obtained in Ref. [1], where E_{Gibbs} and K_{2D} were compared for theoretically generated shapes. For the Span 65 capsules we get $E_{\text{Gibbs}} = 33\,\text{mN/m}$, which is one order of magnitude below the value obtained in the Langmuir-Blodgett trough. We obtained similar values $E_{\text{Gibbs}} \approx 40\,\text{mN/m}$ by applying the oscillating drop method to Span 65 capsules, which explicitly demonstrates that determining the Gibbs modulus with a pendant drop tensiometer leads to misleading results, as already stated in Ref. [1]. The deformed shapes of elastic capsules cannot be fitted accurately with the Laplace-Young equation for fluid interfaces as we have already shown in Fig. 2.12. Moreover, the relation between Gibbs modulus and area compression modulus K_{2D} becomes non-trivial and geometry-dependent because of inhomogeneous elastic stresses in the capsule geometry and the existence of a curved undeformed reference shape of the capsule. Only in a planar geometry, where the elastically relaxed reference state is planar and where stresses remain homogeneous, the Gibbs modulus coincides with the area compression modulus.

2.2.10 Conclusion

We developed an efficient and completely automated C/C++ software in order to perform pendant capsule elastometry in pendant drop devices. The analysis is based on a thin elastic shell model of the capsule interface and, thus, applies for elastic solid capsule materials. Such materials can be recognized, for example, by their ability to develop wrinkles.

The analysis requires a reference shape, for which we usually assume that it can be described by a liquid Laplace-Young shape if the shell material is crosslinked at a liquid interface. A minimum set of two images, one of the reference shape and another of a deformed shape, and two experimental parameters, namely the density difference $\Delta\rho$ and the outer capillary diameter b, are sufficient to run the complete analysis and obtain values for Young's modulus and Poisson's ratio using the Hookean elasticity model, or, alternatively, the Rivlin modulus and the dimensionless shape parameter using the Mooney-Rivlin elasticity model. In addition, if wrinkling occurs, the bending modulus and, thus, the shell thickness can be determined from a wrinkle wavelength measurement.

More interesting results are often obtained, if a whole sequence of deformed states can be analyzed in chronological order, which makes it possible to investigate the dependence of the elastic moduli on the capsule volume. This is where possible phase transitions, hysteresis and aging effects, or plastic deformations of the material could be detected. Future work

should explore whether a frequency-dependent surface shear (storage) modulus μ' can be reliably determined by measurements at different volume change rates.

In our present implementation pendant capsule elastometry does not require experimental information on the pressure p but rather serves itself as a pressure measurement because p is determined by shape fitting. If such pressure is measured independently, this additional information can be readily used to improve the results for the remaining fit parameters by setting p to a constant value within shape regression. This option is supported by the current version of our software. But there are also other possibilities to use the pressure information, e.g., to directly calculate local stresses in the deformed state from additional image information on local curvatures and radii [77]. This additional stress information can then be used to improve the shape fitting procedure beyond simple elimination of one fit parameter [61].

In the present form of the code, we provide linear Hookean elasticity, nonlinear Hookean elasticity, and Mooney-Rivlin or neo-Hookean elasticity to describe the elastic behavior of the shell material. We find that the nonlinear Hookean model gives the best compromise between accuracy and performance. Moreover, we randomly checked the results against Mooney-Rivlin elasticity (which is much slower due to numerical determination of the closure relations). This revealed that both elasticity models give similar results over a wide range of materials and deformation behavior. We find that the simple linear Hookean elasticity can only describe very small deformations compared to nonlinear Hookean or Mooney-Rivlin elasticity. We gained this insight from generating theoretical shapes, where we decreased the pressure successively, thereby simulating proceeding deflation. Numerics for the linear Hookean elasticity failed much earlier in fulfilling the required boundary conditions, which is necessary to generate a valid shape. It remains to be verified systematically, however, what differences eventually arise between fitting with different elasticity models. Fitting with the most appropriate model should produce the least elastic parameter variation as a function of the volume.

For certain materials the use of even more specific elastic models is more appropriate, for example, hydrophobins coating air bubbles [1, 10] act as interfacial rafts of hard particles with soft shells, which require a more refined elastic description to interpret capsule shapes correctly and avoid jumps in elastic constant in elastometry fits [57]. Therefore, future work should also aim at implementing different elastic models in order to compare fit results for different models and determine the most appropriate model from the data. In particular, for the Span 65 investigated in this paper, we suggest to develop such microscopic models, because we found strongly inhomogeneous strains and generally atypical elastic behavior. Moreover fit results revealed a pronounced compression softening, which we did not find for any other capsule material, which also hints to the use of a more appropriate elasticity model.

As we have shown, our software for pendant drop devices is widely applicable. We tested it on different materials and the results are in good agreement with available rheological data. We make the OpenCapsule software freely available under the GPL license [4] at `github.com/jhegemann/opencapsule`.

2.3 Numerics of pendant capsules and shape analysis

Since we explicitly focused on performance and robustness within pendant capsule elastometry, we give a detailed description of the numerical procedure we apply. These numerical details shall also help to understand the source code of the pendant capsule elastometry software `OpenCapsule` provided with this work.

2.3.1 Least squares

Both the shooting method and the shape regression require least square error/deviation minimization. Fitting shape equations to experimental contours is implemented by a nested minimization algorithm, which minimizes the distance between individual shape segments (and the boundary conditions) in an inner loop, which we call *shooting method* (see Sec. 2.3.3 below), and the deviation between theoretical shape and contour in an outer loop, which we call *shape regression* (see Sec. 2.3.4 below). At first, we characterize the error function that has to be minimized within the least square algorithm.

Consider a global residual vector

$$\boldsymbol{F}(\boldsymbol{x}) \;\; = \;\; (\boldsymbol{\varphi}_1(\boldsymbol{x}), \ldots, \boldsymbol{\varphi}_N(\boldsymbol{x}))^T$$

assembling the individual residuals $\boldsymbol{\varphi}_i$ that depend on an arbitrary parameter set $\boldsymbol{x}$. In case of the shooting method, the residuals $\boldsymbol{\varphi}_i$ are defined by the distances between consecutive shape segments and, finally, between the last shape segment and the boundary condition. Thus, the parameter set $\boldsymbol{x}$ can be identified with the set of shooting parameters, which are the initial values of the individual shape segments. In case of the shape regression, the residuals $\boldsymbol{\varphi}_i$ give the shortest distances between the discrete points of the contour (obtained from the image) and the theoretical shape profile given by a solution of the shape equations. Thus, the parameter set $\boldsymbol{x}$ can be identified with the shape parameters characterizing the solutions of either the Laplace-Young equations (2.28) or the elastic shape equations (2.29).

We now introduce the general least square method, stressing again that we use this method for both the shooting method *and* the shape regression. The Jacobian $\mathsf{J}_{\boldsymbol{F}}$ measures the change of $\boldsymbol{F}(\boldsymbol{x})$ at some point $\boldsymbol{x}$. In order to minimize the euclidean norm $\|\boldsymbol{F}(\boldsymbol{x})\|$ with respect to $\boldsymbol{x}$ we linearize $\boldsymbol{F}(\boldsymbol{x})$ within a small region $\Delta\boldsymbol{x}$ according to

$$\|\boldsymbol{F}(\boldsymbol{x} + \Delta\boldsymbol{x})\| \;\; = \;\; \|\boldsymbol{F}(\boldsymbol{x}) + \mathsf{J}_{\boldsymbol{F}}\Delta\boldsymbol{x}\| \;\; \overset{!}{=} \;\; 0$$

yielding the linear and typically over-determined system of equations

$$\mathsf{J}_{\boldsymbol{F}}\Delta\boldsymbol{x} \;\; = \;\; -\boldsymbol{F}(\boldsymbol{x}).$$

Standard algorithms like the Gauss-Newton method solve the quadratic normal equation

$$\mathsf{J}_{\boldsymbol{F}}^T\mathsf{J}_{\boldsymbol{F}}\Delta\boldsymbol{x} \;\; = \;\; -\mathsf{J}_{\boldsymbol{F}}^T\boldsymbol{F}(x),$$

but we prefer to directly solve (2.36), because the condition of $\mathsf{J}_{\boldsymbol{F}}^T\mathsf{J}_{\boldsymbol{F}}$ can be poor in comparison to the condition of $\mathsf{J}_{\boldsymbol{F}}$, i.e.,

$$\mathrm{cond}(\mathsf{J}_{\boldsymbol{F}}^T\mathsf{J}_{\boldsymbol{F}}) \;\; \sim \;\; \mathrm{cond}(\mathsf{J}_{\boldsymbol{F}})^2.$$

We do so by decomposing $\mathsf{J}_{\boldsymbol{F}} = \mathsf{QR}$ via Householder transformations and multiplying with Q^T,

$$\mathsf{R}\Delta\boldsymbol{x} \;\; = \;\; -\mathsf{Q}^T\boldsymbol{F}(x),$$

where we used that $\mathsf{Q}^T\mathsf{Q} = \mathbb{1}$. Note that this yields

$$\mathsf{R} \;\; = \;\; \begin{pmatrix} \mathsf{R}_0 \\ 0 \end{pmatrix}$$

and

$$\mathsf{Q}^T \boldsymbol{F}(x) \;\; = \;\; \begin{pmatrix} \boldsymbol{b}_0 \\ \boldsymbol{b}_1 \end{pmatrix}$$

in case of over-determined systems, such that the solution is given by

$$\Delta\boldsymbol{x} \;\; = \;\; \mathsf{R}_0^{-1}\boldsymbol{b}_0$$

with a finite error

$$\|\boldsymbol{F}(\boldsymbol{x}) + \mathsf{J}_{\boldsymbol{F}}\mathsf{R}_0^{-1}\boldsymbol{b}_0\| \;\; = \;\; \|\boldsymbol{b}_1\|.$$

Applying the parameter shift $\Delta\boldsymbol{x}$ resulting from (2.42) or (2.36) iteratively to the current parameter set finally gives a solution $\boldsymbol{x}^*$, which minimizes $\|\boldsymbol{F}(\boldsymbol{x})\|$, i.e.,

$$\min_{\boldsymbol{x}} \|\boldsymbol{F}(\boldsymbol{x})\| \;\; = \;\; \boldsymbol{x}^*.$$

To obtain the sequence $\{\boldsymbol{x}^k\}$ that finally converges to $\boldsymbol{x}^*$, we use the update scheme

$$\boldsymbol{x}^{k+1} \;\; = \;\; \boldsymbol{x}^k + \lambda_j \Delta\boldsymbol{x}^k,$$

where λ_j is chosen such that $\|\boldsymbol{F}(\boldsymbol{x})\|$ decreases in each step of iteration. Several line search methods may be applied here, but, in view of efficiency, we prefer to chose $\lambda_j = 1/2^j$, where we increase j starting from $j = 0$ until

$$\|\boldsymbol{F}(\boldsymbol{x}^k + \lambda_j \Delta\boldsymbol{x})\| \;\; < \;\; \|\boldsymbol{F}(\boldsymbol{x}^k)\|.$$

This is sometimes referred to as a 'backtracking line search' method. The minimization algorithm will be used for the multiple shooting method, where (2.36) is quadratic, as well as for the final regression of the shape equations, where (2.36) is strongly over-determined. Since we exclusively use numerical differential quotients the algorithm converges linearly, whereas a classical Newton minimization would converge quadratically due to analytical derivatives.

2.3.2 Reference shape

Obtaining a shape profile from the set of shape equations (2.28) is trivial, since there are no shooting parameters. In practice, one integrates the set of shape equations (2.28) (while increasing the arc length s_0) until $r_0(s_0) = a/2$ is satisfied for the second time, meaning that the shape enters the capillary from $r_0 > a/2$ (there is also a solution, which enters the capillary for the first time from $r_0 < a/2$; this solution has a much smaller volume and does usually not correspond to the experimental reference shape). The arc length s_0 that satisfies this condition is chosen as the undeformed contour length L_0, such that $r_0(L_0) = a/2$. Note that the undeformed length L_0 is fixed for the deformed shape profiles. The resulting reference shape

$$\boldsymbol{y}_0(s_0, \boldsymbol{x}_0) \;\; = \;\; \begin{pmatrix} r_0(s_0, \boldsymbol{x}_0) \\ z_0(s_0, \boldsymbol{x}_0) \\ \psi_0(s_0, \boldsymbol{x}_0) \end{pmatrix}$$

is obtained as a function of of the parameter set $\boldsymbol{x}_0 = \{p_0, \rho, \alpha\}$, which are adapted during the shape regression (see Sec. 2.3.4) to optimally match the contour points extracted from the image.

2.3.3 Shooting method

Solving the elastic shape equations requires a shooting method to be applied, because of the unknown initial tension $\tau_s(0) = \mu$ at the capsule's apex. For a given initial value μ we therefore integrate the shape equations starting at the capsule's apex from $s_0 = 0$ to $s_0 = L_0$, where L_0 was determined before by satisfying the boundary condition of the Laplace-Young reference shape. We thereby obtain a deformed shape trajectory $\boldsymbol{y}(s_0; \mu)^T$, which depends on the reference shape via the shape profile $r_0(s_0)$ and the length of the undeformed contour L_0. However, the deformed length $L = \int_0^{L_0} \lambda_s \mathrm{d}s_0$ of course adapts according to the stretch factor λ_s. For a capsule with inner capillary width a centered at $r = 0$ a valid solution has to satisfy the boundary condition

$$f(\mu) = r(L_0; \mu) - a/2 \overset{!}{=} 0.$$

The function $f(\mu)$, which is measured from the solution $\boldsymbol{y}(s_0; \mu)^T$, has to be minimized by applying a bisection with respect to the parameter μ. We recommend a bisection in this case, because the function $f(\mu)$ is very steep, particularly for large area compression moduli K_{2D}. The algorithm is assumed to be converged if $|f(\mu)| < \epsilon_{single}$. Note that our software takes this as a minimum criterion, i.e., it tries to minimize $|f(\mu)|$ even further until the interval within the bisection method becomes smaller than 10^{-16}. It is generally important to minimize $|f(\mu)|$ as far as possible, because the shape trajectories are very sensitive to the initial value μ.

In cases where the required accuracy ϵ_{single} can not be reached, we further improve solutions by applying a multiple shooting method subsequently. For this purpose we divide the interval $[0, L_0]$ in q sub-intervals with $q+1$ grid points at $s_k = k\, L_0/q$, where $k = 0, \ldots, q$. On the sub-interval $[s_k, \, s_{k+1}]$ we define the k-th segment

$$\boldsymbol{y}_k(s_0) \equiv \boldsymbol{y}_k^0 + \int_{s_k}^{s_0} \mathrm{d}s_0' \, \boldsymbol{f}\left(\boldsymbol{y}(s_0'); \, \boldsymbol{y}_k^0\right)$$

by integrating the set of shape equations

$$\boldsymbol{y}' = \boldsymbol{f}\left(\boldsymbol{y}(s_0); \, \boldsymbol{y}_k^0\right),$$

starting at

$$\boldsymbol{y}_k^0 = (r_k^0, z_k^0, \psi_k^0, \tau_k^0) \in \mathbb{R}^4$$

and ending at

$$\boldsymbol{y}_k \equiv \boldsymbol{y}_k(s_{k+1}, y_k^0) \in \mathbb{R}^4.$$

Note that the final segment $\boldsymbol{y}_{q-1}$ has to match the final grid point $\boldsymbol{y}_q$. Having decomposed the continuous solution in q individual segments, we track the k-th residual vector separating the k-th and $(k+1)$-th segment via

$$\varphi_k = \begin{cases} \boldsymbol{y}_k - \boldsymbol{y}_{k+1}^0 \in \mathbb{R}^4 & k = 1 \ldots q - 2 \\ \boldsymbol{y}_{k,1} - \boldsymbol{y}_{k+1,1}^0 \in \mathbb{R}^1 & k = q - 1 \,. \end{cases}$$

The last segment and grid point, $\boldsymbol{y}_{q-1,1} = r_{q-1}(s_q)$ and $\boldsymbol{y}_{q,1}^0 = r_q^0 = a/2$, define the final boundary condition (2.48), where the capillary has to be matched. Any other residual corresponds to continuity conditions that ensure a smooth shape. To arrange the segments into a continuous solution while satisfying the boundary condition at the capillary, we have to set up the Jacobians for each segment $\boldsymbol{y}_k$, where $k \in [0, q-1]$, with respect to the corresponding initial values $\boldsymbol{y}_k^0$. At s_0 only τ_0^0 can be chosen freely, whereas $r_0^0 = 0$, $z_0^0 = \zeta$ and $\psi_0^0 = 0$ are fixed due to axis symmetry. At s_q we have to satisfy the boundary condition $r_{q-1}(s_q) - a/2 = 0$ whereas $z_{q-1}(s_q)$, $\psi_{q-1}(s_q)$ and $\tau_{q-1}(s_q)$ are arbitrary. The Jacobian J_0 corresponding to $\boldsymbol{y}_0$ is a column vector in $\mathbb{R}^4$, the Jacobian J_{q-1} corresponding to $\boldsymbol{y}_{q-1}$ is a row vector in $\mathbb{R}^4$. All intermediate Jacobians J_k with $k = 1, \dots, q-2$ are quadratic matrices in $\mathbb{R}^{4 \times 4}$ and we can write them as

$$\mathsf{J}_0 = \frac{\partial \boldsymbol{y}_0}{\partial \tau_0^0}, \quad \mathsf{J}_k = \frac{\partial \boldsymbol{y}_k}{\partial \boldsymbol{y}_k^0}, \quad \mathsf{J}_{q-1} = \frac{\partial r_{q-1}}{\partial \boldsymbol{y}_{q-1}^0},$$

where we use differential quotients

$$\frac{\partial \boldsymbol{y}_k}{\partial \boldsymbol{y}_{k,i}^0} = \frac{1}{2\Delta} \left(\boldsymbol{y}(s_{k+1}; s_k, \boldsymbol{y}_k^0 + \Delta \boldsymbol{e}_i) - \boldsymbol{y}(s_{k+1}; s_k, \boldsymbol{y}_k^0 - \Delta \boldsymbol{e}_i) \right)$$

with canonical unit vectors $\boldsymbol{e}_i$ and $i = 1, \dots, 4$. Note that we typically use $\Delta = 10^{-6}$. Finally we find the block-matrix

$$\mathsf{J} = \frac{\partial (\boldsymbol{y}_0 - \boldsymbol{y}_1^0, \dots, \boldsymbol{y}_{q-1,1} - \boldsymbol{y}_{q,1}^0)}{\partial (\boldsymbol{y}_0^0, \dots, \boldsymbol{y}_{q-1}^0)} = \begin{pmatrix} \mathsf{J}_0 & -\mathbb{1} & \dots & 0 \\ \vdots & \ddots & \ddots & \vdots \\ \vdots & & \ddots & -\mathbb{1} \\ 0 & \dots & \dots & \mathsf{J}_{q-1} \end{pmatrix},$$

where $\mathbb{1} \in \mathbb{R}^4$ denotes the identity matrix. Applying the least square minimization method described above, i.e., solving the quadratic system $\mathsf{J}_{\boldsymbol{F}} \Delta \boldsymbol{x} = -\boldsymbol{F}$ iteratively, where

$$\boldsymbol{F} = (\boldsymbol{\varphi}_0, \dots, \boldsymbol{\varphi}_{q-1})$$

assembles the residuals and

$$\Delta \boldsymbol{x} = (\Delta \tau_0^0, \Delta \boldsymbol{y}_1^0, \dots, \Delta \boldsymbol{y}_{q-1}^0)$$

is the initial value shift we get in each iteration, we finally converge into the continuous solution. The speed of convergence varies with the number of sub-intervals q, which thus has to be optimized in each iteration. We typically increase q corresponding to $q \to q+4$ starting at $q = 4$ until we achieve convergence. This is efficient, because it keeps q small. Note that adding only a single interval, i.e., $q \to q+1$, leads to four extra dimensions in the quadratic system $\mathsf{J} \Delta \boldsymbol{x} = -\boldsymbol{F}$.

The multiple shooting is assumed to be converged if $\|\boldsymbol{F}\| < \epsilon_{\mathrm{multi}}$, which also implies $|f(\mu)| < \epsilon_{\mathrm{multi}}$. It is thus reasonable to use $\epsilon_{\mathrm{single}} = \epsilon_{\mathrm{multi}}$. Note that the multiple shooting method has to be applied only if the required accuracy in the single shooting method could not be reached.

The resulting deformed shape

$$\boldsymbol{y}(s_0, \boldsymbol{x}) \quad = \quad \begin{pmatrix} r(s_0, \boldsymbol{x}) \\ z(s_0, \boldsymbol{x}) \\ \psi(s_0, \boldsymbol{x}) \\ \tau_s(s_0, \boldsymbol{x}) \end{pmatrix}$$

is obtained as a function of the parameter set $\boldsymbol{x} = \{p, \nu, K_{2\mathrm{D}}\}$, which are adapted during the shape regression (see Sec. 2.3.4) to optimally match the contour points extracted from the image.

2.3.4 Shape regression

In the shape regression we find the material parameters which minimize the deviation/error between contours and theoretical shapes from solving shape equations.

The Laplace-Young equation depends on the parameter set $\boldsymbol{x}_0 = (p_0, \Delta\rho, \alpha)$, where α is a scaling factor, which sets the length scale. The elastic shape equations depend on the parameter set $\boldsymbol{x} = (p, \nu_{2\mathrm{D}}, K_{2\mathrm{D}})$. Let $(\hat{r}_i, \hat{z}_i)$ with $i = 1, \ldots, N$ be a set of contour points resulting from image processing. We translate this set of contour points, such that these are symmetric with respect to the z-axis and the apex is located at $z = 0$. We then accordingly chose $z(0) = \zeta = 0$. We thereby fix the theoretical shape relatively to the contour points at the apex, and minimize the residual along the remaining shape profile.

The residuals

$$\boldsymbol{\varphi}_i \quad = \quad \min_{s_0 \in [0, L_0]} \begin{pmatrix} |\hat{r}_i| - r(s_0, \boldsymbol{x}) \\ \hat{z}_i - z(s_0, \boldsymbol{x}) \end{pmatrix}$$

are calculated by a bisection-like algorithm in the arc length s_0, which terminates when the interval length falls below the threshold ϵ_{rms}. From the residuals $\boldsymbol{\varphi}_i$ we calculate the average mean square deviation

$$\chi \quad = \quad \sqrt{\frac{1}{N} \sum_{i=1}^{N} \|\boldsymbol{\varphi}_i\|^2}$$

between the contour and the theoretical shape, as well as the Jacobians

$$\mathsf{J}_0 \quad = \quad \frac{\partial(\boldsymbol{\varphi}_1, \ldots, \boldsymbol{\varphi}_N)}{\partial(p_0, \Delta\rho, \alpha)}$$

$$\mathsf{J} \quad = \quad \frac{\partial(\boldsymbol{\varphi}_1, \ldots, \boldsymbol{\varphi}_N)}{\partial(p_0, \nu_{2\mathrm{D}}, K_{2\mathrm{D}})}$$

for the reference and the deformed shape. These Jacobians are sufficient to minimize the error χ and find the best fit parameter set $\boldsymbol{x}$ by solving the strongly over-determined system $\mathsf{J}_{\boldsymbol{F}} \Delta \boldsymbol{x} = -\boldsymbol{F}$ iteratively. Note that we have to find the best fit parameter set for the reference shape first, and afterwards perform the shape regression for the deformed shape, using the already determined reference shape. Each iteration of shape regression requires three numerical derivatives to find the elements of the Jacobian, which in turn require two executions of the shooting method. This yields a parameter shift $\Delta \boldsymbol{x}$ in each iteration, which we assume to be converged if we find $\lambda_j \|\Delta \boldsymbol{x}\| < \epsilon_{\mathrm{laplace/hooke}}$ during the backtracking line search. In addition to the minimization algorithm explained above, our software additionally provides the so-called Nelder-Mead downhill simplex method, which

symbol	precision	performance
ϵ_{rms}	10^{-16}	10^{-16}
$\epsilon_{\mathrm{single}}$	10^{-6}	10^{-4}
$\epsilon_{\mathrm{multi}}$	10^{-6}	10^{-4}
$\epsilon_{\mathrm{laplace}}$	10^{-6}	10^{-4}
$\epsilon_{\mathrm{hooke}}$	10^{-6}	10^{-4}
h_{laplace}	10^{-4}	10^{-3}
h_{hooke}	10^{-4}	10^{-3}

Table 2.1: Precision and performance optimized values for the thresholds used in the numerical algorithms.

works without derivatives. In rare cases, where the standard procedure fails, one should try this more robust method.

2.3.5 Numerical thresholds

To ensure convergence of the shape regression and the shooting method, we have to specify thresholds.

For the average mean square displacement (2.59), i.e., the individual residuals (2.58) between the contour points and the theoretical shape we apply a bisection-like algorithm terminating when the interval length falls below the threshold ϵ_{rms}.

For the single and multiple shooting methods we define the thresholds $\epsilon_{\mathrm{single}}$ and $\epsilon_{\mathrm{multi}}$, which have different meanings: the accuracy $\epsilon_{\mathrm{single}}$ is reached if $|f| < \epsilon_{\mathrm{single}}$, see eq. (2.48), is satisfied for the boundary deviation at the capillary, whereas the accuracy $\epsilon_{\mathrm{multi}}$ is reached if $\|\boldsymbol{F}\| < \epsilon_{\mathrm{multi}}$ is satisfied for the global residual, which also implies $|f| < \epsilon_{\mathrm{multi}}$. We define $\epsilon_{\mathrm{laplace}}$ and $\epsilon_{\mathrm{hooke}}$ as thresholds for the euclidean norm of the parameter shift $\lambda_j \Delta \boldsymbol{x}$, which is applied to the parameters of the shape equations during the regression and the backtracking line search, respectively. To integrate the shape equations we use a 4-th order Runge-Kutta method with constant step widths h_{laplace} and h_{hooke}.

In Tab. (2.1) standard values for the numerical algorithms are given. For the analysis of the capsules used in this paper, the numerical thresholds always ranged within the given boundaries. To improve the performance for specific capsules these thresholds can be increased, but it should be checked if the results are still in rough agreement with higher precision measurements, meaning that no systematic errors occur. Note that the parameters of the image processing also change the numerical behavior since the set of contour points results directly from image processing. Changing, for example, the width of the Gaussian smoothing of the image will alter the fitting results.

2.3.6 Image processing

Several filters, transformations and algorithms are applied to the image in order to get a set of contour points, which can be used for shape regression. Initially, we use a Gaussian filter to smoothen the image and run the Canny edge detection. This is common practice to extract contours from images. From the binary image we measure the outer and inner capillary diameter (the latter implicitly in terms of the fit parameter α), which is necessary to relate the length scale set in the image to SI units. Likewise, we measure the height of the capsule and its distance from the bottom of the image. These quantities are necessary to translate the contour points according to the remarks stated in 2.3.4. Furthermore, we extract the contour points and reduce their number to improve efficiency. To ensure that the

capturing algorithm works correctly, images have to meet certain requirements. In principle, all file formats supported by the OpenCV library can be used with our software, but we recommend png-files. Gravity should act downwards along the vertical axis and the capsule should be centered in the image with the capillary entering the image at the top. If these requirements are fulfilled, it is, in contrast to the typical pendant drop software packages, not necessary to select the capsule region manually, since the software detects the capillary and therefore the top side of the capsule automatically. The background should be uniformly colored and clean from small particles or other objects disturbing the edge detection. To ensure a proper automatic wrinkle detection the wrinkles should be visible over the whole width of the capsule. If the edge detection for the wrinkles does not work, one can provide a manually measured wrinkle wavelength in the configuration file. Even if the edge detection for the wrinkles works, one should randomly check the results by measuring the wrinkling length manually since the automatic detection requires uniformly illuminated capsules.

# 3 Cooperative microtubule dynamics in closed elastic compartments

> "It seems reasonable since art copies nature, and men can make various automata which move without thought, that nature should produce its own automata much more splendid than the artificial ones. These natural automata are the animals."

<div align="right">René Descartes</div>

Perpetually changing environmental conditions, in particular climate (atmosphere) and surface structure, led to **emergence of *life***. The origin of the first biological structure on planet earth is still subject of research and typically discussed in the context of abiogenesis [103, 104]. It is assumed that the first cell prototype was formed spontaneously in a 'prebiotic soup' [105], i.e., in presence of energy and the required chemical substances. More recent studies suggest that life evolved in an inorganic compartment, thus lacking a cell membrane [106]. However, starting from unicellular organisms, evolution brought forth a vast variety of different beings by natural selection. From the viewpoint of physics, those are complex biological machines made from $\sim 10^{13}$ cells of size $\sim 10\,\mu m$ (humans) [107]. The human organism evolves from a single cell to a multi-cellular organism via cell division and differentiation. Information needed to guide this process is encoded in a small coiled string of length $\sim 1\,m$ called DNA (deoxyribonucleic acid). It was first present in the original cell and then copied with each cell division. What we call 'life' is mostly referable to self-organization phenomena on the molecular, supra-molecular and cellular level. Interaction energies of order $\sim k_B T$ enable spontaneous assembly of higher order structures, which are commonly referred to as soft matter. The interplay between different participants in cell mechanics seems to be carefully orchestrated, such that small variations or dysfunctions may cause serious disease, or even death. Many of these phenomena express themselves in mechanical properties: It has been reported that the stiffness of cancer cells shows a ten fold decrease compared to normal cells [108] and applying chemotherapy to cancer cells resulted in an increased stiffness [109]. It is thus crucial to reveal and identify the key mechanisms in cell mechanics.

We briefly introduce the **design of animal cells** by focusing on structures involved in their mechanical properties as a whole (see Fig. 3.1). If not stated explicitly, we refer to Refs. [107, 110]. First of all, a cell is a container, which is filled with cytoplasm providing a liquid medium for cellular processes, like filament assembly and chemical reactions. Compartmentalization enables the organism to control chemical conditions on the scale of the cell size, where *elastic* cell membranes allow for additional mechanical feedback loops as well as dynamic shape change in response to external forces. Apart from the cell membrane that will be discussed in detail later, important cellular components are the nucleus, ribosome, mitochondrion and cytoskeleton, where only the latter directly affects mechanical stability. However, the other parts are necessary to provide the building blocks and energy needed by cytoskeletal dynamics. The DNA is stored in the nucleus, which, due to its mass and size, also acts as an obstacle to intracellular diffusion. The ribosome produces proteins by reading the
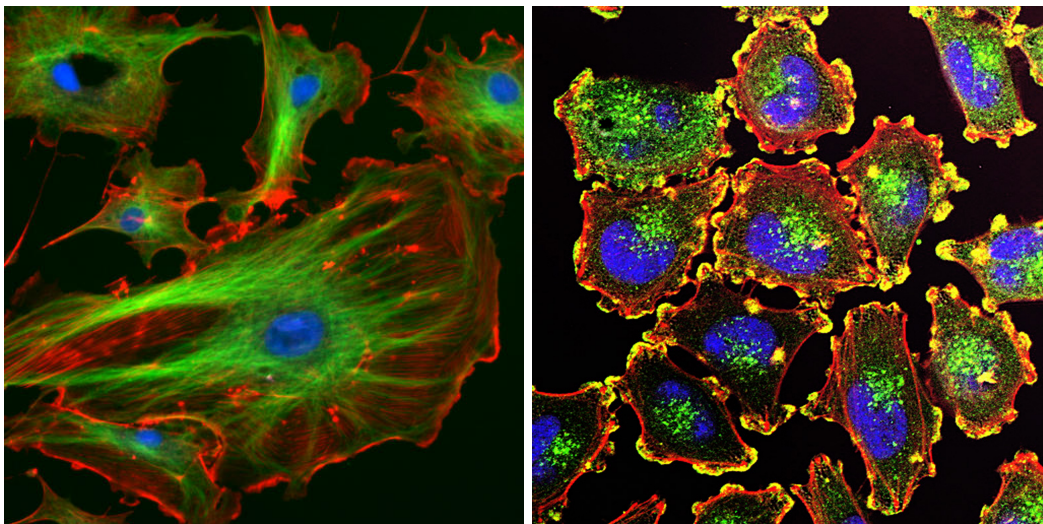
Figure 3.1: Left: Healthy endothelial cells observed through a microscope (public domain [112]). The cell's nucleus is colored blue, microtubules are colored green, actin is colored red. Obviously cell shapes are far from being symmetric due to several shape changing factors. Microtubules grow from the centrosome (or nucleus) towards the cell periphery, where they interact with the (thin) actin cortex. **Right:** Cancerous melanoma cells observed through a microscope (public domain [113]). Here, green indicates actin regulating factors and yellow highlights podosomes, which are actin rich structures associated with cell motility and cancer cell invasion.

RNA previously synthesized in the nucleus and thus serves as a factory that assembles amino acids to proteins. These are essential building blocks of several structures within and outside the cell. The mitochondrion supplies ATP (adenosine triphosphate), which is used as a source of chemical energy by ATPases as e.g. motor proteins, similar to GTP that is produced from GDP during the citric acid cycle and associated with GTPases. Both ATP and GTP work as activating factors for proteins. The cytoskeleton is built from three major filament types, namely F-actin (two filaments assembled from G-actin intertwined in a helix), MTs (microtubules, cylindrical tubulin lattice made of typically 13 straight protofilaments) and intermediate filaments (chain of tetrameric subunits). Only recently, septin has been proposed as the fourth cytoskeletal component [111]. Since we aim to study the interplay between the MT cytoskeleton and the cell periphery in this work, we will start by introducing these parts separately in the following, starting with MTs, which are dynamic protein tubes on the micrometer scale (see green filaments in Fig. 3.1 left).

In animal cells, **MTs fulfill various functions** and are part of several higher order structures. In the mitotic spindle, kinetochore MTs, interpolar MTs and astral MTs collaborate to segregate the chromosomes [114]. Cells can establish cilia or flagella needed for movement in liquid environments and the core of these flexible protrusions is made from a MT bundle, which is called the axoneme [115]. During locomotion of adhered cells, MTs have been reported to interact with FAs (focal adhesions) in two ways [116–120]. FAs are responsible for cellular traction, i.e., they anchor cells to the extracellular matrix. In the cell back MTs trigger disassembly of FAs supporting membrane retraction, whereas in the cell front MTs trigger assembly of FAs and thus guide the adhesion process. MTs might be guided to FAs by interacting with actin stress fibers [121]. Proteins of the CLIP-family promote capturing of MTs at cortical sites through direct interaction with dynein-dynactin [122, 123]. In addition, MTs serve es a dynamic scaffold for the cell membrane and therefore mechanically stabilize the cell as a whole. MTs form a transport network within the cell

and can be utilized by motor proteins for delivery of vesicles from the nucleus to the cell periphery or vice versa [124].

To fulfill all these functions, **subpopulations of MTs** with specific characteristics are required. Local occurrence of specific tubulin isotypes can induce the formation of such subpopulations. MT composition is typically cell-type specific. Both α- and β-tubulin isotypes are encoded by multigene families and most MTs are composed of an isotype mixture. Based on different isotypes, post-translational modifications [125–130] lead to additional differentiation. Excluding (de)acetylation, the C-terminal (carboxy-terminal) of tubulin is used for chemical modifications like (de)glycosylation, (de)phosphorylation, (de)tyrosination or (de)glutamylation. Since the C-terminal is located on the outer surface of the MT, this also affects interactions with MAPs (MT associated proteins) and motor proteins.

MAPs interact with the MT lattice and thereby influence MT characteristics like polymerization velocities, transition rates, interactions with motor proteins or linkage to other cytoskeletal players. MTs participate in formation of axons and growth cones [131], where they exert polymerization forces and deliver vesicles dedicated to extend the plasma membrane and, thus, leading to plastic deformations, which are supported by remodeling of the actin cortex. Dynamic instability enables the growth cone to explore its environment and find its synaptic target. Since such protrusions can reach lengths up to meters, MTs need to be stabilized to maintain the pathway of the axon. This is achieved by MAPs interacting with the MT. The tau-protein, which is highly conserved in neurons, stabilizes MTs and supports MT bundling, for example, in dendrites. Tau has been reported to bind longitudinally to the MT lattice [132] supporting linkage to actin [133] or stiffening of the MT filament [132, 134]. In addition, tau decreases catastrophe rates, increases rescue rates, and slightly increases polymerization velocities above the critical tubulin concentration [132, 135]. Dysfunctions of the tau-protein are related to Alzheimer's disease [136], dementia or other neurological disorders [137]. This highlights the important role of microtubules as one of the essential cytoskeletal filaments.

MTs in the cytoskeleton are constantly growing and shrinking because of their **dynamic instability** [138]. MTs grow radially from a centrosome or MTOC (MT organizing center) towards the cell periphery, where they can directly exert forces onto the cell membrane [139, 140]. In general, force generation by MTs is limited by buckling [141, 142], but MT buckling can be prevented by bundling MT interactions [142] or surrounding filament meshwork providing a supporting elastic medium [143]. MTs can generate forces in the pN-regime, which are sufficient to strongly deform lipid bilayer vesicles [139] or giant liposomes [144], but even cooperatively generated MT forces are presumably not sufficient to directly deform the complete cell cortex [6]. Growing MTs interact, however, with the actin cortex [145–147], in particular via *pioneering* MTs [147–150], where they can trigger actin polymerization and, thus, additional force generation. This mechanism allows polymerizing MTs to induce cell cortex deformations and changes to the cell shape [145, 146]. On the other hand, the cell cortex exerts elastic forces onto polymerizing MTs, which depend on the global shape of the cell and slow down polymerization [141]. This gives rise to an interplay between cell shape and MT organization within the cell via elastic cell cortex forces and MT polymerization forces. Ultimately, this leads to cooperative effects due to force sharing between polymerizing MTs [6, 151].

Dynamic **MTs organize** within a *rigid* compartment enclosed by a cell wall, like in plant cells, either because of mutual collision-induced interactions [152, 153], by motor-induced interactions [154] or as a result of direct interaction with the cell walls [155, 156]. In combination with motor proteins MTs spontaneously form asters under suitable conditions [157, 158]. Aster positioning inside a cell with rigid walls involves pushing forces and motor
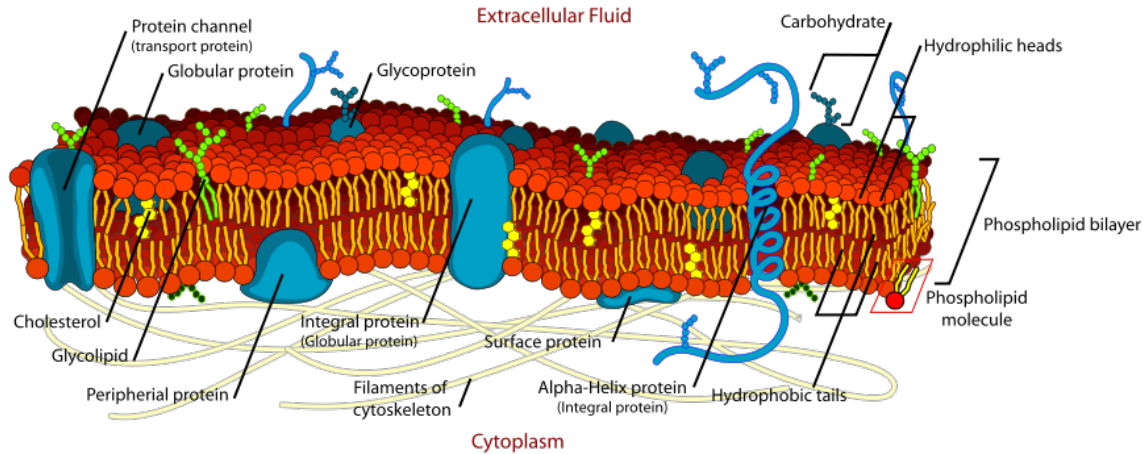
Figure 3.2: Sketch of a cell membrane with multiple different proteins incorporated (public domain [163]). Incorporated proteins modulate the bending rigidity of the plasma membrane. The membrane is attached to filaments of the cytoskeleton via linker proteins.

forces [155, 159–161]. Much less is known about MT organization in a flexible or *elastic* compartment as it is provided by a lipid bilayer membrane [162] or the cell cortex of animal cells. In order to sketch out the properties of a complex object like the cell cortex, we assume that the properties of the individual parts are additive, which allows us to discuss the lipid bilayer and the actin cortex independently. This assumption can be justified as we will point out later.

The **lipid bilayer** (see Fig. 3.2) provides different possibilities of elasticity manipulations [164–167], which, to a large extent, consist in the generation of local bending moments. This can be understood in the context of the so called 'mosaic membrane'. Cell membranes incorporate proteins and, likewise, proteins adhere to the membrane. Apart from specific functions like channeling and sensing, local bending moments generated by those proteins mainly depend on their geometry, which may vary in time due to, e.g., opening and closing of a channel. More specifically, an increasing bilayer stiffness has been observed due to incorporation of sufficient high concentrations of cholesterol [168, 169]. Protein incorporation induces local modulations of the bending modulus since incorporation always involves reordering of the lipids, i.e., change in the lateral packing density and thus change of the bilayer energy. Moreover, the bilayer itself, though it typically occurs in a fluid state, can exhibit phase separation by applied curvature [170]. In brain sphingomyelin cells, phase separation occurs even at low temperatures ranging from 30 to 60C° [171]. Phase separation manifests in the coexistence of solid domains and liquid particles diffusing at the interface. Line tension along the domain border can induce shape changes [59]. Domain formation can also be induced by Ca^{2+} influx locally in the inner leaflet [171]. Though the area of lipid membranes is approximately constant (fluctuations $\sim 4\%$), additional area can be provided by vesicular addition or intracellular stores, such as tiny invaginations or protrusions [172]. Providing area from microscopic folds is sometimes referred to as a 'shrink-wrap-mechanism' [173].

The **actin cortex** [174] is a network of individual actin filaments typically connected by crosslinkers. On the one hand, elastic properties of the cortex are determined by the properties of individual filaments, such as length, bending rigidity and inextensibility [175], and on the other hand by the topology and the constitution of the network, which turn out to be quite diverse in vivo. One may mention here the branching degree, bundle thickness, or mesh size. Assuming a mesh size ξ, the shear modulus scales according to $G' \sim \xi^{-3}$ in

an ideal network [176], and according to $G' \sim \xi^{-2}$ in actin networks [177]. With respect to the actin density c_A it has been reported that $G' \sim c_A^{11/5}$ for an entangled solution, and $G' \sim c_A^{5/2}$ for densely cross-linked gels [177]. For fibroblasts it has been found that $G' \sim 200\,\mathrm{Pa}$ [178]. In general, the shear modulus varies over several orders of magnitude dependent on crosslinker and actin density [179]. Elastic properties are highly dynamic due to continuous polymerization and depolymerization of actin filaments, which can be controlled and triggered either by microtubules [180] or by signals received from the extracellular matrix, for example, via insulin [181]. Active tension in the cortex can be adapted by the amount of motor proteins like dynein or myosin [182], which shift pairs of filaments against each other. As already mentioned, we assume the properties of actin cortex and lipid bilayer to be additive due to structural linking via ERMs, which are introduced in the following.

ERMs (ezrin, radixin, moesin) are responsible for **linking the actin cortex to the plasma membrane**, similar to spectrin. A loss of this linkage leads to blebbing phenomena [182], which have been studied widely, in particular regarding cell death and bleb related motility [183]. ERMs are known to contribute to cortical stiffness [172], for example, moesin during mitosis [184]. Ezrin has been reported to down-regulate Rho activity in neurons [185], which likewise effects cortical rigidity. Due to mechanical linkage between actin cortex and lipid bilayer both parts can be regarded as a structural unit, which we call the cell cortex. We thereby neglect the contribution of ERMs to cortical stiffness and, thus, only consider the linkage character.

Septin has recently been referred to as the 'fourth component of the cytoskeleton' [111]. **Septins** assemble to filaments and other higher order structures, such as rings, meshwork, or scaffolds. Their functions are diverse and reach from controlling cortical rigidity during mitosis or bleb retraction [172, 186] to localizing specific proteins by acting as diffusion barriers [187]. Septin has been reported to build cage-like structures around bacteria [111], which have invaded the cell. Once engulfed, bacteria exploit the actin cytoskeleton to move towards the nucleus. Interaction with actin and thereby movement can be effectively prevented by septin cages. Most importantly, septins interact with MTs, actin and the phospholipid bilayer. Regarding the latter one, it has been shown that septins are able to apply morphological changes to phospholipid based liposomes in vitro [188].

The most important family of proteins involved in cellular signaling pathways is the Rho family [189] including the proteins Rho, RhoB, RhoC, Rac1, Rac2, Rac3 and Cdc42. These are called **GTPases** since they are capable of binding guanosine to its G-domain, which gives rise to a switching process between active GTP (guanosine triphosphate) bound states and inactive GDP (guanosine diphosphate) bound states. GTP is produced from GDP during the citric acid cycle. Hydrolysis of GTP to GDP releases energy $\sim 20\,k_B T$; the reverse pathway from GDP to GTP via a condensation reaction consumes the same amount of energy. The change in the protein energy landscape can trigger folding processes, which are necessary for the protein to perform dedicated tasks. Due to many different participating GTPases residing in the actin cortex, complex activation patterns emerge, which orchestrate actin dynamics. Crosstalk between the MT and the actin cytoskeleton is enabled by pioneering MTs that regulate GTPases residing in the actin cortex. Such regulation is typically realized by the corresponding mediators, see Fig. 3.3.

Cytoskeletal dynamics, i.e., dynamics of microtubules and actin filaments, is regulated by **activation patterns** via GTP resources, which are mediated by GEFs (guanosine exchange factors), GAPs (guanosine activating proteins), and GDIs (guanosine nucleotide dissociation inhibitors) (see Fig. 3.3). GEFs promote activation of Rho GTPases by catalyzing conversion from GDP to GTP, GAPs lead to deactivation via the reverse pathway by promoting hydrolysis from GTP to GDP, and GDIs compete with GEFs by stabilizing GDP-bound
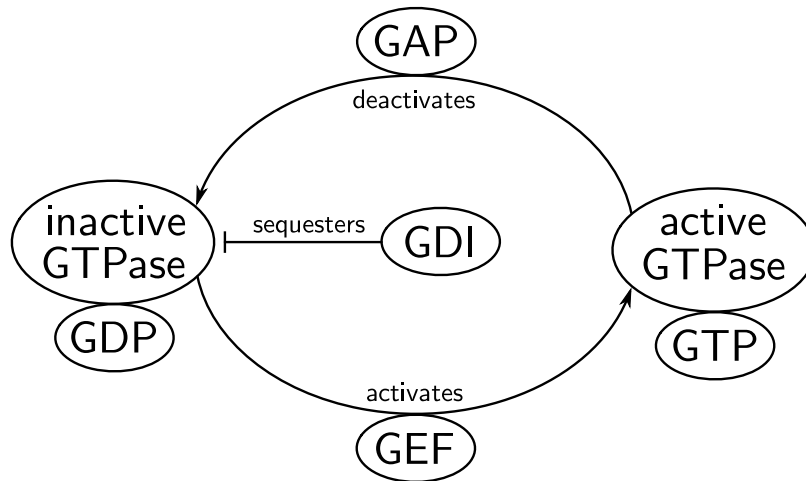
Figure 3.3: Controlling GTPase activation patterns via GEFs, GAPs and GDIs.

GTPase states. Together, these three players allow tight regulation of GTP/GDP incidence and therefore several GTP/GDP activation/deactivation dependent processes.

Due to their dynamic instability, MTs can be regarded as **stochastic oscillators**. In a cell, MT oscillations are coupled via mechanical interaction with the elastic cell cortex. Systems of coupled oscillators are known to exhibit collective oscillations under suitable conditions. Typical phenomena, which have been studied concerning synchronization, are firefly populations synchronizing by light flashes [190] and neuronal networks synchronizing by electric activity [191]. The standard model to describe synchronization phenomena is the Kuramoto model, which predicts spontaneous synchronization at a critical coupling strength [192]. The existence of a similar transition for MT ensembles in dependence of elastic membrane properties or MT parameters might give rise to controlling mechanisms, which allow cells to switch between collective and non-collective behavior. Regarding a ring with nearest neighbor coupling, the Kuramoto model predicts that the frequency of the phase-locked solution is given by the arithmetic mean of the individual oscillator frequencies [193]. Neglecting long-range interactions this rule might similarly apply to an MT cytoskeleton interacting with a surrounding elastic shell.

While the phase-locked solution describes a symmetric state of the MT aster, and cortex deformations will be reversible if one assumes a purely elastic cortex, a major question is **how MT asters are involved in permanent changes of the cell shape**. Typical cell shapes are spheres (onset of mitosis), platelets (blood cells), star-like (adhered to ECM), or ellipsoidal shapes (lamellipodium). To become polar, the cell has to break a spherical symmetry either spontaneously or induced by an external trigger. Polarity is achieved by shape transformations of the surrounding cell membrane *and* changes of cytoskeletal dynamics. These changes arise, for example, from spatial inhomogenities in the viscosity of the cell plasm, the elasticity of the cortex, filament assembly, or signalling proteins. Breaking the spherical symmetry is necessary, in particular for swimming or migrating cells [194]. Even transient, asymmetric shapes might become long-lived by remodeling of the actin cortex, which allows plastic deformations to a certain degree [174].

In the following sections, we study the mutual influence between cell shape and MT organization within the elastic cell cortex by a simplified model that captures only essential features of cell dynamics. We will neglect buckling and consider an ensemble of straight MTs growing radially outwards from a centrosome forming an aster-like structure. Both the cell membrane and the actin cortex exhibit elastic behavior, and we regard them as

a single structural unit, which we treat as an effective membrane with stretching and bending elasticity. We assume that a growing MT can deform this effective elastic membrane, mimicking cell cortex and membrane, by steric interaction. MT ensembles have been modeled as active gels [195], for example, in a description of the mitotic spindle [196]; other models are based on individual MTs [151, 197]. Here, we follow the latter approach and couple the polymerization dynamics of the MT aster modeled on an individual basis to the deformation of the elastic confinement which encloses the MT aster.

In general, we distinguish two possible possible effects on MT dynamics: structural and regulatory. Within the structural analysis we investigate steric interactions, polymerization kinetics and elastic deformations. This model serves as a basic setup for further investigation of regulatory mechanisms including signaling cascades via GTPases, and interactions with MAPs. These mechanisms enter our model via temporal or spatial inhomogenities encoded in properties of the cell cortex or the MT cytoskeleton. We develop a simulation model, which mechanically couples the stochastic dynamics of an MT aster with an effective elastic membrane. This can be seen as a minimal model for a primitive eucaryotic cell. *In vivo*, cells are surrounded by the ECM (extracellular matrix), which can be arranged in many different ways, for example, in a dense cell compound, where cells interact mechanically [198]. The cell interior is a mixture of cytoplasm, cytoskeletal filaments, and various other components, such as organelles. We reduce this complexity by assuming the ECM *and* the cell interior to be a homogeneous, viscous medium. Therefore, we describe the effective elastic membrane by overdamped dynamics characterized by a Stokes friction constant. In the limit of vanishing mechanical attenuation, membrane dynamics is much faster than MT dynamics, which is equivalent to a membrane with zero relaxation time, thus maintaining static force equilibrium.

For the sake of simplicity, we develop the model in two-dimensional space. Though, especially the membrane is expected to behave differently in three dimensions, as it can release stress in one extra dimension, the two-dimensional approach is suitable, e.g., for flat cells adhered to a substrate. We could regard our two dimensional model as a projection (slice) of a three dimensional, flattened cell. From this perspective, we could argue that the two dimensional projection can fluctuate freely in its area and contour length, since there is a material exchange between the slice and the bulk.

Within this work we try to answer several questions emerging from cell mechanics. Employing a two-dimensional simulation model we investigate the parameter dependence of typical observables in both a symmetric and an asymmetric (polarized) state and compare our results, as far as possible, to one-dimensional mean-field approaches. We also discuss unique features of the two-dimensional model, such as synchronization of the MT ensemble, i.e., collective length fluctuations. As it turns out, collective events trigger cell polarization in a setup including a Rac-Rho feedback mechanism, which is a combination between two, mutual exclusive, MT regulated feedback mechanisms.

3.1 Single MT dynamics

MTs are stiff filamentous proteins consisting of tubulin-dimers (called monomers in the following), which are organized in a tube-like structure and form a helical lattice, see Fig. 3.4. While new monomers attach and detach stochastically at the tip, the whole MT switches stochastically between phases of growth and phases of rapid shrinkage. This behavior originates in the hydrolysis of tubulin dimers with the MT and is known as dynamic instability [138]. If in a growing phase the stabilizing GTP-tubulin cap is lost by hydrolysis

the MT undergoes a catastrophe and starts to shrink rapidly; if the GTP-cap is re-formed the MT is rescued and growth resumes.

3.1.1 Fokker-Planck equation

A simple stochastic model for this process is based on four parameters [199, 200]: Assembly and disassembly are modeled by two (deterministic) velocities, a shrinking velocity v_- and a growth velocity v_+. MTs stochastically switch from the growing to the shrinking state with the catastrophe rate ω_c and back to the growing state with the rescue rate ω_r. In vivo, all these parameters are modified by various biochemical processes. A comprehensive list of how MAPs influence, for example, the growth velocity v_+ and the catastrophe rate ω_c is given in Ref. [201]. The stochastic process can be described by a Fokker-Planck equation [200, 202],

$$\partial_t \boldsymbol{p} = \left(\Omega - \mathsf{V}\partial_l \right) \boldsymbol{p}, \tag{3.1}$$

where the matrices

$$\Omega = \begin{pmatrix} -\omega_c & \omega_r \\ \omega_c & -\omega_r \end{pmatrix} \quad \text{and} \quad \mathsf{V} = \begin{pmatrix} v_+ & 0 \\ 0 & -v_- \end{pmatrix}$$

define the time evolution of the vectorial probability density

$$\boldsymbol{p}(l,t) = (p_+(l,t), p_-(l,t))^T.$$

Here, $p_\pm(l,t)\mathrm{d}t$ are the probabilities of finding the MT in the growing or in the shrinking state. In the following, we will always use a reflecting boundary at $l = 0$,

$$v_+ p_+(0,t) = v_- p_-(0,t),$$

corresponding to the situation that a shrinking MT undergoes a forced rescue or re-nucleation at $l = 0$. In an MT ensemble this condition corresponds to a constant number M of MTs, i.e., $M = \mathrm{const}$. The growth dynamics is governed by the characteristic length parameter

$$\lambda \equiv \frac{v_+ v_-}{v_+ \omega_r - v_- \omega_c}. \tag{3.2}$$

If $\lambda < 0$, the average length loss after a catastrophe exceeds the average length gain, in case of $\lambda > 0$, the average length gain exceeds the average length loss. Without confining boundary in $(+)$-direction, but including a reflective boundary in $(-)$-direction (at the origin), a stationary length distribution can only be obtained for bounded growth with $\lambda < 0$. Then, $\partial_t \boldsymbol{p} = 0$ in eq. (3.1) leads to
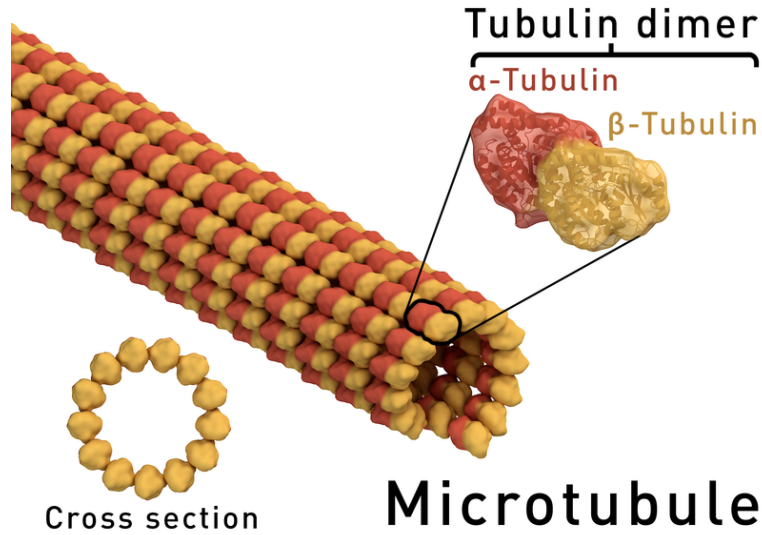
$$\partial_l \boldsymbol{p} = \mathsf{V}^{-1} \Omega \boldsymbol{p}$$

with the general solution

$$\boldsymbol{p}(l) = \exp \left(\mathsf{V}^{-1} \Omega l \right) \boldsymbol{p}_0.$$

Using $p \equiv p_+ + p_-$ and the normalization condition $\int_0^\infty \mathrm{d}l\, p \equiv 1$ yields an exponential length distribution

$$p(l) = \frac{1}{|\lambda|} e^{-l/|\lambda|},$$

Figure 3.4: Sketch of the cylindrical MT lattice, which is made from tubulin dimers (image provided by T. Splettstoesser [203] and licensed under CC BY-SA 4.0 [32]). Tubulin dimers are composed of two subunits, namely α- and β-tubulin. Due to polar dimers, the MT lattice has a polar structure with $(+)$- and $(-)$-end, which is exploited by motor-proteins to control their direction of movement. The hollow cylinder formed by tubulin dimers has a diameter $\sim 25\,\mathrm{nm}$ and is typically made from 13 protofilaments. After a catastrophe, these curl outwards and the MT switches to a phase of rapid shrinking.

where $|\lambda| = \langle l \rangle$ is the average MT length. For unbounded growth, i.e., $\lambda > 0$, $\langle l \rangle$ grows with constant velocity, there is no steady state solution, and for long times $p(l,t)$ asymptotically approaches a Gaussian distribution, where the average MT length

$$\langle l \rangle \approx Jt \quad \text{with} \quad J = \frac{v_+ \omega_r - v_- \omega_c}{\omega_r + \omega_c} \tag{3.3}$$

and the variance

$$\langle l^2 \rangle - \langle l \rangle^2 \approx 2 D_J t \quad \text{with} \quad D_J = \frac{\omega_c \omega_r (v_+ + v_-)^2}{(\omega_c + \omega_r)^3} \tag{3.4}$$

are time-dependent [199, 200]. It has been shown that single unconfined MTs with $\lambda > 0$ essentially self-organize to $\lambda^{-1} = 0$ when they are inserted into an elastic confinement [204]. MTs confined by an elastic obstacle thus always remain in the bounded regime, even for non-zero rescue-rate. Many MTs cooperate and generate more mean force than single MTs [6].

3.1.2 Rigid confinement

Though we discuss elastic obstacles in this thesis, solutions for rigid confinements can provide suitable approximations in the limits of very soft or stiff obstacles. Here we consider a one-dimensional box of size L. To transfer the obtained solutions we could, for example, set the box size L to the maximum possible elongation of the elastic obstacle.

A rigid obstacle can neither be moved nor be passed by the MT. By reaching the boundary the MT instantly stops growth and undergoes a catastrophe after a short time. In a box

$[0, L]$ with rigid walls MT lengths are described by the probability density [204, 205]

$$p(l) = \mathcal{N}e^{l/\lambda}\left(1 + \frac{v_+}{v_-}\right) \quad \text{with} \quad l \in [0, L].$$

MT lengths thus follow an exponential distribution, where, in case of bounded growth, the probability of finding a length l decreases, and, in case of unbounded growth, the probability increases towards the barrier. Solving the corresponding Fokker Planck equation yields $p_+(l) = \mathcal{N}e^{l/\lambda}$ and $p_-(l) = \mathcal{N}\frac{v_+}{v_-}e^{l/\lambda}$ [204]. The probability Q_+ of finding the MT stuck at the boundary is given by

$$Q_+ = \mathcal{N}\frac{v_+}{\omega_{c,L}}e^{L/\lambda}, \tag{3.5}$$

assuming a constant catastrophe rate $\omega_{c,L}$ for the stalled MT [204]. The normalization constant derives as

$$\mathcal{N}^{-1} = \lambda\left(1 + \frac{v_+}{v_-}\right)\left(e^{L/\lambda} - 1\right) + \frac{v_+}{\omega_{c,L}}e^{L/\lambda}.$$

Together, $p_+(l)$ and $Q_+(l)$ give the fraction of growing MTs and we can derive the probability of undergoing a catastrophe by weighting with the catastrophe rate, which yields a piecewise defined probability density

$$p_c(l) = \begin{cases} \mathcal{C}\omega_c e^{l/\lambda}, & l < L \\ \mathcal{C}v_+ e^{l/\lambda}\delta(l - L), & l = L \end{cases}$$

with a normalization constant

$$\mathcal{C}^{-1} = v_+ e^{L/\lambda} + \int_0^L \mathrm{d}l\, \omega_c e^{l/\lambda} = v_+ e^{L/\lambda} + \omega_c\lambda(e^{L/\lambda} - 1).$$

The probability $p_c(l)\mathrm{d}l$ grows exponentially when approaching the static barrier at $l = L$. Though the MT stalls immediately at reaching the barrier, the catastrophe probability remains finite, meaning that the resting time remains finite, too. We obtain the average catastrophe length by taking the expectation value

$$\langle l_{\max}\rangle = \mathcal{C}\int_0^L \mathrm{d}l\, l\omega_c e^{l/\lambda} + \mathcal{C}\int_0^L \mathrm{d}l v_+ e^{l/\lambda}\delta(l - L)$$

$$= \mathcal{C}\omega_c\lambda^2\left[1 + e^{L/\lambda}\left(\frac{L}{\lambda} - 1\right)\right] + \mathcal{C}Lv_+ e^{L/\lambda}.$$

Note that we always have $\langle l_{\max}\rangle < L$ as long as $\omega_c > 0$, which implies a finite catastrophe probability before reaching the barrier. From $p(l)$ we find the average MT length [204]

$$\langle l\rangle = \mathcal{N}\int_0^L \mathrm{d}l\, lP(l) + \mathcal{N}LQ_+$$

$$= \mathcal{N}\left(1 + \frac{v_+}{v_-}\right)\lambda^2\left[1 + e^{L/\lambda}\left(\frac{L}{\lambda} - 1\right)\right] + \mathcal{N}L\frac{v_+}{\omega_{c,L}}e^{L/\lambda}$$

and the mean square displacement

$$\langle l^2 \rangle = \mathcal{N} \int_0^L \mathrm{d}l \, l^2 P(l) + \mathcal{N} L^2 Q_+$$
$$= \mathcal{N} \left(1 + \frac{v_+}{v_-}\right) \lambda e^{L/\lambda} (2\lambda^2 - 2\lambda L + L^2) - 2\mathcal{N} \left(1 + \frac{v_+}{v_-}\right) \lambda^3 + \mathcal{N} L^2 \frac{v_+}{\omega_{c,L}} e^{L/\lambda}.$$

The maximum and the average MT length give rather similar results, since the MT shrinking velocity is large against the growth velocity, i.e., $v_- \gg v_+$. This leads to small shrinking fractions, which contribute to $\langle l \rangle$, but not to $\langle l_{\max} \rangle$. In both cases, bounded and unbounded growth, length fluctuations $\langle l^2 \rangle$ reach a maximum in the limit $|\lambda| \to 0$ (uniform length distribution) and, analogously, vanish in the limit $|\lambda| \to \infty$ (delta peak length distribution).

3.1.3 Plastic confinement

Analogous to the limit of a rigid confinement corresponding to a diverging elastic modulus, we discuss the limit of a plastic obstacle corresponding to a vanishing elastic modulus. Such an obstacle either moves at velocity v_+ or holds its position at the maximum length the MT has ever reached in its history. Rarely, the MT overcomes this maximum length, moves the obstacle further at velocity v_+, then undergoes a catastrophe and leaves the obstacle at the new maximum length, where the obstacle stays until the MT returns to again exceed its maximum length. This states a common problem from classical extreme value theory [206, 207].

In the following, we investigate how the maximum turning point of the MT evolves in time. Therefore, we assume at first that MT growth is bounded and, thus, $\lambda < 0$. The probability that the MT does *not* reach the maximum MT length l_c within $n_c \geq 1$ cycles is given by

$$P_{n_c}(l < l_c) = \left(\int_0^{l_c} \mathrm{d}l \, \frac{1}{|\lambda|} e^{-l/|\lambda|} \right)^{n_c} = \left(1 - e^{-l_c/|\lambda|} \right)^{n_c}.$$

The probability $P_{n_c}(l > l_c)$ that the MT exceeds the maximum MT length l_c within n_c cycles is complementary to $P_{n_c}(l < l_c)$, i.e.,

$$P_{n_c}(l > l_c) = 1 - \left(1 - e^{-l_c/|\lambda|} \right)^{n_c}.$$

From this probability we derive the probability density via differentiation with respect to l_c leading to

$$p_{n_c}(l_c) = \frac{n_c}{|\lambda|} e^{-l_c/|\lambda|} \left(1 - e^{-l_c/|\lambda|} \right)^{n_c-1} = \frac{n_c}{|\lambda|} \sum_{k=0}^{n_c-1} \binom{n_c-1}{k} (-1)^k e^{-(k+1)l_c/|\lambda|}.$$

We now calculate the expectation value of l_c after n_c growth cycles to

$$\langle l_c \rangle (n_c) = \frac{n_c}{|\lambda|} \sum_{k=0}^{n_c-1} \binom{n_c-1}{k} (-1)^k \underbrace{\int_0^\infty \mathrm{d}l_c \, l_c e^{-(k+1)l_c/|\lambda|}}_{=|\lambda|^2/(k+1)^2} = |\lambda| \sum_{k=1}^{n_c} \binom{n_c}{k} (-1)^{k-1} \frac{1}{k}$$

$$= |\lambda| \sum_{k=1}^{n_c} \frac{1}{k} \approx |\lambda| (\gamma_{\mathrm{em}} + \ln(n_c)),$$

where γ_{em} is the Euler-Mascheroni constant. Obviously, the average maximum length $\langle l_c \rangle$ grows logarithmically with the number n_c of growth cycles. Since we investigate a plastic obstacle here, this scaling transfers directly to the obstacle elongation, which thus likewise grows logarithmically. Assuming that a single cycle typically takes a time t_c we can substitute $n_c = t/t_c$ to find $\langle l_c \rangle \sim |\lambda| \ln(t)$. For the expectation value of the quadratic maximum length we find

$$\langle l_c^2 \rangle(n_c) = \frac{n_c}{|\lambda|} \sum_{k=0}^{n_c-1} \binom{n_c - 1}{k} (-1)^k \underbrace{\int_0^\infty \mathrm{d}l_c\, l_c^2 e^{-(k+1)l_c/|\lambda|}}_{=2|\lambda|^3/(k+1)^3} = 2|\lambda|^2 \sum_{k=1}^{n_c} \binom{n_c}{k} (-1)^{k-1} \frac{1}{k^2}$$

$$\approx |\lambda^2|(\gamma_{\mathrm{em}} + \ln(n_c))^2 + |\lambda|^2 \left(\frac{\pi^2}{6} - \frac{1}{n_c} \right),$$

where we used Stirling's formula for $n_c \gg 1$ and again approximated the harmonic series with $\sum_{k=1}^{n} 1/k \approx \gamma_{\mathrm{em}} + \ln(n)$. Using our results for $\langle l_c^2 \rangle$ and $\langle l_c \rangle$ we see that the variance

$$\langle l_c^2 \rangle - \langle l_c \rangle^2 = |\lambda|^2 \left(\frac{\pi^2}{6} - \frac{1}{n_c} \right)$$

becomes constant in the limit $n_c \to \infty$, i.e.,

$$\lim_{n_c \to \infty} \left(\langle l_c^2 \rangle - \langle l_c \rangle^2 \right) = \frac{\pi^2}{6} |\lambda|^2.$$

Note that, in the same limit, the relative standard deviation

$$\lim_{n_c \to \infty} \frac{\sqrt{\langle l_c^2 \rangle - \langle l_c \rangle^2}}{\langle l_c \rangle} = 0 \tag{3.6}$$

vanishes, because the variance approaches a constant in the limit $n_c \to \infty$, whereas the expectation value $\langle l_c \rangle$ grows logarithmically.

For unbounded MT-growth we found $\langle l \rangle \sim t$ for the average MT length (3.3) and $\langle l^2 \rangle - \langle l \rangle^2 \sim t$ for the MT length variance (3.4), such that the relative standard deviation vanishes,

$$\lim_{t \to \infty} \frac{\sqrt{\langle l^2 \rangle - \langle l \rangle^2}}{\langle l \rangle} = 0, \tag{3.7}$$

in the limit $t \to \infty$. These results also hold for the maximum MT length l_c, if $J \approx v_+$ such that $\langle l_c \rangle - \langle l \rangle \approx \mathrm{const}$.

Though we presented our results here in the context of a plastic barrier, they can likewise be used to explain how MTs explore space. Ballistic behavior, like for unbounded MT growth, leads to a phase exploration that is linear in time. In contrast, due to their dynamic instability, bound MTs sample space only logarithmically in time. This logarithmical phase exploration is accompanied with fluctuations that sharply increase for small times $t \sim t_c$ and then saturate. Now that we have investigated the limit cases of rigid and plastic confinements, we introduce elastic confinements in the following.

3.1.4 Force-dependent MT growth

The single MT dynamics model is completed by the force dependence of polymerization velocities and catastrophe rate. The shrinkage velocity v_- is assumed to be force-independent,

parameter	symbol	value
effective monomer length	d_m	$0.6 \cdot 10^{-9}\,\mathrm{m}$
characteristic force	F_0	$6.67 \cdot 10^{-12}\,\mathrm{N}$
shrinking velocity	v_-	$3.0 \cdot 10^{-7}\,\mathrm{m/s}$
random hydrolysis rate	r	$3.7 \cdot 10^{6}\,\mathrm{m^{-1}s^{-1}}$
vectorial hydrolysis velocity	v_h	$4.2 \cdot 10^{-9}\,\mathrm{m/s}$
on-rate	ω_{on}	$70.0\,\mathrm{s^{-1}}$
off-rate	ω_{off}	$6.0\,\mathrm{s^{-1}}$

Table 3.1: Parameters of MT dynamics as used within this thesis.

since it is barely concerned by axial loads and releases stress from the tip. For similar reasons, we assume the rescue rate to be constant. MT growth, on the other hand, is slowed down by an opposing force. Assuming that force only affects to on-rate, we use [140, 208]

$$v_+(f) = d_m \left(\omega_{\mathrm{on}} e^{-f/F_0} - \omega_{\mathrm{off}} \right) , \tag{3.8}$$

where $d_m = 8\,\mathrm{nm}/13$ is the length difference induced by the attachment of a single monomer, $F_0 = k_B T/d_m \sim 6.6\,\mathrm{pN}$ is the force scale set by thermal fluctuations and f is an axial load acting on the MT tip. For strong forces $f \gg F_0$, the Arrhenius factor e^{-f/F_0} effectively suspends the attachment of new monomers at the tip. The Arrhenius factor is related to the Brownian ratchet model, which assumes a fluctuating barrier in front of the MT tip [208]. In the force-free case, v_+ becomes the net on-rate multiplied by the effective monomer length, i.e., $v_+(0) = d_m(\omega_{\mathrm{on}} - \omega_{\mathrm{off}})$. The critical point of the function (3.8) is obtained by inversion, i.e., $f_{\mathrm{stall}} = f(v_+ = 0)$, which gives the stall force $f_{\mathrm{stall}} = F_0 \ln(\omega_{\mathrm{on}}/\omega_{\mathrm{off}})$, at which MT growth stops. The stall force is uniquely related to a stall length $l_{\mathrm{stall}} = x_{\mathrm{stall}}$, if an invertible force relation $f(x)$ is provided. Here, x denotes the obstacle elongation and l the MT length. Both stall force and stall length represent insuperable limits for the MT. Note that such an invertible force relation can only be provided in simple systems where single MTs interact with a well-defined barrier. In more complex systems, where multiple MTs collaborate to elongate the obstacle (which might also change its shape), the stall force becomes history dependent and can thus only be determined as a statistical average.

It has turned out that the catastrophe rate, in contrast to the rescue rate, also exhibits a force-dependence via the growth velocity. Several models for catastrophe rates have been proposed, experimental and theoretical ones [209, 210]. Flyvbjerg et al. [210] derived an exact analytical result for ω_c, which depends on v_+, the random hydrolysis rate r and the vectorial hydrolysis velocity v_h, see Tab. 3.1 for the corresponding values. The random hydrolysis rate concerns single tubulin dimers that hydrolize stochastically within the lattice, whereas the vectorial hydrolysis velocity concerns hydrolysis waves that propagate through the lattice with constant velocity. The dimensionless catastrophe rate α is given by the smallest solutions of [210]

$$\mathrm{Ai}'(\xi^2 - \alpha) = -\xi \mathrm{Ai}(\xi^2 - \alpha) \tag{3.9}$$

with the Airy function Ai, $\xi \equiv (v_+ - v_h)D^{-2/3}r^{-1/3}$ and the diffusion constant $D \equiv d_m(v_+ + v_h)/2$. We numerically solve eq. (3.9) for $-10 \leq \xi \leq 10$. Beyond this interval we use the asymptotics $\alpha \sim 1/2\xi$ for $\xi \geq 10$ and $\alpha \sim \xi^2$ for $\xi \leq -10$ [210]. We obtain ω_c through comparison with $\alpha \equiv \omega_c D^{-1/3}r^{-2/3}$. The Flyvbjerg catastrophe model is characterized by $\omega_c \sim v_+^{-2/3}$ for intermediate growth velocities resulting in an exponentially increasing catastrophe rate under force via the exponentially decreasing growth velocity according to eq.

(3.8). Janson et al. [209] obtained a slightly different dependence $\omega_c \sim v_+^{-1}$ in experiments. Both models give an exponentially increasing catastrophe rate above the characteristic force F_0. For MT dynamics under force this is typically the essential property, which gives rise to a certain robustness of results with respect to different catastrophe models [6, 204].

An increasing force exponentially slows down MT growth while, at the same time, the catastrophe rate increases exponentially. Both effects decrease the inverse growth parameter λ^{-1}, see eq. (3.2). This is an essential feature of MTs, which makes it possible to confine a single MT within some elastic barrier: the MT increases its length and, thus, the elastic force until the inverse growth parameter λ^{-1} vanishes and MT growth becomes bounded, i.e., the MT essentially self-organizes to a bound state with $\lambda^{-1} = 0$ [204].

Based on the force-dependent single MT dynamics, MTs in the ensemble interact by force re-distribution via the elastic membrane configuration, which depends on the whole aster configuration. In our final model (3.4), the elastic obstacle dynamically reacts to stochastic displacements produced by multiple MTs and changes its shape. This alters local forces onto MTs which, in turn, adapt their growth velocities accordingly. This mechanism can give rise to cooperative behavior, such as collective catastrophes and rescues events [6, 151], as well as collective length oscillations [6].

Before taking the full stochastics into account, we explore mean-field approaches for single and multiple MTs. We begin by quantifying the dynamic properties of single MTs, which are limited by an elastic barrier.

3.2 Mean-field theory

We investigate a one dimensional model, in which a single MT of length $l(t)$ grows against a spring of length $x(t)$. Both the spring and the MT are attached to the MTOC, which is placed in the origin. The dynamics of the system is driven by stochastic growth and shrinkage of the MT, while the spring adapts dynamically to the current MT length. The spring has a rest length x_0 and we have $x(t) \geq x_0$ for all times. For $l(t) < x_0$ the MT is always detached and follows its free dynamics. For $l(t) > x_0$ the MT is occasionally attached and, in case of contact and growth, the spring opposes a force $E(x(t) - x_0) = E(l(t) - s_0)$. If the MT is detached and we have $x(t) > x_0$ the spring relaxes following an overdamped dynamics, i.e., relaxes exponentially. Without confining spring, the MT switches stochastically between free growth and shrinkage. In a confinement, a phase of growth under force enters between the former and the latter. Thus, three phases have to be considered regarding the MT (cp. Fig. 3.5):

**1** The MT grows force free with $l(t) < x(t)$ and is described by

$$\partial_t l = v_+(0),$$

which takes a time $\tau_{+,0}$. Free growth ends when the MT encounters the relaxing spring or undergoes a catastrophe. The MT can therefore occasionally skip phase **2**.

2 After attachment, which happens at $x_{\min}$, where the situation changes from $l(t) < x(t)$ to $l(t) = x(t)$, MT growth is slowed down by the force $E(l(t) - x_0)$ and described by

$$\partial_t l = v_+(E(l - x_0)),$$

which takes a time $\tau_{+,1}$ and is, taking fluctuations into account, an *optional* phase.
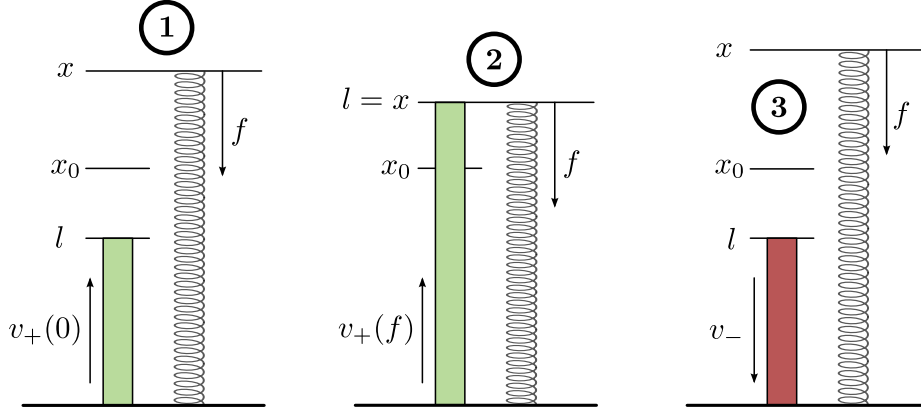
Figure 3.5: Simplified model for a single MT growing against a membrane. Phases of elongation (pushing MT) and phases of relaxation alternate and perform a continuous cycle with constant frequency.

3 After detachment at $l = x_{\max}$ or a catastrophe at $l = l_{\max}$ the MT shrinks following

$$\partial_t l = -v_-$$

for a time τ_- determined by the distance to the MTOC and the apparent rescue rate. After shrinking, the MT is rescued at $l_{\min}$.

If phase **2** took place, $x_{\max}$ and $l_{\max}$ coincide. Otherwise the MT undergoes a catastrophe before reaching the spring, which thus does not stop its relaxation. Spring dynamics alternates between two different states:

M1 During force free growth or shrinkage of the MT the spring relaxes following

$$\gamma \partial_t x = -E(x - x_0)$$

with a Stokes friction coefficient γ.

**M2** During growth under force, the spring follows the same dynamics as the MT, i.e.

$$\partial_t x = v_+(E(x - x_0)).$$

As wee see, the MT can take a lot more oscillations than the spring in the same time, since it does not necessarily reach the spring. This effect becomes stronger with increasing friction. Even for an infinite fast spring, the MT potentially performs more oscillations than the spring, if it undergoes a catastrophe before reaching x_0. Only if $x_0 = 0$ and $\gamma \to 0$ the MT and the spring can be part of one single oscillation, where free growth is completely excluded.

In a mean-field approach, we determine the average oscillation cycle of the MT defined by passing subsequently all three phases **1**, **2** and **3**. The occasional skip of phase **2** will be included in the mean first contact time that is needed to pass phase **1**. If convenient, we use abbreviations $\bar{l} \equiv l - x_0$ and $\bar{x} \equiv x - x_0$.

3.2.1 Oscillation cycle

To characterize the oscillation cycle we introduce average times, namely the time MTs spend attached to the membrane and exert force $\tau_{+,1}$, the time of free growth $\tau_{+,0}$, and the time
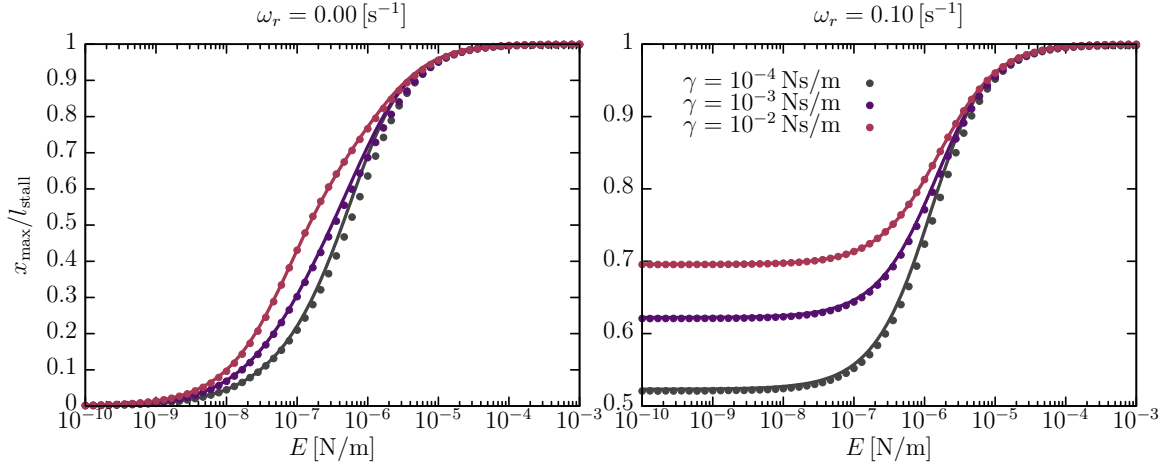
Figure 3.6: Average maximum membrane elongation $x_{\max}$ in units of the MT stall length versus elastic modulus. Dots are simulation results for a single MT confined by an overdamped spring and lines are solutions of (3.15).

of shrinking τ_-. One also might consider to reformulate these quantities via the catastrophe time $\tau_c = \tau_{+,0} + \tau_{+,1}$ and the rescue time $\tau_r = \tau_-$, or the attached time $\tau_{\mathrm{att}} = \tau_{+,1}$ and the detached time $\tau_{\mathrm{det}} = \tau_- + \tau_{+,0}$, where we implicitly assume that shrinking MTs are *not* attached, i.e., that attached MTs always grow. Note that, in the following, we always refer to times averaged over the stochastic MT dynamics, i.e., we drop the brackets in our notation and assume $\tau \equiv \langle \tau \rangle$. Similarly, we always refer to oscillation limits averaged over the stochastic MT dynamics, i.e., $x \equiv \langle x \rangle$ or $l \equiv \langle l \rangle$

From the time periods introduced above several other interesting quantities derive directly, such as the effective catastrophe and rescue frequency $\omega_c = 1/\tau_c$ and $\omega_r = 1/\tau_r$. More importantly, we can specify the probability of each state in the oscillation cycle, as, for example, the probability of being attached and detached

$$p_{\mathrm{att}} = \tau_{\mathrm{att}}/\tau_{\mathrm{tot}} \quad \text{and} \quad p_{\mathrm{det}} = \tau_{\mathrm{det}}/\tau_{\mathrm{tot}}$$

where the total duration of the oscillation cycle

$$\tau_{\mathrm{tot}} = \tau_{+,0} + \tau_{+,1} + \tau_- = \tau_{\mathrm{att}} + \tau_{\mathrm{det}} = \tau_c + \tau_r$$

gives the characteristic timescale of MT dynamics confined by the elastic obstacle. Note that this timescale of course differs from the timescale corresponding to a free MT growing permanently force-free, which would be

$$\tau_{\mathrm{tot}}^{\mathrm{free}} = \tau_{+,0} + \tau_- = \tau_{\mathrm{det}} = \tau_c + \tau_r.$$

In order to quantify the duration of the three phases (Fig. 3.5), we solve the differential equations describing MT dynamics and obstacle elongation in the following, and investigate the three phases separately.

3.2.2 Obstacle elongation

At first, we consider the growth phase from $l = x_{\min}$ to $l = l_{\max} = x_{\max}$ under force. This phase and the obtained oscillation maximum are identical for both the MT and the spring. Nevertheless, we differentiate between both in our notation. We have $l_{\max} = x_{\max}$, because

detachment and catastrophe happen simultaneously. The MT is rescued at $l_{\min}$, afterwards attaches at $x_{\min}$, and finally detaches while simultaneously undergoing a catastrophe at $l = l_{\max} = x_{\max}$. We introduce the probability $p_{+,1}(t)$ that the MT is still growing after a time t, which fulfills

$$\partial_t p_{+,1} = -\omega_c(v_+(E\bar{x}(t)))\, p_{+,1}. \tag{3.10}$$

For convenience, we neglect rescue events at the moment. Since $\omega_c(v_+)$ is a non-trivial function we cannot find a closed solution, but write

$$p_{+,1}(t) = p_{+,1}(0) \exp\left(-\int_0^t \mathrm{d}t'\, \omega_c(v_+(E\bar{x}(t')))\right),$$

where $p_{+,1}(0)$ is the probability that the MT is still intact at $t = 0$ respectively $l = x_{\min}$. The MT has to overcome the distance $x_{\min} - l_{\min}$ without undergoing a catastrophe to enter the growth phase under force. Integrating equation (3.10) gives

$$
\begin{aligned}
\int_{p_{+,1}(0)}^{p_{+,1}(\tau_{+,1})} \frac{\mathrm{d}p_{+,1}}{p_{+,1}} &= -\int_0^{\tau_{+,1}} \mathrm{d}t\, \omega_c(v_+(E\bar{x}(t))) \\
\ln p_{+,1}(\tau_{+,1}) - \ln p_{+,1}(0) &= -\int_{\bar{x}_{\min}}^{\bar{x}_{\max}} \mathrm{d}\bar{x}\, \frac{\omega_c(v_+(E\bar{x}))}{v_+(E\bar{x})}.
\end{aligned} \tag{3.11}
$$

A good approximation for the mean stochastic growth time $\tau_{+,1}$ consists in the condition $p_{+,1}(\tau_{+,1}) = 1/e$, which produces the exact result for a constant catastrophe rate. Assuming further the MT has definitely reached the membrane after a time $\tau_{+,0}$, we can use $p_{+,1}(0) = 1$ to find

$$f_1(\bar{x}_{\min}, \bar{x}_{\max}) = 1 - \int_{\bar{x}_{\min}}^{\bar{x}_{\max}} \mathrm{d}\bar{x}\, \frac{\omega_c(v_+(E\bar{x}))}{v_+(E\bar{x})} = 0. \tag{3.12}$$

from Eq. (3.11). For a fast spring we can set $\bar{x}_{\min} = 0$ and directly solve for $\bar{x}_{\max}$, which coincides with $\bar{l}_{\max}$ here. To solve for both oscillation limits we need an additional condition, which will be derived in 3.2.3. Depending on the two oscillation limits $\bar{x}_{\min}$ and $\bar{x}_{\max}$, the growth time under force can be calculated to

$$\tau_{+,1} = \int_{\bar{x}_{\min}}^{\bar{x}_{\max}} \frac{\mathrm{d}\bar{x}}{v_+(E\bar{x})} = \tau_e \ln\left(\frac{\tilde{\omega}_{\mathrm{on}} - e^{E\bar{x}_{\min}/F_0}}{\tilde{\omega}_{\mathrm{on}} - e^{E\bar{x}_{\max}/F_0}}\right),$$

where the relative on-rate $\tilde{\omega}_{\mathrm{on}} = \omega_{\mathrm{on}}/\omega_{\mathrm{off}}$ and the characteristic elongation time $\tau_e = F_0/Ed_m\omega_{\mathrm{off}}$ are introduced. The growth time $\tau_{+,1}$ is positive if $0 < \bar{x}_{\min} < \bar{x}_{\max} < \bar{l}_{\mathrm{stall}}$ holds. In the limit $E \to 0$, i.e., unconfined MT, we find $\bar{x}_{\max} = \bar{x}_{\min} + v_+(0)/\omega_c(v_+(0))$ from (3.12), which gives the correct result for the free MT. In the following, we derive the second condition that is required to solve for both oscillation limits.

3.2.3 Obstacle relaxation

Detached MTs either shrink or grow force-free. Meanwhile, the spring relaxes from $\bar{x}_{\max}$ to $\bar{x}_{\min}$ according to $\bar{x}_{\min}(t) = \bar{x}_{\max} \exp(-t/\tau_0)$, where $\tau_0 = \gamma/E$ is the characteristic relaxation time of the spring.

Force-free growth: For the free growth time we additionally consider catastrophe events, which occur before the MT contacts the spring. The lifetime distribution for a the free MT
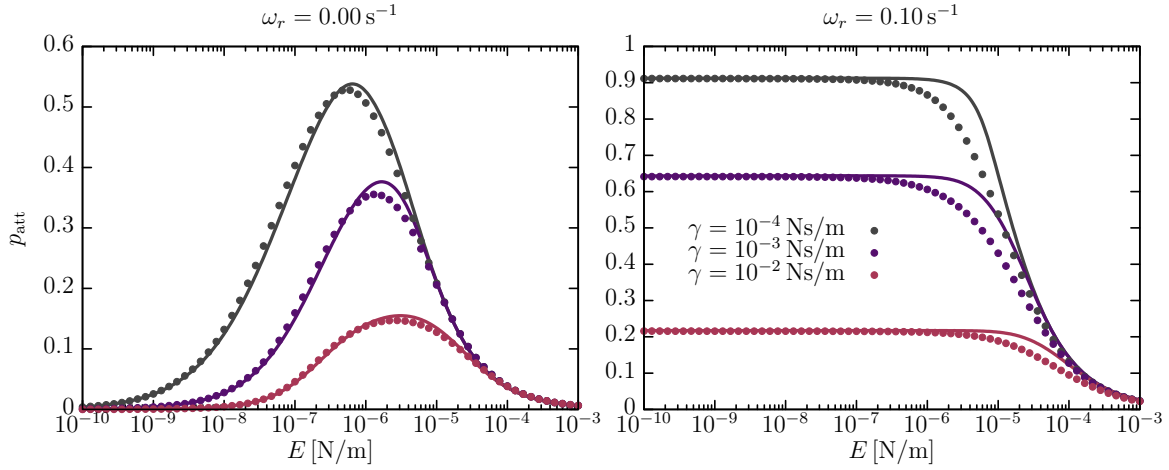
Figure 3.7: Attachment probability versus elastic modulus. Without rescues, the spring exhibits a sweet spot for intermediate elastic moduli, where the attachment probability is maxed out. In presence of rescue events, the attachment probability saturates for small elastic moduli.

is given by the simple exponential $p_{+,0}(t) = \exp(-\omega_c(v_+(0))t)$. The probability to reach the membrane without undergoing a catastrophe is thus given by $p_{+,0}(x_{\min}/v_+(0))$. One single cycle, in which the MT grows from $l = 0$ to $l = l_{\max}$ and shrinks back to $l = 0$, occurs with probability $1 - p_{+,0}(s_{\min}/v_+(0))$. In general, the MT performs n cycles before reaching the membrane. The mean first contact time for the MT to contact the membrane at $x_{\min} > l_{\max}$ can thus be approximated by

$$\tau_{+,0} = \sum_{n=0}^{\infty} \left(\frac{x_{\min} - l_{\min}}{v_+(0)} + n l_{\max} \left(\frac{1}{v_+(0)} + \frac{1}{v_-} \right) \right) (1 - p_{+,0})^n p_{+,0}$$

$$= \frac{x_{\min} - l_{\min}}{v_+(0)} + l_{\max} \left(\frac{1}{v_+(0)} + \frac{1}{v_-} \right) \left(\exp\left((x_{\min} - l_{\min}) \frac{\omega_c(v_+(0))}{v_+(0)} \right) - 1 \right).$$

In the above expression, the n-th term accounts for the contribution of performing n cycles before reaching the membrane. The sum can be evaluated by reducing it to geometric series. We choose $l_{\max}$ to be the average length after a catastrophe as expected for a MT in a rigid box of size $x_{\min} - l_{\min}$ in order to avoid contributions from $l > x_{\min}$ to the mean first contact time. Though we neglected rescues in Eq. (3.10), we take rescues into account for the mean first contact time by transforming $x_{\min} \to x_{\min} - l_{\min}$.

Shrinking: Analogously to catastrophes, rescue events follow an exponential probability density

$$p_-(t) = \begin{cases} \omega_r e^{-\omega_r t}, & t < \frac{l_{\max}}{v_-} \\ e^{-\omega_r t} \delta \left(t - \frac{l_{\max}}{v_-} \right), & t \geq \frac{l_{\max}}{v_-} \end{cases}$$

but at the MTOC MTs are immediately rescued, which leads to a cut-off of the rescue time probability density at $t = l_{\max}/v_-$. Thus, probabilities accumulate at the MTOC, which leads to an average shrinking time

$$\tau_-(l_{\max}) = \begin{cases} \omega_r^{-1}(1 - e^{-\omega_r l_{\max}/v_-}), & \omega_r > 0 \\ l_{\max}/v_-, & \omega_r = 0 \end{cases} \tag{3.13}$$

where we took the expectation value with respect to the probability density $p_-(t)$. Using the shrinking time just obtained we find the relation $l_{\min}(l_{\max}) = l_{\max} - v_- \tau_-(l_{\max})$ and, finally,

$$f_2(\bar{x}_{\min}, \bar{x}_{\max}) = \bar{x}_{\max} \exp(-(\tau_- + \tau_{+,0})/\tau_0) - \bar{x}_{\min} = 0. \tag{3.14}$$

This is the second condition that is needed to solve for both oscillation limits. Equation (3.14) has to be solved together with (3.12), i.e.,

$$\begin{pmatrix} f_1(\bar{x}_{\min}, \bar{x}_{\max}) \\ f_2(\bar{x}_{\min}, \bar{x}_{\max}) \end{pmatrix} = \mathbf{0}. \tag{3.15}$$

This equation lets us determine $\bar{x}_{\min}$ and $\bar{x}_{\max}$ with (3.12) and (3.14). We thus find a complete solution by applying, for example, a Newton method to solve (3.15).

Solutions of eq. (3.15) are shown in Fig. 3.6 and Fig. 3.7. The former shows the oscillation maximum $x_{\max}$ in units of the stall length l_{stall} for both presence and absence of rescues. In both cases, when increasing the elastic modulus E, MTs smoothly transition from non-stalling to stalling in the limit $E \to \infty$. In the limit $E \to 0$, however, $x_{\max}/l_{\text{stall}}$ vanishes in absence of rescues but converges to a finite value in presence of rescues.

Regarding the attachment probability shown in Fig. 3.7 we can state that the rich behavior is clearly related to the inflection point, i.e., the transition regime observed for the oscillation maximum in Fig. 3.6. The attachment probability undergoes a maximum in absence of rescues and saturates in presence of rescues. Actually, the MT thereby passes three different regimes of obstacle interaction. In the limit $E \to 0$, we observe a free MT due to an effectively absent obstacle, which is pushed far away from the MT seed once, but never returns as the relaxation time diverges, i.e., $\tau_0 \to \infty$. While increasing E starting from $E = 0$, the MT enters a regime where elasticity dominates and timescales of MT and obstacle relaxation match. Increasing E further until $E \to \infty$ we actually observe interaction with a rigid obstacle. The same argumentation applies also for anharmonic springs as the limit cases remain the same, meaning that our results are robust against changing the elastic model. However, the interval of elastic moduli, where the elastic features are observed, probably changes when changing the elastic model.

3.2.4 Polymerization force

To calculate the average force $\langle f \rangle = E \langle x \rangle$, we have to average over the trajectories $\bar{x}_{\max}(t)$ and $\bar{x}_{\min}(t)$ during one oscillation cycle of the spring. From $\partial_t \bar{x} = v_+(E\bar{x})$ we find the trajectory

$$\bar{x}_{\max}(t) = \frac{F_0}{E} \ln \left(\tilde{\omega}_{\text{on}} - \left(\tilde{\omega}_{\text{on}} - e^{E\bar{x}_{\min}/F_0} \right) e^{-t/\tau_e} \right)$$

for spring elongation during force exertion. In the limit $t \to \infty$ the force $E\bar{x}_{\max}(t)$ approaches the MT stall force $F_0 \ln \tilde{\omega}_{\text{on}}$. Together with the relaxation trajectory $\bar{x}_{\min}(t) = \bar{x}_{\max} \exp(-t/\tau_0)$ we find the expressions

$$\langle f \rangle_+ = \frac{F_0}{\tau_{+,1}} \int_0^{\tau_{+,1}} \ln \left(\tilde{\omega}_{\text{on}} - \left(\tilde{\omega}_{\text{on}} - e^{E\bar{x}_{\min}/F_0} \right) e^{-t/\tau_e} \right) \, \mathrm{d}t,$$

$$\langle f \rangle_- = \frac{E\bar{x}_{\max}}{\tau_- + \tau_{+,0}} \int_0^{\tau_- + \tau_{+,0}} e^{-t/\tau_0} \, \mathrm{d}t$$

for the average force $\langle f \rangle_+$ during force exertion and the average force $\langle f \rangle_-$ during spring relaxation. The former corresponds to the polymerization force which is exerted directly
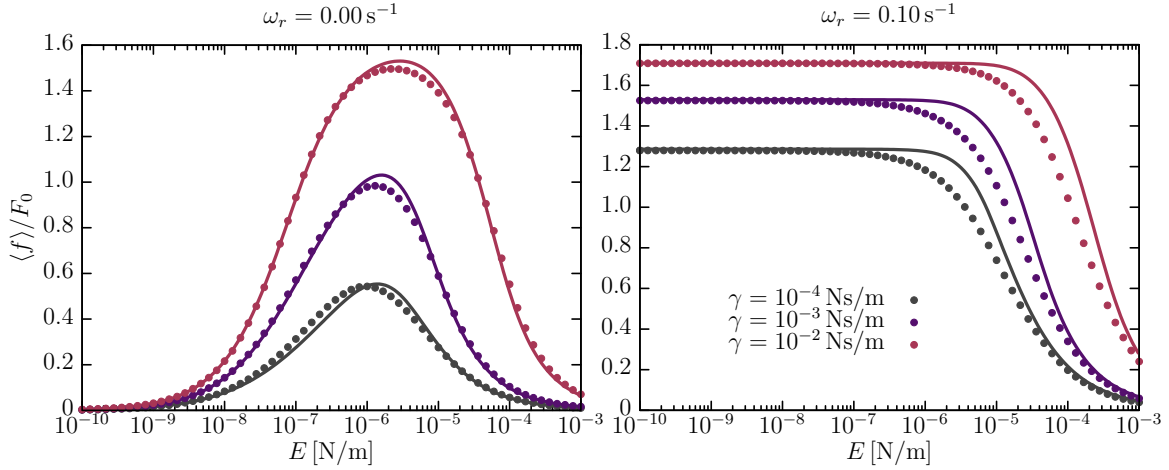
Figure 3.8: The average force acting on the membrane during a complete oscillation cycle undergoes a maximum in absence of rescues and saturates for vanishing elastic moduli in presence of rescues, similar to the attachment probability. However, in contrast to the attachment probability, the average force $\langle f \rangle$ increases with increasing friction due to larger relaxation times τ_0.

by the MT, whereas the latter originates in the relaxation process of the spring taking a time $\tau_{+,0} + \tau_-$. However, both functions $\langle f \rangle_+(E)$ and $\langle f \rangle_-(E)$ qualitatively follow the same course, which thus also transfers to the average polymerization force over a complete cycle given by

$$\langle f \rangle = p_{\text{att}} \langle f \rangle_+ + p_{\text{det}} \langle f \rangle_-.$$

Its behavior is qualitatively similar to the attachment probability: in absence of rescues it exhibits a maximum for intermediate elastic moduli, whereas in presence of rescues it saturates for vanishing elastic moduli (Fig. 3.8). The average polymerization force increases, however, with increasing friction due to larger relaxation times τ_0. This is in contrast to the attachment probability, where we observe the opposite behavior.

3.2.5 Conclusion

We investigated a single MT coupled to an overdamped spring in a one dimensional toy model and found analytic solutions, which are in good agreement with simulations. The attachment probability exhibits a maximum for intermediate elastic moduli of the spring, which is the most important result here. Furthermore the attachment probability increases with decreasing friction. In the limit of a stiff spring, but also for the free MT the attachment probability vanishes in absence of rescue events as expected. In contrast, when rescue events are present, the attachment probability saturates for vanishing elastic moduli, since the MT length parameter λ is sufficiently increased to follow the spring and stretch it to a critical extent.

In view of the two-dimensional analysis performed in section 3.4, where an ensemble of MTs is coupled by a closed elastic membrane, the attachment probability plays an important role, since it is a is a measure for the coupling strength. Though the coupling modulates the results just obtained, the one-dimensional model gives a first hint to what happens in the closed elastic compartment.

3.3 Ensemble mean-field theory

So far, we analyzed a single MT interacting with an elastic barrier following an overdamped dynamics in a mean-field approach. Now, we extend our interest to multiple MTs interacting via an elastic barrier and thereby focus on a collective growth state of the MT ensemble, by which we refer to a state with a non-zero fraction of growing MTs that interact with the barrier. Note that this is not necessarily a restriction since it is in principle possible to find a system in a permanent collective growth state. We take two types of barriers into account, which are (i) a barrier that exerts a constant force and (ii) a barrier that exerts a force growing monotonically in time, due to enduring and non-stationary obstacle elongation.

Based on stochastic switching and directional persistence, individual MT velocities are dichotomous Markov noises, which behave partially diffusive and partially wavelike [211]. MT arrays interacting with an elastic obstacle thus exhibit complex pinning and de-pinning dynamics, meaning that adsorption and desorption events occur stochastically. To describe this process, we utilize a system of one-step master equations corresponding to a birth-death process, where birth and death are associated to adsorption and desorption events.

An MT population of M MTs can be subdivided into n_+ attached and n_- detached MTs, where the total MT number $M = n_+ + n_-$ is conserved. Attached MTs participate in elongating the elastic obstacle by uniformly sharing its opposed force. Detached MTs reside in the cell interior and after some time potentially re-enter the (moving) boundary. Attachment and detachment events change the current boundary occupation. This process is described by effective rates, which of course depend on the current boundary occupation and the force exerted by the elastic obstacle. Technically, these effective rates depend on the *stochastic* number n_+ of attached MTs and the total force F exerted by the obstacle. In a mean-field approach we replace F by its expectation value $\langle F \rangle$ with respect to many realizations of the stochastic n_+ dynamics, meaning that all these realizations experience one and the same force $\langle F \rangle$. Note that we chose the number n_+ as a discrete variable and consider an infinite number of collective MT systems, which contain M MTs each. Together, these systems are characterized by one-step master equations concerning the probabilities $p_{n_+}(t)$. The probability to find a system with n_+ MTs exerting force at a given time t is $p_{n_+}(t)$, which, in case of a monotonically growing force, depends on the history of the force $\langle F \rangle$, i.e., its time evolution.

In the following, we derive the time evolution for the probabilities $p_{n_+}(t)$ employing a system of $(M+1)$ one-step master equations dependent on the force $\langle F \rangle$. For constant force, i.e., $\langle F \rangle = \text{const}$, we calculate the steady state $\langle n_+ \rangle_{\text{eq}}(\langle F \rangle)$ and the mean first-passage time $T(\langle F \rangle)$, i.e., the endurance of the collective state of growth. Assuming a linear force relation $\langle F \rangle = E(\langle x \rangle - x_0)$ leads to a time evolution $\partial_t \langle F \rangle = E \partial_t \langle x \rangle = E v_+(\langle F \rangle / n_+)$ for a given boundary occupation n_+. This time evolution drives the system out of its stationary state. For such a system, we determine the ensemble stall force defined by $\langle v_+(\langle F \rangle / n_+) \rangle = 0$ and the nullcline defined by $\partial_t \langle n_+ \rangle = 0$, both by sampling individual phase space trajectories with reasonable initial conditions.

The theory we derive holds for MT bundles pushing against a one dimensional obstacle as well as asters confined by a circular *symmetric* membrane, because both systems are equivalent. Effects of asphericity or shape fluctuations, which apparently occur in simulations like in sec. 3.4, are therefore neglected. In contrast to Ref. [6], we take the full stochastics of the variable n_+ into account and, similar to Ref. [6], we treat the force with a mean-field approach. Moreover, we do not compare to simulation results like in Ref. [6], where theory and simulation results are in reasonable agreement.

3.3.1 Collective rates

In order to describe adsorption and desorption of MTs at the membrane with a system of one-step master equations we define effective rates. Desorption is associated with the backward rate, and adsorption is associated with the forward rate. The former decreases and the latter increases the boundary occupation. The backward rate $r_{n_+} = n_+ \omega_c(\langle F \rangle / n_+)$ for $n_+ > 0$ (Fig. 3.9 right) is a generalization of the catastrophe rate for ensembles under uniform force sharing, where we assume that catastrophe rates are independent from each other and thereby additive. The forward rate $g_{n_+} = (M - n_+)/\tau(\langle F \rangle / n_+)$ for $n_+ < M$ (Fig. 3.9 left) is proportional to the inverse average catch-up time $\tau(\langle F \rangle / n_+)$, which is obtained from the shrinking time τ_- (cp. (3.13)) and the time τ_+ of free growth. Effective rates very similar to r_{n_+} and g_{n_+} defined above have been derived in Ref. [6]. However, we use a more accurate expression for the shrinking time τ_-. We quantify the times τ_- and τ_+ in the following.

By assuming a linear and invertible average force $\langle F \rangle = E(\langle x \rangle - x_0)$ we implicitly assume an average obstacle position $\langle x \rangle$, which can be used to determine the shrinking time $\tau_-(\langle x \rangle) = \tau_-(\langle F \rangle / E + x_0)$ using (3.13). In order to determine the time of free growth, we state that in a system with n_+ MTs exerting a force $\langle F \rangle$ the boundary moves at velocity $v_+(\langle F \rangle / n_+)$, if we assume uniform force sharing. Note that this implies a moving boundary according to $\partial_t \langle x \rangle = v_+(\langle F \rangle / n_+)$ for a given boundary occupation n_+. During shrinking, MTs move away from the boundary at a relative velocity $v_- + v_+(\langle F \rangle / n_+)$. During force-free growth, MTs catch up at a relative velocity $v_+(0) - v_+(\langle F \rangle / n_+)$. The ratio of these two relative velocities is the same as the ratio of the free growth time τ_+ and the shrinking time τ_-, because the MT has to overcome the same relative distance in both phases. From these considerations we gain the relation

$$\tau_+(\langle F \rangle / n_+) = \tau_-(\langle x \rangle) \frac{v_- + v_+(\langle F \rangle / n_+)}{v_+(0) - v_+(\langle F \rangle / n_+)},$$

which gives the time between rescue and re-entering the group of MTs that exert force. This relation enables us to find

$$\tau(\langle F \rangle / n_+) = \tau_-(\langle x \rangle) + \tau_+(\tau_-(\langle x \rangle)) = \tau_-(\langle x \rangle) \left(1 + \frac{v_- + v_+(\langle F \rangle / n_+)}{v_+(0) - v_+(\langle F \rangle / n_+)} \right)$$

for the overall catch-up time, which is simply the sum of τ_+ and τ_-. In contrast to Ref. [6], we use the average shrinking time $\tau_-(\langle x \rangle)$ from eq. (3.13) obtained within the one-dimensional mean-field theory in section 3.2. MTs that undergo a catastrophe during collective force exertion, catch up on average after a time $\tau(\langle F \rangle / n_+)$. Note that the free growth time $\tau_+(\langle F \rangle / n_+)$ differs from the free growth time $\tau_{+,0}$ employed in the one-dimensional mean-field theory from section 3.2. Here, the obstacle does not relax during the catch-up process. Instead, the system is still in a state of collective growth, during which the remaining MTs participate in elongating the obstacle.

3.3.2 Boundary occupation

Using the forward and backward rates we can describe the MT population in a stochastic manner, i.e., set up the one step master equations. In case of a constant force $\langle F \rangle = \text{const}$ the boundary is stationary at $\langle x \rangle = \langle F \rangle / E + x_0 = \text{const}$. In case of a time-dependent force $\partial_t \langle F \rangle = E \langle v_+(\langle F \rangle / n_+) \rangle$ the boundary itself is dynamic according to $\partial_t \langle x \rangle = \langle v_+(\langle F \rangle / n_+) \rangle$. Here, we averaged over the stochastic n_+ dynamics, i.e., took the expectation value with respect to the probabilities $p_{n_+}(t)$. We aim to predict the fractions of the population
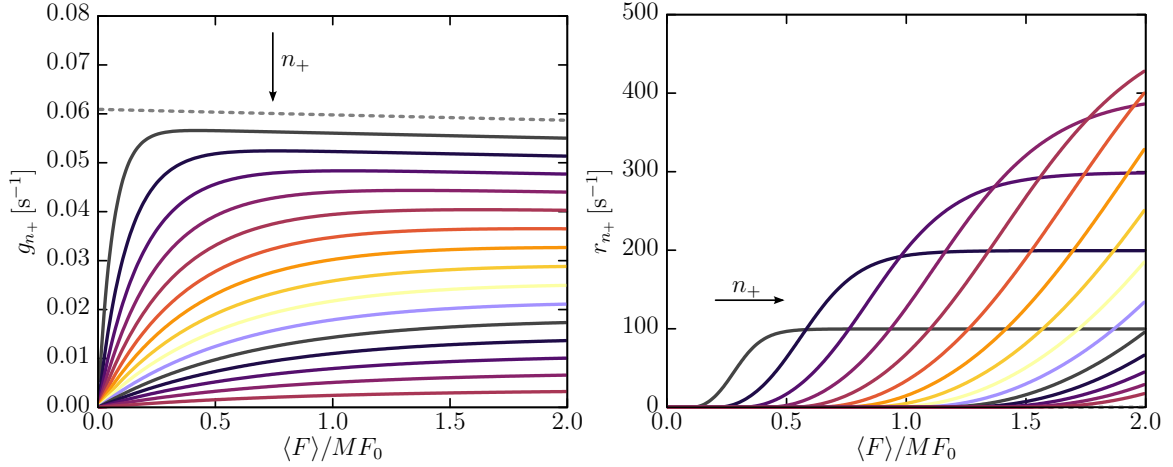
Figure 3.9: Left: Forward rate g_{n_+} for $\omega_r = 0.0\,\mathrm{s}^{-1}$ and several values $n_+ = 0\ldots 15$ from top to bottom. The forward rate decreases with an increasing number of force exerting MTs due to an increased obstacle velocity and, thus, an increased catch-up time. **Right:** Backward rate r_{n_+} for several values $n_+ = 1\ldots 16$ from left to right. The backward rate is identical to the Flyvbjerg catastrophe rate multiplied by the integral number n_+.

residing at the boundary and in the cell interior during a collective growth phase. Therefore, we consider a set of $M + 1$ discrete occupation levels $n_+ \in [0, M]$ under individual loads $\langle F \rangle / n_+$ and investigate the evolution of the probabilities $\boldsymbol{p}(t) = (p_0, p_1, \ldots, p_M)^T \in \mathbb{R}^{M+1}$ in continuous time. Exchange between adjacent levels occurs with forward rate $g_{n_+} = (M - n_+)/\tau(\langle F \rangle / n_+)$ and backward rate $r_{n_+} = n_+ \omega_c(\langle F \rangle / n_+)$. Note that $1 - p_0(t)$ gives the fraction at the boundary and $p_0(t)$ the fraction currently residing in the cell interior either shrinking or growing force-free.

Constant force: Assuming a constant force the time evolution of the probabilities $\boldsymbol{p}(t)$ is given by the system of master equations

$$\partial_t \boldsymbol{p}(t) = \mathsf{M} \boldsymbol{p}(t), \tag{3.16}$$

with a time-independent tridiagonal transition matrix

$$\mathsf{M} = \begin{pmatrix} -g_0 & r_1 & 0 & \ldots & & 0 \\ g_0 & -(g_1 + r_1) & r_2 & & & \\ 0 & g_1 & -(g_2 + r_2) & & & \vdots \\ & & & & & 0 \\ \vdots & & & & -(g_{M-1} + r_{M-1}) & r_M \\ 0 & & \ldots & 0 & g_{M-1} & -r_M \end{pmatrix}.$$

Note that we have $\sum_{i=0}^{M} \mathsf{M}_{ij} = 0$ for all columns j. From the occupation probabilities we obtain the expectation value

$$\langle n_+ \rangle = \sum_{n_+=0}^{M} n_+ p_{n_+}. \tag{3.17}$$

The steady state of eq. (3.16) can be obtained from the equilibrium condition $g_n p_n^{\text{eq}} = r_{n+1} p_{n+1}^{\text{eq}}$ corresponding to a locally vanishing probability net flux. Using this condition we express all probabilities

$$p_{n_+}^{\text{eq}} = p_0^{\text{eq}} \prod_{i=0}^{n_+ - 1} \frac{g_i}{r_{i+1}}$$

in terms of p_0^{eq}, which can be obtained via normalization

$$p_0^{\text{eq}} = \frac{1}{1 + \sum_{n_+=1}^{M} \prod_{i=0}^{n_+ - 1} \frac{g_i}{r_{i+1}}}.$$

Using the steady state, we find the expectation value

$$\langle n_+ \rangle_{\text{eq}} = \sum_{n_+=0}^{M} n p_{n_+}^{\text{eq}}. \tag{3.18}$$

This steady state might be reached in the limit $E \ll F_0/x_0$ of a soft barrier, where the force exerted by the obstacle is small and approximately constant. In the continuous limit and neglecting fluctuations, i.e., assuming that $p(n_+) = \delta(n_+ - \langle n_+ \rangle)$, we find

$$\partial_t \langle n_+ \rangle = g(n_+) - r(n_+) = \frac{M - \langle n_+ \rangle}{\tau(\langle F \rangle / \langle n_+ \rangle)} - \langle n_+ \rangle \omega_c(\langle F \rangle / \langle n_+ \rangle). \tag{3.19}$$

from eq. (3.17). The nullcline defined by $\partial_t \langle n_+ \rangle = 0$ in (3.19) is obtained from the self-consistent equation [6]

$$\langle n_+ \rangle = \frac{1}{1 + \omega_c(\langle F \rangle / \langle n_+ \rangle) \tau(\langle F \rangle / \langle n_+ \rangle)} \tag{3.20}$$

and has a loop shape in the $(\langle F \rangle, \langle n_+ \rangle)$-plane consisting of a stable upper branch and an unstable lower branch merging at a saddle node bifurcation, where $\partial \langle F \rangle / \partial \langle n_+ \rangle = 0$, i.e. the loop has a vertical slope (Fig. 3.10 right). This point marks the maximum possible polymerization force of the MT ensemble [6]. Beyond this critical force the expectation value $\langle n_+ \rangle$ spontaneously drops to zero.

Passage time for constant force: The following calculations are adapted from Refs. [212, 213] To deduce the mean first passage time needed to pass from n_+ to zero, we start with the recursive expression

$$T_{n_+} = \begin{cases} 0 & n_+ = 0 \\ \tau_{n_+}^{\text{esc}} + \tau_{n_+}^{\text{esc}} g_{n_+} T_{n_++1} + \tau_{n_+}^{\text{esc}} r_{n_+} T_{n_+-1} & 0 < n_+ < M \\ \tau_M^{\text{esc}} + \tau_M^{\text{esc}} r_M T_{M-1} & n_+ = M \end{cases} \tag{3.21}$$

where we have to use an absorbing boundary at $n_+ = 0$, i.e., $g_0 = 0$ and $T_0 = 0$, as well as a reflecting boundary at $n_+ = M$, i.e., $g_M = 0$. On the one hand, by reaching the state $n_+ = 0$ the system is trapped, on the other hand $n_+ = M$ is the highest accessible state.
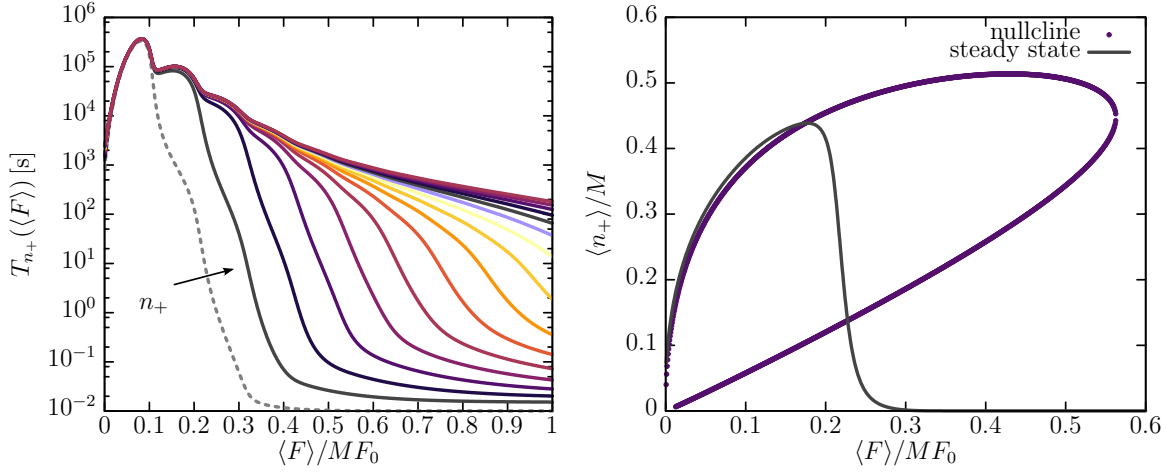
Figure 3.10: Left: Mean first passage time for microtubule ensemble under constant force from $n_+ = 1$ (left line) to $n_+ = 16$ (right line). The mean first passage time decreases for decreasing number of force exerting MTs n_+ as well as for increasing average force $\langle F \rangle$. **Right:** Numerical solution of the nullcline $\partial_t \langle n_+ \rangle = 0$ (cp. Eq. (3.20)) and analytic steady state expression (3.18). The intersection of nullcline and steady state defines a fixed point. Phase space trajectories are attracted by this fixed point.

The escape time

$$
\tau_{n_+}^{\text{esc}} = \begin{cases} \infty & n_+ = 0 \\ 1/(g_{n_+} + r_{n_+}) & 0 < n_+ < M \\ 1/r_M & n_+ = M \end{cases}
$$

is the average time spent in state n_+. During this time, the system moves forward with probability $\tau_{n_+}^{\text{esc}} g_{n_+}$, which leads to contributions from the passage time T_{n_++1}. The same applies for the backward move with probability $\tau_{n_+}^{\text{esc}} r_{n_+}$ and the passage time T_{n_+-1}. By substituting $S_{n_+} = T_{n_++1} - T_{n_+}$ we find $S_{M-1} = 1/r_M$ from (3.21). We can thus solve via the recursive relation $S_{n_+-1} = (1 + g_{n_+} S_{n_+})/r_{n_+}$ for the remaining differences

$$
S_{n_+} = \sum_{j=n_++1}^{M} \frac{\prod_{k=n_++1}^{j-1} g_k}{\prod_{k'=n_++1}^{j} r_{k'}}.
$$

Now, since $T_0 = 0$ we have $S_0 = T_1$ and thus

$$
T_{n_+}(F) = \sum_{i=1}^{n_+} \sum_{j=i}^{M} \frac{\prod_{k=i}^{j-1} g_k}{\prod_{k'=i}^{j} r_{k'}}
$$

for the mean first passage time of a collective force exertion phase under *constant* force (Fig. 3.10 left).

Monotonically increasing force: If transition rates depend on time, equation (3.16) has to be recast to describe a non-equilibrium, i.e., semi-Markovian process, since the transition matrix M becomes time-dependent. Then, the system of master equations reads

$$
\boldsymbol{p}(t) = \exp\left(\int_0^t \mathrm{d}t' \, \mathsf{M}(t') \right) \boldsymbol{p}(0). \tag{3.22}
$$
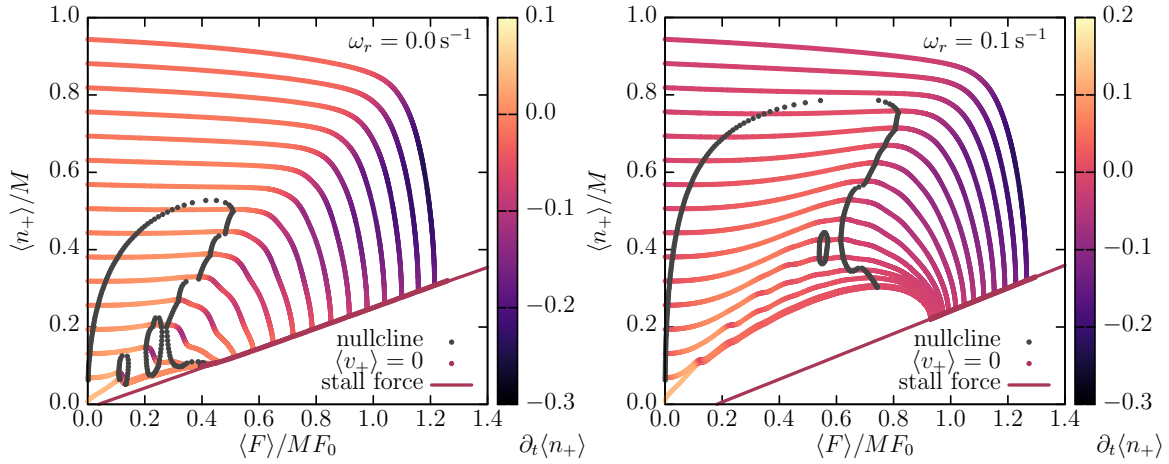
Figure 3.11: Steady state, nullclines and phase space trajectories for $\omega_r = 0.00\,\mathrm{s}^{-1}$ (left) and $\omega_r = 0.10\,\mathrm{s}^{-1}$ (right). The colored phase space trajectories were calculated with the algorithm from sec. 3.3.3 using an elastic modulus $E = 10^{-4}\,\mathrm{N/m}$, which corresponds to a stiff barrier compared to Ref. [6]. Using a soft barrier with $E = 10^{-7}\,\mathrm{N/m}$ should result in trajectories that are attracted by the upper branch of the nullcline, because, in this limit, the $\langle n_+ \rangle$-dynamics is much faster than the $\langle F \rangle$-dynamics. The nullcline $\partial_t \langle n_+ \rangle = 0$ (gray dots) is directly determined from the zeros of the phase space trajectories. Compared to Ref. [6] we find additional substructures in the phase space, which originate in fluctuations of the stochastic variable n_+, and can be interpreted as finite size effects. Within these elliptical substructures we have negative mean-field flow $\partial_t \langle n_+ \rangle$, which destabilizes the state of collective growth. The effect of fluctuations is reduced by increasing the rescue rate.

The transition matrix M depends on $\langle F \rangle$ and n_+ via the forward and backward rates. In general, $\langle F \rangle$ is time dependent and increases monotonically during the pushing phase. Distributing the force $\langle F \rangle$ equally on the number n_+ of MTs currently exerting force leads to a force $\langle F \rangle / n_+$ acting on single, pushing MTs. The time evolution of $\langle F \rangle$ can be obtained to

$$\partial_t \langle F \rangle = E \langle v_+(F/n_+) \rangle = E \sum_{n_+=1}^{M} p_{n_+} v_+(\langle F \rangle / n_+) - p_0 E d_m \omega_{\mathrm{off}} \tag{3.23}$$

where we used $\partial_t \langle x \rangle = \langle v_+(\langle F \rangle / n_+) \rangle$ and $\partial_x \langle F \rangle = E$, i.e., assumed a linear force relation $\langle F \rangle = E(\langle x \rangle - x_0)$ as in the previous section, but now in a mean-field approach averaging the force $\langle F \rangle$ over the stochastic n_+ dynamics or, in other words, calculating the expectation value $\langle F \rangle$ with respect to the probabilities $p_{n_+}(t)$. Starting from $\langle F \rangle = 0$ at $\langle x \rangle = x_0$ the force increases monotonically and approaches the stall force of the MT ensemble, which corresponds to $\langle v_+(\langle F \rangle / n_+) \rangle = 0$ and defines the nullcline of eq. (3.23). Using the approximation $\langle v_+(\langle F \rangle / n_+) \rangle \approx v_+(\langle F \rangle / \langle n_+ \rangle)$ like in Ref. [6] we find $F_{\mathrm{stall}} = \langle n_+ \rangle F_0 \ln(\omega_{\mathrm{on}} / \omega_{\mathrm{off}})$, which is a linear function in $\langle n_+ \rangle$ and lies above the nullcline given by (3.23) This is consistent with Fig. 3.11, where we numerically verify a linear relation for the time-dependent system.

3.3.3 Phase space dynamics

We derived the time evolution of the MT population, subdivided into attached and detached MTs, and the elastic force confining the MT ensemble, where we applied a mean-field approach to the latter. The occupation probability dynamics (3.22) has been derived dependent on the average force; the dynamics of the average elastic force (3.23) has been

derived dependent on the occupation probabilities. Both evolutions (3.22) and (3.23) are coupled and have to be solved together. For this purpose, we suggest the following algorithm:

1 initialize distribution $\boldsymbol{p}^k = \delta(n_+ - \langle n_+ \rangle)$ and let $\langle F \rangle^k = \epsilon$,

2 evolve occupation probability $\boldsymbol{p}^{k+1} = \exp\left(\mathsf{M}(\langle F \rangle^k)\Delta t\right)\boldsymbol{p}^k$,

3 update force $\langle F \rangle^{k+1} = \langle F \rangle^k + \Delta t E \langle v_+(\langle F \rangle^k/n_+)\rangle_{\boldsymbol{p}^k}$,

4 measure $\langle n_+ \rangle_{\boldsymbol{p}^k}$ and $\partial_t \langle n_+ \rangle_{\boldsymbol{p}^k}$,

5 let $\boldsymbol{p}^k = \boldsymbol{p}^{k+1}$, $\langle F \rangle^k = \langle F \rangle^{k+1}$, $k = k + 1$ and go to **2**.

Note that the resulting trajectories go beyond Ref. [6]. We find that each trajectory in the phase space undergoes at least one saddle node bifurcation, where $\langle v_+(\langle F \rangle/n_+)\rangle = 0$ and $\partial \langle F \rangle / \partial \langle n_+ \rangle = 0$. After crossing the first bifurcation point, trajectories oscillate closely around $\langle v_+(\langle F \rangle/n_+)\rangle = 0$ and meanwhile alternate between stable and unstable branches. Time evolutions are attracted by the fixed point given by the intersection between the line $\langle v_+(\langle F \rangle/n_+)\rangle = 0$ and the steady state $\langle n_+ \rangle_{\mathrm{eq}}(\langle F \rangle)$. Our results suggest a linear relation $F_{\mathrm{stall}} \sim \langle n_+ \rangle$ (see Fig. 3.11), where the slope can be determined from numerical calculations. In contrast to Ref. [6], where the stable limit cycle given by eq. (3.19) (Fig. 3.10 right) has been calculated, the algorithm above reveals additional elliptical substructures in the phase space (Fig. 3.11). Though we likewise find a linear relation between the stall force F_{stall} and $\langle n_+ \rangle$, our results suggest a different slope as in Ref. [6].

3.3.4 Conclusion

As we found out in this section, multiple MTs collaborating in elongating an elastic obstacle exhibit phases of collective force exertion as can be concluded from the observed stable limit cycle. Equivalently, we can conclude that MTs perform collective length oscillations. Increasing the rescue rate increases both the maximum possible number of participating MTs and the generated polymerization force, as can be seen from Fig. 3.11, from which we additionally gathered a linear relationship $F_{\mathrm{stall}} \sim \langle n_+ \rangle$. Future work should aim at systematically investigating the slope of these linear functions dependent on, for example, the rescue rate. In the following, we now finally derive the complete two-dimensional simulation model in order to verify the collective effects discovered in this section, but also the effects for single MTs found in the previous section.

3.4 Simulation model for multiple MTs within a cell cortex

Now that we have investigated the stochastic dynamics of single MTs interacting with an overdamped elastic obstacle and, in addition, multiple MTs that equally share a unique force, both in a one-dimensional geometry and by means of mean-field theories, we extend our interest to a two-dimensional model. In both the single and the ensemble mean-field theories we gained important insights regarding MT interactions: in the single MT mean-field theory we found that the attachment probability as well as the polymerization force exhibit a maximum for intermediate elastic moduli in absence of rescues. In presence of rescues we found a saturation for vanishing elastic modulus. In a multiple MT mean-field theory similar to Ref. [6] we found a stable limit cycle in the $(\langle n_+ \rangle, \langle F \rangle)$-phase-space, which clearly indicates that collective force exertion takes place when many MTs are coupled via an elastic obstacle and share its opposed force uniformly. By collective force exertion we refer to stable

growth maintained by a MT cluster. The end of such a collective growth phase is typically marked by a collective catastrophe, which is defined by a collective break-down of all MTs and has been observed experimentally by Laan et al. [151].

Our perspective in this chapter is that coupling multiple MTs with an overdamped elastic obstacle that can change its shape leads to a combination of both effects, i.e, cooperative behavior that depends on the intrinsic ability of the MT ensemble to synchronize and the shape of the elastic obstacle. We therefore refrain from mean-field approximations and take the full stochastics into account, meaning that we model each MT individually and introduce a two-dimensional circular and discretized membrane that is not restricted by symmetry. Regarding the average shapes, however, circular symmetry will be conserved at the moment, but we discuss symmetry breaking mechanisms in the next section.

In the sense of this work, we combine the description of elastic capsules with the modeling of the polymerization kinetics of microtubules. This way we introduce a very simple and well comprehensible model for a primitive eucaryotic cell, similar to two-dimensional phase field models that have been investigated earlier [214, 215]. In contrast to these models, which employ actin polymerization explicitly but neglect microtubules, we explicitly simulate microtubules and incorporate the actin polymerization forces effectively in both the membrane dynamics *and* the microtubule polymerization kinetics. Coarse graining techniques allow us to reach large timescales where synchronization and polarization phenomena can be accurately measured.

In our two-dimensional model, the cell boundary is given by a closed line. The elasticity of this one-dimensional line is derived from a two-dimensional elastic ribbon that can be seen as a virtual extension of the line into the third dimension, perpendicular to the two-dimensional simulation plane. In other words, we consider a slice (with a finite height) of a three dimensional spherical cell. This gives rise to a more realistic elasticity and allows us to use literature values for the elastic constants. Considering only a slice of a three dimensional object there is no need to employ surface area or volume constraints, since the single slice can exchange surface area or volume with the bulk it has been cut from.

3.4.1 Elastic shell

We model the closed membrane in two-dimensional space as a discretized polygonal chain with N vertices at $\boldsymbol{x}_n = r_n \boldsymbol{e}_n$, where we use polar coordinates with the distance r_n of vertex $n = 1, ..., N$ from the centrosome at $r = 0$ and with unit vectors $\boldsymbol{e}_n = (\cos \phi_n, \sin \phi_n)^T$. We distribute the vertices equidistantly in angular space at fixed angles $\phi_n = 2\pi n/N$ but variable radii $r_n \geq 0$. Vertices are connected by bonds with stretching and bending energy.

Within the closed membrane an ensemble of M MTs is growing radially starting at the centrosome at $r = 0$. We choose the number of vertices N to be a multiple of the number of MTs M and distribute MTs isotropically, i.e., we choose a *fixed* number of bonds between two MTs (usually we consider $M = 16 \ldots 64$ MTs enclosed by a membrane consisting of $N = 64 \ldots 256$ bonds). The configuration of the MT aster is described by the MT tip vectors $\boldsymbol{l}_m = l_m \boldsymbol{e}_{mq}$ ($m = 1, ..., M$ and $n = 0, \ldots N-1$), where the index $n(m) = mq$ with $q = N/M$ gives the radial growth direction of the m-th MT.

After some time MTs push radially outwards against a vertex of the membrane, which generates an opposing force. An MT couples to the membrane if it attaches to the polygonal membrane, i.e., $l_m = r_{mq}$ (by choosing N a multiple of M, the existence of a vertex at this location is guaranteed). As long as $l_m < r_{mq}$, no force is transmitted to the growing MT; as soon as $l_m = r_{mq}$ during growth, the MT keeps pushing the vertex outwards but the membrane exerts an opposing force, which decreases the growth velocity and increases the
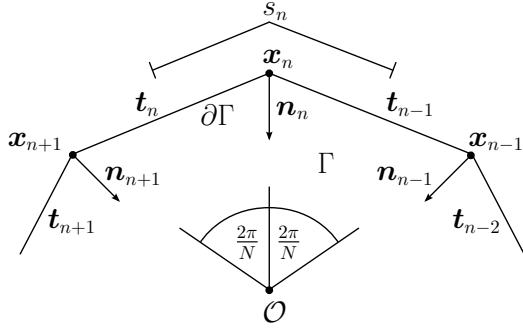
Figure 3.12: Sketch of the cell membrane explaining quantities in 3.24. Membrane vertices $\boldsymbol{x}_n$ are connected by the bond vectors $\boldsymbol{t}_n$. The inward directed normal vectors $\boldsymbol{n}_n$ are given by the difference between adjacent bond vectors. The interface is denoted by $\partial\Gamma$ and the enclosed domain by Γ. Every vertex has a corresponding arc length s_n.

catastrophe rate according to the rules defined in sec. 3.1.4. The elastic force is derived from an elastic energy functional for the membrane.

In general, soft and elastic materials have elastic energy contributions from bending energy induced by curvature and stretching energy induced by strain. The membrane enclosing the MT aster is a model for the actin cortex and the phospholipid bilayer. Note that similar systems, i.e., liposomes with actin cortices have also been realized experimentally [216, 217]. Assuming that both parts are structurally linked and their properties are additive, their elastic contributions can be treated individually. In principle, we also expect an additional tension contribution, which could be caused, for example, by motor proteins in the actin cortex [182]. This would result in a uniformly precompressed cortex and, thus, a smaller equilibrium shape. Such a contribution will be neglected here.

In our two-dimensional cell model the enclosing membrane will be treated as a one-dimensional polygonal chain, whose elasticity is obtained from the elasticity of a two-dimensional ribbon by integrating over the width d_c of the latter. Using a typical number of ~ 600 MTs in a cell of radius $R_0 = 10\,\mu\mathrm{m}$ [218], a typical distance between neighbored MTs is $d_c \sim 0.2\,\mu$m. A reasonable choice of a shape free energy is

$$\mathcal{F}[\{\boldsymbol{x}_n\}] = \frac{1}{2}\sum_{n=1}^{N} \varkappa_n s_n \left(\boldsymbol{n}_n/s_n^2 - c_0 \hat{\boldsymbol{n}}_n\right)^2 + \frac{1}{2}\sum_{n=0}^{N-1} Y_n \ell \left(|\boldsymbol{t}_n|/\ell - 1\right)^2 \tag{3.24}$$

with periodic boundary conditions $\boldsymbol{x}_0 \equiv \boldsymbol{x}_N$. However, we like to stress that the choice of (3.24) is not unique, i.e., other choices are possible and similarly reasonable, but the above energy functional allows us to obtain reliable results and, moreover, satisfies some technical requirements.

The bond vectors are given by $\boldsymbol{t}_n = \boldsymbol{x}_{n+1} - \boldsymbol{x}_n$ and the inward directed normals by $\boldsymbol{n}_n = \boldsymbol{t}_n - \boldsymbol{t}_{n-1}$, see Fig. 3.12. In static force equilibrium, bond vectors have a length $|\boldsymbol{t}_n| = \ell$ and normal vectors have a length $|\boldsymbol{n}_n| = \ell^2 c_0$, where $c_0 = 1/R_0$ is the spontaneous curvature of the cell contour. Note that both terms in (3.24) are integrated over the width d_c of the ribbon, which is assumed be constant, even if the ribbon is stretched or bent. Though not explicitly stated in (3.24), the width d_c is included in the one-dimensional bending rigidity $\varkappa$ and the one-dimensional Young modulus Y, which are related to the corresponding two-dimensional values via $\varkappa = \varkappa_{2\mathrm{D}} d_c$ and $Y = Y_{2\mathrm{D}} d_c$. We require the ribbon to have zero curvature and zero strain in z-direction, which is the direction perpendicular to the enclosed cell area Γ. We thus mapped the elasticity of the two-dimensional ribbon to the cell contour line $\partial\Gamma$ by employing effective one-dimensional elasticity constants. Details of this mapping are given below.

The first term in (3.24) is a discretized version of a Hookean bending energy

$$E_B = \frac{d_c}{2} \oint_{\partial\Gamma} \mathrm{d}s\, \varkappa_{2\mathrm{D}}(s)\, (\kappa_s - c_0)^2 \qquad (3.25)$$

of the contour $\partial\Gamma$ enclosing the two-dimensional domain Γ with a function $\varkappa_{2\mathrm{D}}(s)$ giving the local bending rigidity. The ribbon is bent only in s-direction and no bending occurs in the z-direction, i.e., $\kappa_\phi = 0$. Thus, the bending energy can be readily integrated over the width d_c of the ribbon. We include this effectively by introducing the one-dimensional bending rigidity $\varkappa = \varkappa_{2\mathrm{D}} d_c$. The curvature κ_s is measured per arc length $s_n = (1/2)(|\boldsymbol{t}_{n-1}| + |\boldsymbol{t}_n|)$ and can be approximated by a differential quotient $\kappa_s = |\partial_s^2 \boldsymbol{x}| \approx |\boldsymbol{n}_n|/s_n^2$ within the discrete model. Since bending occurs at the vertices, we have to average the arc length over adjacent bond vectors. The integral in (3.25) is transformed to a sum via

$$\oint_{\partial\Gamma} \mathrm{d}s \to \sum_n s_n.$$

Within this transformation, we refrain from a small strain approximation $s_n \approx \ell$, because this leads to shape artifacts in numerical simulations, in particular for equilibrium membranes, which are minimized in each timestep. With respect to the rest radius R_0 of the membrane we choose the spontaneous curvature $c_0 = 1/R_0$, which corresponds to a constant area difference between the two leaflets of the bilayer and, thus, inhibited lipid exchange.

The second term in (3.24) is a discretized version of a Hookean stretching energy

$$E_\mathrm{S} = \frac{d_c}{2} \oint_{\partial\Gamma} \mathrm{d}s\, Y_{2\mathrm{D}}(s)(\lambda_s - 1)^2 \qquad (3.26)$$

describing a polymeric linear elasticity, where we assumed a Poisson ratio $\nu_{2\mathrm{D}} = 0$ and thereby a constant width d_c of the ribbon, i.e., $\lambda_\phi = 0$. The function $Y_{2\mathrm{D}}(s)$ gives the local surface Young modulus dependent on the arc length. Again, we can readily integrate over the width d_c of the ribbon by introducing the one-dimensional Young modulus $Y = Y_{2\mathrm{D}} d_c$. When discretizing the above energy, the resting length ℓ of the spring enters via the strain $\lambda_s = \mathrm{d}s/\mathrm{d}s_0 \approx |\boldsymbol{t}_n|/\ell$ of the contour $\partial\Gamma$. With respect to the rest radius R_0 we choose the rest length $\ell = 2R_0 \sin(\pi/N)$, according to a regular polygon. Here, we discretize the integral along the undeformed contour by weighting directly with the resting length and thereby assume small strains, i.e.,

$$\oint_{\partial\Gamma} \mathrm{d}s \to \sum_n \ell,$$

A contribution like in (3.26) will arise from the polymer meshwork in the actin cortex. The resulting force on the vertices increases *linearly* with spring extension.

The bending and stretching energies in (3.24) vanish independently in the reference state of the membrane, which is a regular polygon with outer radius R_0. The material properties of the enclosing membrane are described by the one-dimensional Young modulus Y and the one-dimensional bending rigidity $\varkappa$, respectively the elasticity fields $Y(s) \to Y_n$ and $\varkappa(s) \to \varkappa_n$. These effective values already contain the mapping from the two-dimensional ribbon to the one-dimensional cell contour line $\partial\Gamma$.

The elastic properties of the actin cortex have been investigated in Ref. [182]: Typical values for the two-dimensional modulus of cortex elasticity are $Y_{2\mathrm{D}} \sim 0.24 \cdot 10^{-3}\,\mathrm{N/m}$ corresponding to a bulk modulus $Y_{3\mathrm{D}} \sim 2.4 \cdot 10^3\,\mathrm{N/m^2}$, assuming a typical cortex thickness of $h = 0.1\,\mu\mathrm{m}$. In live HeLa cells a cortex thickness of $h \sim 0.2\,\mu\mathrm{m}$ has been found [219]. In

experimental model systems, i.e., artificially produced liposomes with actin cortices, the cortex thickness varied between 0.05 and 0.5 μm [216, 217], and was found to depend strongly on the size of the liposome [217]. Within this work, we focus on thin cell membranes of thickness $h \sim 0.05 \, \mu$m, because these require less computational cost in numerical simulations. However, our model allows, in principle, arbitrary values for h and future studies should clarify in which way an increased cortex thickness changes the results. Based on isotropic linear elasticity we could expect a bending modulus $\varkappa_{\mathrm{2D}} \sim Y_{\mathrm{2D}} h^2 \sim 2.4 \cdot 10^{-18}$ Nm for a membrane material with thickness h. For the one-dimensional effective membrane model, this leads to estimates $Y \sim Y_{\mathrm{2D}} d_c \sim 4.8 \cdot 10^{-11}$ N and $\varkappa \sim \varkappa_{\mathrm{2D}} d_c \sim 4.8 \cdot 10^{-25}$Nm^2. In simulations we use only Young's modulus Y as a parameter and fix the bending rigidity via $\varkappa = Y h^2 / 12$ (corresponding to $\nu_{\mathrm{2D}} = 0$) with a constant cortex thickness $h \approx 0.06 \, \mu$m.

3.4.2 Liquid interface

MT asters have been confined in liquid droplets in vitro [220]. The shape of a droplet is determined by balance between surface tension and pressure. Instead of a hydrostatic pressure that has been used for the elastic capsules, we refer to an osmotic pressure here, which originates in different concentrations of freely diffusing non-solvent particles inside and outside the cell. Elastic capsules have been investigated under the influence of osmotic pressure in Ref. [62]. Note that the outer concentration is experimentally controllable, for example, via salt concentrations. Assuming that osmotically active particles behave like an ideal gas, the free energy of the liquid interface accounting for the inner and outer solutions in two-dimensional space is given by

$$\mathcal{F} = \sigma L - k_B T N_{\mathrm{in}} \ln \left(\frac{\mathrm{e}}{\lambda_B^2} \frac{A}{N_{\mathrm{in}}} \right) - k_B T N_{\mathrm{ex}} \ln \left(\frac{\mathrm{e}}{\lambda_B^2} \frac{A_{\mathrm{ex}} - A}{N_{\mathrm{ex}}} \right),$$

where λ_B is the thermal de Broglie wavelength $\lambda_B = h/\sqrt{2\pi m k_B T}$ with the Planck constant h. The numbers N_{in} and N_{ex} denote the particle numbers residing in the cell interior respectively the extracellular matrix. The area,

$$A = \iint_\Gamma \mathrm{d}A = \sum_{n=0}^{N-1} |\boldsymbol{x}_n \times \boldsymbol{x}_{n+1}|/2,$$

of Γ is enclosed by the cell contour $\partial\Gamma$ and depends on the current cell shape; the area A_{ex} is the size of the experimental container. The line tension σ acts as a Lagrange parameter concerning the length

$$L = \oint_{\partial\Gamma} \mathrm{d}s = \sum_{n=1}^{N} |\boldsymbol{t}_n|$$

of the cell contour $\partial\Gamma$. In the limit $A_{\mathrm{ex}} \gg A$ we can rewrite the above free energy as

$$\mathcal{F} = \sigma L - k_B T N_{\mathrm{in}} \ln (A) + k_B T \frac{N_{\mathrm{ex}}}{A_{\mathrm{ex}}} A + \mathrm{const},$$

where the outer concentration $N_{\mathrm{ex}}/A_{\mathrm{ex}}$ is the experimental control parameter. Using van't Hoff's law we identify the external pressure $p_{\mathrm{ex}} = k_B T N_{\mathrm{ex}}/A_{\mathrm{ex}}$ and the internal pressure $p_{\mathrm{in}} = k_B T N_{\mathrm{in}}/A$ leading to

$$\mathcal{F} = \sigma L - p_{\mathrm{in}} A \ln (A) + p_{\mathrm{ex}} A + \mathrm{const}. \tag{3.27}$$

The first contribution in (3.27) describes an energy associated with a line tension σ, which would, in an elastic membrane, arise from additional active forces generated by motor proteins or actin polymerization [182]. Here, σ arises from the fluid interface and describes a simple surface tension. The last two terms arise from the osmotic pressure, which mimics a semi-permeable membrane and allows for solvens conduction from inside to outside and vice versa.

We assume the number N_{in} of osmotically active particles residing in the cell interior to be constant, which means that these particles cannot diffuse across the membrane. Likewise, particles from the external reservoir cannot enter the cell. In the reference state, the number N_{in} shall also satisfy the Laplace-Young equation, which derives directly from (3.27) via differentiation and requiring force balance. These considerations result in

$$p_{\text{in}} = \frac{A_0}{A} \left(\frac{\sigma}{R_0} + p_{\text{ex}} \right)$$

for the internal pressure. In other words, we choose the inner pressure such that the equilibrium shape of the two-dimensional drop is a circle of radius R_0, for given external pressure p_{ex} and surface tension σ, which both serve as parameters in simulations. Inserting the above relation in the free energy (3.27) allows us to eliminate the internal pressure p_{in} leading to

$$\mathcal{F} = \sigma \left(L - \frac{A_0}{R_0} \ln A \right) + p_{\text{ex}} \left(A - A_0 \ln A \right).$$

Note that the inner pressure p_{in} is not a constant since it naturally depends on the area A, which fluctuates due to MT induced deformations of the drop interface.

In contrast to the elastic membrane, where bending and stretching forces vanish independently in the equilibrium configuration, the equilibrium liquid interface is defined by balance between contractile line tension forces and expansive pressure forces. In other words, the length of the contour $\partial\Gamma$ tends to be small, whereas the area of the domain Γ tends to be large. Both effects compete and thereby define the equilibrium configuration of the two dimensional droplet.

For a pure liquid interface we have $\sigma_{2\text{D}} \sim 10\,\text{nN}/\mu\text{m}$ [5] and, thus, $\sigma \sim \sigma_{2\text{D}} d_c \sim 2\,\text{nN}$. However, the surface tension can be decreased significantly by surfactants that adsorb to the interface. For the external pressure we could assume $p_{2\text{D}} = 5 \cdot 10^5\,\text{N/m}^2$ [182] leading to $p_{\text{ex}} \sim p_{2\text{D}} d_c \sim 0.1\,\text{N/m}$, but such a high pressure value is equivalent to a sharp area constraint. Since we consider the two-dimensional cell domain Γ as a slice of a three dimensional capsule, this is incompatible with our model. Hence, we focus on an approximation for large systems with $A_{\text{ex}} \gg A$ or, in other words, small exterior concentrations, such that $p_{\text{ex}} \ll p_{\text{in}} \ln(A)$.

3.4.3 Boundary dynamics

From the elasticity of the enclosing membrane or interface we can deduce the force onto a vertex at $\boldsymbol{x}_n$ by taking the negative gradient $-\nabla_{\boldsymbol{x}_n}\mathcal{F}$ of the free energies (3.24) and (3.27). We assume that the radial component of this force opposes growth of a MT that is attached to this vertex.

Derivating the elastic shape free energy 3.24 with respect to the vertex configuration $\boldsymbol{X} \equiv (\boldsymbol{x}_1, \ldots, \boldsymbol{x}_N)^T$ gives the force field

$$\boldsymbol{T}(\boldsymbol{X}) = -\nabla_{\boldsymbol{X}}\mathcal{F} = -\left(\frac{\partial\mathcal{F}}{\partial\boldsymbol{x}_1}, \ldots, \frac{\partial\mathcal{F}}{\partial\boldsymbol{x}_N} \right)^T = (\boldsymbol{f}_1, \boldsymbol{f}_2, \ldots, \boldsymbol{f}_N)^T.$$

The elastic force acting on the n-th membrane vertex can be readily calculated to

$$\boldsymbol{f}_n^{\text{elastic}} = \boldsymbol{f}_{n,\|}^{\varkappa_{n-1}} + \boldsymbol{f}_{n,\|}^{\varkappa_{n+1}} + \boldsymbol{f}_{n,\perp}^{\varkappa_{n-1}} + \boldsymbol{f}_{n,\perp}^{\varkappa_n} + \boldsymbol{f}_{n,\perp}^{\varkappa_{n+1}} + \boldsymbol{f}_n^{Y_{n-1}} + \boldsymbol{f}_n^{Y_n}, \qquad (3.28)$$

where we decomposed the bending force vectors in lateral and normal contributions. In addition, we ordered terms with respect to the elasticity fields $\varkappa_n$ and Y_n, which become important in the context of feedback mechanisms employing local elasticity manipulations, see sec. 3.5. The individual terms in eq. (3.28) are the normal bending forces

$$\boldsymbol{f}_{n,\perp}^{\varkappa_{n-1}} = -\frac{\varkappa_{n-1}}{2}\left[\frac{2\boldsymbol{n}_{n-1}}{s_{n-1}^3} - \frac{2c_0\hat{\boldsymbol{n}}_{n-1}}{s_{n-1}}\right],$$

$$\boldsymbol{f}_{n,\perp}^{\varkappa_n} = \frac{\varkappa_n}{2}\left[\frac{4\boldsymbol{n}_n}{s_n^3} - \frac{4c_0\hat{\boldsymbol{n}}_n}{s_n} + \left(\frac{3\boldsymbol{n}_n^2}{2s_n^4} - \frac{c_0|\boldsymbol{n}_n|}{s_n^2} - \frac{c_0^2}{2}\right)(\hat{\boldsymbol{t}}_{n-1} - \hat{\boldsymbol{t}}_n)\right],$$

$$\boldsymbol{f}_{n,\perp}^{\varkappa_{n+1}} = -\frac{\varkappa_{n+1}}{2}\left[\frac{2\boldsymbol{n}_{n+1}}{s_{n+1}^3} - \frac{2c_0\hat{\boldsymbol{n}}_{n+1}}{s_{n+1}}\right],$$

the lateral bending forces

$$\boldsymbol{f}_{n,\|}^{\varkappa_{n-1}} = \frac{\varkappa_{n-1}}{2}\left(\frac{3\boldsymbol{n}_{n-1}^2}{2s_{n-1}^4} - \frac{c_0|\boldsymbol{n}_{n-1}|}{s_{n-1}^2} - \frac{c_0^2}{2}\right)\hat{\boldsymbol{t}}_{n-1},$$

$$\boldsymbol{f}_{n,\|}^{\varkappa_{n+1}} = \frac{\varkappa_{n+1}}{2}\left(\frac{3\boldsymbol{n}_{n+1}^2}{2s_{n+1}^4} - \frac{c_0|\boldsymbol{n}_{n+1}|}{s_{n+1}^2} - \frac{c_0^2}{2}\right)(-\hat{\boldsymbol{t}}_n),$$

and the stretching forces

$$\boldsymbol{f}_n^{Y_{n-1}} = -Y_{n-1}\left(\frac{|\boldsymbol{t}_{n-1}|}{\ell} - 1\right)\hat{\boldsymbol{t}}_{n-1},$$

$$\boldsymbol{f}_n^{Y_n} = Y_n\left(\frac{|\boldsymbol{t}_n|}{\ell} - 1\right)\hat{\boldsymbol{t}}_n.$$

Note, that we have $\boldsymbol{f}_n^{\text{elastic}} \equiv \boldsymbol{f}_n(\boldsymbol{x}_{n-2}, \dots, \boldsymbol{x}_{n+2})$, i.e., the force at the n-th vertex depends on two neighbors in both directions, thus vertices are locally coupled.

From the liquid interface shape free energy (3.27) we obtain the force vectors

$$\boldsymbol{f}_n^{\text{liquid}} = \boldsymbol{f}_n^\sigma + f_n^{\Delta p} = \sigma(\hat{\boldsymbol{t}}_n - \hat{\boldsymbol{t}}_{n-1}) + (p_{\text{in}} - p_{\text{ex}})\left(\mathsf{R}_{-\pi/2}\boldsymbol{x}_{n+1} + \mathsf{R}_{\pi/2}\boldsymbol{x}_{n-1}\right)/2 \quad (3.29)$$

acting on the n-th vertex of the interface. In the above expression, R_α is a two-dimensional rotation matrix.

The force vectors $\boldsymbol{f}_n^{\text{elastic}}$ and $\boldsymbol{f}_n^{\text{liquid}}$ associated with the free energy functionals (3.24) and (3.27) vanish in the equilibrium configuration of the cell boundary, which is a regular polygon.

We state that membrane and consequently MT dynamics is driven by the force field $\boldsymbol{T}(\boldsymbol{X})$. The time evolution of the membrane is described by the $2N$-dimensional overdamped equation of motion

$$\gamma\,\partial_t\boldsymbol{X} = \boldsymbol{T}(\boldsymbol{X})\,,$$

where $\gamma = 6\pi R_h\eta$ is the Stokes friction coefficient of the membrane with the viscosity η of the surrounding medium [221] and the hydrodynamic radius R_h. We typically use $\gamma = 10^{-5}\,\text{Ns/m}$, assuming, for example, $R_h = 1\cdot10^{-7}\,\text{m}$ and $\eta = 5\,\text{Ns/m}^2$, where the

latter corresponds to a dilute polymer melt. Throughout this work, we consider the radial projection of the above equation, which is a reasonable approximation for small and radial perturbations and leads to a system of N equations,

$$\gamma \, \partial_t r_n = f_n(\boldsymbol{X}), \tag{3.30}$$

where $f_n = \boldsymbol{f_n}\boldsymbol{e_n}$ and $r_n = \boldsymbol{x_n}\boldsymbol{e_n}$; lateral forces are thereby neglected. In principle, any configuration being a regular polygonal chain is a possible equilibrium configuration according to the free energy functionals (3.24) and (3.27), but the spherical parametrization we employ (movement only in radial direction) limits the infinite number of regular polygons to only one regular polygon, whose center is the origin, i.e., $r_n = R_0 \, \forall \, n \in [1, N]$.

Let us briefly discuss the consequences of these assumptions. Suppose we have $r_n = R_0$ and $\boldsymbol{f_n} = \boldsymbol{0}$ for all n vertices. By translating the polygon in an arbitrary direction, the lengths $|\boldsymbol{t_n}|$ of the tangents $\boldsymbol{t_n}$ change, since they are defined by the intersection with the angular grid we chose. During translation, forces (induced by the parametrization) are generated that lead to a re-localization of the membrane into the state $r_n = R_0$. This is artificial and might be interpreted as a drawback of our model, since translations of the membrane relative to the centrosome (at the origin) are suppressed. Nevertheless, it is a reasonable approximation in overdamped environments and, most importantly, exhibits several advantages: The spherical parametrization trivializes the collision detection, because each MT has only one related vertex that has to be checked for collision. This implies that collisions of MTs with bonds, i.e., between vertices, are inhibited, such that there is no need to implement torques and slipping mechanisms of MTs at the membrane. In addition, overlaps of the membrane are excluded and the shape of the membrane always remains stellar with respect to the origin, since any point within the area Γ can be reached from the origin via a straight line.

3.4.4 Equilibrium boundary

In the limit of vanishing Stokes friction, $\gamma = 0$ (corresponding to $\eta \to 0$ or $R_h \to 0$), we have to minimize the energy functional (3.24) instead of solving the dynamical equations (3.30). In such a system, MT induced deformations unfold their full potential since mechanical attenuation is absent. The minimization of (3.24) can be seen as a mapping $\chi(\boldsymbol{L}) = \boldsymbol{X}$, which gives the geometry of the membrane in dependence of the current MT aster configuration. Minimization with constraints is quite demanding from a technical point of view. Transforming vertices with a monotonic function, and thereby changing to generalized coordinates $\tilde{r}_n$ and the corresponding forces $\tilde{f}_n$, allows us to use standard minimization techniques, instead of taking the constraints explicitly into account.

Coordinate transformation

We use the function $m(n) = n/q$ to find the m-th MT associated with the n-th membrane vertex and inhibit intersections of MTs and membrane by introducing the constraints $r_n \geq l_{n/q}$. These are handled by changing to generalized coordinates,

$$\tilde{r}_n = \begin{cases} \ln\left(r_n - l_{n/q}\right), & n = mq \\ \ln(r_n), & n \neq mq \end{cases}$$

obtained by transforming with the logarithm. The domain of the coordinates thereby changes from

$$r_n \in \begin{cases} [l_{n/q}, \infty), & n = mq \\ [0, \infty), & n \neq mq \end{cases}$$

to the full space of real numbers

$$\tilde{r}_n \in (-\infty, \infty) \; \forall \; n \in \{1, \dots N\}.$$

For vertices without related MT we obviously use $l_{n/q} = 0$. The radial forces acting on the transformed vertices $\tilde{\boldsymbol{x}}_n$,

$$\tilde{f}_n = f_n \frac{\partial r_n}{\partial \tilde{r}_n} = f_n e^{\tilde{r}_n},$$

are used to determine the gradient of the energy functional (3.24) in the generalized coordinate space.

Conjugated gradients

We use a modified Polak-Ribière-Polyak method, which is a conjugated gradient method [222, 223]. The mapping χ can be applied by following descent directions with respect to the shape free energy (3.24). This has to be done iteratively until the equilibrium of the membrane is reached. To obtain the sequence $\{\boldsymbol{X}_k\}$, which converges to the equilibrium configuration $\boldsymbol{X}^*$, we use the iteration scheme

$$\boldsymbol{X}_{k+1} = \boldsymbol{X}_k + \alpha_k \boldsymbol{q}_k,$$

where k is the index of the iteration and α_k the step-length, which has to be chosen such that Armijo and strong curvature conditions are fulfilled. A descent direction $\boldsymbol{q}_k$ can be obtained by

$$\boldsymbol{q}_k = \begin{cases} \boldsymbol{T}_k, & k = 0, \\ \boldsymbol{T}_k + \beta_k^{\mathrm{PRP}} \boldsymbol{q}_{k-1} - \theta_k (\boldsymbol{T}_{k-1} - \boldsymbol{T}_k), & k > 0, \end{cases}$$

where $\beta_k^{\mathrm{PRP}} = -\boldsymbol{T}_k(\boldsymbol{T}_{k-1} - \boldsymbol{T}_k)/\|\boldsymbol{T}_{k-1}\|^2$ and $\theta_k = -\boldsymbol{T}_k \boldsymbol{q}_{k-1}/\|\boldsymbol{T}_{k-1}\|^2$. During the line-search we need to find a step length α_k, which satisfies the conditions

$$\mathcal{F}(\boldsymbol{X} + \alpha_k \boldsymbol{q}_k) \leq \mathcal{F}(\boldsymbol{X}) - c_1 \alpha_k \boldsymbol{q}_k^T \boldsymbol{T}_k,$$
$$|\boldsymbol{q}_k^T \boldsymbol{T}_{k+1}| \leq c_2 |\boldsymbol{q}_k^T \boldsymbol{T}_k|,$$

where $c_1 = 10^{-4}$ and $c_2 = 0.3$ turn out to optimize convergence in our specific case. Therefore we start with $\alpha_0 = 1/\|\boldsymbol{q}_k\|$ and proceed with $\alpha_l = \alpha_0/2^l$ until the above conditions hold. The sequence $\{\boldsymbol{X}_k\}$ is assumed to be converged if $\alpha_k < \epsilon$. In equilibrium, dynamics is driven by the field $\boldsymbol{T}(\boldsymbol{X}^*)$, where $\boldsymbol{X}^*$ is a solution of

$$\mathcal{F}_0 = \min_{\boldsymbol{X}} \mathcal{F}(\boldsymbol{X}),$$

i.e., has been obtained by the iteration scheme above with respect to the given boundary conditions $\boldsymbol{L} = (\boldsymbol{l}_1, \dots, \boldsymbol{l}_M)^T$. In general, $\boldsymbol{T}(\boldsymbol{X}^*)$ is non-zero due to arbitrary boundary conditions.

The equilibrium membrane approach replicates the maximum coupling strength between MTs, because deformations propagate instantaneously along the membrane. This corresponds to the elastic capsules that have been investigated in static force equilibrium earlier in this work, with the difference that the boundary conditions are given by geometric constraints (aster configuration) here, instead of hydrostatic forces as for the elastic capsules.

3.4.5 MT coupling

We now introduce an algorithm which numerically couples the MT ensemble to the polygonal chain, which can behave either according to the energy functional (3.24) or (3.27). For the polymerization kinetics we sample single realizations from the master equation (3.1), where the catastrophe rate $\omega_c(v_+)$ and the growth velocity v_+ now both depend on the force acting on the corresponding vertex. This force can be derived for both the elastic shell and the liquid interface as it has been explained above. For an overview of the involved quantities and state transitions refer to Fig. 3.13. Samples from (3.1) are obtained by applying Euler steps for the current velocity, i.e.,

$$l_m^{k+1} = \begin{cases} l_m^k + \Delta t v_+(f_{mq}), & (+) - \text{state} \\ l_m^k - \Delta t v_-, & (-) - \text{state} \end{cases}$$

followed by a stochastic MT state shift with transition probabilities

$$p_{c,m} = \int_t^{t+\Delta t} \mathrm{d}t\, \omega_c[v_+[f_{mq}(t)]]e^{-\omega_c[v_+[f_{mq}(t)]]\,t} = 1 - e^{-\omega_c[v_+[f_{mq}(t)]]\,\Delta t}$$
$$p_{r,m} = \int_t^{t+\Delta t} \omega_r e^{-\omega_r t}\mathrm{d}t = 1 - e^{-\omega_r \Delta t}, \tag{3.31}$$

where we assume that the catastrophe rate $\omega_c[v_+[f_{mq}(t)]]$ is constant over the small time interval $[t, t + \Delta t]$. Again, we find the n-th vertex associated with the m-th MT via the function $n(m) = mq$. For a compact notation we define the outward directed tubulin net flow of the MT aster as a super position of the outward and inward directed velocity fields,

$$\boldsymbol{u} = \boldsymbol{u}_+ + \boldsymbol{u}_- \quad \text{with} \quad \boldsymbol{u}_+ = \mathsf{C}\boldsymbol{v}_+ \quad \text{and} \quad \boldsymbol{u}_- = -(\mathbb{1} - \mathsf{C})\boldsymbol{v}_-, \tag{3.32}$$

where we introduced the MT state tensor

$$\mathsf{C} = \mathrm{diag}(c_1, \ldots, c_M) \tag{3.33}$$

with $c_m = 1$ for MTs in the growing and $c_m = 0$ in the shrinking state. The vectors $\boldsymbol{v}_+$ and $\boldsymbol{v}_-$ aggregate the state dependent velocities for each MT, including their directional information, i.e., $\boldsymbol{v}_{+,m} = v_{+,m}\boldsymbol{e}_{mq}$ and $\boldsymbol{v}_{-,m} = v_-\boldsymbol{e}_{mq}$. The time evolution of the MT aster configuration can now be written as $\partial_t \boldsymbol{L} = \boldsymbol{u}(\boldsymbol{T})$, respectively

$$\partial_t l_m = c_m v_{+,m}(f_{mq}) - (1 - c_m)v_-. \tag{3.34}$$

Actually, $\boldsymbol{u}\,\mathrm{d}t$ is a stochastic displacement, which is added to the aster configuration $\boldsymbol{L}$ in each time step. In case of contact, the aster therefore perturbs the membrane configuration $\boldsymbol{X}$. Due to this perturbation the membrane generates an opposing force, which triggers global shape alteration. One can summarize the whole simulation in a few steps:

1 switch MT states (3.33) stochastically with probabilities (3.31),

2 perform timestep of MT dynamics (3.34),
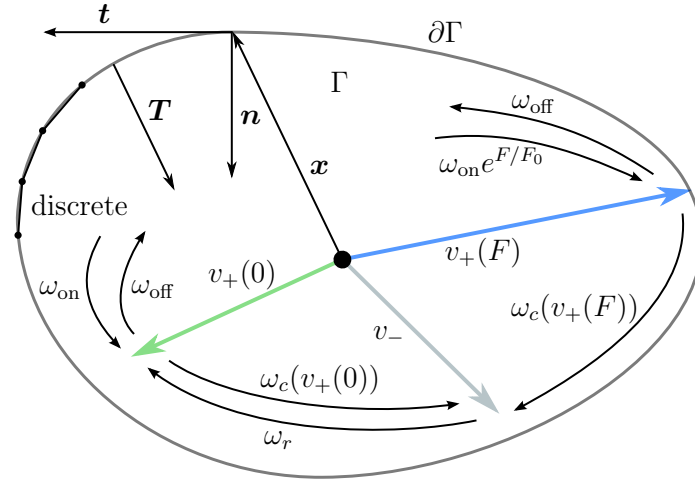
Figure 3.13: Sketch of MT dynamics in a closed elastic compartment. Green color indicates force-free MT growth, blue color indicates force-dependent MT growth, gray color indicates shrinking MTs. Note that we use a discretized cell boundary within numerical simulations. MTs that exert force onto the cell boundary induce shape change and, thus, restoring stresses that, in turn, affect the polymerization velocity. This generates a coupling leading ultimately to collective behavior.

3 perform timestep of shape dynamics (3.30),

4 derive force field (3.28) or (3.29) from membrane geometry,

5 update velocity field (3.32).

This algorithm allows us to explore both, the parameter space of the MT ensemble and the cell membrane. In contrast to the mean-field approaches that we investigated earlier in this work, the simulation model is totally stochastic and brings up macroscopic observables like asphericity and synchronicity.

3.4.6 Observables

In the following, we introduce observables allowing us to discuss results obtained with the above calculation scheme. We denote the time average of a quantity X by $\langle X \rangle$ whereas $X(t)$ usually refers to a quantity that has been calculated from the set of MT tip-vectors $\{l_m\}$ or the set of membrane vertices $\{x_n\}$. The times characterizing the MT oscillation cycle, which have been introduced in sec. 3.2, are measured via

$$\langle \tau \rangle = \frac{1}{M} \sum_{\mu=1}^{M} \frac{1}{N_\mu} \sum_{\nu=1}^{N_\mu} \tau_{\mu,\nu}$$

where we assume N_μ measurements of the time τ for the μ-th MT, where $\mu \in \{1, \ldots, M\}$. The average times $\langle \tau \rangle$ describe the oscillation cycle of individual MTs in a mean-field fashion and, thereby, allow the direct determination of the probabilities p_{att} and p_{det}. These can be generalized for multiple MTs by multiplying with M yielding the occupation of the cell boundary and interior, i.e.,

$$\langle n_+ \rangle = M p_{\text{att}} \quad \text{and} \quad \langle n_- \rangle = M p_{\text{det}},$$

which coincides with

$$\langle n_+ \rangle = \frac{1}{N_{\text{mes}}} \sum_{\nu=1}^{N_{\text{mes}}} \sum_{\mu=1}^{M} c_{\mu,\nu} \Theta(l_{\mu,\nu} - r_{\mu q,\nu} + d_m),$$

$$\langle n_- \rangle = \frac{1}{N_{\text{mes}}} \sum_{\nu=1}^{N_{\text{mes}}} \sum_{\mu=1}^{M} \Theta(r_{\mu q,\nu} - d_m - l_{\mu,\nu}).$$

Here, we use the effective monomer length d_m as a numerical threshold and average over N_{mes} measurements. The ensemble polymerization force grows linearly with the MT number for small ensembles and logarithmically for larger ensembles [6]. As we have shown in section 3.3, $\langle n_+ \rangle$ and $\langle F \rangle$ exhibit a stable limit cycle, meaning that consistent phases of collective growth exist. This complex phase space dynamics, which has been described up to here only in a mean-field approach, can also be measured from the full stochastic model. We measure the polymerization force using the definitions

$$\langle f \rangle = \frac{1}{N_{\text{mes}}} \sum_{\nu=1}^{N_{\text{mes}}} \frac{1}{M} \sum_{\mu=1}^{M} c_{\mu,\nu} \Theta(l_{\mu,\nu} - r_{\mu q,\nu} + d_m) f_{\mu q,\nu} \quad \text{and} \quad \langle F \rangle = M \langle f \rangle.$$

Note that only growing MTs contacting the membrane contribute to the exerted polymerization force. The polymerization force can be directly determined from the membrane forces, because only MTs deform the membrane, which is force-free without the MT ensemble. In addition, forces exerted by MTs are exclusively transmitted to the membrane. Back-propagation of forces through the MT lattice, i.e., force transmission to the centrosome, is inhibited by fixing the centrosome in the origin and negligence of buckling. We thereby implicitly assume that the centrosome exerts a counter-force $-\boldsymbol{f}_n$ to the force $\boldsymbol{f}_n$ that is exerted by the membrane, according to Newton's third law.

Though we do not cover the dynamics of the centrosome, it can nevertheless align *relatively* due to membrane deformations. Aster positioning inside the cell is highly important from the biological point of view. During mitosis, localization of the spindle poles is important to mechanically stabilize the spindle. In other situations a more flexible centrosome might be required, e.g., in a movement cycle or as a response to a deformation triggered by external forces. To measure how strong the centrosome is localized, i.e., its flexibility, we define the centroid of the membrane via

$$\boldsymbol{R}_C = \frac{1}{N} \sum_{\nu=1}^{N} \boldsymbol{x}_\nu.$$

Note that the time average of $\boldsymbol{R}_C$ vanishes,

$$\langle \boldsymbol{R}_C \rangle = \frac{1}{N_{\text{mes}}} \sum_{\nu=1}^{N_{\text{mes}}} \boldsymbol{R}_{C,\nu} = \boldsymbol{0}, \tag{3.35}$$

due to stochastic and isotropic forces applied by the MT ensemble. Since we placed the centrosome in the origin, the centrosome is perfectly centered if $\boldsymbol{R}_C = \boldsymbol{0}$. A measure for the flexibility of the centrosome can now be obtained via

$$\langle |\boldsymbol{R}_C| \rangle = \frac{1}{N_{\text{mes}}} \sum_{\nu=1}^{N_{\text{mes}}} \left| \frac{1}{N} \sum_{\mu=1}^{N} \boldsymbol{x}_{\mu,\nu} \right|, \tag{3.36}$$

which gives the average distance of the centroid to the origin. In a rigid confinement we have $|\boldsymbol{R}_C|/R_0 \leq 1$, whereas a flexible confinement allows $|\boldsymbol{R}_C|/R_0 > 1$. Due to the fact that the chosen parametrization limits the possible equilibrium shapes to only one single circle with its center at the origin, we expect $\langle|\boldsymbol{R}_C|\rangle/R_0 \approx 0$ in a stiff confinement. The linear centroid (3.35) can be used as a measure for asymmetry, but only for single samples and not as a time average, due to its isotropy. For a single configuration the centroid gives the magnitude and the direction of the polarization. The quadratic centroid (3.36), however, is a measure of asphericity that gives the centrosome elongation averaged over time, which comes at the cost of unavailable directional information.

In addition to the centroid, we measure some other aspects of the geometry characterizing the shape and size of the cell. The most simple measure of the cell size is the average distance between vertices and origin,

$$\langle R \rangle = \frac{1}{N_{\text{mes}}} \sum_{\nu=1}^{N_{\text{mes}}} \frac{1}{N} \sum_{\mu=1}^{N} r_{\mu,\nu},$$

which we call the average radius. Though this is a reasonable measure for the size of the cell, it cannot account for asymmetry, in contrast to the centroid.

A common measure of asphericity [224, 225], which has been used e.g. for polymer rings, can be defined via the radius of gyration tensor

$$\mathsf{Q}_{kl} = \frac{1}{2N^2} \sum_{i=1}^{N} \sum_{j=1}^{N} (\boldsymbol{x}_k^{(i)} - \boldsymbol{x}_k^{(j)})(\boldsymbol{x}_l^{(i)} - \boldsymbol{x}_l^{(j)}) \,.$$

With $\hat{\mathsf{Q}}_{kl} = \mathsf{Q}_{kl} - \delta_{kl}\mathsf{Tr}(\mathsf{Q})/2$ the time average of the asphericity in two dimensions is given by

$$\langle \Delta \rangle = \frac{1}{N_{\text{mes}}} \sum_{\nu=1}^{N_{\text{mes}}} \frac{2\mathsf{Tr}\,\hat{\mathsf{Q}}_\nu^2}{(\mathsf{Tr}\,\mathsf{Q}_\nu)^2}$$

and varies between zero and one, where zero belongs to a two-dimensional symmetric shape and one describes a one-dimensional object. The asphericity Δ measures symmetry with respect to the centroid: two points that lie on a straight line segment crossing the centroid contribute the quadratic difference of their distances to the centroid. We see that not only circular shapes have zero asphericity, but any shape where opposing vertices have the same distance to the centroid. Together, the centroid elongation $|\boldsymbol{R}_C|$ and the asphericity Δ completely describe the asymmetry of the cell contour $\partial\Gamma$.

3.4.7 Macroscopic elasticity

In sec. 3.2 we investigated a one-dimensional model with a single MT growing against a spring described by an overdamped equation of motion. To relate the parameters of this one-dimensional model to the full two-dimensional model we identify the linear effective elastic modulus of the membrane by rewriting the free energy 3.24 for circular symmetric membranes with radius $R \equiv \langle R \rangle$ in the limit of a large number of vertices, i.e., $2\pi/N \ll 1$. We find the shape free energy

$$\mathcal{F}(R) = \varkappa\pi R(1/R - 1/R_0)^2 + Y\pi R_0(R/R_0 - 1)^2 + \text{const} \tag{3.37}$$

as a function of the radius. By neglecting the asphericity of the shape, the two-dimensional model, where MTs grow radially outwards, becomes equivalent to a one-dimensional model,

where MTs grow in a potential described by the free energy (3.37). This corresponds to a MT bundle growing against an elastic obstacle as, for example, in an optical trap, which can be realized experimentally [151]. Corresponding to the free energy potential (3.37), the force needed to stretch the membrane is given by

$$F(R) = -\partial_R \mathcal{F}(R) = \varkappa \pi (1/R^2 - 1/R_0^2) - 2\pi Y (R/R_0 - 1).$$

Expanding in leading order at $R = R_0$,

$$F(R) = F(R_0) + E(R - R_0) + \mathcal{O}((R - R_0)^2),$$

where $F(R_0) = 0$ as it is evident from (3.37), results in a linear effective elastic modulus

$$E = 2Y \left(\frac{\pi h^2}{12 R_0^3} + \frac{1}{R_0} \right)$$

of the membrane. To obtain this expression, we used the relation $\varkappa = Y h^2/12$ as already introduced above. Hence, for small deformations, results of the two-dimensional full stochastic model should be comparable to the one-dimensional mean-field approximation in sec. 3.2. Note that, in principle, results from the mean-field theory for single MTs can only be transferred to the full stochastic model or serve as an approximation, if MTs are effectively uncoupled. Introducing an effective elastic modulus E enables us to easily compare between the two-dimensional cell model and the one-dimensional model introduced earlier in sec. 3.2.

In numerical simulations, it is only possible for an MT to deform the cortex if a critical effective elastic modulus is not exceeded. This modulus is given by

$$E_{\text{max}} = \frac{F_0 \ln \omega_{\text{on}}/\omega_{\text{off}}}{v_+(0)\Delta t}.$$

In case of $E > E_{\text{max}}$, a single MT length update would exceed the MT stall force. Values that are typically used within this work lead to $E_{\text{max}} \approx 40 \, \text{mN/m}$. As we have seen, approximating the full two-dimensional (3.24) model by a circular symmetric membrane (3.37) gives a rather similar system to the one-dimensional model 3.2 that has been investigated earlier in this work. We therefore expect both systems to behave qualitatively similar, in particular for small deformations and effectively uncoupled MTs.

3.4.8 Discussion

In order to smoothly segue into the discussion of results obtained with the simulation scheme introduced in this section, we at first revisit observables that already have been discussed in the one-dimensional model in chapter 3.2 and can be simply transferred to the two-dimensional model by averaging over the individual MTs participating in the MT ensemble. In particular, we discuss the probability p_{att} of being attached and in a growing state at the same time. This probability is of central importance due its positive correlation with a couple of observables, such as the average number $\langle n_+ \rangle$ of MTs that exert force onto the membrane, and the polymerization force $\langle f \rangle$ exerted by the MT ensemble. We thereby again differentiate between bounded growth, i.e., absence of rescues with $\omega_r = 0.0 \, \text{s}^{-1}$, and unbounded growth, i.e., presence of rescues with $\omega_r = 0.1 \, \text{s}^{-1}$. Both cases are physiologically relevant, because the rescue rate can be tuned via MAPs like, for example, the Tau protein. In the following, we discuss Fig. 3.14, which shows measurements for both regimes.

Attachment probability in absence of rescues: The maximum seen in Fig. 3.14 left can be understood from the limit cases $E \to 0$ and $E \to \infty$. The argumentation is analogous to the one we employed in the one-dimensional model, though the two-dimensional model of course differs by shape fluctuations leading to a slightly blurred effect. Note that, due to the remarks in 3.4.7, E is interchangeable with Y in the following discussion.

In case of $E \to \infty$, the membrane is actually a rigid and perfectly circular confinement, where MTs stall immediately when reaching the membrane, hence undergo a catastrophe rapidly. The attachment probability is thereby determined by the short stall time and the relatively long time that MTs spend detached, either shrinking or growing force-free. Precisely speaking, the attachment probability becomes equal to the probability Q_+ from eq. (3.5) that has been obtained for one-dimensional rigid containers in sec. 3.1.2. Since the Flyvbjerg catastrophe rate does not diverge but saturate for $F \to \infty$, the stall time and, thus, also the attachment probability p_{att} remains, in principle, finite in the limit $E \to \infty$. However, in numerical simulations, the limit case $E \to \infty$ is actually reached earlier at $E = E_{\max}$, according to the remarks in 3.4.7. Thus, p_{att} effectively nearly vanishes depending on the size of the container, which sets the re-arrival time of MTs assuming constant velocities of shrinking and force-free growth.

In case of $E \to 0$, MTs push the membrane far away from the MTOC, because their growth velocity is unaffected by weak forces $F \ll F_0$ exerted by the membrane, such that $v_+(f) \approx v_+(0)$. Being that far away, the membrane does not return to its starting point due to a diverging relaxation time $\tau_0 = \gamma/E \to \infty$. Rarely, fluctuations produce very long MTs pushing the membrane even further. Remember that MT growth is bounded here, meaning that MTs are in a steady state preferring a finite average length. Taken together, these effects lead, as for the limit case $E \to \infty$, to a vanishing attachment probability p_{att}.

Since we found arguments for vanishing attachment probabilities in both limit cases $E \to 0$ and $E \to \infty$, we rationalize a maximum in between, which is verified numerically in Fig. 3.14.

Attachment probability in presence of rescues: The saturation seen in Fig. 3.14 right can likewise be understood from the limit cases $E \to 0$ and $E \to \infty$, where we in parts readopt the above argumentation.

In case of $E \to \infty$, we have the same situation as in absence of rescues, i.e., short stall times at the membrane and relatively longer re-arrival times, with the difference that the latter can now be directly tuned respectively shortened by increasing the rescue rate. Nevertheless, this eventually leads to the same limit behavior of vanishing attachment probabilities, though shifted to higher values of the elastic modulus.

In case of $E \to 0$, we observe a monotonically increasing attachment probability p_{att} that saturates because it is naturally limited, i.e., $p_{\text{att}} \leq 1$. Again, we have $\tau_0 \to \infty$ and the membrane stays where it has been placed by the MT tip, but, in contrast to the bounded case with $\lambda < 0$, MTs are now capable to follow up the membrane continuously. Eventually, MTs and membrane assemble to a state with $v_+(f)\omega_r = v_-\omega_c(v_+(f))$, i.e., the average length loss equals the average length gain. However, due to forces $f \sim F_0$ phases of force exertion take a long time compared to phases of shrinking and free growth, leading to a plateau in the attachment probabilities for small elastic moduli.

Correlated observables: As stated above, the attachment probability p_{att} is equivalent to the average number $\langle n_+ \rangle$ of MTs that exert force, and positively correlated to the average individual polymerization force $\langle f \rangle$, because MTs can only exert force onto the membrane when they are attached to it. Therefore, both observables $\langle n_+ \rangle$ and $\langle f \rangle$ show the same
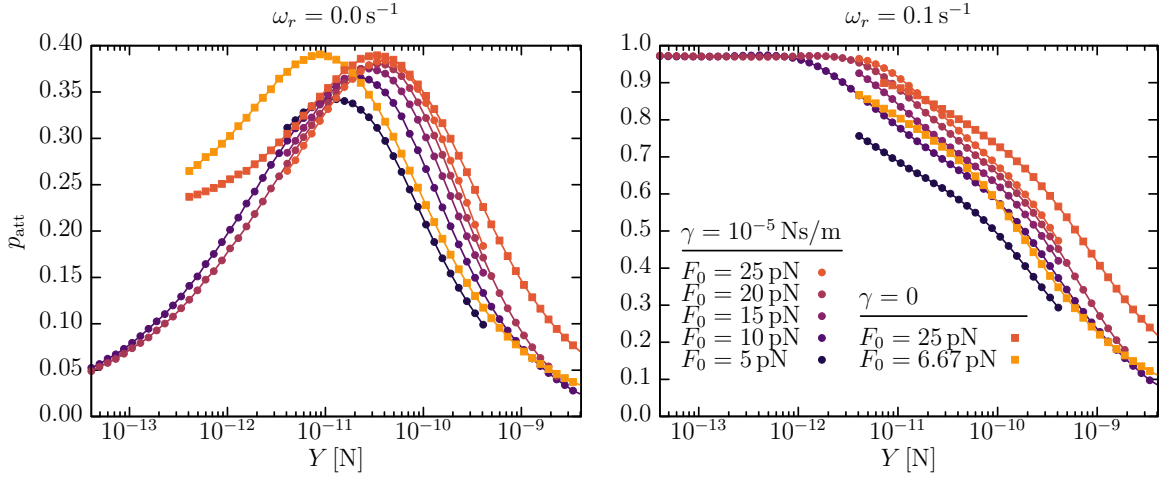
Figure 3.14: Probability p_{att} of being attached to an elastic shell for an individual MT in the coupled system dependent on Young's modulus Y. Measurements were obtained with $M = 16$ MTs and $N = 256$ membrane vertices. Colors indicate different characteristic forces from $F_0 = 5\,\mathrm{pN}$ (dark blue) to $F_0 = 25\,\mathrm{pN}$ (orange) accounting for additional force generation generated by actin polymerization. In the left plot, where $\omega_r = 0.0\,\mathrm{s}^{-1}$, the probability p_{att} undergoes a maximum in the regime of intermediate membrane stiffness $Y \sim 10^{-11}\,\mathrm{N}$. In the right plot, where $\omega_r = 0.1\,\mathrm{s}^{-1}$, the probability p_{att} monotonically increases with decreasing stiffness of the membrane and saturates in the limit $Y \to 0$. This behavior is analogous, i.e., qualitatively similar, to the one dimensional system analyzed in section 3.2. For an overdamped membrane (circles), additional actin force generation has two effects: On the one hand, it increases attachment probabilities and, on the other hand, it leads to an effective softening of the membrane. For the equilibrium membrane (quads), we observe only the latter effect.

qualitative behavior as the attachment probability p_{att}, which is why we refrain from showing the corresponding data here.

Additional force generation by actin: In our measurements, we vary the characteristic force F_0, which sets the force-scale in the velocity profile $v_+(f)$, to account for additional forces generated by actin polymerization. We thereby implicitly assume that actin polymerization triggered by an MT gives an additional constant and positive force contribution to the characteristic force, which increases the attachment probability, the number of MTs that exert force, and the individual polymerization forces. In addition, we observe a shift of the curves to higher elastic moduli, which can be interpreted as an effective softening of the membrane. Regarding the equilibrium membrane, we observe only this softening effect but no pronounced increase of the attachment probability and the related quantities. Hence, this amplification is clearly related to a finite friction constant.

Synchronicity

In contrast to the one-dimensional models from sections 3.2 and 3.3, the two-dimensional model exhibits several extra features. Multiple MTs that grow isotropically in two-dimensional space and fluctuate in their lengths are coupled via an elastic shell. Length fluctuations of the MT ensemble resulting from stochastic filament assembly are transferred to the shell and return as elastic forces opposing MT growth. The result is a stochastically driven $\mathcal{N}$-particle system with the potential ability to exhibit collective phenomena. What we have primarily in mind here are collective MT length fluctuations, i.e., a pulsating cell where
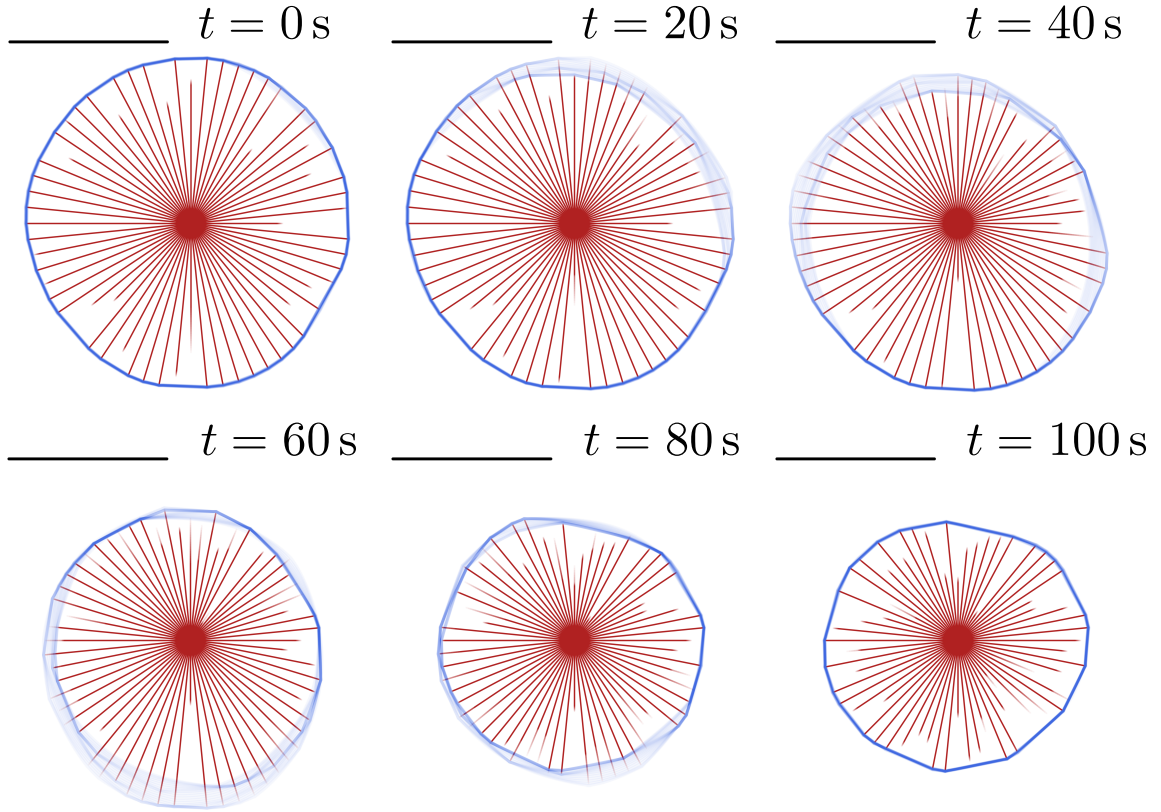
Figure 3.15: Simulation snapshots of an elastic shell in the synchronous regime with $M = 64$ MTs and $N = 256$ shell vertices. Each snapshot is averaged over 20 seconds to indicate motion of membrane and MTs. The scale bar has a length of $20\,\mu$m. Clearly, the collective catastrophe begins at the upper right and propagates along the cell boundary until it arrives at the lower left. The collective catastrophe takes less than $100\,$s, which is *short* compared to typical phases of force exertion.

spherical symmetry is conserved. Such a system could be recognized by synchronous MTs that concurrently switch their states at the same length.

In order to measure synchronicity we need a distinct definition. Synchronous systems can be recognized by the occurrence of collective catastrophe events, as it has been shown by Laan et al. [151] for the first time. During a collective catastrophe a group of MTs collapses simultaneously and the number of pushing MTs rapidly decreases from its current value to zero, see Fig. 3.15. Depending on the degree of synchronicity, collective catastrophes may occur in regular intervals, in spates, or randomly. Even asynchronous systems exhibit collective catastrophe events, but only as a rare product of randomness and not as a consequence of velocity coupling.

We now introduce a statistical measure of synchronicity and investigate its behavior dependent on Young's modulus Y. We detect collective catastrophe events using the DBSCAN cluster algorithm [226]. DBSCAN is a density based cluster algorithm and identifies groups of events, which exceed a minimum size and a critical density. Once identified, the algorithm expands the cluster as long as at least one unvisited point in the cluster satisfies the cluster condition. Two parameters are needed to deploy the algorithm to a series $\mathcal{S} = \{t_k \,|\, k = 1, \dots, N_e\}$ of timestamps marking single catastrophe events: (i) the number of events m_c each cluster must at least contain and (ii) the neighborhood radius r_c which is queried for potential new cluster points. We choose $m_c = M$ as the minimum
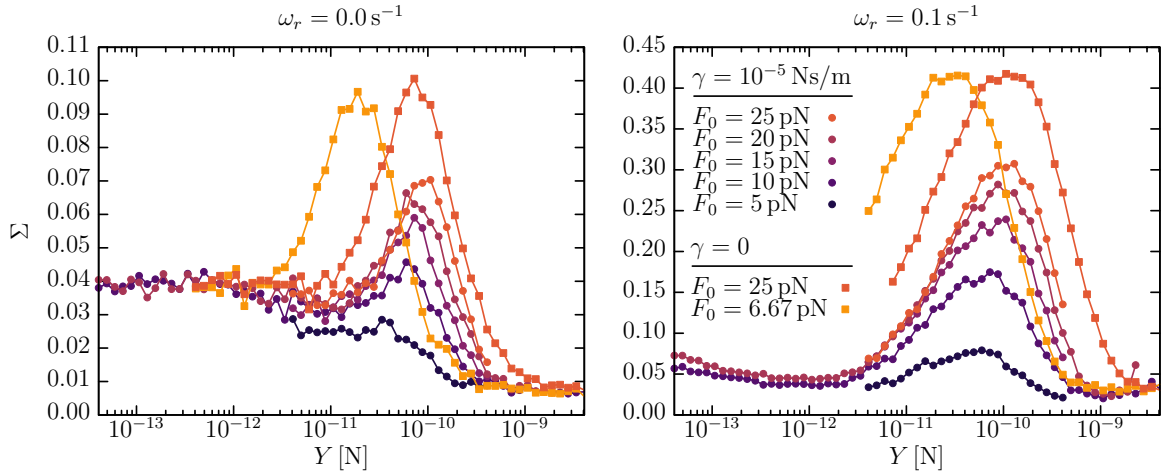
Figure 3.16: The synchronicity Σ (defined by the probability of drawing a collective event) for MTs confined within an elastic shell dependent on Young's modulus Y in absence of rescues (left) and in presence of rescues (right). Measurements were obtained with $M = 16$ MTs and $N = 256$ membrane vertices. Both measurements reveal a maximum for intermediate Young moduli $Y \sim 10^{10}\,\mathrm{N}$, but the system including rescues (right) is about four-fold more synchronous. In vivo, collective length fluctuations could be triggered, for example, by interaction with the tau protein or other MAPs that modulate the MT rescue rate. Note that, in both measurements, we observe underground fluctuations ranging in amplitude up to $\Sigma \sim 0.05$. These are random collective events that do *not* occur as a consequence of velocity coupling.

number of MTs in the aster participating in a collective catastrophe. The neighborhood radius r_c is chosen with respect to the average event density

$$\rho = \frac{1}{N_e - 1} \sum_{k=1}^{N_e - 1} (t_{k+1} - t_k)$$

with a total number of N_e events. We choose $r_c = m_c \rho/4$, which requires the cluster density to be twice as large as the average density ρ, i.e., we claim a critical density $\rho_c = 2\rho$. Events that are not related to a specific cluster are marked as noise. Performing the DBSCAN cluster algorithm results in a number N_n of noise events and $N_e - N_n$ synchronous events. Thus, for a given partitioning, we obtain the probability

$$\Sigma = \frac{N_e - N_n}{N_e} = 1 - \frac{N_n}{N_e}$$

of drawing a single event, which belongs to a collective event, i.e., is part of a cluster.

As can be seen from Fig. 3.16, synchronization occurs in both absence and presence of rescues at intermediate elastic moduli E, though clearly more pronounced in presence of rescues. In both cases, additional force generation via actin polymerization amplifies the effect. Again, we try to understand this behavior by investigating the limit cases $E \to 0$ and $E \to \infty$.

In case of $E \to \infty$, it is directly clear that MTs decouple or desynchronize due to very short interaction times in such a rigid confinement.

In case of $E \to 0$, the situation actually corresponds to absence of the membrane, i.e., again decoupled and asynchronous MTs.

Increasing rescue rates leads to a more localized MT length distribution in an elastic confinement, as it has been shown in Ref. [204], i.e., increasing rescue rates decreases length
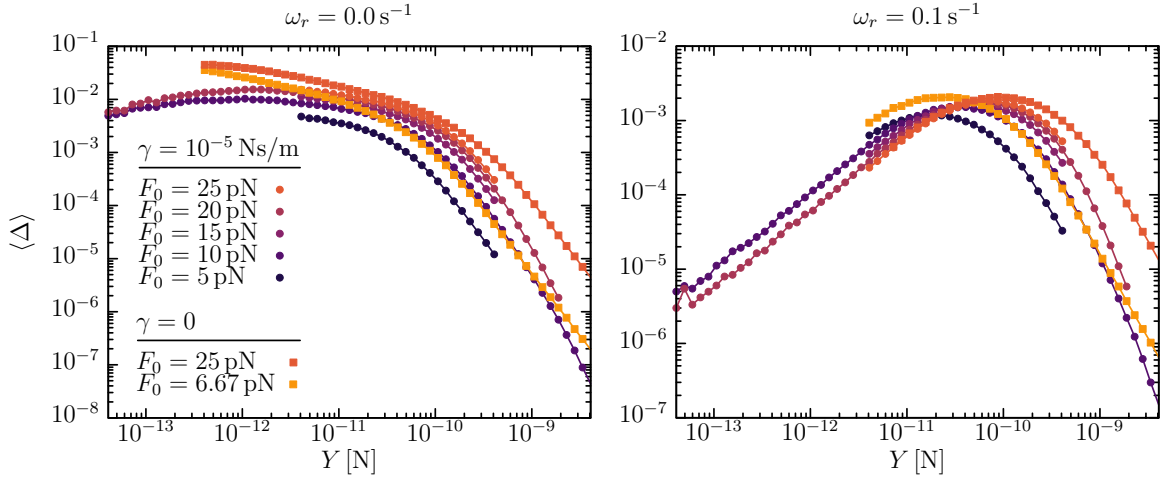
Figure 3.17: Asphericity measurement for MTs confined within an elastic shell dependent on Young's modulus Y in absence of rescues (left) and in presence of rescues (right). Measurements were obtained with $M = 16$ MTs and $N = 256$ membrane vertices. Note that, particularly in presence of rescues, the maximum of the asphericity coincides with the maximum of the synchronicity. **Left:** The asphericity Δ seems to decrease monotonically with increasing Young's modulus. However, two measurements for characteristic forces $F_0 = 10\,\mathrm{pN}$ and $F_0 = 20\,\mathrm{pN}$ reach very small Young's moduli $Y \sim 10^{-13}\,\mathrm{N}$ and thereby indicate a broad maximum in the asphericity Δ. This maximum can be rationalized by theoretical considerations, see sec. 3.1.3. **Right:** The asphericity Δ exhibits a sharp maximum, which becomes more pronounced for increasing characteristic force F_0. For small values of Young's modulus Y, the asphericity Δ increases linearly with Young's modulus Y.

fluctuations. Since synchronization is a counter-effect to fluctuations as it requires symmetric shapes, it is reasonable that increasing rescue rates increases the effect of synchronization. In this context, we like to note that, particularly in presence of rescues, the maximum of the asphericity coincides with the maximum of the synchronicity.

Asphericity

The asphericity (see Fig. 3.17) exhibits a broad maximum in absence of rescues and a sharp maximum in presence of rescues. **In case of $E \to \infty$**, both systems show the same limit behavior, which is a vanishing asphericity due to an undeformable and, thus, circular cortex. In case of $E \to 0$ we have to investigate both systems (absence and presence of rescues) separately.

Asphericity in absence of rescues for $E \to 0$: This case corresponds to absence of a membrane and MTs push the membrane far away from the MTOC. Due to $\tau_0 \to \infty$ the membrane does not relax. In addition, deformations are local and do not spread over the membrane, which manifests in tiny tubes that are formed by MTs. The resulting star-like shapes of the membrane are predominantly determined by the turning points, where MTs undergo a catastrophe, i.e., switch to a shrinking state. Due to uncoupled MTs as $E \to 0$, we assume that the asphericity of the shape is positively correlated to the relative standard deviation of these turning points, which decreases to zero for $t \to \infty$, see eq. (3.6) in sec. 3.1.3. The asphericity should similarly vanish in the limit $E \to 0$ and, indeed, we observe a broad maximum for some of the curves in Fig. 3.17 left. Within the analysis in sec. 3.1.3, we particularly found that the average maximum turning lengths evolve logarithmically in time and, thus, diverge for $t \to \infty$. This results in an infinite equilibration time in the limit
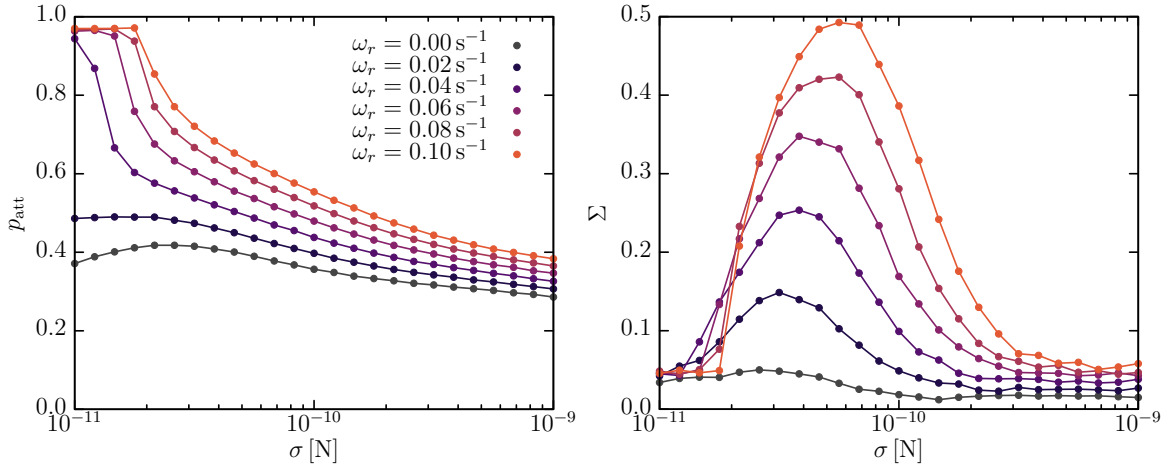
Figure 3.18: Attachment probability and synchronicity for an MT aster confined within a liquid droplet. Measurements were obtained for $M = 16$ MTs and $N = 64$ interface vertices. Observables are shown dependent on the surface tension σ for negligible external pressure $p_{\mathrm{ex}} = 10^{-8}\,\mathrm{N/m}$, i.e., in the approximation of a large simulation box $A_{\mathrm{ex}} \gg A$. Both the attachment probability and the synchronicity show qualitatively the same behavior as for the elastic shell, i.e., the attachment probability p_{att} undergoes a maximum in absence of rescues and saturates for decreasing surface tension in presence of rescues. The synchronicity Σ exhibits a pronounced maximum in presence of rescues.

$E \to 0$, which makes it difficult to obtain reliable simulation results for very small values of E. However, we conclude from theoretical considerations that the asphericity Δ vanishes in the limit $E \to 0$ and thereby rationalize the broad maximum observed in Fig. 3.17 left.

Asphericity in presence of rescues for $E \to 0$: Again we have to analyze the evolution of the MT turning points to obtain the asphericity in the limit $E \to 0$, while considering that MT growth is unbounded here. As we have shown in sec. 3.1.3, the relative standard deviation of the MT turning lengths vanishes for $t \to \infty$ in absence of a barrier, see (3.7). Again we conclude, now for unbounded MT growth in presence of rescues, that the asphericity Δ has to vanish in the limit $E \to 0$ and thereby rationalize the maximum observed in Fig. 3.17 right. We like to stress that this maximum is strongly localized compared to the broad maximum observed in absence of rescues. This is due to reduced MT length fluctuations induced by a finite rescue rate.

Droplet

In addition to the elastic energy functional (3.24) we also introduced the functional (3.27) describing liquid droplets subjected to line tension and osmotic pressure. Performing the same kind of simulations using the liquid droplet instead of the elastic shell functional we obtain the results presented in Fig. 3.18 and 3.19. Results are obtained in the approximation of a large simulation box with $A_{\mathrm{ex}} \gg A$. In addition, we fixed the characteristic force at its typical value $F_0 \sim 6.6\,\mathrm{pN}$ due to absence of a actin cortex.

We observe qualitatively the same features as for elastic shells: the attachment probability exhibits a maximum in absence of rescues and saturates for vanishing surface tension in presence of rescues. The synchronicity exhibits a pronounced maximum in presence of rescues. All these effects are reasonable using the same argumentation as for elastic shells. In contrast to the elastic shell, we observe a strong centrosome elongation even for nearly circular shapes that occur for high interfacial surface tensions $\sigma \sim 10^{-9}\,\mathrm{N}$. The functional (3.27) seems to
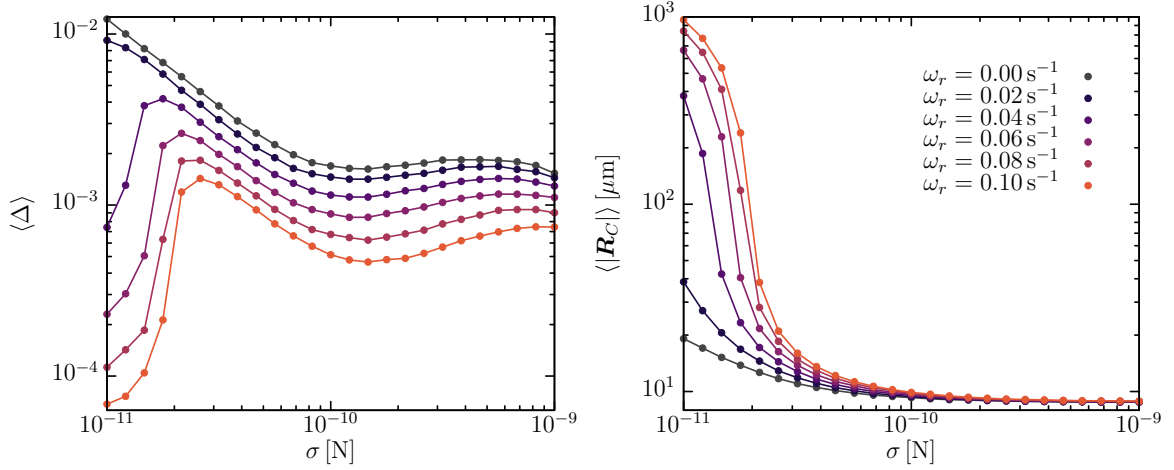
Figure 3.19: Asphericity and absolute value of the centroid for an MT aster confined within a liquid droplet. Measurements were obtained with $M = 16$ MTs and $N = 64$ interface vertices. Both observables are shown dependent on the surface tension σ for negligible external pressure $p_{\text{ex}} = 10^{-8}\,\text{N/m}$, i.e., in the approximation of a large simulation box $A_{\text{ex}} \gg A$. The asphericity Δ exhibits a maximum in presence of rescues. Compared to the elastic shell, we do not see a vanishing asphericity Δ in the limit $\sigma \to \infty$. Actually, shapes for $\sigma \approx 10^{-9}\,\text{N}$ are perfectly circular, but the asphericity gives non-zero values, because vertices on the shifted circle are not distributed equidistantly due to the angular grid. The absolute value of the centroid increases monotonically for decreasing surface tension. It is, however, important to note that the centrosome is strongly elongated even for $\sigma \sim 10^{-9}\,\text{N}$, where the membrane is nearly circular, which is due to the fact that the energy functional (3.27) seems to be less sensitive to translations of the cell boundary than the energy functional (3.24) for elastic shells.

be less sensitive to translations of the cell contour, which eventually supports pronounced aster positioning. Centrosome elongation paired with strongly circular shapes also leads to over-estimated asphericity values, because vertices are not distributed equidistantly along the cell boundary due to the angular grid we chose. In principle, the asphericity should vanish in the limit $\sigma \to \infty$, similar to the elastic shell, where the asphericity vanishes in the limit $E \to \infty$.

Equilibrium cell boundaries

As an important limit case of membrane dynamics regarding the friction constant we investigate equilibrium cell membranes with $\gamma = 0$, i.e., instantaneous relaxation according to $\tau_0 = 0$. This limit case is realized by minimizing the shape in each time step with respect to the boundary conditions given by the MT ensemble, instead of performing the overdamped shape dynamics, which corresponds to the static elastic shells that have been investigated earlier in this work using hydrostatic forces as boundary conditions.

Elastic shells: It is clear that such an instantaneously relaxing cell membrane with $\gamma = 0$ maximizes the attachment probability with respect to finite frictions $\gamma > 0$, as MTs reattach to the membrane earlier. All effects and phenomena investigated within the analysis of the two-dimensional model appear more pronounced for $\gamma = 0$ (see quads in Figs. 3.14, 3.16, 3.17), and are effectively switched off by applying the opposite case $\gamma \to \infty$. In particular, increasing the characteristic force F_0 corresponds to a pure softening for the equilibrium membrane, whereas for the overdamped membrane we additionally see that the magnitudes

of p_{att} and Σ increase with additional actin polymerization forces added to the characteristic force F_0.

Regarding the asphericity values for the equilibrium shell in Fig. 3.17 (quads), we observe monotonic behavior in contrast to the broad maximum observed for overdamped elastic shells. This is due to the vertices between adjacent MTs: In case of the overdamped shell these vertices stay at their initial rest position, whereas MTs form tiny membrane tubes. In case of the equilibrium membrane, these vertices actually change their position because MT induced deformations are global, i.e., propagate instantaneously along the membrane. If $E = 0$, the equilibrium configuration is undefined and, in principle, no unique shape can be determined for a given set of boundary conditions.

Liquid droplets: We find significantly increased synchronicity values due to vanishing mechanical attenuation. For the liquid interface these effects are, however, clearly less pronounced compared to the elastic shell. In particular, for the attachment probability and the asphericity, we observe only small deviations from the overdamped shape dynamics.

3.4.9 Conclusion

We developed a two dimensional model for an MT aster confined within a closed elastic shell or a liquid droplet. We discussed the corresponding shape free energies and deduced the force fields. No symmetry breaking mechanisms were applied yet, instead we referred to the symmetric case and investigated collective length oscillations, i.e., pulsating cells. We find that systems synchronize for intermediate elastic moduli, which can be understood from simple arguments.

The degree of synchronicity can be tuned via the rescue rate or the characteristic MT polymerization force. The former can be influenced by interaction with MAPs, the latter by MT regulated or triggered actin polymerization. We defined synchronicity as the occurrence of collective (simultaneous) catastrophes, and verified their occurrence by use of the DBSCAN cluster algorithm. Simulation results for the two dimensional model are in qualitative agreement with mean-field results obtained from the one dimensional model 3.2. Moreover, we found collective behavior in agreement with the ensemble mean-field theory 3.3.

Our results suggest that collective length oscillations can be found independently from the employed elasticity model, i.e., show a certain robustness. Therefore, we expect also robustness against changing from the spherical parametrization to a non-approximative one. To perform this change, one has to include collision detection, torques, and slipping mechanisms.

We investigated cell behavior in dependence of different parameters like Young's modulus, surface tension, rescue rate, and characteristic polymerization force, but still there are many parameters that have not been investigated yet, like the on-rate, the cortex thickness, internal MT hydrolysis, i.e., vectorial hydrolysis velocity and random hydrolysis rate, external pressure, and resting radius.

We proceed with regulatory mechanisms, which add an additional degree of complexity to the system.

3.5 Rac-Rho feedback mechanism

In this section, we study regulatory mechanisms relying on MT dynamics that enable polar cell shapes, which are particularly necessary for migrating cells. Cell migration is

crucial for many physiological processes, such as wound healing or tumor metastasis. In general, we have to distinguish between undirected und directed cell movement. The latter originates in external stimuli as, for example, chemotaxis (concentration gradient) [227] or alternative mechanisms, which signal actin polymerization in a preferred direction; the former is triggered by fluctuations either cell internal or external.

Though it has been shown that in some cases locomotion can be carried out exclusively by the actin cortex in collaboration with actin stress fibers [228], MTs are necessary for movement in most cases [229]. The typical locomotion cycle works as follows: In an initially spherical cell, actin polymerization is triggered locally in the actin cortex (by Rho GTPases) and induces a protrusion (lamellipodium), which is often referred to as the *leading edge*. Actin stress fibers meanwhile contract to pull the *trailing edge* of the cell in the same direction. Stress fiber contraction is usually supported by MTs targeting focal adhesions at the trailing edge. Focal adhesion complexes disassemble when interacting with a MT tip and then detach from the extracellular matrix. Once the cell has been detached from the substrate at the trailing edge, stress fiber induced cell contraction can proceed and the cell returns to a spherical shape. MTs at the leading edge mechanically stabilize protrusions made by actin, but also activate Rho GTPases triggering actin polymerization. An inhomogenity in activity once triggered by an external signal or an internal fluctuation can thus be maintained by MT activity, which might be important for cells to pass domains, where no signals can be generated in the ECM.

In the following, we study two coupled feedback mechanisms referred to as the Rac-Rho feedback mechanism. This mechanism seems to be suitable from several point of views. First, it is commonly mentioned in literature in the context of cell polarization [230–232]. Second, it is computationally efficient, as we can solve the master equation on a non-equidistant mesh and, thus, circumvent a particle based approach. And last, we find persistently polarized shapes that have been observed experimentally with a similar Rac-Rho feedback mechanism.

Within the Rac-Rho feedback mechanism, MTs participate in two different feedback cycles. At the leading edge, MT growth activates Rac, which induces actin polymerization. This additional polymerization forces can be effectively included in the characteristic MT polymerization force and, thus, leads to a positive feedback cycle. At the trailing edge, MT shrinkage activates Rho, which induces contractile actin structures. These contractile structures stiffen the actin cortex, increase restoring membrane stresses and thereby MT shrinkage and, thus, likewise lead to a positive feedback cycle. Both feedback cycles in combination polarize the cell persistently, see Fig. 3.21. Note that various feedback cycles concerning Rac and Rho have been investigated in the context of cell migration, where often also Cdc42 is investigated as a third participant in this complex process [233, 234]. However, to the author's knowledge, none of these models have been investigated in combination with MT dynamics. Regarding all these models (overview in Ref. [234]), the model we employ is closest to the model proposed Ref. [235], which states mutual exclusive Rac and Rho activity during neurite formation. In the following, we at first discuss both feedback cycles separately and then integrate these mechanisms in the two-dimensional cell model from sec. 3.4.

3.5.1 Actin force generation

In sec. 3.4 we already discussed the effect that additional forces generated by actin polymerization have on MT and cell dynamics. In particular, we found out that an increasing characteristic force increases the attachment probability (or coupling strength) and synchronization. In this chapter we again use this mechanism but add a spatial dependence to account for local GTPase activation processes.

In addition to forces $\sim 6.6\,\mathrm{pN}$ generated by single MTs, the actin cortex itself can generate forces $\sim 16\,\mathrm{pN}$ [236]. Though theses forces can be generated independently from MTs, regulation by the MT cytoskeleton is common, and necessary for particular tasks. Actin polymerization can be triggered by MTs, for example, via the two following pathways:

(i) MTs have been reported to activate Rac1 during growth [237]. It is assumed that both GEFs and inactive Rac1 proteins bind to the MT lattice leading to Rac1 activation. Once activated, Rac1 proteins detach from the MT lattice and diffuse back into the actin cortex, where they trigger actin polymerization via the Arp2/3 complex, which leads to branching of the actin meshwork. Mechanism (i) commonly takes place in protrusions or lamellipodia formed by migrating cells. Since it requires the MT lattice to be in spatial proximity to actin filaments, it is typically related to MTs growing deep into the lamellipodium. In so doing, MTs become flexible and likely turn around by reaching the plasma membrane. This enables MTs to control the actin retrograde flow via interaction with motor proteins.

(ii) A mechanism commonly related to phagocytosis involves the MT tip binding proteins EB1 and CLIP-170 interacting with mDia1, which belongs to the formin family [180, 238]. Formins serve as actin nucleation sites and thereby promote actin polymerization, even in absence of CLIP-170, but CLIP-170 amplifies the effect of mDia1 by a factor 3 to 4. The mechanism works in a hierarchical order: EB1 binds to the MT tip, where it additionally recruits CLIP-170. Together, these two proteins form a complex, which in turn recruits mDia1. As a result, the MT tip provides multiple actin nucleation sites, which effectively increase actin polymerization rates 14 fold. Mechanism (ii) works without EB1, but EB1 amplifies the effect, probably since the EB1/CLIP-170 complex provides more nucleation sites than provided by sole CLIP-170. In addition, in absence of EB1, CLIP-170 is not strictly localized to the MT tip.

By assuming that force generation is localized to the MT tip, we can take actin forces into account by modifying the characteristic MT force F_0. Therefore, we could assume a growth velocity

$$\boldsymbol{v}_{+,m} = d_m \left(\omega_{\mathrm{on}} e^{-f_{mq}/\chi_m^{\mathrm{Rac}} F_0} - \omega_{\mathrm{off}} \right) \boldsymbol{e}_{mq}, \tag{3.38}$$

where $\chi_m^{\mathrm{Rac}} \geq 1$ is a local amplifying factor. This method is well suited for mechanism (ii) since it is strongly localized to the MT tip, in particular if EB1 is involved. Mechanism (i) would actually require a more detailed model, but (3.38) is an adequate approximation.

3.5.2 Cortex stiffening

In the trailing edge of migrating cells, MT induced cortex stiffening (via Rho) has been reported [237, 239]. Likewise Rho activity is required for tail retraction, for example, in leukocytes [240]. During growth, GEFs accumulate at the MT lattice and are released during shrinkage. In the actin cortex, released GEFs lead to activation of Rho, which in turn activates myosin-II via promoting myosin light chain phosphorylation. This leads to a local stiffening of the cortex and supports retraction after detachment from the substrate. This mechanism could be modeled by time-dependent modulations of the Young modulus proportional to the concentration of active Rho proteins, i.e.,

$$Y_n = \chi_n^{\mathrm{Rho}} Y.$$
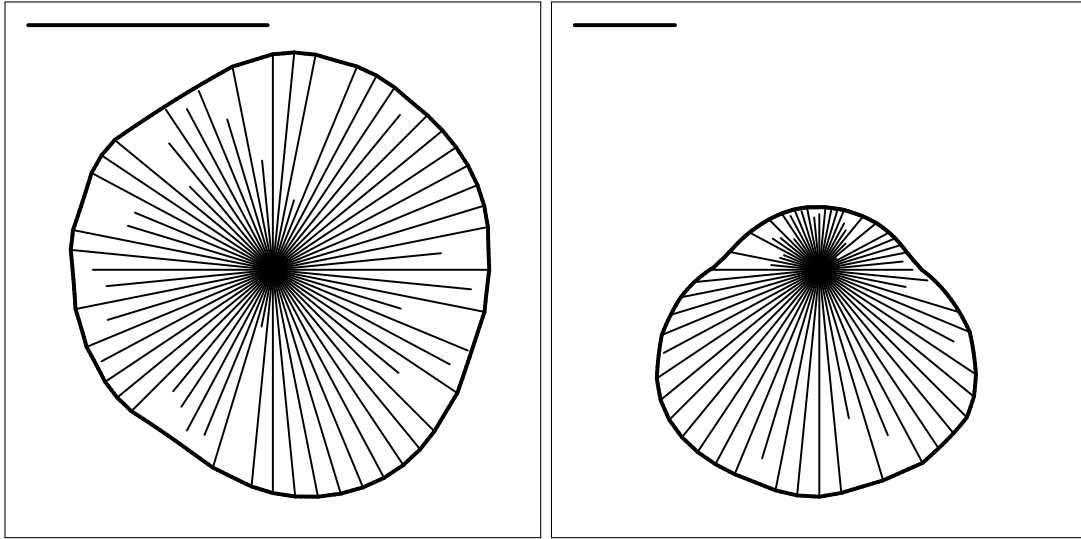
Figure 3.20: Snapshots of a reference system (left) and an a priori chemically polarized system (right), where the characteristic force has been increased for MTs in the lower halfspace, and the Young modulus of the membrane has been increased in the upper halfspace. The scale bar indicates the reference cell diameter, which is $20\,\mu$m.

In vivo, contractions of the cell rear actually marks the beginning for the cell to take again a spherical shape and move towards the traction points the cell attached to by focal adhesions in the front. In our model, contraction of the cell rear does not fulfill this function, instead, it is just a counter-effect to the protrusion formed in the cell front. One could therefore assume that we look at one specific, intermediate, phase of the movement cycle.

3.5.3 Prescribed chemical polarization

Now that we have included actin polymerization into the MT growth velocities via the force generating factors χ_μ^{Rac} and cortex stiffening into Young's modulus via the stiffening factors χ_n^{Rho}, we could presume that the cell is chemically polarized, i.e., prescribe an asymmetric pattern with the factors χ_μ^{Rac} and χ_n^{Rho}. The simplest method to do so is setting both factors to a constant in exclusive regions. In Fig. 3.20 we used $\chi_\mu^{\mathrm{Rac}} = 4$ for $M/2 < \mu < M$ and $\chi_n^{\mathrm{Rho}} = 4$ for $0 < n < N/2$, where we additionally ensured a smooth transition at the domain borders. As a result, the cell polarizes along the prescribed direction, which is the vertical axis in Fig. 3.20. This is not surprising though, but at least it shows that MTs adapt to the prescribed chemical polarization pattern and successfully maintain the polarized shape.

3.5.4 MT induced chemical polarization

It seems to be accepted in literature that polarization occurs due to mutually exclusive mechanisms at the cell front and the cell back [230–232]. MTs that exert force onto the membrane activate Rac proteins and shrinking MTs activate Rho proteins. Active Rac leads to additional force generation and active Rho leads to cortex stiffening. Assuming that active Rac excludes active Rho and vice versa, MTs might be able to trigger segregation of both populations. This gives rise to a symmetry breaking mechanism, which enables the cell to polarize in a random direction. Polarization can persist in time, if segregation of populations is stable, i.e, maintained by MTs. Without MT dependent activation, we do not observe segregation. A sketch of the two feedback mechanisms is shown in Fig. 3.21. To
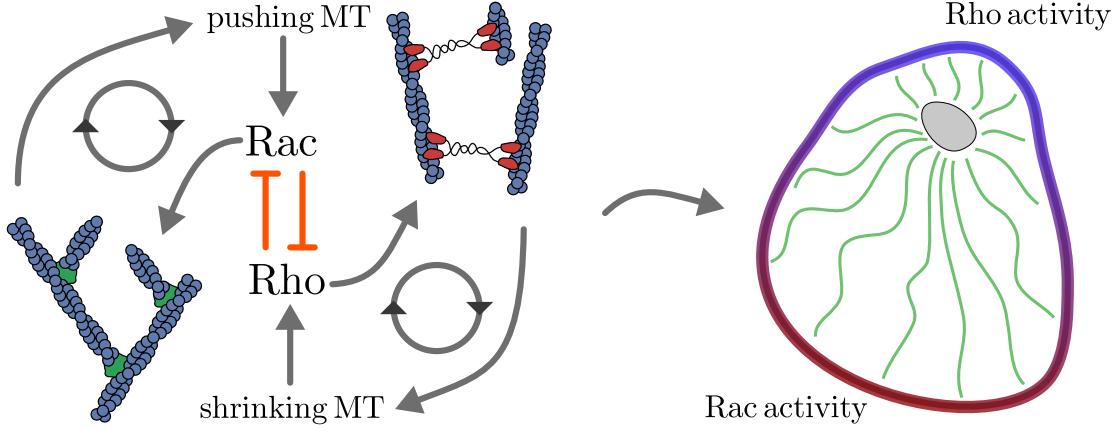
Figure 3.21: Illustration of the Rho-Rac-switch leading to cell polarity. Two different feedback cycles are involved (left), one related to shrinking and one related to pushing MTs. Shrinking MTs trigger Rho, which in turn leads to formation of contractile structures made from myosin and actin. Myosin motor proteins are concurrently attached to two actin filaments and thereby shift these filaments against each other leading to contractile tension. Pushing MTs activate Rac, which in turn leads to formation of protrusive actin structures made from the Arp2/3 complex and actin. The directional branched actin network generates additional polymerization force. Ultimately, both mechanisms together lead to stable cell polarity (right), where MTs collaborating with Rac induce a protrusion in the cell front and MTs collaborating with Rho induce a contraction or stiffening in the cell back. Due to a limited number of actin filaments and, more importantly, due to a substantially different actin filament ordering (lateral contractile structures and normal protrusive structures) both mechanisms exclude each other [241].

describe the dynamics of the protein populations we use a system of four coupled master equations accounting for the fractions of inactive/active Rac and inactive/active Rho in the cortex. Let $a_n^+(t)$ be active Rac, $a_n^-(t)$ inactive Rac, $b_n^+(t)$ active Rho and $b_n^-(t)$ inactive Rho, such that the stochastic process can be written as

$$
\begin{aligned}
\partial_t a_n^+(t) &= -\omega^- a_n^+(t) + a_n^{\text{act}}(t)\omega^+ a_n^-(t) + D\partial_{ss}a_n^+(t), \\
\partial_t b_n^+(t) &= -\omega^- b_n^+(t) + b_n^{\text{act}}(t)\omega^+ b_n^-(t) + D\partial_{ss}b_n^+(t), \\
\partial_t a_n^-(t) &= \omega^- a_n^+(t) - a_n^{\text{act}}(t)\omega^+ a_n^-(t) + D\partial_{ss}a_n^-(t), \\
\partial_t b_n^-(t) &= \omega^- b_n^+(t) - b_n^{\text{act}}(t)\omega^+ b_n^-(t) + D\partial_{ss}b_n^-(t),
\end{aligned}
\tag{3.39}
$$

where $\omega^+ = 5\,\text{s}^{-1}$ and $\omega^- = 0.001\,\text{s}^{-1}$ are the activation respectively deactivation rates and D is the cortex diffusivity. The activation rate ω^+ actually controls the strength of the feedback coupling, such that $\omega^+ = 0$ corresponds to absence of the feedback coupling. Increasing the number M of MTs would have a similar effect. We use $D = 9.47\,\text{m}^2/\text{s}$ which is consistent with values obtained in Ref. [227]. In addition to sink and diffusion terms, we include source terms being proportional to the activation factors

$$
a_n^{\text{act}}(s,t) = \sum_{\mu=1}^{M} \frac{c_\mu \Theta(l_\mu - (r_{\mu q} - d_m))\delta_{n,\mu q}}{1 + (b_n^+(t)/k_d)^3},
$$

$$
b_n^{\text{act}}(s,t) = \sum_{\mu=1}^{M} \frac{(1 - c_\mu)\delta_{n,\mu q}}{1 + (a_n^+(t)/k_d)^3},
$$
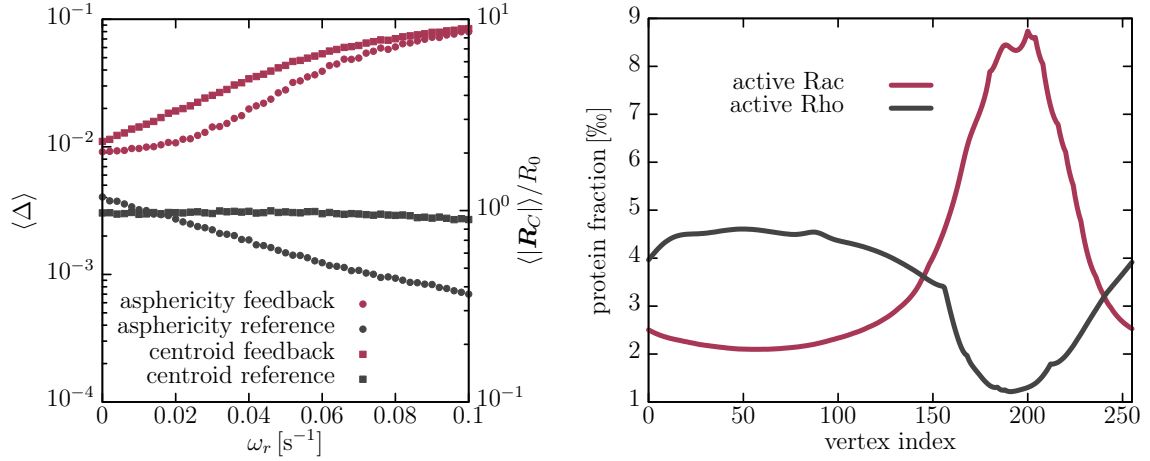
Figure 3.22: Simulation results for an elastic shell including the two mutually exclusive feedback mechanisms implementing the Rac-Rho feedback mechanism. **Left:** Asphericity dependent on the rescue rate for the feedback system (gray) and the reference system (purple). Polarization is successfully triggered in the feedback system when MT growth becomes unbounded, i.e., exceeds a critical value of the rescue rate. Thereafter, the asphericity increases linearly with increasing rescue rates. For the reference measurement or control group, the asphericity even decreases with increasing rescue rates. **Right:** Snapshot of the Rac and Rho density profiles plotted against the vertex index. Note that arc-lengths between adjacent vertices are not constant due to extensible bonds. As we see, two stable populations have been formed, where the Rac population forms a more pronounced and localized maximum as the Rho population. However, details, i.e., width and amplitude of the maxima, depend on the various parameters in our model, such as MT ensemble properties, but also diffusion constants and switching rates assumed for the proteins populating the membrane.

which unlock the activation branches from inactive to active forms of Rac and Rho respectively. This is where the coupling to the MT ensemble enters. The Kronecker delta $\delta_{n,\mu q}$ localizes the μ-th trigger to the correct vertex $n = \mu q$ and the Heavy-side function $\Theta(l_\mu - (r_{\mu q} - d_m))$ becomes 1 if the MT is in spatial proximity to the cortex. The factor $(1 - c_\mu)$ becomes 1 if the MT is shrinking; c_μ becomes 1 if the MT is growing. Both populations are conserved, meaning that

$$\sum_{n=1}^{N} \left[a_n^+(t) + a_n^-(t) \right] = 1,$$

$$\sum_{n=1}^{N} \left[b_n^+(t) + b_n^-(t) \right] = 1,$$

is fulfilled for all times t. Exchange from a_n^- to a_n^+ or from b_n^- to b_n^+ is exclusively possible via MT triggering. Mutual exclusion enters on the activation level via the Hill function, which is also used, for example, in gene transcription models. Activation is suppressed proportional to the presence of the inhibiting factor. The factor k_d is the characteristic active protein fraction that suppresses activation of the opponent protein by exactly a factor two. We choose $k_d = 2\,‰$ for our measurements. On the feedback level, we assume that at a given location and time only a one of both feedback mechanisms can be applied, which is a model of mutual exclusive structures in the cortex [241]. We make the even stronger assumption that the active parts of the Rac and Rho populations extinguish each other. Having calculated the fractions of active Rac and Rho by solving the master equations
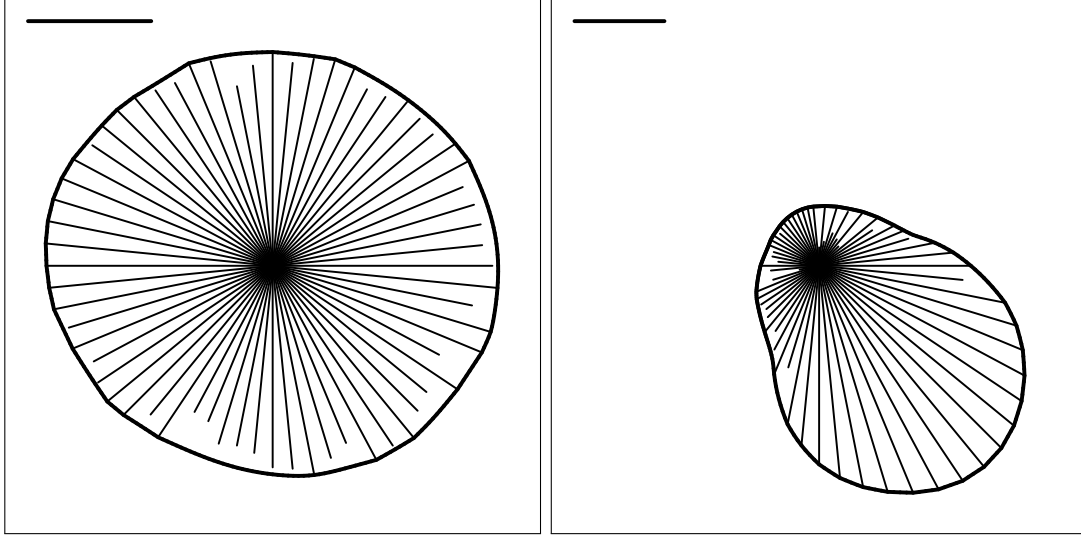
Figure 3.23: Simulation snapshots of a reference system (left) and a persistently polarized system (right) employing the Rac-Rho feedback mechanism, both in presence of rescues with $\omega_r = 0.1\,\mathrm{s}^{-1}$. The scale bar indicates the reference cell diameter, which is $20\,\mu\mathrm{m}$. The direction of polarization is random, i.e., fluctuates in time.

(3.39), we can assume that

$$\frac{F_0^{\mu}(t)}{F_0\chi^{\mathrm{rho}}N} = 1 + \max(a_{\mu q}^+(t) - b_{\mu q}^+(t),\,0),$$

$$\frac{\varkappa_n(t)}{\varkappa\chi^{\mathrm{rac}}N} = 1 + \max(b_n^+(t) - a_n^+(t),\,0),$$

$$Y_n(t) = (\varkappa_n(t) + \varkappa_{n+1}(t))/2h^2,$$

to couple protein dynamics to the two dimensional cell model from sec. 3.4. Here, we directly modulated the bending rigidity $\varkappa$ and determined the Young modulus Y as an average of two neighbored vertices. We could also have directly modulated the Young modulus Y and then determine the bending rigidity as an average. Both approaches are equivalent since we assume an isotropic and homogeneous material which implies a linear dependence between both quantities $\varkappa$ and Y. Using the maximum function employs the boundary condition $a^+(t) = b^+(t) = 0$ at the domain border between Rac and Rho populations. In consequence, no feedback mechanism is applied directly at the domain border, which prevents jumps in the amplitude of the applied feedback mechanisms. Due to extensible bond vectors we have to solve (3.39) on a non-equidistant mesh. Therefore we use the differential quotients

$$\partial_s f_n \approx \frac{f_{n+1} - (1 - \alpha_n^2)f_n - \alpha_n^2 f_{n-1}}{\alpha_n(1 + \alpha_n)|\boldsymbol{t}_{n-1}|}$$

$$\partial_{ss} f_n \approx \frac{f_{n+1} - (1 + \alpha_n)f_n + \alpha_n f_{n-1}}{(\alpha_n/2)(1 + \alpha_n)|\boldsymbol{t}_{n-1}|^2},$$

where f serves as a placeholder for $a^{\pm}$ and $b^{\pm}$. The factor $\alpha_n = |\boldsymbol{t}_n|/|\boldsymbol{t}_{n-1}|$ describes the relative elongation of consecutive bond vectors. Note that the system of equations (3.39) has to be solved simultaneously to the numerical model explored in sec. (3.4).

By describing protein dynamics within the membrane with a master equation, we already spared computational cost compared to a particle approach. Nevertheless we can further
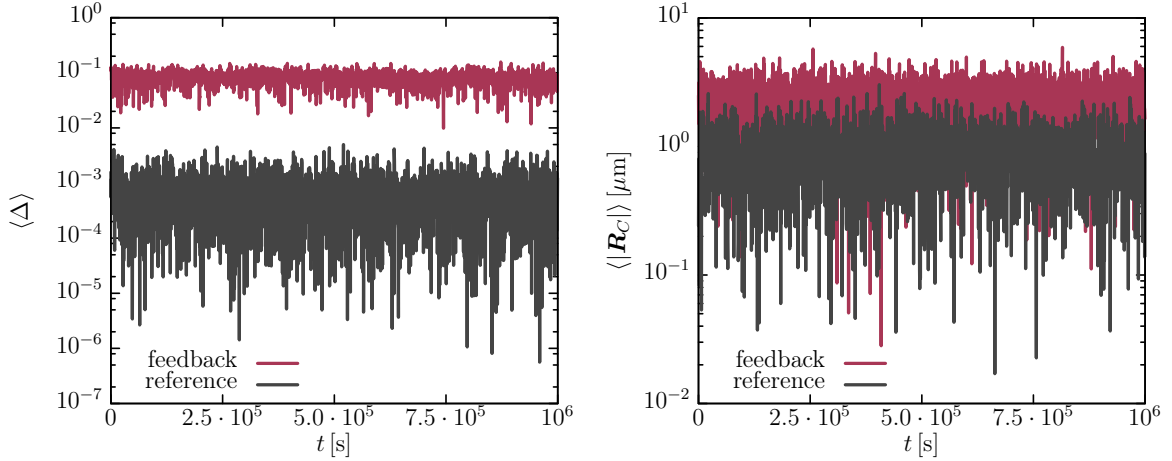
Figure 3.24: Verification of *persistent* cell polarization for a simulation time of $t_{\max} = 11.57$ hours. For comparison a reference measurement is shown. **Left:** Asphericity dependent on the simulation time. The polarized system exhibits less fluctuations and is persistently polarized. In contrast, the reference system is less aspherical and fluctuates regularly to $\Delta \approx 0$. **Right:** Absolute value of the centroid depending on the simulation time. The same argumentation as suggested for the asphericity applies here. In contrast to the reference state, the polarized system shows a persistently elongated centrosome.

simplify by assuming that the *passive* forms of Rac and Rho can not only diffuse within the membrane, but also through the cytosol. Since this is a sort of spatial abbreviation for the proteins, this assumption leads to much higher effective diffusion constants. Ultimately, we could assume that the passive forms diffuse instantaneously to any location in the actin cortex, which allows us to replace the spatial grid used for the passive forms by a single container giving the bulk concentration. This effectively halves the computational cost, because we discarded roughly the half of all grid computations.

3.5.5 Discussion

In Fig. 3.22 we analyze the polarization capabilities of the model just introduced. Fig. 3.23 shows corresponding snapshots for a rescue rate $\omega_r = 0.10\,\text{s}^{-1}$. Clearly, the cell polarizes when increasing the rescue rates, which can be seen from an increasing asphericity Δ. In the discussion of symmetric cells in chapter 3.4 we found asphericity values up to $\Delta \approx 0.01$. Including the two mutual exclusive feedback mechanisms we exceed this value by a factor 10. In fact, there is another difference between both asphericity measurements. Whereas for the symmetric shell the asphericity fluctuates upwards from $\Delta \approx 0$, i.e., the system returns regularly to values $\Delta \approx 0$, we find a constantly non-zero asphericity here, i.e., $\Delta(t) > 0$, see Fig. 3.24. This clearly proves that the system broke the spherical symmetry.

In the sec. 3.4 we verified the occurrence of collective catastrophes and, particularly in presence of rescues, we found strong collective behavior. One might ask in which way the observed polarization behavior depends on those collective catastrophes. The fact that we find polarization only in presence of rescues already suggests a correlation. And indeed, when we initialize the system in an unpolarized state with all MTs at the centrosome in a growing state, we observe the following polarization process: MTs attach to the membrane after about 200 s and then cooperatively exert force onto the membrane. Meanwhile, Rac is activated all along the membrane whereas Rho is completely suppressed. The cell blows up due to a stable phase of collective force exertion by the MT ensemble and, after all, randomly a single MT undergoes a catastrophe, which propagates in a collective catastrophe

along the membrane. Since all these subsequent catastrophes produce active Rho stiffening the cortex, the collective catastrophe propagates even faster than without this feedback mechanism. Now, since Rac and Rho exclude each other, and the whole membrane was flooded with Rac before, the collective catastrophe establishes a stable Rho population. As a key of this mechanism, the collective catastrophe aborts, because it cannot enter the Rac population, due to mutual exclusion of Rac and Rho.

In the regime of persistent polarization, i.e., $\omega_r = 0.10\,\mathrm{s}^{-1}$, a single collective catastrophe is sufficient to polarize the cell once and for all. Afterwards, no collective events occur while the cell maintains its polarized shape. In the regime of transient polarization at $\omega_r = 0.05\,\mathrm{s}^{-1}$, the polarized state decays after some time. Then, a new collective event again polarizes the cell and this process is repeated in time.

3.5.6 Conclusion

In this section, we discussed the Rac-Rho feedback mechanism and its integration into the two-dimensional cell model introduced in sec. 3.4. This mechanism has not been, to the author's knowledge, theoretically investigated earlier in feedback cycles with MTs, which actually give rise to stable and persistent cellular polarization as it also has been observed experimentally. Future work should clarify, if this is really a spontaneous transition triggered by MT length fluctuations, or if segregation of populations is inherently included in the model and only amplified by MT excitations. However, both cases represent possible polarization pathways. In vivo, populations typically segregate as a response to extracellular signals. It is thus still not quite clear which role MTs play during this process, i.e., if they are involved in the triggering process, or rather maintain the segregation. However, we showed that MTs are capable of both triggering and maintaining segregation, but it remains to be clarified which of both processes is key to cellular polarization.

4 Conclusion and outlook

In this work, we investigated elastic shells in static force equilibrium as well as an elastic cell cortex coupled to an internal active cytoskeleton. The shape analysis of pendant elastic capsules or elastic shells adsorbed to planar liquid-liquid interfaces exhibits multiple possible applications in industry and research. The two-dimensional active shell model mimicking an animal cell is capable of rationalizing experimentally observed cellular polarization mechanism by employing mutual exclusive Rac and Rho activity. Such polarization mechanisms are of fundamental interest in cell biology and clinical applications.

Regarding cell mechanics, we pursued a variety of approaches. We started with one-dimensional mean-field calculations, both for single and multiple MTs, proceeded with a stochastic two-dimensional model taking shape alterations into account, and finally implemented regulatory mechanisms exhibiting cellular polarization. Our results suggest that microtubules play an essential role in cell mechanics as they synchronize when interacting via an elastic shell. In cooperation with the actin cortex and GTPases, microtubules participate in polarization mechanisms and are capable to persistently maintain polarized shapes, if the cortex has been chemically polarized before, and even for a totally unpolarized cortex and shape. All these results could, in principle, be verified in experimental setups as in Refs. [216, 217].

One of the drawbacks of our two-dimensional cell model is the spherical parametrization, which permits only stellar shapes neglecting lateral forces. Since microtubules in the aster-like geometry only exert stellar forces, this approximation is reasonable, but for shapes deviating strongly from a circular symmetric shape, we observe artifacts, as, for example, increasing asphericity values when translating a spherical membrane with respect to the origin. We found qualitatively similar results when employing different elasticity models for shells and droplets, and therefore expect our results to be also robust against taking lateral forces into account. However, by using a spherical parametrization and thereby excluding overlaps, and by coarse-graining the membrane and the microtubules, we achieve a significant speedup allowing the simulation to capture the complete relevant cell-life timescale, which is of order 24 h. For comparison, typical molecular dynamic simulations reside within the μs scale.

Future implementations should model microtubules as worm-like chains to account for buckling and also take lateral forces onto the membrane into account. In order to achieve this, microtubule-bond collisions have to be included and, in consequence, also torques and maybe slipping mechanisms. Another possibility is to take fluctuations of the membrane into account, i.e., to implement the Brownian ratchet model explicitly. It would be interesting if one would find the same features in such a, more refined, model.

We included actin polymerization forces effectively and regulated by microtubules. However, our model would also allow to directly take actin polymerization into account by introducing ghost forces located to the membrane vertices. Actin polymerization could occur spontaneously or in response to extracellular signals. Then, MTs are not necessary to regulate actin dynamics but could be an additional regulating factor. In a three-dimensional model the actin cortex could be taken into account via individual filament modeling, which would also correctly account for microscopic filament ordering effects. For example, microtubules growing deep into the lamellipodium, i.e., a dense actin filament meshwork, become flexible, which might be important concerning direct microtubule membrane interactions.

Regarding the shape analysis of elastic capsules, either hanging from a capillary as in a pendant drop tensiometer or adsorbed to a liquid-liquid interface, we achieved significant progress in this thesis. The shape analysis of pendant elastic capsules was successfully applied using elastic shape equations in the past. In this thesis, we improved this method with respect to several aspects. We adapted the shape parameters, i.e., the elastic moduli of the membrane material, in continuous space, whereas in the past they were optimized on a spatial grid. Further, we significantly improved the performance of the shape analysis, automatized it to large degree, and implemented additional constitutive laws, that allow to find the most appropriate elastic model for a given material. With this work, we provide an Open Source Software called *OpenCapsule* that is freely available on the internet and can be used by companies or research institutes to analyze capsule materials on a large scale.

The shape analysis of elastic capsules adsorbed to liquid-liquid interfaces is a completely new approach that is introduced for the first time in this work. In principle, the same kind of rigorous numerical analysis can be applied to capsules at liquid-liquid interfaces, like for pendant elastic capsules. However, we also derived analytic results that allow the direct determination of the shell's bending modulus by measuring the curvature of the capsule at the three phase contact line, the surface tension within the liquid-liquid interface, and the thickness of the shell material. Moreover, Young's modulus can be determined from the height of an elastic lens or, alternatively, the contact angle at the three phase contact line.

Together, both methods form a comprehensive framework to quantify the material properties of elastic materials. Such materials have technical applications in the pharma industry, but are also important for biological model containers. In future work, different hydrostatic setups could be investigated, and eventually be included in the OpenCapsule Software we provide with this work.

Bibliography

[1] Knoche, S. *et al.* (2013), *Langmuir*, **29**(40):12463–12471.
Elastometry of Deflated Capsules: Elastic Moduli from Shape and Wrinkle Analysis

[2] Hegemann, J. *et al.* (2018), *submitted to Soft Matter*, to be published...
Elastic Capsules at Liquid-Liquid Interfaces

[3] Hegemann, J. and Kierfeld, J., *URL[1]*.
OpenCapsule C/C++ Software

[4] *URL[2]*.
GNU General Public License

[5] Hegemann, J. *et al.* (2018), *J. Colloid Interface Sci.*, **513**:549–565.
Pendant Capsule Elastometry

[6] Zelinski, B. and Kierfeld, J. (2013), *Phys. Rev. E*, **87**(1):012703.
Cooperative Dynamics of Microtubule Ensembles: Polymerization Forces and . . .

[7] Vert, M. *et al.* (2012), *Pure and Applied Chemistry*, **84**(2):377–410.
Terminology for Biorelated Polymers and Applications (IUPAC . . .

[8] Rehage, H. *et al.* (2002), *Rheol. Acta*, **41**(4):292–306.
From Two-Dimensional Model Networks to Microcapsules

[9] Dinsmore, A. D. *et al.* (2002), *Science*, **298**(5595):1006–9.
Colloidosomes: Selectively Permeable Capsules Composed of Colloidal Particles.

[10] Aumaitre, E. *et al.* (2013), *Eur. Phys. J. E*, **36**(3):22.
Wrinkling in the Deflation of Elastic Bubbles

[11] Donath, E. *et al.* (1998), *Ang. Chem. Int. Ed.*, **37**(16):2201–2205.
Novel Hollow Polymer Shells by Colloid-Templated Assembly of Polyelectrolytes

[12] De Cock, L. J. *et al.* (2010), *Angew. Chem. Int. Ed.*, **49**(39):6954–6973.
Polymeric Multilayer Capsules in Drug Delivery

[13] Orive, G. *et al.* (2004), *Trends Biotechnol.*, **22**(2):87–92.
History, Challenges and Perspectives of Cell Microencapsulation

[14] Cook, M. T. *et al.* (2012), *Journal of Controlled Release*, **162**(1):56–67.
Microencapsulation of Probiotics for Gastrointestinal Delivery

[15] Mondal, S. (2008), *Applied Thermal Engineering*, **28**(11):1536–1550.
Phase Change Materials for Smart Textiles--An Overview

[16] Martins, I. M. *et al.* (2014), *Chemical Engineering Journal*, **245**:191–200.
Microencapsulation of Essential Oils with Biodegradable Polymeric Carriers for . . .

[17] Aïssa, B. *et al.* (2012), *Adv. Mater. Sci. Eng.*, **2012**.
Self-Healing Materials Systems: Overview of Major Approaches and Recent . . .

[18] White, S. R. *et al.* (2001), *Nature*, **409**(6822):794–797.
Autonomic Healing of Polymer Composites

[19] Gharsallaoui, A. *et al.* (2007), *Food Research International*, **40**(9):1107–1121.

---

[1] https://github.com/jhegemann/opencapsule
[2] https://www.gnu.org/licenses/gpl-3.0.en.html

Applications of Spray-Drying in Microencapsulation of Food Ingredients: An . . .

[20] Buenemann, M. and Lenz, P. (2008), *Physical Review E*, **78**(5):051924.
Elastic Properties and Mechanical Stability of Chiral and Filled Viral Capsids

[21] Thompson, K. L. *et al.* (2015), *J. Colloid Interface Sci.*, **447**:217–228.
Colloidosomes: Synthesis, Properties and Applications

[22] Dinsmore, A. *et al.* (2002), *Science*, **298**(5595):1006–1009.
Colloidosomes: Selectively Permeable Capsules Composed of Colloidal Particles

[23] Yow, H. N. and Routh, A. F. (2006), *Soft Matter*, **2**(11):940–949.
Formation of Liquid Core--Polymer Shell Microcapsules

[24] Vaccari, L. *et al.* (2015), *Soft Matter*, **11**(30):6062–6074.
Films of Bacteria at Interfaces: Three Stages of Behaviour

[25] Vinogradova, O. I. *et al.* (2006), *Annu. Rev. Mater. Res.*, **36**(1):143–178.
Mechanical Behavior and Characterization of Microcapsules

[26] Neubauer, M. P. *et al.* (2014), *Adv. Colloid Interface Sci.*, **207**:65–80.
Microcapsule Mechanics: From Stability to Function

[27] Hu, J. *et al.* (2009), *Materials Chemistry and Physics*, **118**(1):63–70.
Mechanical Properties of Melamine Formaldehyde Microcapsules for Self-Healing . . .

[28] Freund, J. B. (2013), *Physics of Fluids*, **25**(11):110807.
The Flow of Red Blood Cells Through a Narrow Spleen-Like Slit

[29] Van Raamsdonk, J. and Chang, P. (2001), *J. Biomed. Mater. Res.*, **54**(2):264–271.
Osmotic Pressure Test: a Simple, Quantitative Method to Assess the Mechanical . . .

[30] Poncelet, D. and Neufeld, R. J. (1989), *Biotechnol. Bioeng.*, **33**(1):95–103.
Shear Breakage of Nylon Membrane Microcapsules in a Turbine Reactor

[31] Gorin, D. A. *et al.* (2008), *Phys. Chem. Chem. Phys.*, **10**(45):6899–6905.
Magnetic/Gold Nanoparticle Functionalized Biocompatible Microcapsules with . . .

[32] Commons, C., *URL³ (24.11.2017)*.
CC BY-SA 4.0

[33] Wikimedia Commons user *Aidar.Seralin*, *URL⁴ (24.11.2017)*.
Droplet of Water on 5 Grains of Hydrophopic Sand

[34] Commons, C., *URL⁵ (24.11.2017)*.
CC BY 3.0

[35] Chen, H. and Ouyang W. and Martoni, C. and Prakash, S., *URL⁶ (24.11.2017)*.
Microphotopgraphs of Alginate-Chitosan Microcapsules

[36] Seifert, U. (1997), *Advances in physics*, **46**(1):13–137.
Configurations of Fluid Membranes and Vesicles

[37] Khairy, K. *et al.* (2008), *Cellular and molecular bioengineering*, **1**(2-3):173.
Shapes of Red Blood Cells: Comparison of 3D Confocal Images with the . . .

[38] Landau, L. (1986), *Course of theoretical physics*, **7**:5.
EM Lifshitz Theory of Elasticity

[39] Cuenot, S. *et al.* (2004), *Physical Review B*, **69**(16):165410.

---

³`https://creativecommons.org/licenses/by-sa/4.0/deed.en`
⁴`https://commons.wikimedia.org/w/index.php?title=File:Water_droplet_on_a_5_grains_of_`
`hydrophobic_sand.jpg&oldid=219230247`
⁵`https://creativecommons.org/licenses/by/3.0/deed.en`
⁶`https://commons.wikimedia.org/w/index.php?title=File:AC_microcapsule_microphotographs.`
`png&oldid=237807056`

Surface Tension Effect on the Mechanical Properties of Nanomaterials Measured . . .

[40] Gomez, M. *et al.* (2016), **472**(2187):20150732.
The Shallow Shell Approach to Pogorelov's Problem and the Breakdown of . . .

[41] Vaziri, A. (2009), *Thin-Walled Structures*, **47**(6):692–700.
Mechanics of Highly Deformed Elastic Shells

[42] Vella, D. *et al.* (2011), *Journal of the Royal Society Interface*, rsif20110352.
The Indentation of Pressurized Elastic Shells: from Polymeric Capsules to Yeast . . .

[43] Vella, D. *et al.* (2011), *Physical review letters*, **107**(17):174301.
Wrinkling of Pressurized Elastic Shells

[44] Knoche, S. and Kierfeld, J. (2011), *Phys. Rev. E*, **84**(4):046608.
Buckling of Spherical Capsules

[45] Knoche, S. and Kierfeld, J. (2014), *arXiv preprint arXiv:1408.0946*.
The Secondary Buckling Transition: Wrinkling of Buckled Spherical Shells

[46] Shim, J. *et al.* (2012), *Proc. Natl. Acad. Sci. USA*, **109**(16):5978–5983.
Buckling-Induced Encapsulation of Structured Elastic Shells under Pressure

[47] Finken, R. and Seifert, U. (2006), *Journal of Physics: Condensed Matter*, **18**(15):L185.
Wrinkling of Microcapsules in Shear Flow

[48] Khairy, K. and Howard, J. (2011), *Soft Matter*, **7**(5):2138–2143.
Minimum-Energy Vesicle and Cell Shapes Calculated using Spherical Harmonics . . .

[49] Audoly, B. and Pomeau, Y. (2010), *Elasticity and Geometry: from Hair Curls to. . .*
Oxford University Press

[50] Park, B. J. *et al.* (2011), *Soft Matter*, **7**(14):6413–6417.
Janus Particles at an Oil--Water Interface

[51] Park, B. J. and Lee, D. (2012), *Soft Matter*, **8**(29):7690–7698.
Configuration of Nonspherical Amphiphilic Particles at a Fluid--Fluid Interface

[52] Richtering, W. (2012), *Langmuir*, **28**(50):17218–17229.
Responsive Emulsions Stabilized by Stimuli-Sensitive Microgels: Emulsions . . .

[53] Mehrabian, H. *et al.* (2016), *Soft Matter*, **12**(4):1062–1073.
Soft Particles at a Fluid Interface

[54] Geisel, K. *et al.* (2015), *Langmuir*, **31**(48):13145–13154.
Hollow and Core--Shell Microgels at Oil--Water Interfaces: Spreading of Soft . . .

[55] Style, R. W. *et al.* (2015), *Soft Matter*, **11**(37):7412–7419.
Adsorption of Soft Particles at Fluid Interfaces

[56] Rauh, A. *et al.* (2017), *Soft Matter*, **13**(1):158–169.
Compression of Hard Core--Soft Shell Nanoparticles at Liquid--Liquid Interfaces: . . .

[57] Knoche, S. and Kierfeld, J. (2015), *Langmuir*, **31**(19):5364–5376.
Elasticity of Interfacial Rafts of Hard Particles with Soft Shells

[58] Bresme, F. and Oettel, M. (2007), *J. Phys. Condens. Matter*, **19**(41):413101.
Nanoparticles at Fluid Interfaces

[59] Jülicher, F. and Lipowsky, R. (1996), *Physical Review E*, **53**(3):2670.
Shape Transformations of Vesicles with Intramembrane Domains

[60] Zumdieck, A. *et al.* (2007), *PloS one*, **2**(8):e696.
Stress Generation and Filament Turnover During Actin Ring Constriction

[61] Nagel, M. *et al.* (2017), *Advances in Colloid and Interface Science*, **247**:33–51.
From Drop-Shape Analysis to Stress-Fitting Elastometry

[62] Knoche, S. and Kierfeld, J. (2014), *Soft Matter*, **10**(41):8358–8369.
Osmotic Buckling of Spherical Capsules

[63] Libai, A. and Simmonds, J. G. (1998), *The Nonlinear Theory of Elastic Shells*
Cambridge University Press

[64] Do Carmo, M. P. (1994), 77–98.
Differential Geometry of Surfaces

[65] Pozrikidis, C. (2003), *Modeling and Simulation of Capsules and Biological Cells*
CRC Press

[66] Boltz, H.-H. and Kierfeld, J. (2015), *Phys. Rev. E*, **92**(3):033003.
Shapes of Sedimenting Soft Elastic Capsules in a Viscous Fluid

[67] Boltz, H.-H. and Kierfeld, J. (2016), *Eur. Phys. J. Spec. Top.*, **225**(11-12):2269–2285.
Stationary Shapes of Deformable Particles Moving at Low Reynolds Numbers

[68] Blecua, P. *et al.* (2006), *Langmuir*, **22**(26):11041–11059.
Line Tension Effects for Liquid Droplets on Circular Surface Domains

[69] Landau, L. and Lifschitz, E. (1970), *Theory of Elasticity*
Pergamon Press, Oxford

[70] Pogorelov, A. V. (1988), *Bendings of Surfaces and Stability of Shells*
American Mathematical Soc.

[71] Knoche, S. and Kierfeld, J. (2014), *EPL*, **106**(2):24004.
Secondary Polygonal Instability of Buckled Spherical Shells

[72] Ferri, J. K. *et al.* (2010), *Adv. Colloid Interface Sci.*, **161**(1-2):29–47.
From Surfactant Adsorption Kinetics to Asymmetric Nanomembrane Mechanics: . . .

[73] Carvajal, D. *et al.* (2011), *Soft Matter*, **7**(22):10508.
Mechanics of Pendant Drops and Axisymmetric Membranes

[74] Ferri, J. K. *et al.* (2012), *Soft Matter*, **8**(40):10352.
Elastic Nanomembrane Metrology at Fluid–Fluid Interfaces using Axisymmetric . . .

[75] Erni, P. *et al.* (2012), *Soft Matter*, **8**(26):6958–6967.
Interfacial Viscoelasticity Controls Buckling, Wrinkling and Arrest in Emulsion . . .

[76] Alexandrov, N. A. *et al.* (2012), *J. Colloid Interface Sci.*, **376**(1):296–306.
Interfacial Layers from the Protein HFBII Hydrophobin: Dynamic Surface . . .

[77] Danov, K. D. *et al.* (2015), *J. Colloid Interface Sci.*, **440**:168–178.
Capillary Meniscus Dynamometry--Method for Determining the Surface Tension . . .

[78] Salmon, A. R. *et al.* (2016), *Langmuir*, **32**(42):10987–10994.
Microcapsule Buckling Triggered by Compression-Induced Interfacial Phase Change

[79] Cramer, A. D. *et al.* (2017), *Phys. Chem. Chem. Phys.*, **19**:23781–23789.
The Influence of Polyanion Molecular Weight on Polyelectrolyte Multilayers at . . .

[80] Andreas, J. M. *et al.* (1937), *J. Phys. Chem.*, **42**(1):1001–1019.
Boundary Tension By Pendant Drops

[81] Stauffer, C. E. (1965), *J. Phys. Chem.*, **69**(6):1933–1938.
The Measurement of Surface Tension by the Pendant Drop Technique

[82] Cabezas, M. G. *et al.* (2006), *Langmuir*, **22**(24):10053–10060.
Determination of Surface Tension and Contact Angle from the Shapes of . . .

[83] Berry, J. D. *et al.* (2015), *J. Colloid Interface Sci.*, **454**:226–237.
Measurement of Surface and Interfacial Tension using Pendant Drop Tensiometry

[84] Freer, E. M. *et al.* (2003), *J. Pet. Sci. Eng.*, **39**(1-2):137–158.

The Role of Interfacial Rheology in Reservoir Mixed Wettability

[85] Russev, S. C. *et al.* (2008), *Rev. Sci. Instrum.*, **79**(10):1–10.
Instrument and Methods for Surface Dilatational Rheology Measurements

[86] Guzman, E. *et al.* (2009), *J. Phys. Chem. B*, **113**:7128–7137.
Adsorption Kinetics and Mechanical Properties of Ultrathin Polyelectrolyte . . .

[87] Miller, R. *et al.* (2010), *Colloid Polym. Sci.*, **288**(9):937–950.
Rheology of Interfacial Layers

[88] Kovalchuk, V. I. *et al.* (2010), *Adv. Colloid Interface Sci.*, **161**(1-2):102–114.
Capillary Pressure Studies under Low Gravity Conditions

[89] Noskov, B. A. *et al.* (2011), *Adv. Colloid Interface Sci.*, **168**(1-2):179–197.
Dilational Surface Visco-Elasticity of Polyelectrolyte/Surfactant Solutions: . . .

[90] Erni, P. *et al.* (2003), *Rev. Sci. Instrum.*, **74**(11):4916–4924.
Stress- and Strain-Controlled Measurements of Interfacial Shear Viscosity and . . .

[91] Koleva, I. and Rehage, H. (2012), *Soft Matter*, **8**(13):3681–3693.
Deformation and Orientation Dynamics of Polysiloxane Microcapsules in Linear . . .

[92] Pieper, G. *et al.* (1998), *J. Colloid Interface Sci.*, **202**(2):293–300.
Deformation of a Capsule in a Spinning Drop Apparatus

[93] Vandebril, S. *et al.* (2010), *Rheol. Acta*, **49**(2):131–144.
A Double Wall-Ring Geometry for Interfacial Shear Rheometry

[94] Reynaert, S. *et al.* (2008), *J. Rheol.*, **52**(1):261–285.
Analysis of the Magnetic Rod Interfacial Stress Rheometer

[95] Barthès-Biesel, D. (2012), *Microhydrodynamics and Complex Fluids*
CRC Press

[96] Libai, A. and Simmonds, J. G. (1998), *The Nonlinear Theory of Elastic Shells*
Cambridge University Press

[97] Barthès-Biesel, D. *et al.* (2002), *J. Fluid Mech.*, **460**:211–222.
Effect of Constitutive Laws for Two-Dimensional Membranes on Flow-Induced . . .

[98] Le Tirilly, S. *et al.* (2014), *ACS Macro Letters*, **4**(1):25–29.
Interplay of Hydrogen Bonding and Hydrophobic Interactions to Control the . . .

[99] Torcello-Gómez, A. *et al.* (2011), *J Nonnewton Fluid Mech*, **166**(12):713–722.
Surface Rheology of Sorbitan Tristearate and β-Lactoglobulin: Shear and . . .

[100] Krishnaswamy, R. *et al.* (2007), *Langmuir*, **23**(26):12951–12958.
Nonlinear Viscoelasticity of Sorbitan Tristearate Monolayers at Liquid/Gas . . .

[101] Erni, P. *et al.* (2005), *Langmuir*, **21**(23):10555–10563.
Sorbitan Tristearate Layers at the Air/Water Interface Studied by Shear and . . .

[102] Rehage, H. *et al.* (2001), *Colloid and Polymer Science*, **279**(6):597–606.
Ultrathin Dynamic Networks Formed by the Surfactant SPAN 65 at the Air-- . . .

[103] Oparin, A. I. (2003), *The Origin of Life*
Courier Corporation

[104] Miller, S. L. *et al.* (1953), *Science*, **117**(3046):528–529.
A Production of Amino Acids under Possible Primitive Earth Conditions

[105] Bada, J. L. and Lazcano, A. (2003), *Science*, **300**(5620):745–746.
Prebiotic Soup--Revisiting the Miller Experiment

[106] Koonin, E. V. and Martin, W. (2005), *Trends Genet.*, **21**(12):647–654.
On the Origin of Genomes and Cells Within Inorganic Compartments

[107] Alberts, B. *et al.* (2008), *Molecular Biology of the Cell*
Garland Science

[108] Lekka, M. *et al.* (1999), *European Biophysics Journal*, **28**(4):312–316.
Elasticity of Normal and Cancerous Human Bladder Cells Studied by Scanning . . .

[109] Suresh, S. (2007), *Acta Materialia*, **55**(12):3989–4014.
Biomechanics and Biophysics of Cancer Cells

[110] Phillips, R. *et al.* (2012), *Physical Biology of the Cell*
Garland Science

[111] Mostowy, S. and Cossart, P. (2012), *Nat. Rev. Mol. Cell Bio.*, **13**(3):183–194.
Septins: the Fourth Component of the Cytoskeleton

[112] *URL[7] (24.11.2017).*
Fluorent Cells

[113] Valencia, J. C., *URL[8] (24.11.2017).*
Melanoma Cells

[114] Dumont, S. and Mitchison, T. J. (2009), *Current Biology*, **19**(17):R749–R761.
Force and Length in the Mitotic Spindle

[115] Carvalho-Santos, Z. *et al.* (2011), *J Cell Biol*, **194**(2):165–175.
Tracing the Origins of Centrioles, Cilia, and Flagella

[116] Broussard, J. A. *et al.* (2008), *Curr. Opin. Cell Biol.*, **20**(1):85–90.
Asymmetric Focal Adhesion Disassembly in Motile Cells

[117] Ezratty, E. J. *et al.* (2005), *Nature cell biology*, **7**(6):581–590.
Microtubule-Induced Focal Adhesion Disassembly Is Mediated by Dynamin and . . .

[118] Wehrle-Haller, B. and Imhof, B. A. (2003), *Int. J. Biochem. Cell Biol.*, **35**(1):39–50.
Actin, Microtubules and Focal Adhesion Dynamics During Cell Migration

[119] Mitra, S. K. *et al.* (2005), *Nat. Rev. Mol. Cell Bio.*, **6**(1):56–68.
Focal Adhesion Kinase: in Command and Control of Cell Motility

[120] Efimov, A. and Kaverina, I. (2009), *Cell Adh Migr*, **3**(3):285–287.
Significance of Microtubule Catastrophes at Focal Adhesion Sites

[121] López, M. P. *et al.* (2014), *Nature communications*, **5**(4778).
Actin--Microtubule Coordination at Growing Microtubule Ends

[122] Honore, S. *et al.* (2005), *Cell. Mol. Life Sci.*, **62**(24):3039–3056.
Understanding Microtubule Dynamics for Improved Cancer Therapy

[123] Lansbergen, G. *et al.* (2004), *The Journal of cell biology*, **166**(7):1003–1014.
Conformational Changes in CLIP-170 Regulate its Binding to Microtubules . . .

[124] Vale, R. D. (1987), *Annual review of cell biology*, **3**(1):347–378.
Intracellular Transport using Microtubule-Based Motors

[125] Wloga, D. and Gaertig, J. (2010), *J Cell Sci*, **123**(20):3447–3455.
Post-Translational Modifications of Microtubules

[126] Janke, C. and Kneussel, M. (2010), *Trends in neurosciences*, **33**(8):362–372.
Tubulin Post-Translational Modifications: Encoding Functions on the Neuronal . . .

[127] Janke, C. and Bulinski, J. C. (2012), *Nat. Rev. Mol. Cell Bio.*, **13**(4):276–276.
Post-Translational Regulation of the Microtubule Cytoskeleton: Mechanisms . . .

---

[7] `https://imagej.nih.gov/ij/images/FluorescentCells.jpg`
[8] `https://commons.wikimedia.org/w/index.php?title=File:Metastatic_Melanoma_Cells_`
`Nci-vol-9872-300.jpg&oldid=220163104`

[128] Sirajuddin, M. *et al.* (2014), *Nature cell biology*, **16**(4):335–344.
Regulation of Microtubule Motors by Tubulin Isotypes and Post-Translational . . .

[129] Garnham, C. P. and Roll-Mecak, A. (2012), *Cytoskeleton*, **69**(7):442–463.
The Chemical Complexity of Cellular Microtubules: Tubulin Post-Translational . . .

[130] Hammond, J. W. *et al.* (2008), *Curr. Opin. Cell Biol.*, **20**(1):71–76.
Tubulin Modifications and their Cellular Functions

[131] Tanaka, E. M. and Kirschner, M. W. (1991), *J. Cell Biol.*, **115**(2):345–363.
Microtubule Behavior in the Growth Cones of Living Neurons During Axon . . .

[132] Al-Bassam, J. *et al.* (2002), *The Journal of cell biology*, **157**(7):1187–1196.
MAP2 and Tau Bind Longitudinally Along the Outer Ridges of Microtubule . . .

[133] Elie, A. *et al.* (2015), *Scientific reports*, **5**.
Tau Co-Organizes Dynamic Microtubule and Actin Networks

[134] Hawkins, T. L. *et al.* (2013), *Biophysical journal*, **104**(7):1517–1528.
Mechanical Properties of Doubly Stabilized Microtubule Filaments

[135] Drechsel, D. N. *et al.* (1992), *Molecular biology of the cell*, **3**(10):1141–1154.
Modulation of the Dynamic Instability of Tubulin Assembly by the Microtubule- . . .

[136] Goedert, M. and Spillantini, M. G. (2006), *science*, **314**(5800):777–781.
A Century of Alzheimer's Disease

[137] Avila, J. *et al.* (2004), *Physiological reviews*, **84**(2):361–384.
Role of Tau Protein in Both Physiological and Pathological Conditions

[138] Mitchison, T. and Kirschner, M. (1984), *Nature*, **312**(5991):237–242.
Dynamic Instability of Microtubule Growth

[139] Fygenson, D. *et al.* (1997), *Phys. Rev. Lett.*, **79**(22):4497–4500.
Mechanics of Microtubule-Based Membrane Extension

[140] Dogterom, M. *et al.* (2005), *Curr. Opin. Cell Biol.*, **17**(1):67–74.
Force Generation by Dynamic Microtubules.

[141] Dogterom, M. and Yurke, B. (1997), *Science*, **278**(5339):856–60.
Measurement of the Force-Velocity Relation for Growing Microtubules.

[142] Kühne, T. *et al.* (2009), *EPL*, **86**(6):68002.
Zipping Mechanism for Force Generation by Growing Filament Bundles

[143] Brangwynne, C. P. *et al.* (2006), *J. Cell Biol.*, **173**(5):733–41.
Microtubules Can Bear Enhanced Compressive Loads in Living Cells Because . . .

[144] Hotani, H. *et al.* (1999), *Curr. Opin. Colloid Interface Sci.*, **4**(5):358–368.
Giant Liposomes: from Membrane Dynamics to Cell Morphogenesis

[145] Waterman-Storer, C. M. *et al.* (1999), *Nat. Cell. Biol.*, **1**(1):45–50.
Microtubule Growth Activates Rac1 to Promote Lamellipodial Protrusion in . . .

[146] Rodriguez, O. C. *et al.* (2003), *Nat. Cell. Biol.*, **5**(7):599–609.
Conserved Microtubule-Actin Interactions in Cell Movement and Morphogenesis.

[147] Etienne-Manneville, S. (2004), *Traffic*, **5**(7):470–477.
Actin and Microtubules in Cell Motility: Which One Is in Control?

[148] Waterman-Storer, C. M. and Salmon, E. D. (1997), *J. Cell Biol.*, **139**(2):417–34.
Actomyosin-Based Retrograde Flow of Microtubules in the Lamella of Migrating . . .

[149] Wittmann, T. *et al.* (2003), *J. Cell Biol.*, **161**(5):845–51.
Regulation of Leading Edge Microtubule and Actin Dynamics Downstream of Rac1.

[150] Zeitz, M. and Kierfeld, J. (2014), *Biophysical journal*, **107**(12):2860–2871.

Feedback Mechanism for Microtubule Length Regulation by Stathmin Gradients

[151] Laan, L. *et al.* (2008), *Proc. Natl. Acad. Sci. USA*, **105**(26):8920–8925.
Force-Generation and Dynamic Instability of Microtubule Bundles

[152] Tindemans, S. H. *et al.* (2010), *Phys. Rev. Lett.*, **104**(5):058103.
Survival of the Aligned: Ordering of the Plant Cortical Microtubule Array

[153] Deinum, E. E. and Mulder, B. M. (2013), *Curr. Opin. Plant Biol.*, **16**(6):688–692.
Modelling the Role of Microtubules in Plant Cell Morphology

[154] Dogterom, M. and Surrey, T. (2013), *Curr. Opin. Cell Biol.*, **25**(1):23–9.
Microtubule Organization in Vitro.

[155] Holy, T. E. *et al.* (1997), *Proc. Natl. Acad. Sci. USA*, **94**(12):6228–31.
Assembly and Positioning of Microtubule Asters in Microfabricated Chambers.

[156] Lagomarsino, M. C. *et al.* (2007), *Biophys. J.*, **92**(3):1046–1057.
Microtubule Organization in Three-Dimensional Confined Geometries: . . .

[157] Nédélec, F. J. *et al.* (1997), *Nature*, **389**(6648):305–8.
Self-Organization of Microtubules and Motors.

[158] Nédélec, F. and Surrey, T. (2001), *C. R. Acad. Sci.*, **2**(6):841–847.
Dynamics of Microtubule Aster Formation by Motor Complexes

[159] Burakov, A. *et al.* (2003), *The Journal of cell biology*, **162**(6):963–969.
Centrosome Positioning in Interphase Cells

[160] Pavin, N. *et al.* (2012), *New J. Phys.*, **14**(10):105025.
Positioning of Microtubule Organizing Centers by Cortical Pushing and Pulling . . .

[161] Kozlowski, C. *et al.* (2007), *Cell*, **129**(3):499–510.
Cortical Microtubule Contacts Position the Spindle in C. Elegans Embryos

[162] Baumann, H. and Surrey, T. (2014), *J. Biol. Chem.*, **289**(32):22524–22535.
Motor-Mediated Cortical Versus Astral Microtubule Organization in Lipid- . . .

[163] Ruiz, M., *URL⁹ (24.11.2017).*
Cell Membrane

[164] McMahon, H. T. and Gallop, J. L. (2005), *Nature*, **438**(7068):590–596.
Membrane Curvature and Mechanisms of Dynamic Cell Membrane Remodelling

[165] Phillips, R. *et al.* (2009), *Nature*, **459**(7245):379–385.
Emerging Roles for Lipids in Shaping Membrane-Protein Function

[166] Janmey, P. and Kinnunen, P. (2006), *Trends in cell biology*, **16**(10):538–546.
Biophysical Properties of Lipids and Dynamic Membranes

[167] Zimmerberg, J. and Kozlov, M. M. (2006), *Nat. Rev. Mol. Cell Bio.*, **7**(1):9–19.
How Proteins Produce Cellular Membrane Curvature

[168] Duwe, H. *et al.* (1990), *Journal de Physique*, **51**(10):945–961.
Bending Elastic Moduli of Lipid Bilayers: Modulation by Solutes

[169] Lemmich, J. *et al.* (1996), *European biophysics journal*, **25**(1):61–65.
Solutes in Small Amounts Provide for Lipid-Bilayer Softness: Cholesterol, . . .

[170] Parthasarathy, R. *et al.* (2006), *Langmuir*, **22**(11):5095–5099.
Curvature-Modulated Phase Separation in Lipid Bilayer Membranes

[171] Sackmann, E. (1994), *FEBS letters*, **346**(1):3–16.
Membrane Bending Energy Concept of Vesicle-and Cell-Shapes and Shape- . . .

---

[9] `https://commons.wikimedia.org/w/index.php?title=File:Cell_membrane_detailed_diagram_en.svg&oldid=166425223`

[172] Gilden, J. and Krummel, M. F. (2010), *Cytoskeleton*, **67**(8):477–486.
Control of Cortical Rigidity by the Cytoskeleton: Emerging Roles for Septins

[173] Heidemann, S. R. and Wirtz, D. (2004), *Trends in cell biology*, **14**(4):160–166.
Towards a Regional Approach to Cell Mechanics

[174] Salbreux, G. *et al.* (2012), *Trends in cell biology*, **22**(10):536–545.
Actin Cortex Mechanics and Cellular Morphogenesis

[175] Fletcher, D. a. and Mullins, R. D. (2010), *Nature*, **463**(7280):485–92.
Cell Mechanics and the Cytoskeleton.

[176] De Gennes, P.-G. (1979), *Scaling Concepts in Polymer Physics*
Cornell university press

[177] MacKintosh, F. *et al.* (1995), *Physical review letters*, **75**(24):4425.
Elasticity of Semiflexible Biopolymer Networks

[178] Ananthakrishnan, R. *et al.* (2006), *Journal of theoretical biology*, **242**(2):502–516.
Quantifying the Contribution of Actin Networks to the Elastic Strength of . . .

[179] Gardel, M. *et al.* (2004), *Science*, **304**(5675):1301–1305.
Elastic Behavior of Cross-Linked and Bundled Actin Networks

[180] Henty-Ridilla, J. L. *et al.* (2016), *Science*, **352**(6288):1004–1009.
Accelerated Actin Filament Polymerization from Microtubule Plus Ends

[181] Da Silva, J. S. and Dotti, C. G. (2002), *Nature Reviews Neuroscience*, **3**(9):694–704.
Breaking the Neuronal Sphere: Regulation of the Actin Cytoskeleton in . . .

[182] Tinevez, J.-Y. *et al.* (2009), *Proc. Natl. Acad. Sci. USA*, **106**(44):18581–6.
Role of Cortical Tension in Bleb Growth.

[183] Paluch, E. K. and Raz, E. (2013), *Curr. Opin. Cell Biol.*, **25**(5):582–590.
The Role and Regulation of Blebs in Cell Migration

[184] Kunda, P. *et al.* (2008), *Current Biology*, **18**(2):91–101.
Moesin Controls Cortical Rigidity, Cell Rounding, and Spindle Morphogenesis . . .

[185] Matsumoto, Y. *et al.* (2014), *PloS one*, **9**(8):e105435.
Ezrin Mediates Neuritogenesis Via Down-Regulation of RhoA Activity in . . .

[186] Gilden, J. K. *et al.* (2012), *The Journal of cell biology*, **196**(1):103–114.
The Septin Cytoskeleton Facilitates Membrane Retraction During Motility and . . .

[187] Hu, Q. *et al.* (2010), *Science*, **329**(5990):436–439.
A Septin Diffusion Barrier at the Base of the Primary Cilium Maintains Ciliary . . .

[188] Tanaka-Takiguchi, Y. *et al.* (2009), *Current Biology*, **19**(2):140–145.
Septin-Mediated Uniform Bracing of Phospholipid Membranes

[189] Hall, A. (2005), *Biochemical Society Transactions*, **33**(5):891–895.
Rho GTPases and the Control of Cell Behaviour

[190] Ávila, G. R. *et al.* (2011), *EPL (Europhysics Letters)*, **94**(6):60007.
Firefly Courtship as the Basis of the Synchronization-Response Principle

[191] Mirollo, R. E. and Strogatz, S. H. (1990), *SIAM J. Appl. Math.*, **50**(6):1645–1662.
Synchronization of Pulse-Coupled Biological Oscillators

[192] Acebrón, J. A. *et al.* (2005), *Reviews of modern physics*, **77**(1):137.
The Kuramoto Model: A Simple Paradigm for Synchronization Phenomena

[193] Chopra, N. and Spong, M. W. (2009), *IEEE Trans. Autom. Control*, **54**(2):353–357.
On Exponential Synchronization of Kuramoto Oscillators

[194] Bornens, M. (2008), *Nat. Rev. Mol. Cell Bio.*, **9**(11):874–886.

Organelle Positioning and Cell Polarity

[195] Fan, H. and Li, S. (2014), *Computational Materials Science.*
Modeling Microtubule Cytoskeleton Via an Active Liquid Crystal Elastomer Model

[196] Brugués, J. and Needleman, D. (2014), *Proc. Natl. Acad. Sci. USA*, 201409404.
Physical Basis of Spindle Self-Organization

[197] Nedelec, F. and Foethke, D. (2007), *New J. Phys.*, **9**(11):427.
Collective Langevin Dynamics of Flexible Cytoskeletal Fibers

[198] Sampathkumar, A. *et al.* (2014), *eLife*, **3**.
Subcellular and Supracellular Mechanical Stress Prescribes Cytoskeleton . . .

[199] Verde, F. *et al.* (1992), *J. Cell Biol.*, **118**:1097–1108.
Control of Microtubule Dynamics and Length by Cyclin A- and Cyclin B- . . .

[200] Dogterom, M. and Leibler, S. (1993), *Phys. Rev. Lett.*, **70**(9):1347.
Physical Aspects of the Growth and Regulation of Microtubule Structures

[201] Bowne-Anderson, H. *et al.* (2015), *Trends in cell biology*, **25**(12):769–779.
Regulation of Microtubule Growth and Catastrophe: Unifying Theory and . . .

[202] Yarahmadian, S. *et al.* (2011), *J. Math. Biol.*, **63**(3):459–92.
Existence and Stability of Steady States of a Reaction Convection Diffusion . . .

[203] Splettstoesser, T., *URL*[10] *(24.11.2017).*
Diagram Showing a Microtubule and the Alpha/Beta-Tubulin Heterodimer.

[204] Zelinski, B. *et al.* (2012), *Phys. Rev. E*, **86**(4):041918.
Dynamics and Length Distribution of Microtubules under Force and Confinement

[205] Mulder, B. M. (2012), *Physical Review E*, **86**(1):011902.
Microtubules Interacting with a Boundary: Mean Length and Mean First- . . .

[206] Arnold, B. C. *et al.* (2011), *Records*
John Wiley & Sons

[207] Wergen, G. (2013), *Record Statistics Beyond the Standard Model - Theory and . . .*
Dissertation, University of Cologne

[208] Peskin, C. S. *et al.* (1993), *Biophysical journal*, **65**(1):316–324.
Cellular Motions and Thermal Fluctuations: the Brownian Ratchet

[209] Janson, M. E. *et al.* (2003), *The Journal of cell biology*, **161**(6):1029–1034.
Dynamic Instability of Microtubules Is Regulated by Force

[210] Flyvbjerg, H. *et al.* (1996), *Phys. Rev. E*, **54**(5):5538.
Microtubule Dynamics: Caps, Catastrophes, and Coupled Hydrolysis

[211] Bicout, D. J. (1997), *Physical Review E*, **56**(6):6656.
Green's Functions and First Passage Time Distributions for Dynamic Instability . . .

[212] Gardiner, C. W. (1985).
Handbook of Stochastic Methods for Physics, Chemistry, and the Natural Sciences

[213] Van Kampen, N. G. (1992), *Stochastic Processes in Physics and Chemistry*
Elsevier

[214] Dreher, A. *et al.* (2014), *New Journal of Physics*, **16**(5):055007.
Spiral Actin-Polymerization Waves Can Generate Amoeboidal Cell Crawling

[215] Löber, J. *et al.* (2014), *Soft matter*, **10**(9):1365–1373.
Modeling Crawling Cell Movement on Soft Engineered Substrates

---

[10]`https://commons.wikimedia.org/w/index.php?title=File:Microtubule_structure.png&oldid=`
`242661664`

[216] Pontani, L.-L. *et al.* (2009), *Biophysical journal*, **96**(1):192–198.
Reconstitution of an Actin Cortex Inside a Liposome

[217] Carvalho, K. *et al.* (2013), *Proc. Natl. Acad. Sci.*, **110**(41):16456–16461.
Cell-Sized Liposomes Reveal How Actomyosin Cortical Tension Drives Shape . . .

[218] Schulze, E. and Kirschner, M. (1987), *J. Cell Biol.*, **104**(2):277–288.
Dynamic and Stable Populations of Microtubules in Cells

[219] Clark, A. G. *et al.* (2013), *Biophysical journal*, **105**(3):570–580.
Monitoring Actin Cortex Thickness in Live Cells

[220] Pinot, M. *et al.* (2009), *Current Biology*, **19**(11):954–960.
Effects of Confinement on the Self-Organization of Microtubules and Motors

[221] Bausch, A. R. *et al.* (1998), *Biophysical journal*, **75**(4):2038–2049.
Local Measurements of Viscoelastic Parameters of Adherent Cell Surfaces by . . .

[222] Li, C. (2013), *Journal of Applied Mathematics*, **2013**.
A Conjugate Gradient Type Method for the Nonnegative Constraints . . .

[223] Zhang, L. *et al.* (2006), *IMA Journal of Numerical Analysis*, **26**(4):629–640.
A Descent Modified Polak--RibièRe--Polyak Conjugate Gradient Method and . . .

[224] Aronovitz, J. and Nelson, D. (1986), *Journal de Physique*, **47**(9):1445–1456.
Universal Features of Polymer Shapes

[225] Alim, K. and Frey, E. (2007), *Phys. Rev. Lett.*, **99**(19):198102.
Shapes of Semiflexible Polymer Rings

[226] Sander, J. *et al.* (1998), *Data mining and knowledge discovery*, **2**(2):169–194.
Density-Based Clustering in Spatial Databases: The Algorithm Gdbscan and . . .

[227] Postma, M. *et al.* (2004), *EMBO reports*, **5**(1):35–40.
Chemotaxis: Signalling Modules Join Hands at Front and Tail

[228] Borisy, G. G. and Svitkina, T. M. (2000), *Curr. Opin. Cell Biol.*, **12**(1):104–112.
Actin Machinery: Pushing the Envelope

[229] Vasiliev, J. M. *et al.* (1970), *J. Embryol. Exp. Morphol.*, **24**(3):625–640.
Effect of Colcemid on the Locomotory Behaviour of Fibroblasts

[230] Li, R. and Gundersen, G. G. (2008), *Nat. Rev. Mol. Cell Bio.*, **9**(11):860–873.
Beyond Polymer Polarity: How the Cytoskeleton Builds a Polarized Cell

[231] Verkhovsky, A. B. *et al.* (1999), *Current Biology*, **9**(1):11–S1.
Self-Polarization and Directional Motility of Cytoplasm

[232] Narang, A. (2006), *Journal of theoretical biology*, **240**(4):538–553.
Spontaneous Polarization in Eukaryotic Gradient Sensing: a Mathematical . . .

[233] Sadok, A. and Marshall, C. J. (2014), *Small GTPases*, **5**(4):e983878.
Rho GTPases: Masters of Cell Migration

[234] Jilkine, A. *et al.* (2007), *Bulletin of mathematical biology*, **69**(6):1943–1978.
Mathematical Model for Spatial Segregation of the Rho-Family GTPases Based . . .

[235] Van Leeuwen, F. N. *et al.* (1997), *The Journal of cell biology*, **139**(3):797–807.
The Guanine Nucleotide Exchange Factor Tiam1 Affects Neuronal Morphology; . . .

[236] Weichsel, J. and Schwarz, U. S. (2010), *Proc. Natl. Acad. Sci. USA*, **107**(14):6304–6309.
Two Competing Orientation Patterns Explain Experimentally Observed . . .

[237] Waterman-Storer, C. M. and Salmon, E. D. (1999), *Curr. Opin. Cell Biol.*, **11**(1):61–67.
Positive Feedback Interactions between Microtubule and Actin Dynamics During . . .

[238] Lewkowicz, E. *et al.* (2008), *The Journal of cell biology*, **183**(7):1287–1298.

The Microtubule-Binding Protein CLIP-170 Coordinates MDia1 and Actin . . .

[239] Al-Rekabi, Z. *et al.* (2014), *Experimental cell research*, **322**(1):21–29.
Microtubules Mediate Changes in Membrane Cortical Elasticity During . . .

[240] Worthylake, R. A. and Burridge, K. (2003), *J. Biol. Chem.*, **278**(15):13578–13584.
RhoA and ROCK Promote Migration by Limiting Membrane Protrusions

[241] Xu, J. *et al.* (2003), *Cell*, **114**(2):201–214.
Divergent Signals and Cytoskeletal Assemblies Regulate Self-Organizing Polarity . . .

Acknowledgements

Ich bedanke mich bei Jan Kierfeld für intensive Diskussionen, konstruktive Ideen, kritische Anmerkungen und die Eröffnung neuer Kontakte und Kooperationen. In diesem Kontext möchte ich auch Timo Betz für seine Tipps bezüglich möglicher Polarisations-Mechanismen danken.

Ich bedanke mich bei meinen Kollegen Tobias Alexander Kampmann und Horst-Holger Boltz, die mir während meiner Zeit an der Universität zunächst als Mentoren und schließlich als Freunde zur Seite standen. Ich bedanke mich bei Sebastian Knoche und Björn Zelinski für die Einführung in mein Master- und Dissertations-Thema sowie die theoretischen Arbeiten, die sie mir und anderen hinterlassen haben. Außerdem möchte ich Felix Schwietert für viele kritische Anmerkungen und Ideen danken.

Ich bedanke mich bei den Mitgliedern des Lehrstuls für physikalische Chemie II an der TU Dortmund, namentlich Simon Egger, Maureen Kott, Sarah Demand, Anja Unverfehrt, Patrick Degen und Elena Zwar für die produktive Zusammenarbeit. Besonderer Dank gilt Heinz Rehage, der diese Zusammenarbeit mit ermöglicht und vorangetrieben hat. Ich bedanke mich bei Andrew Salmon und Chris Abell für die experimentellen Daten, die sie mir zu Verfügung stellten. Für Gleiches danke ich Sandrine Le Tirilly und Cécile Monteux.

Besonders bedanke ich mich bei meinen Eltern Silvia und Winfried Hegemann für die Liebe und vielseitige Unterstützung, die sie mir, nicht nur während meiner Dissertation, haben zukommen lassen.